UNIVERSITY OF CAMERINO

SCHOOL OF ADVANCED STUDIES

Chemical and Pharmaceutical Sciences and Biotechnologies Area

Ph.D. Curriculum in Chemical Science

XXXVII Cycle

Doctoral Thesis

Cathodes Development and Cell Manufacturing for Innovative Li-ion and Na-ion Batteries

Ph.D. Candidate

Luca Minnetti

Supervisor

Prof. Francesco Nobili

Academic Year 2021/2022 – 2023/2024

“Ma l’impresa eccezionale,

dammi retta, è essere normale”

ABSTRACT

The present thesis work is focused on the study of cathode materials and the related cell manufacturing to obtain Li-ion and Na-ion batteries for possible practical applications. In particular, the use of a Fe/Mn-based mixed olivine cathode in both systems, the scalability of electrode processing and manufacturing in Li-ion cells, and the proof-of-concept evaluation of full-cell balancing, coupling layered oxide cathodes and Sn- or Si-based alloying anodes, are herein studied in this thesis.

Energy production has been worldwide moving toward renewable sources to overcome the several drawbacks presently attributed to the massive use of fossil fuels. In these regards, electrochemical energy storage (EES) systems, in particular rechargeable batteries, play the most relevant role in storing green energy. Relevantly, to achieve the goals of sustainability, good management, and safety, non-toxic, cheap, and stable polyanionic phospho-olivines have been promoted and largely used in commercial batteries, despite low ionic and electronic conductivity and relatively low working potential (*i.e.* 3.45 V vs. Li^+/Li for $LiFePO_4$), which could be increased using other transition metals, such as Mn. Additionally, the possible implementation of Na-ion batteries for stationary storage could also increase the sustainability of EES systems, due to the abundancy of sodium with respect to lithium, while the alkali metal substitution requires notable and dedicated studies. Furthermore, the optimization of other practical aspects regarding electrodes and cell manufacturing (*i.e.* slurry properties, coating procedure, electrode balancing etc.) is another key parameter to obtain improvement on battery performances, especially on industrial scale. On the other hand, the high energy density of layered oxide cathodes is required in different applications, making relevant the study of these materials, particularly when combined with anodes with high theoretical capacity (*i.e.* alloying-based anodes).

In the first chapter a mixed $LiFe_{0.6}Mn_{0.4}PO_4$ (LFMP) olivine cathode was synthesized and characterized in terms of structure, morphology and electrochemical features in lithium metal cell. Therefore, due to the positive results in conventional electrolyte, LFMP was studied in a lithium metal polymer battery with a solid configuration, using a polyethylene glycol dimethyl ether-based electrolyte, showing promising outcomes in terms of capacity, efficiency, and retention. Subsequently, LFMP was electrochemically converted to $NaFe_{0.6}Mn_{0.4}PO_4$ (NFMP) with triphylite structure for application in Na-ion battery. The NFMP cathode was deeply characterized in terms of structure, morphology and electrochemical features in sodium metal cell with encouraging findings, and afterwards compared with the lithium analogue LFMP in terms of ion transport and interfacial characteristics using various electrochemical techniques, combined with the calculation of the

distribution of relaxation times (DRT) functions. Furthermore, the electrochemical reaction mechanism and structure of NFMP cathode were additionally investigated by means of *ex-situ* and *in-situ* (*operando*) XAS experiments.

In the second chapter the role of conductive carbon additives and the refining of electrode manufacturing using commercial $LiMn_{0.7}Fe_{0.3}PO_4$ (LMFP73) as active material have been studied. The optimization of additive content, mixing protocol, solid content, coating speed, and electrode loading was carried out to produce electrodes suitable for industrial use, subsequently coupled with graphite anode to achieve lab-scale coin-type full-cells and upscaled single-layer pouch cell, presenting promising stable capacity retained for over 100 cycles and good energy density at the electrodes level.

The last chapter is focused on full-cell balancing using layered oxide cathodes and alloying-based anodes. $LiNi_{0.2}Co_{0.2}Al_{0.1}Mn_{0.45}O_2$ (LNCAM) was synthetized and deeply characterized in Li-cell. Particularly, its relevant irreversibility during first charge is advantageously exploited for compensating the pristine inefficiency of a Li-alloying silicon oxide composite without any preliminary treatment in proof-of-concept full-cells with different N/P ratios. Moreover, a sodiated version of a tin-carbon (Sn-C) alloying material was obtained exploiting a versatile chemical strategy, and the Na_xSn-C anode was combined with sodium-deficient layered oxide cathode ($NaNi_{0.2}Co_{0.2}Al_{0.1}Mn_{0.45}O_2$, NCAM) for application in proof-of-concept Na-ion full-cell investigated by electrochemical impedance spectroscopy and *ex-situ* measurements. For both studied systems the applicability of the proposed balancing methods is evidenced, despite further optimization is required to enhance the efficiency of the batteries.

PREFACE

The present doctoral thesis reports the results obtained during the three-year PhD course with curricula in Chemical Sciences carried out at the University of Camerino (Italy), under the supervision of Prof. Francesco Nobili. It is also referred to the results acquired during a seven-month internship in collaboration with the Warwick Manufacturing Group – WMG (United Kingdom), under the supervision of Prof. Ivana Hasa. This work also involved collaboration with the University of Ferrara (Italy), thanks to Prof. Jusef Hassoun.

The research project reported in this thesis is the subject of some of the scientific publications, patents, and conference proceedings produced during the three years of PhD and listed below.

Scientific Publications:

1) Minnetti L., Marangon V., Hassoun J. (2022) Synthesis and Characterization of a $LiFe_{0.6}Mn_{0.4}PO_4$ Olivine Cathode for Application in a New Lithium Polymer Battery. *Adv. Sustain. Syst.*, 6 (5), 2100464. DOI: 10.1016/j.jechem.2024.04.028.

2) Sbrascini L., Staffolani A., Bottoni L., Darjazi H., Minnetti L., Minicucci M., Nobili F. (2022) Structural and Interfacial Characterization of a Sustainable Si/Hard Carbon Composite Anode for Lithium-Ion Batteries. *ACS Appl. Mater. Interfaces,* 14 (29), 33257-33273. DOI: 10.1021/acsami.2c07888.

3) Minnetti L., Marangon V., Andreotti P., Staffolani A., Nobili F., Hassoun J. (2023) Reciprocal irreversibility compensation of $LiNi_{0.2}Co_{0.2}Al_{0.1}Mn_{0.45}O_2$ cathode and silicon oxide anode in new Li-ion battery. *Electrochim. Acta*, 452, 142263. DOI: 10.1016/j.electacta.2023.142263.

4) Patriarchi A., Darjazi H., Minnetti L., Sbrascini L., Elia G.A., Castorani V., Munoz-Marquez M.A., Nobili F. (2024) All-Solid-State Li-Metal Cell Using Nanocomposite TiO_2/Polymer Electrolyte and Self-Standing $LiFePO_4$ Cathode. *Batteries*, 10 (1), 11. DOI: 10.3390/batteries10010011.

5) Minnetti L., Sbrascini L., Staffolani A., Marangon V., Nobili F., Hassoun J. (2024) Unravelling the ion transport and the interphase properties of a mixed olivine cathode for Na-ion battery. *J. Energy Chem.,* 96, 300-317. DOI: 10.1016/j.jechem.2024.04.028

6) Staffolani A., Sbrascini L., Bottoni L., Minnetti L., Darjazi H., Trapananti A., Paparoni F., Rezvani S.J., Minicucci M., Harfouche M., Nobili F. (2024) *Energy Advances,* 3, 1726. DOI: 10.1039/D4YA00335G.

7) Patriarchi A., Triolo C., Minnetti L., Munoz-Marquez M.A., Nobili F., Santangelo S., (2025) Evaluation of high-entropy (Cr, Mn, Fe, Co, Ni)-oxide nanofibers and nanoparticles as passive fillers for solid composite electrolytes. *Electrochim. Acta,* 512, 145425. DOI: 10.1016/j.electacta.2024.145425.

8) Patriarchi A., Caroni J., Minnetti L., Sbrascini L., Darjazi H., Nobili F., Munoz-Marquez M.A., (2025) Impact of Prussian Blue Particle Size Distribution on Electrochemical Performance of Gel Polymer Electrolyte-based Na-ion cells. *Chemelectrochem*, e202400350. DOI: 10.1002/celc.202400350.

9) Minnetti L., Maddar F.M., Haridas A.K., Capener M., Nobili F., Hasa I., (2024) Assessing Manufacturing-Performance Correlation On $LiMn_{0.7}Fe_{0.3}PO_4$ Electrodes For Application In Upscaled Li-ion Battery Cells. *Batteries & Supercaps*, e202400645. DOI: 10.1002/batt.202400645.

10) Staffolani A., Sbrascini L., Carbonari G., Maroni F., Minnetti L., Bottoni L., Nobili F., (2024) Tailoring the Electrochemical Performance of SnO_2-based Anodes for Li-Ion Batteries: Effect of Morphology and Composite Matrix. *Adv. Mater. Technol.*, **Under Revision**.

11) Minnetti L., Sbrascini L., Nobili F., Hassoun J., (2024) Chemical approach to achieve sodiated alloying anode for direct application in Na-ion battery. *Mater. Chem. Phys.*, **Under Revision**.

12) Minnetti L., Paparoni F., Zitolo A., Torretti E., Rezvani S.J., Nobili F., (2025) An operando X-ray absorption study of the sodium insertion in $NaFe_{0.6}Mn_{0.4}PO_4$ electrode. *Acta Materialia*, **In preparation**.

Patents:

1) Patent (**granted**) "METODO PER LA RELITIAZIONE AD ELEVATA SOSTENIBILITA' DELLA MATERIA ATTIVA DI UNA BATTERIA LFP ESAUSTA, NONCHE' POLVERE RELITIATA CON TALE METODO E METODO PER LA REALIZZAZIONE DI UNA BATTERIA LFP A PARTIRE DALLA POLVERE RELITIATA" **Inventors:** Dr. Antunes Staffolani (University of Camerino), Prof. Francesco Nobili (University of Camerino), Luca Minnetti (University of Camerino), Filippo Girardi (Midac S.p.A).

Conference Proceedings:

1) Minnetti L., Marangon V., Hassoun J – *Synthesis and Characterization of a $LiFe_{0.6}Mn_{0.4}PO_4$ Olivine Cathode for Application in a New Lithium Polymer Battery.* Symposium for Young

Chemists (SYNC 2022), University of Rome (Sapienza), Italy, 20-23/06/2022 – **Oral communication (accepted speaker)**.

2) Minnetti L., Marangon V., Hassoun J– *Synthesis and Characterization of a $LiFe_{0.6}Mn_{0.4}PO_4$ Olivine Cathode for Application in a New Lithium Polymer Battery.* Giornate dell'Elettrochimica Italiana (GEI 2022), Orvieto, Italy, 11-15/09/2022 – **Poster**.

3) Minnetti L., Marangon V., Hassoun J– *Synthesis and Characterization of a $LiFe_{0.6}Mn_{0.4}PO_4$ Olivine Cathode for Application in a New Lithium Polymer Battery.* 2nd Italian Workshop on Energy Storage (IWES 2023), Bressanone, Italy, 25-27/01/2023 – **Oral communication (accepted speaker)**.

4) Minnetti L., Marangon V., Andreotti P., Staffolani A., Nobili F., Hassoun J – *Reciprocal irreversibility compensation of $LiNi_{0.2}Co_{0.2}Al_{0.1}Mn_{0.45}O_2$ cathode and silicon oxide anode in new Li-ion battery.* Congresso Interregionale TUMA 2023, Francavilla al Mare, Italy, 22-23/06/2023 – **Oral communication (accepted speaker)**.

5) Minnetti L., Sbrascini L., Staffolani A., Marangon V., Nobili F., Hassoun J. – *Transport and Interphase Features of a Converted Mixed Olivine Cathode for Sodium-Ion Batteries.* 37th Topical Meeting of the International Society of Electrochemistry (ISE), Stresa, Italy, 09-12/06/2024 – **Pitch presentation (accepted speaker)**.

Awards:

1) Best Oral Communication, *Synthesis and Characterization of a $LiFe_{0.6}Mn_{0.4}PO_4$ Olivine Cathode for Application in a New Lithium Polymer Battery.* 2nd Italian Workshop on Energy Storage (IWES 2023), Bressanone, Italy, 25-27/01/2023.

2) Best Pitch Award, *Transport and Interphase Features of a Converted Mixed Olivine Cathode for Sodium-Ion Batteries.* 37th Topical Meeting of the International Society of Electrochemistry (ISE), Stresa, Italy, 09-12/06/2024.

TABLE OF CONTENTS

1. Introduction ..... 1—10

1.1 Electrochemical Energy Storage Systems (EESSs) ..... 1—12

1.2 Lithium-ion Batteries (LIBs) ..... 1—14

1.3 Sodium-ion Batteries (SIBs) ..... 1—18

1.4 Cell Materials and Components ..... 1—20

1.4.1 Cathode Materials ..... 1—20

1.4.2 Anode Materials ..... 1—30

1.4.3 Electrolytes ..... 1—40

1.5 Electrodes Processing and Manufacturing ..... 1—43

1.6 Distribution of Relaxation Time (DRT) Function ..... 1—45

1.7 Aim of the work ..... 1—47

2. Structural, Electrochemical and Interfacial Characterization of $AFe_{0.6}Mn_{0.4}PO_4$ (A = Li, Na) Mixed-Olivine Cathodes for Li-ion and Na-ion Batteries ..... 2—48

2.1 Experimental Section ..... 2—50

2.2 Synthesis, Characterization, and Application in Lithium Polymer Battery of $LiFe_{0.6}Mn_{0.4}PO_4$ Mixed-Olivine Cathode ..... 2—58

2.2.1 Structural, Morphological and Electrochemical Characterization of LFMP Cathode ..... 2—58

2.2.2 Lithium Polymer Cell Employing LFMP Cathode and PEGDME_CPE Electrolyte ..... 2—71

2.3 Transport and Interphase Features of a Converted Mixed Olivine Cathode for Sodium-Ion Batteries ..... 2—74

2.3.1 Electrochemical Conversion of LFMP to NFMP ..... 2—74

2.3.2 Electrochemical Characterization of NFMP ..... 2—79

2.3.3 Ion Transport and Interphase Features of LFMP and NFMP ..... 2—88

2.4 Operando X-ray Absorption Study of Na Insertion Mechanism in $NaFe_{0.6}Mn_{0.4}PO_4$ Structure ..... 2—104

2.5 Conclusions ..... 2—113

3. Investigation of Formulation Effect and Manufacturing Process on $LiMn_{0.7}Fe_{0.3}PO_4$ Cathode for Application in Upscaled Li-ion Batteries ..... 3—116

3.1 Experimental Section ..... 3—118

3.2 Results and Discussion ..... 3—121

3.2.1 Investigation of the Impact of SWCNTs Content inLMFP73 Electrodes ..... 3—123

3.2.2 Investigation of the Impact of Slurry and Electrode Processing Parameters ..... 3—134

3.2.3 Investigation of the Impact of Electrode Loading and Upscaling to Single Layer Pouch Cells ..... 3—139

3.3 Conclusions ..... 3—146

4. Investigation of Full-Cells Balancing Employing Layered Oxide Cathodes and Alloying-Based Anodes ..... 4—148

4.1 Experimental Section ..... 4—150

4.2 Reciprocal Irreversibility Compensation of Layered Oxide Cathode and Silicon Oxide Anode in Proof-of-Concept Li-ion Battery ..... 4—155

4.2.1 Structural, Morphological, and Electrochemical Characterization of LNCAM Cathode in Lithium Batteries ..... 4—155

4.2.2 Investigation of Proof-of-Concept SiO_x-C|LNCAM Full-Cells with Different N/P Ratios ..... 4—166

4.3 Chemical Approach to Achieve Sodiated Alloying Anode for Direct Application in Na-ion Battery ..... 4—174

4.4 Conclusions ..... 4—186

5. General Conclusions ..... 5—188

6. References ..... 6—190

1. Introduction

Global climate change is one of the most important problems that society is currently facing, with a great impact for the environment and ecosystems all over the world, as well as to economic losses and fatalities, as reported in **Figure 1.1 (**taken from the European Environment Agency (EEA) website).[1] Several effects could be already observed because of this phenomenon, such as progressively dissolution of Artic glaciers, rising of sea levels, expansion of deserts, extinction of many animals' species, and extreme weather phenomena, that are related to the decreasing of food and water for human beings.[1,2]

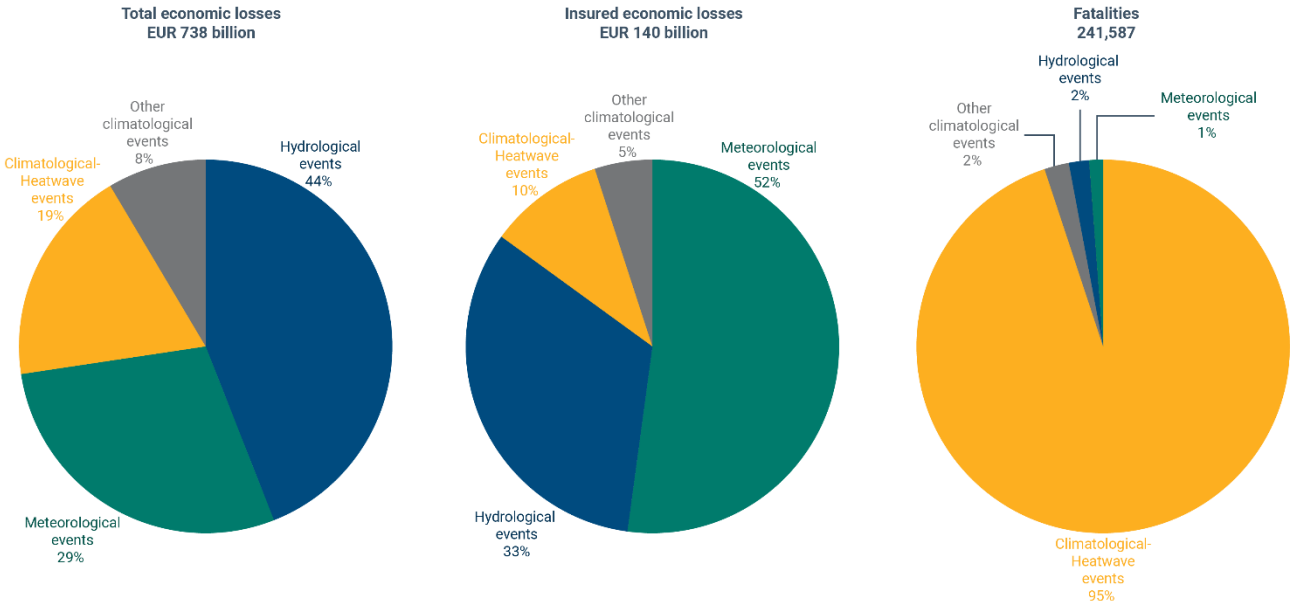

Figure 1.1: *Economic losses and fatalities caused by weather and climate, and related extreme events in EU Member States (1980-2023) per hazard type. Image taken from EEA website.*[1]

As reported by the National Centers for Environmental Information (NCEI), in 2023 the annual global surface temperature was from 0.55 to 0.6 °C higher than the average of the 1991 – 2020, making 2023 the warmest years since records began in the mid to late 1800s (**Figure 1.2**), following the trend of the previous eight years.[3] This trend of increasing temperature could lead to alarming consequences, as described above, such as the risk of tipping the ocean circulation in the Atlantic, which could lead to extreme weather conditions in the northern countries in the next few decades.[2,4]

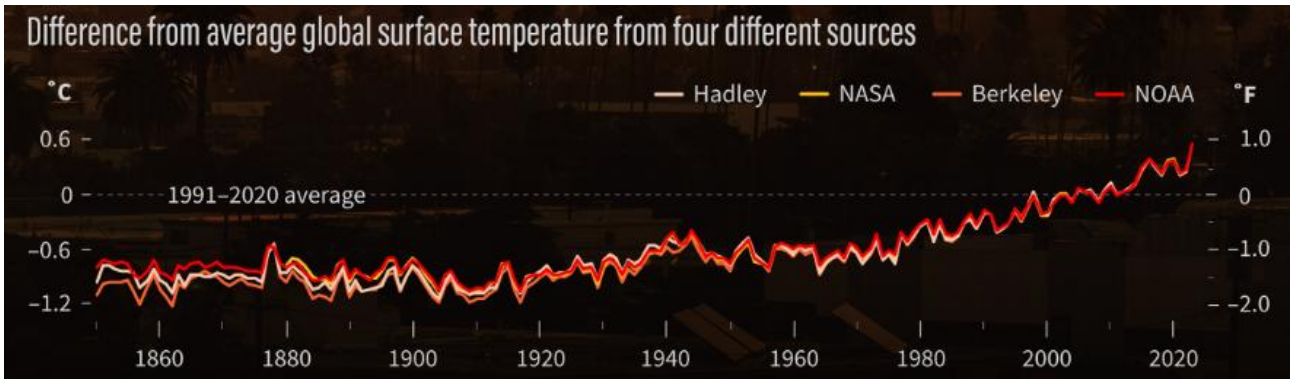

Figure 1.2: *Yearly global surface temperature compared to the 1991-2020 average from 1850 to 2023, based on data from four different sources. Image taken from the NCEI website.*[3]

The observed changes in the climate, especially related to the increase of the global temperature, which is expected to continue to rise for many decades, have the main causes in the emission into the atmosphere of greenhouse gases (GHGs) such as methane and CO_2, that are a directly connected to human activities, especially after the XVIII century. Indeed, the concentration of CO_2 in the atmosphere constantly increasing since pre-industrial revolution levels, with an increment of 46% during the last decades (**Figure 1.3**).[2,3,5]

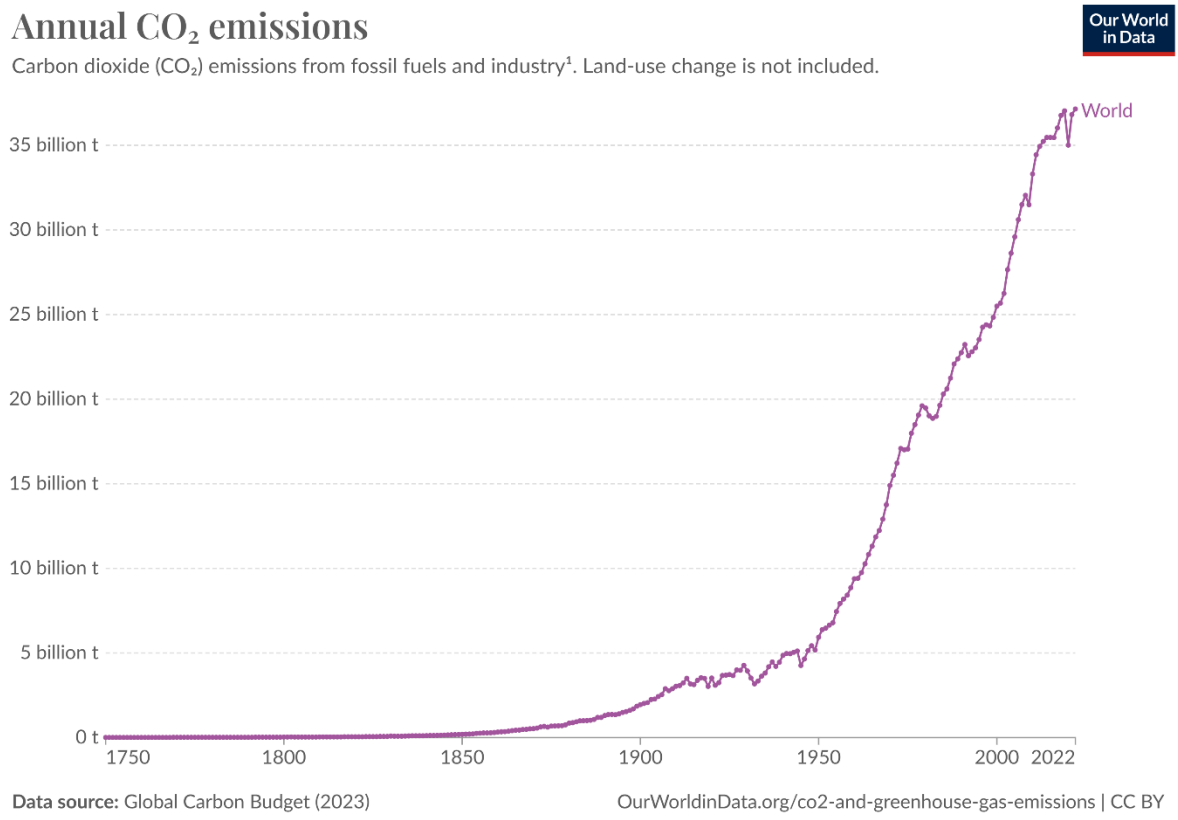

Figure 1.3: *Trend of CO_2 emissions from fossil fuels and industry worldwide measured in CO_2eq. Image taken from ourworldindata.org website.*[5]

To meet the goals stated in the Paris Agreement, a fast reduction in CO_2 emissions to reach the Net Zero Scenario by 2050 is mandatory, requiring several policy approaches and correctives, particularly related to key factors such as energy efficiency, renewable energies, electrification, and carbon capture/storage.[6,7] In these regards, over 50 billion tons of CO_2 are produced every year due to fossil fuels consumption.[2] Therefore, the global power sector (electricity and heat production) and the transport sector are those where an action is required to break down the total emissions, which account for ~ 73% of the total worldwide.[2,8]

The data presented clearly show the necessity to improve energy production, with a transition from limited and polluting fossil fuels (*i.e.* oil, coal and natural gas) to more sustainable, renewable, and environmentally friendly sources such as solar, wind, hydroelectric or geothermal. For this purpose, building sustainable infrastructure to produce electricity from renewable sources on a large scale is imperative, due to the intrinsic intermittent nature of the latter. Indeed, resources like sun or wind are unsuitable for widespread adoption and integration in the energy grid and don't match the increasing energy demand.[9,10] Nevertheless, decarbonization will be achieved by moving forward from fossil fuels, which implies that continuous supply of renewable energy is necessary, and it can only be reached by the presence and the implementation of appropriate energy storage systems (ESS).[9]

1.1 Electrochemical Energy Storage Systems (EESSs)

Electrochemical energy storage systems (EESSs) have a relevant importance for the transition to a low-carbon energy consumption, because electricity is the preferential way for storing energy. All the devices able to store and release electrical energy by taking advantage of redox reactions are included in the EESSs. These are divided into several classes, as shown in **Figure 1.4**:

- *Capacitors* and *supercapacitors* are devices which mainly exploit capacitive surface charge process to store electrical energy.
- *Batteries* exploit bulk reactions within the electrode structure occurring through charge transfer process as the main drivers for energy storage.
- *Fuel cells* possess the highest energy density but still require continuous input of reactant and a backup system to store and produce energy.

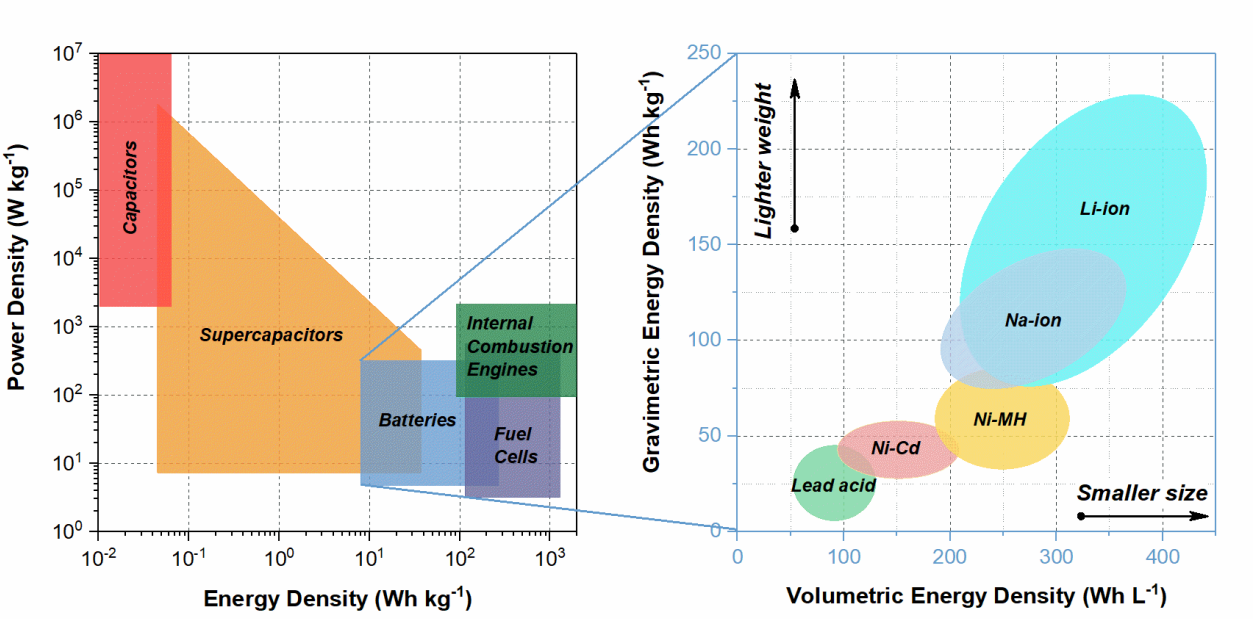

Figure 1.4: *Ragone plot showing different EESSs in comparison to internal combustion engines, with emphasis on the different types of batteries.*

For energy demanding applications, secondary rechargeable batteries represent the most promising devices to substitute the internal combustion engines in the electrical grid, due to their high energy density coupled with acceptable power density. Nevertheless, many key parameters including nominal voltage, cycle life, energy and power densities, and stability mostly depend on the cell chemistry of the battery.[11–13]

Considering all different types of batteries, two technologies seem to be the most applicable and are expected to dominate the market in the future:

- Already established Li-ion battery technology, that is the most used one since its commercialization by SONY Corporation in 1991.[14] Li-ion batteries predominate the market of portable electronic devices and large-scale stationary storage due to their prevailing volumetric and gravimetric energy densities in comparison with other battery systems (*i.e.* Ni-Cd, Ni-MH, and Lead Acid), thus arising in better output despite maintaining a small size and weight of devices.
- Recently or near to be commercialized Na-ion battery technology (*i.e.* by CATL, Faradion, Natron).[15–18] Na-ion batteries were initially studied in parallel research lines with respect to the lithium ones, gaining in last year's more attention as alternative to Li-ion batteries in particular applications, owing to their environmental and economical sustainability.

1.2 Lithium-ion Batteries (LIBs)

Lithium-ion batteries (LIBs) currently are the most exploited power source systems used in portable electronic devices and large-scale applications, like electric (EVs), hybrid (HEVs), or plug-in hybrid (PHEVs) vehicles and stationary energy storage, thanks to the characteristic above described and have been constantly improved over the last 30 years.[11] Li metal has always represented an attractive choice as possible anode material in batteries, thanks to its properties such as low atomic mass (6.941 a.m.u.), low standard electrode potential (-3.04 V vs. SHE), and high theoretical specific capacity (3860 mAh g^{-1}), making its possible use in primary batteries a deeply studied topic in combination with different cathodes, until their commercialization in the 1960's.[19–22] Subsequently, in the 1970's M. Armand conceptualized the first prototype of lithium-ion battery based on Li-ion intercalation into two different materials for both anode and cathode.[20,23] The intercalation into host materials and the lithium transfer into the electrodes during charge/discharge processes was later demonstrated by Scrosati and Lazzari in 1980,[24] and they called it "*rocking-chair*" mechanism referred to the peculiar shuttling of Li^+ ions. Particularly, Wittingham demonstrated in the previous years (around 1975) Li^+ intercalation in the layered structure of several dichalcogenides,[25] and among them TiS_2 appeared a valuable choice for its peculiarities (*i.e.* low cost, low molecular weight, good electronic conductivity). Indeed, TiS_2 presented the ability to intercalate lithium with a potential of 2 V vs. Li^+/Li and a theoretical capacity of about 240 mAh g^{-1}.[26] The results discovered for this material encouraged EXXON to attempt to produce secondary Li-ion batteries by using Li metal as the counter electrode and nonaqueous liquid electrolytes.[27] On the other hand, the use of TiS_2 presented severe problems in terms of synthesis and storage of the material, caused by its high moisture sensitivity, with consequential decomposition in TiO_2 and H_2S.[28] Furthermore, the formation of the so-called Solid Electrolyte Interphase (SEI) surface layer when alkali metals were combined with the mentioned electrolytes was observed.[29] SEI is ionic conductive but electrically insulating, suggesting beneficial effects thanks to the passivation of lithium surface and its related stability in the electrolyte; nevertheless, the instability of the SEI layer upon prolonged cycles was observed, resulting in possible cracks and lithium exposure to the electrolyte.[30] This behavior leads to electrolyte and active lithium consumption due to the repeated formation/dissolution of the passivation layer, coupled with the necessity to design secondary batteries with metal Li excess to achieve suitable coulombic efficiencies.[31] Furthermore, the deposition and availability of lithium on the unstable SEI surface conducts to safety issues, related to the formation of highly reactive dendrites and *"dead lithium"* spots, which could cause a decrease of thermal stability of the batteries (undesired exothermic reactions), derived from internal short-circuit and sparks (**Figure 1.5**).[32]

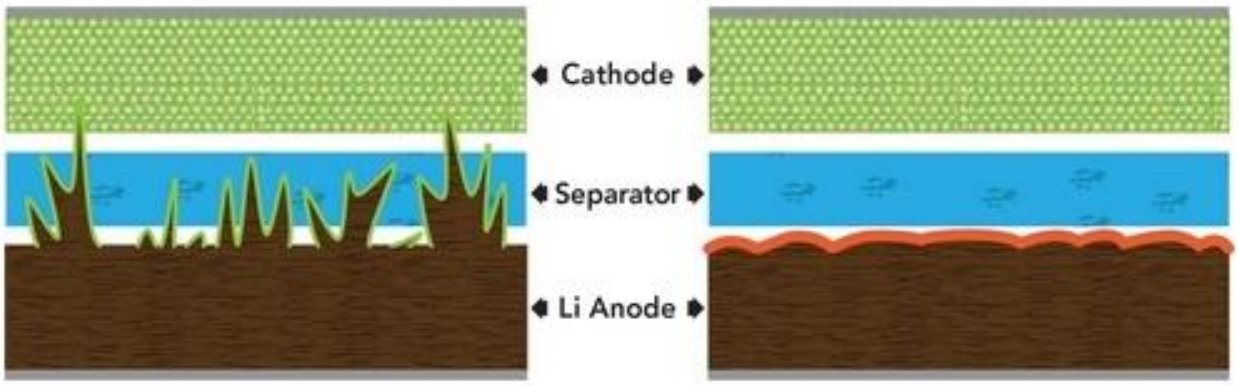

Figure 1.5: *Schematic internal representation of a secondary cell highlighting the difference between the formation of a suitable passivation layer and the parasitic formation of dendrites. Adapted from [32].*

First attempts to lower the dendritic growth were conducted by employing Li/Al or Li/Mg alloys at the anode side,[33,34] while accompanied by capacity and electrode potential losses, making the combination with TiS_2 less appealing for commercialization. The necessity to overcome safety issues related to the use of lithium metal brought Besenhard and Eichinger to conduct in 1976 first studies of Li^+ intercalation into graphite, with related potential close to the thermodynamic one of Li metal and reversible intercalation up to LiC_6.[31,35,36] Anyway, the lack of suitable electrolytes which prevented solvent co-intercalation with consequent exfoliation of lithiated lamellar graphite and fast capacity fading, limited its use in cell as cathode material,[37,38] while in 1978 Armand demonstrated its suitability as negative electrode by using a polymer electrolyte.[39] The promising results obtained for graphite as a feasible substitute of metal Li had lead Basu in 1979 to develop a synthesis of LiC_6 by using molten lithium,[40] according to the results obtained by Bell labs,[38] while its use was limited by the high operating temperatures (375 – 500 °C). Furthermore, in 1985 Yoshino developed a battery with an anode of petroleum coke, which could host Li^+ ions.[41,42]

In concomitance with the discovery of the *"rocking-chair"* mechanism, Goodenough developed in 1980 a high-voltage layered $LiCoO_2$ (LCO) cathode, from which lithium is reversibly de-intercalated to an upper cut-off voltage of 4.2 V vs. Li^+/Li.[43] Subsequently, Dahn demonstrated in 1990 the stability of graphite in nonaqueous electrolyte solutions, established by a combination of ethylene carbonate (EC) and propylene carbonate (PC) as solvents, with little capacity fading, thanks to the formation of a stable SEI layer at 0.8 V vs. Li^+/Li.[44] As a direct consequence, solvent mixtures of cyclic (EC or PC) and linear (dimethyl carbonate, DMC, or diethyl carbonate, DEC) esters with lithium hexafluorophosphate ($LiPF_6$) as salt, are the commonly adopted electrolytes in LIBs.[45] The conducted research brought to the commercialization of the first Li-ion battery, proposed by Sony Corporation in 1991, with the related worldwide success until nowadays.[14] Furthermore, M. S. Whittingham, J. B. Goodenough, and A. Yoshino were awarded in 2019 the Nobel Prize in Chemistry, for their contribution to the development of Li-ion technology.[46]

Despite a progressive optimization of the various components that compose LIBs over the years, they still hinge on the same basic design of 35 years ago; indeed, Li-ion batteries main components are the cathode, anode, electrolyte solution, separator, and the current collectors, as displayed in **Figure 1.6**.[47]

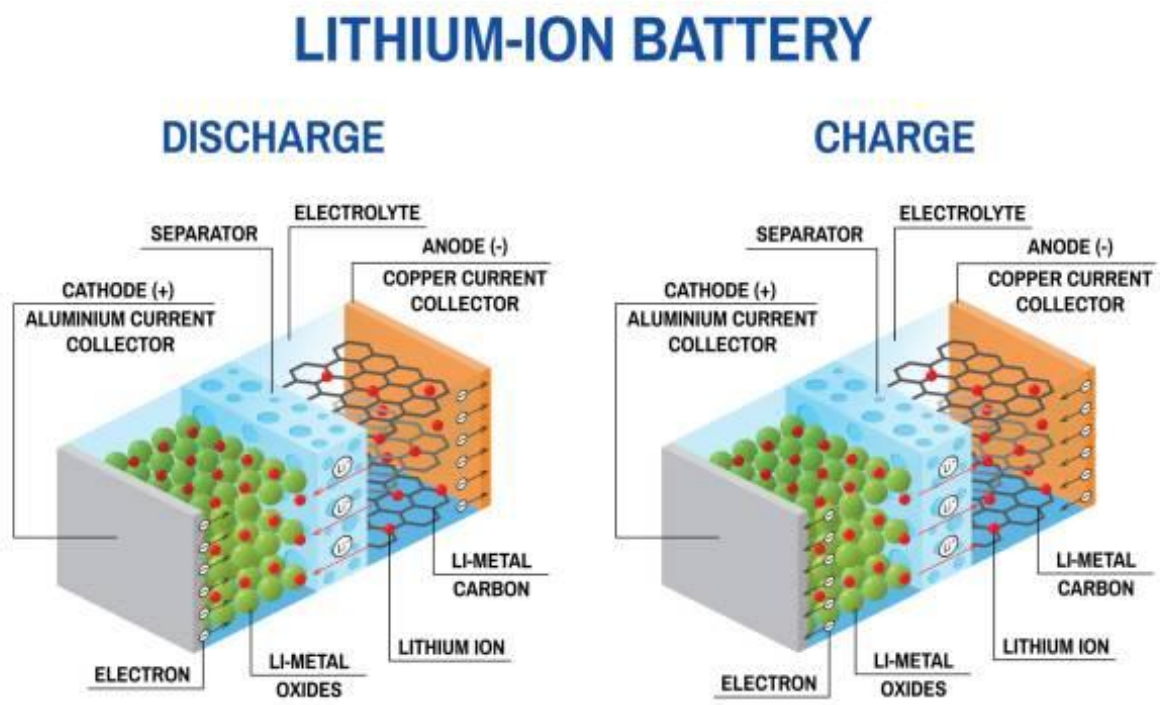

Figure 1.6: *Schematic illustration of a Li-ion battery, with related discharge and charge processes.*[47]

As illustrated in the figure above, the cathode is the electrode at the higher potential, which is oxidized during the charge of the cell, while the anode is the lower potential electrode, which is reduced during the same process. During discharge, the anode and cathode processes are reversed. Upon subsequent charge/discharge, electrons flow from one side to the other by an external circuit connected to the two electrodes, whereas Li^+ ions migrate from one electrode to the other through the electrolyte solution to guarantee the charge balance and to provide the rush of ionic current. The electrodes are divided by a microporous polymeric separator, made of polyethylene or polypropylene, immersed in the electrolyte to ensure its permeability, which prevents short circuit from direct contact. Moreover, anodic and cathodic active materials are cast onto current collectors (Cu for the former and Al for the latter) which behave as rigid and electronically conductive supports. The active materials are attached to Al or Cu by means of a polymeric binder able to guarantee adhesion and flexibility of the coatings.

The reversible charge/discharge mechanism for the illustrated state of the art Li-ion battery based on a graphite anode and a LCO cathode is summarized by following equations (**Equation 1.1 – 1.3**):

Cathode $LiCoO_2 \rightleftarrows Li_{1-x}CoO_2 + xLi^+ + xe^-$ **(1.1)**

Anode $6C_{(graphite)} + xLi^+ + xe^- \rightleftarrows Li_xC_6$ **(1.2)**

Overall $LiCoO_2 + 6C_{(graphite)} \rightleftarrows Li_{1-x}CoO_2 + Li_xC_6$ **(1.3)**

Upon charge, Co is oxidized from Co^{+3} to Co^{+4}, releasing Li^+ ions which migrate to the anode through the electrolyte solution, and electrons which move to the same direction via the external circuit. On the anode side, graphite is gradually reduced with Li^+ insertion within the graphene layers. The discharge of the cell follows the opposite process. The overall theoretical energy density is about 250 Wh Kg^{-1}

As above mentioned, during the 1st cycle of the cell the anode (in lower measure also the cathode) could react with the electrolyte to form a passivation layer on the electrode/electrolyte interface, called SEI. **Figure 1.7** depicts a schematic representation of SEI and Cathode Electrolyte Interphase (CEI) formation.[48] SEI layer is generated from the electrolyte decomposition at the lower (or higher for CEI) potential cut-off, where it is unstable, and it generally act as an ionic conductor and an electronic insulator, protecting the electrodes from additional reactions with the electrolyte. Nevertheless, SEI formation is an irreversible reaction and causes an initial efficiency loss. The stability of the passivation layer is determined by the nature of the electrolyte, particularly its solvents, while some compositions are favorable, and some may not.[49,50]

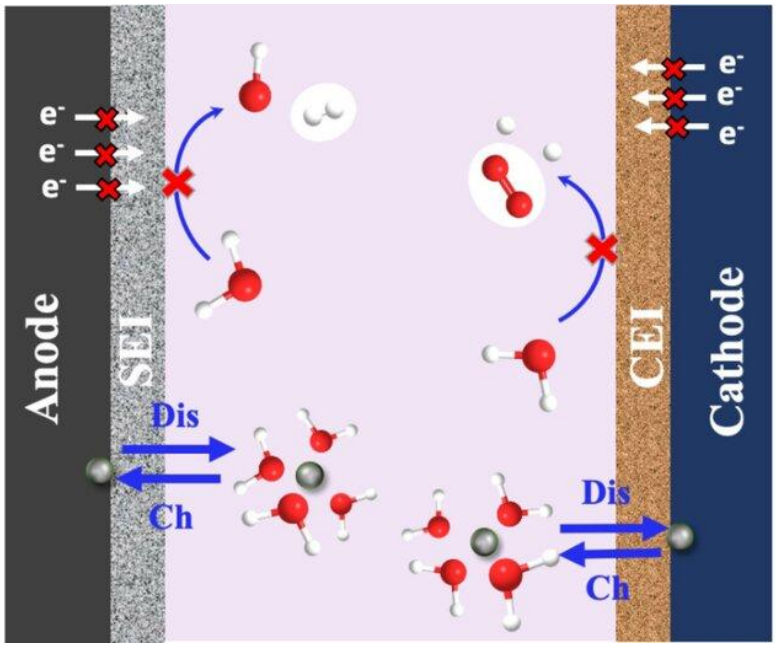

Figure 1.7: *Schematic illustration of the functions of SEI and CEI.*[48]

Although the constant optimization performed in the last three decades, LIBs still present some drawbacks, such as the possibility of permanent damage of the cell outside indicated temperature

range, high costs in comparison to other batteries, and irreversible degradation due to overcharge or excessive lowering of the potential of the cell. Furthermore, currently used chemistries have problems reaching the optimal energy density for uninterrupted powering EVs for very long ranges, despite permitting an adequate driving range per single charge.[51,52]

1.3 Sodium-ion Batteries (SIBs)

The research on sodium-ion batteries (SIBs) is correlated with that on the Li-ion counterpart, but it was delayed as a consequence of commercialization and rapid growth of LIBs. In the early 1980s Delmas discovered layered metal oxides of the $NaMO_2$ family, while in the meantime Goodenough proposed to employ $LiMO_2$ as cathodes in Li-ion batteries;[53,54] however, Li-based materials had resulted more attractive thanks to their higher electrochemical features. Furthermore, carbonaceous materials that intercalate lithium at low potential (soft carbons or graphite) presented a capacity almost tenfold lower in SIBs compared to LIBs, hindering the research on Na-ion systems.[55–57] Significant developments were performed only in high-temperatures Na-ion batteries like ZEBRA cell or sodium-sulfur (Na-S) system, working in the 250 – 350 °C range,[58] which were adopted for stationary energy storage and space missions.[59] Subsequently, a renewed interest in room-temperature SIBs derived from the discovery of Na intercalation into hard carbons (HC) by Stevens and Dahn in 2000, with similar performance with respect to graphite in LIBs.[60,61] From this achievement, research on Na-ion batteries started to increase, with an exponential rise of publication after 2010.

The development of EVs requires higher gravimetric and volumetric energy densities, accordingly a greater number of battery factories is needed to satisfy the demand for Li-ion batteries production, and their optimization in terms of capacity, lifetime, safety, and price to meet the car producers' requests. Furthermore, Li is limitedly available and geolocalized in few areas worldwide, a fact that is becoming alarming due to the price increase of raw materials,[62] resulting in possible supply shortage or geopolitical problems with exporting countries.[63] These issues, also related to the critical role played by LIBs in the transition towards climate neutrality, especially considering the stationary energy storage for renewable sources already under development,[9,64] could be mitigated by means of employing of SIBs. Indeed, while energy density is a key parameter in portable electronics and EVs, the main features considered for stationary storage are price and power, suggesting the application of Na-ion technology an equally viable one compared to LIBs.

Figure 1.8 summarizes the characteristic of Na as compared to Li.[65] Indeed, SIBs research and investments are rapidly growing, since they are the devices that have the higher possibilities to match the LIBs performances.[66]

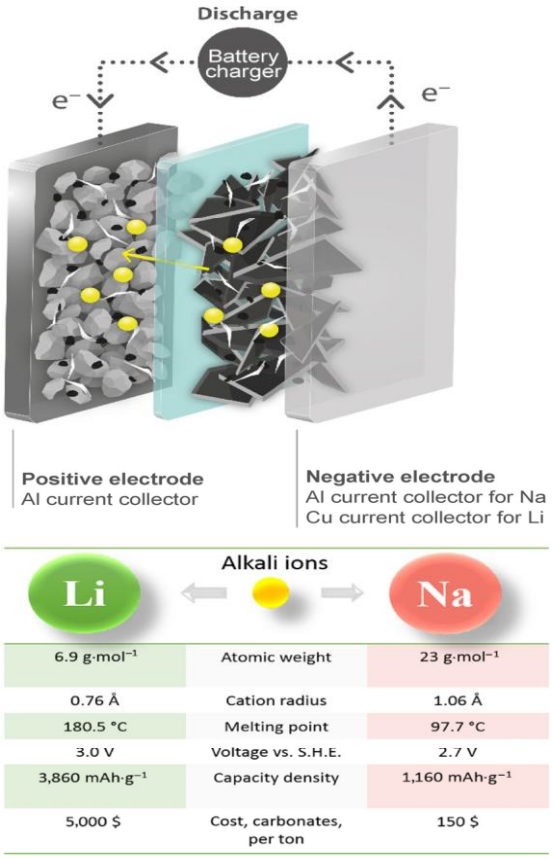

Figure 1.8: *Schematic representation of a Na-ion cell and comparison of LIBs and SIBs in terms of cation properties and cost of materials.*[65]

Lithium and sodium are both alkali metals, sharing most of their chemistry. Indeed, the working principles of SIBs are basically the same as LIBs, with Na^+ ions reversibly migrating from one electrode to another through the electrolyte solution upon charge/discharge of the cell. Nevertheless, Li^+ and Na^+ ions present important electrochemical differences, which have to be considered for practical applications. As illustrated in **Figure 1.8**, sodium has higher atomic weight, larger ionic radius, and a slightly higher redox potential vs. SHE compared to lithium, resulting in slower ion transport, less stable interphase formation, larger volume variations, and an inevitably lower energy and capacity density.[65] Howbeit, the advantages of SIBs count in the higher availability, less geolocalization of raw materials, and lower costs of the whole battery production, even including the possibility to use cheaper Al current collector at the anode, while Li alloys with Al at low potentials.[66]

As already described for LIBs, the formation of a passivation layer at the electrodes interfaces during the first cycle is present in SIBs. Furthermore, this is a most complex phenomenon compared to Li-

ion systems due to the high reactivity of sodiated materials, whereas the electrolyte decomposes into oxygen-rich compounds (*i.e.* sodium carbonates). Moreover, the passivation layer is partially soluble in carbonate-based electrolytes, leading to a dynamic formation/dissolution process, which progressively consumes active Na from the electrolyte.[67] For these reasons, the characteristics of the SEI in SIBs is a key parameter, possessing a fundamental role for the implementation of this technology.

Na-ion rechargeable batteries are very promising EES systems and could create a bridge between renewable energy generation and storage and related energy supply.[66,68,69] Indeed, companies like CATL, Natron or Faradion are pushing this technology to commercialization for large scale applications: CATL announced the launch of a second-generation Na-ion battery with an energy density of 200 Wh Kg^{-1}, while Natron achieves first-ever commercial-scale production of SIBs in the U.S.[15,16,70]

1.4 Cell Materials and Components

All the main components described above which compose the final cell have an influence on the battery performance, especially when considering anode and cathode materials. In these regards, many compound families have already been investigated as proper electrode materials along with strategies to enhance their performance, but the interest is also focused on the development of new materials possessing encouraging peculiarities (*i.e.* organic cathodes, host materials for anode-less batteries).[71,72] Another key component is the electrolyte solution, because of its crucial role in the SEI/CEI formation and stability, along with its role in the ionic conductivity of the system. For these reasons, research on possible salts-solvents combinations is conducted, also considering the possibility of using additives that could improve the stability of the passivation layer or enlarge the electrochemical stability window (ESW) of the electrolyte solution.

In the following **Subsections 1.4.1**, **1.4.2**, and **1.4.3** an overview of the abovementioned components in Li-ion and Na-ion batteries is provided, with particular emphasis for the ones adopted in this work.

1.4.1 Cathode Materials

Cathodes can accept alkali ions during discharge (reduction) and release them during charge (oxidation), granting the cyclic working of the cell. In commercial batteries, the cathode is the component limiting their performance, and it is also generally the most expensive part, due to the presence of transition metals in the structure. In the last decades, the research was focused on

transition metals compounds with suitable stable structures permitting high Li^+ ion mobility without significant volume changes. Additionally, optimal cathodes should possess high capacity, chemical stability, low toxicity and safety, and high working potential vs. Li^+/Li or Na^+/Na redox couples. Transition metal oxides and phosphates are currently the most used cathodes in commercial Li-ion batteries, with high oxidation states despite a neutral charge upon ion release, and they could be divided in three main classes according to their crystal structure: olivine phosphates, layered oxides, and spinel oxides.[73] In SIBs, due to the greater Na^+ dimensions with respect to Li^+, volume changes are more significant, reducing the ion diffusion and mobility into materials. Therefore, ad hoc studies on cathodes structures presenting small volume changes are necessary, to exploit faster ion exchange. The most used compounds in Na-ion batteries are Prussian blue analogues, layered oxides, and polyanionic compounds.[74]

Olivine Phosphates

Olivine cathodes presented the general formula $LiMPO_4$ with M is a transition metal (M = Fe, Mn, Co, Ni), with their crystal structure extensively studied over the last years.[75] Particularly, $LiFePO_4$ (LFP) generated a lot of attention by the scientific community since its demonstrated ability to (de-)insert lithium discovered in 1997,[76] leading to the practical application of LFP in commercial batteries since the early 2000.[77] LFP, and generally all olivine compounds, is formed by an orthorhombic system with punctual group D_{2h}^{16} and space group *Pnma*, consisting in distorted hcp oxygen array with Li and Fe in half of the octahedral sites and P in one-eight of the tetrahedral sites, generating FeO_6 octahedra with a distorted geometry (**Figure 1.9**).[78] Furthermore, the tetrahedral PO_4 groups have a common edge with one FeO_6 octahedron and two edges with LiO_6 octahedra, with Fe^{2+} ions which occupy the center of the octahedron units and are also distributed to form FeO_6 octahedra isolated from each other. In summary, LFP olivine is built by layers of FeO_6 octahedra sharing corners and mixed layers of LiO_6/PO_4 octahedra, possessing a lattice with a strong two-dimensional character, and where Li^+ ions can be inserted and removed in the 1D tunnel-like structure, as evidenced in **Figure 1.9**.[78]

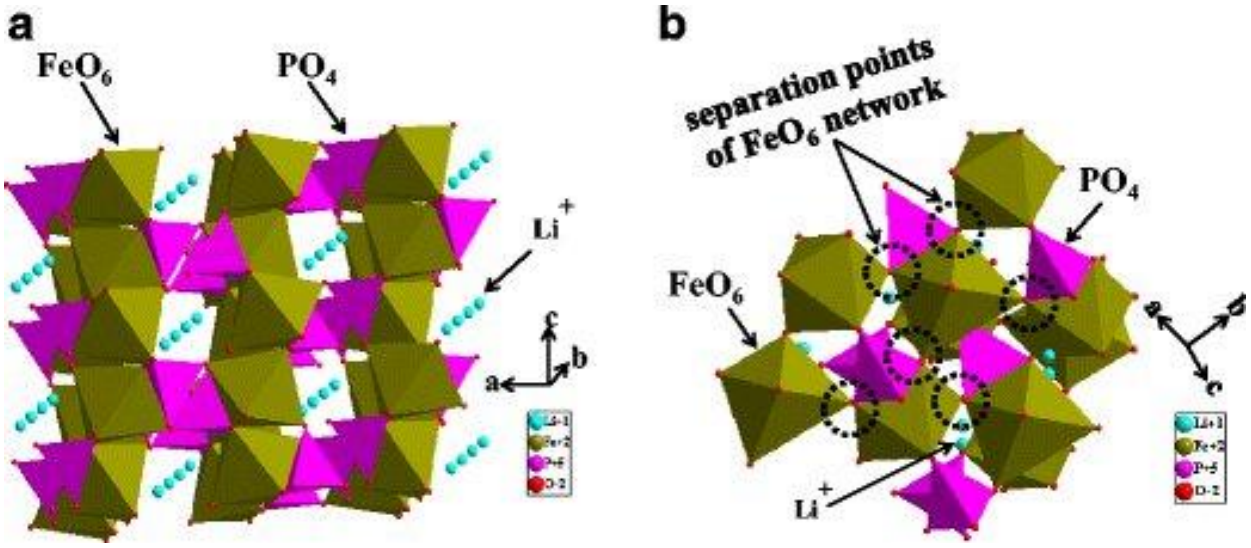

Figure 1.9: *The crystal structure of olivine $LiFePO_4$ evidencing separation point of FeO_6 network and Li^+ ions moving through the 1D framework.*[78]

This class of compounds presented a high theoretical capacity of about 170 mAh g^{-1} and a working potential depending on the transition metal employed,[79] which remains constant during the whole redox processes associated with Li^+ (de-)insertion.[80,81] During the reversible redox reaction of $LiMPO_4$ one mole of Li^+ ions per unit formula is released following the above reaction (**Equation 1.4**):

$$LiMePO_4 \rightleftarrows Li^+ + e^- + MePO_4 \qquad \textbf{(1.4)}$$

Moreover, the M^{3+}/M^{2+} redox couple potential for every considered transition metal is higher in the olivine lattice with respect in the conventional layered lattice, due to the inductive effect of the phosphate group $(PO_4)^{3-}$.[82]

Generally, olivine cathodes display advantageous characteristics such as low toxicity and environmental impact, average low costs, and high structural and thermal stability, as illustrated in the Arrhenius plot of LFP in **Figure 1.10**.[83,84] Furthermore, the dangerous oxygen release at high temperatures and voltage in layered oxide cathodes is suppressed in olivine compounds, since oxygen can form strong covalent bonds with phosphorous (P^{5+}) in the $(PO_4)^{3-}$ tetrahedra.[85] Despite their good properties, the main disadvantages of olivine cathodes are the low electronic and ionic conductivity, and the presence of channels in the olivine structure where Li^+ ions can accumulate, limiting their one-dimensional (1D) diffusion.[76,84] These problems could be overcome by adopting thin carbon coatings on the surface of active material particles, or by the addition of different conductive additives at the electrode formulation level (*i.e.* carbon nanotubes, carbon nanowires, graphene).[86–89]

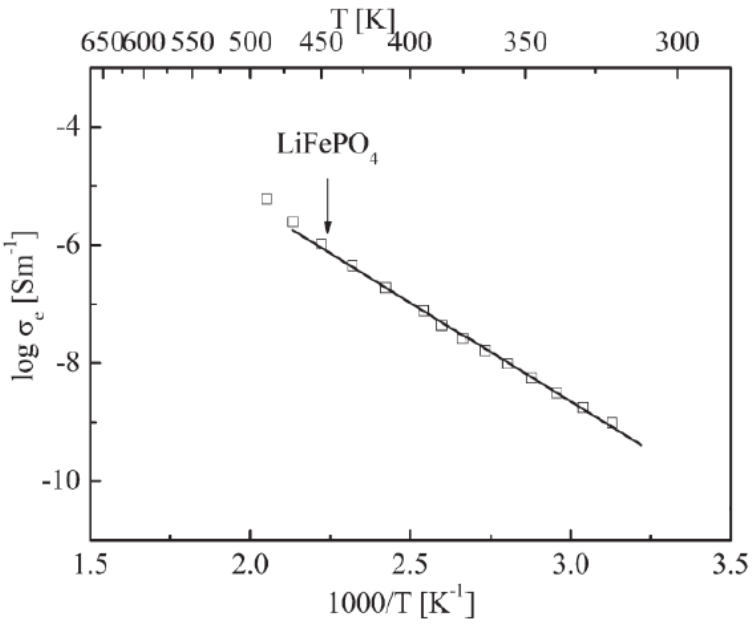

Figure 1.10: *Arrhenius plot of electronic conductivity as a function of temperature of LFP.*[83]

The commercial success of LFP has driven researchers to study other olivine materials with different transition metals, also because they have higher energy densities and operating voltages than LFP, maintaining comparable specific capacities and thermal stabilities.[90–94] **Table 1.1** resume the described characteristic.

Table 1.1: *Summary of working potential, theoretical specific capacity, and theoretical energy density for several LiMPO4 (M = Fe, Mn, Co, Ni).* [90–94]

Metal	Olivine	Working potential vs. Li^+/Li	Theoretical specific capacity	Theoretical energy density
Fe	$LiFePO_4$	3.4 V	170 mAh g^{-1}	578 Wh kg^{-1}
Mn	$LiMnPO_4$	4.1 V	168 mAh g^{-1}	689 Wh kg^{-1}
Co	$LiCoPO_4$	4.8 V	167 mAh g^{-1}	802 Wh kg^{-1}
Ni	$LiNiPO_4$	5.1 V	166 mAh g^{-1}	847 Wh kg^{-1}

Despite higher theoretical energy densities compared to LFP, other olivine systems present some problems that hinder their commercialization beside the iron counterpart. $LiMnPO_4$ (LMP) undergoes local pseudo Jahn-Teller distortion of the lattice around Mn^{3+} ion (**Figure 1.11**) during cycling, which limits the practical capacity delivered by the cell,[95] while their performance could be increased by adopting particular synthetic strategies.[96] $LiCoPO_4$ (LCP) has a relatively high working potential (4.8 V vs. Li^+/Li), very promising for application in LIBs, but the electrochemical performances reveal a significant capacity loss upon cycling with capacity values lower than the theoretical ones.[92]

$LiNiPO_4$ (LNP) presents the highest working potential around 5.1 V vs. Li^+/Li, which is outside of the ESW of conventional electrolytes, requiring an ad hoc study of alternative electrolyte solutions, strongly limiting material application.[91]

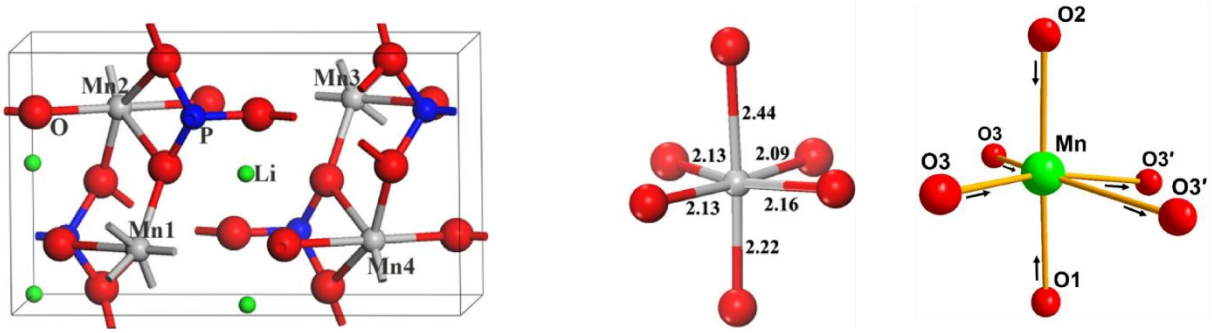

Figure 1.11: *Schematic views of atomic structure of LMP and representations of pseudo Jahn-Teller distortion of the MnO_6 octahedron around Mn2.*[95]

A good strategy to improve the performance of olivine cathodes is the combination of different transition metals in a mixed LiM'M"PO_4 compounds.[79,97] Furthermore, the use of this multi-metal concept could provide a better comprehension of electrochemical behavior of the single redox couples in the olivine structure, helping to a further improvement of these materials.[97] Moreover, the redox couple potential in a mixed-olivine cathode slightly vary with respect to the bare reference material, because of an initial solid-solution-like behavior coexisting with the typical two-phase mechanism[98–101] Among mixed-olivine cathodes, $LiFe_{1-x}Mn_xPO_4$ compounds are the most attractive due to the low cost and environmental impact of the transition metals utilized.[102,103] Indeed, the presence of iron in the olivine lattice increases electronic and ionic conductivity, and reduces Jah-Teller deformation, earning in higher working potential compared to LFP.[95,102,104] The maximum charge is obtained when $x = 0.5$, while when $x > 0.8$ the instability of the crystalline lattice deriving from Jahn-Teller distortion leads to an abrupt capacity loss and material deterioration.[76,95] Moreover, with $0.6 < x < 0.8$ the coexistence of the two-phase region is achieved (*i.e.* 3.5 V for Fe^{2+}/Fe^{3+} and 4.1 V for Mn^{2+}/Mn^{3+}), with high-capacity values following optimized synthetic routes.[82] These properties brought $LiFe_{1-x}Mn_xPO_4$ mixed-olivines to be commercialized in the last years, and they are currently used in the market as Li-ion systems delivering higher energy densities compared to the LFP ones.[105]

Regarding Na-ion batteries, the most developed olivine-type material is $NaFePO_4$, (NFP) exploiting a theoretical capacity of 154 mAh g^{-1}, suggesting its possible application as the sodium counterpart of LFP, presenting similar structural, electrochemical, and chemical-physical features.[106–108] Nevertheless, the application of sodium-based olivines have not been deeply studied due to challenging synthesis conditions. Indeed, considering the various polymorphs, the electrochemically active triphylite NFP, which have the same structure with one dimensional Na^+ diffusion channel as

LFP, cannot be obtained by direct synthesis, as it would produce the more thermodynamically stable, but electrochemical inactive, maricite NFP, which does not have cationic channels for Na^+ diffusion (**Figure 1.12**). [106,109,110]

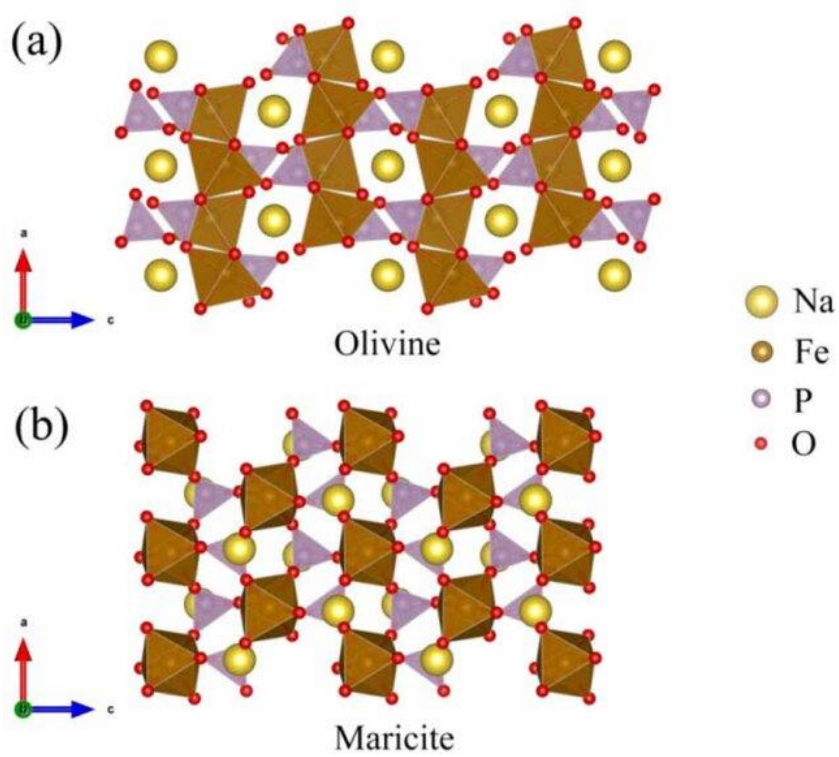

Figure 1.12: *Crystal structures of* ***(a)*** *olivine* $NaFePO_4$ *and* ***(b)*** *maricite* $NaFePO_4$.[109]

Electrochemically active triphylite has been achieved through conversion strategies involving electrochemical or chemical de-lithiation of LFP and subsequent sodiation of heterosite $FePO_4$, which is considered a reasonable method to obtain Na-based olivine cathode, while electrochemical alkali exchange is difficult to perform at an industrial scale.[111–113] On the other hand, the lithium extracted from the precursor during the de-lithiation step can be recovered from the electrolyte by simple evaporation (electrochemical conversion) or from the precursor solution by precipitation (chemical conversion) and reused for olivine precursor into a green loop which limits the overall impact of the process.[111,114]

The need for alternatives to lithium materials at the large scale has triggered research for developing sodium-based olivine electrodes with increased capacity and energy density.[113,115,116] Analogously to LFP, a suitable strategy to improve the performance of NFP is the partial substitution of iron with other transition metals to achieve a mixed olivine $NaFe_{1-x}M_xPO_4$ (M = Ni, Co, Mn),[115,116] that was first developed in 2011 by Nazar.[117] As above described, the manganese-to-iron substitution to achieve the $NaFe_{1-x}Mn_xPO_4$ triphylite appeared to be one of the most promising pathways to achieve efficient Na^+ (de-)insertion electrochemical process into the olivine structure.[115] However, sodium olivines based on Mn can suffered by the presence of the electrochemically inactive natrophilite

phase, in which Na and Mn exchange their positions leading to antisite mixing where half of the Na^+ ions occupies M1 sites, and the other half occupies M2 sites.[118] Indeed, the research interest was hindered in this class on materials, with few works reported in the last years, despite promising features for possible application in stationary electrochemical storage.

Layered Oxides

Layered oxide cathodes hold in their family the mainly used material during LIBs development, *i.e.* $LiCoO_2$ (LCO). Therefore, all oxides with general formula $LiMO_2$ (M = Co, Mn, Ni, Al or a mixture of them) possess a layered structure. From a structural perspective, these compounds are isostructural to α-$NaFeO_2$, natural salt which have a distorted structure, and own a distribution of Li and metal ions in octahedral sites separated by layers of cubic close-packed (ccp) oxygen array, with an ABCABC stacking sequence, which defines the O3-type structure (**Figure 1.13**).[119–121] The described ionic disposal in the crystal lattice corresponds to a $R\bar{3}m$ trigonal structure, allowing reversible (de-)insertion of the alkali metal through a two-dimensional (2D) framework.[122] Indeed, during cycling Li^+ ions are reversibly (de-)intercalated into the framework, generating or wiping out vacancies within the planes.

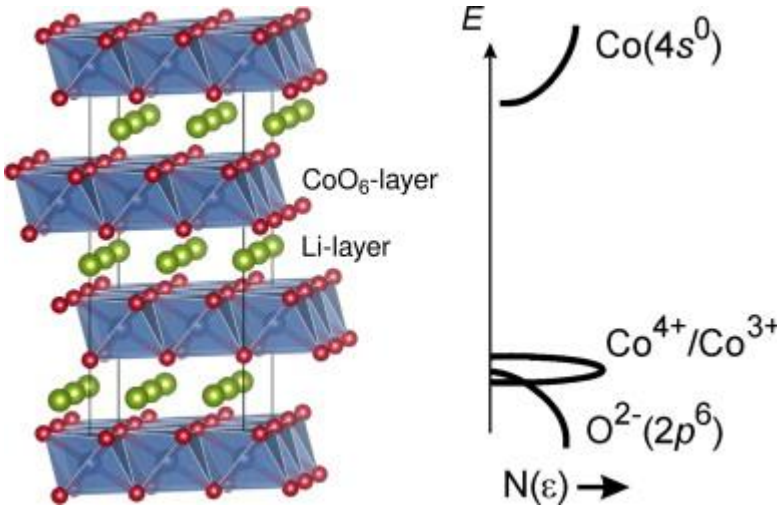

Figure 1.13: *Crystal structure (left) and schematic electronic structure (right) for Li_xCoO_2.*[119]

Nevertheless, the vacancies forming upon lithium removal from LCO (theoretical capacity 274 mAh g^{-1}), as illustrated in **Figure 1.13**, can promote structural change or electronic transitions. Indeed, in Li_xCoO_2, for $1 \geq x > 0.5$ the charge compensation upon Li extraction succeeds via removal of d-electrons with oxidation of Co from +3 to +4, maintaining valence band mainly unchanged.[123] At $x = 0.5$, the structure preferred to rearrange as an interplanar stacking leading to an equivalent chemical makeup for all Co ions, with consequent intermediate oxidation state of +3.5, with eventual associated transition to a monoclinic structure.[124] Upon further Li removal, for $x < 0.5$ the (CoO_6)-layer

distances tend to decrease, with charge compensation for de-lithiation leading to partial oxidation of O^{2-} ions and subsequent oxygen release, resulting in poor capacity retention of the material and also limiting the practical specific capacity in the range of 130 – 150 mAh g^{-1}.[125,126]

In current battery technologies, the typical LCO cathode has been almost fully replaced by multi-metal oxides possessing the same structure, such as $Li(Ni_xCo_yMn_{1-x-y})O_2$ (NMC), in which the expensive and toxic cobalt is partially substituted with other transition metals, thus achieving further bonuses including adequate operating voltage, specific capacity, sustainability, and thermal stability of the de-lithiated phase.[127–129] Despite the remarkable performance and wide use of $LiNi_{1/3}Co_{1/3}Mn_{1/3}O_2$ (NMC333) and $LiNi_{0.8}Co_{0.1}Mn_{0.1}O_2$ (NMC811) cathodes,[130,131] they still suffer from capacity decay upon prolonged cycling and possible safety issues due to the already described phase changes, involving material delamination and oxygen loss at de-lithiated state.[132] Furthermore, side reaction at the first cycle has been reported as one of the main issues of voltage hysteresis during the subsequent cycles, particularly in Li-rich compounds, causing instability of material structure.[133] Moreover, layered oxides could be affected by possible cation mixing between Ni^{2+} and Li^+ because of their similar ionic radii (0.69 Å and 0.76 Å, respectively), which may lead to deterioration of electrochemical performance.[134]

Several strategies have been employed to avoid the progressive breakdown of the cathode and related instability and safety issues, such as metal doping,[135–137] acid treatments,[138] partial substitution of Co with Al,[139–141] and surface modification by metal oxides coating (*i.e.* ZrO_2, Al_2O_3, TiO_2),[142,143] have proven to be effective, particularly in the stabilization of the structure.

Similarly to LIBs, layered oxides could be employed in Na-ion systems, presenting a general formula Na_xMO_2 (with M transition metal) containing stacked layers of edge-sharing MO_6 octahedra with Na^+ inserted in between. Sodium layered oxides can be classified in two different categories depending on the number of unique oxide layer packings and the site where Na^+ ions are located: O3-phase, with Na^+ ions in octahedral sites and 3 unique interlayers, and P2-phase, with Na^+ ions in prismatic sites and 2 unique interlayers (**Figure 1.14**). Additionally, when is present a distorted phase is added the notation (') after the letter (*e.g.* O'3 or P'2).[144,145] Sodium stoichiometry has a large influence on the formation of a preferred structure for Na_xMO_2, as described below:

- O3-phase belongs to $R\bar{3}m$ space group and is favored when $1.0 \geq x > 0.7$, composed by edge-sharing NaO_6 and MO_6 octahedra ordered into alternated layers, establishing NaO_2 and MO_2 sheets with an ABCABC pattern. Na^+ ions are located in octahedral sites between MO_2 layers (**Figure 1.14**).[144]
- P2-phase belongs to $P6_3/mmc$ space group and is favored when $0.7 > x > 0.6$, with Na^+ ions accommodated in prismatic sites. Despite consisted of MO_2 layers, P2-phase has a different

Na environment due to the larger ionic radius of Na^+ compared to Li^+, resulting in oxide layers stacked in an ABBA pattern, which stabilize the structure (**Figure 1.14**).[144]

The mechanism of sodium de-insertion from both structures may induce phase transitions (**Figure 1.14**). Particularly, from the O3-phase a P3-type phase could be obtained, with oxide layers stacked in an ABBCCA pattern, which can also be synthetically achieved.[146] However, from P2-phase the O2-type phase is gained, with oxide layers stacked in an ABACAB fashion, which often induces the formation of stacking faults after Na extraction.[145]

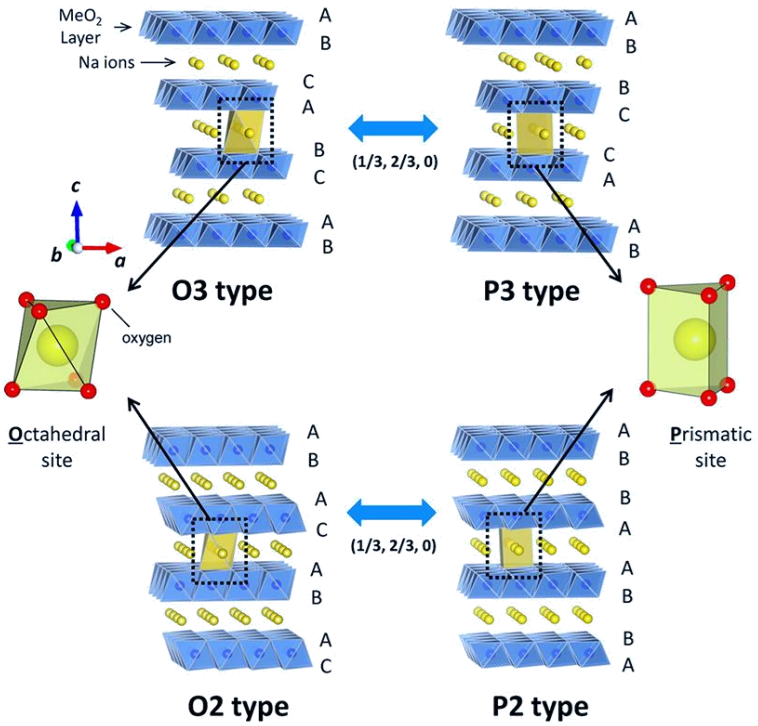

Figure 1.14: *Classification of Na_xMO_2 layered structures with related phase transition processes upon Na de-insertion.*[144]

Na_xMO_2 systems, similarly to $LiCoO_2$, are studied as starting point to implementation of more complex binary systems, whereas each transition metal displays distinctive electrochemical performance in terms of working potential, delivered capacity, and capacity retention. It is underlined that the kinetics for electrochemical processes are widely influenced by crystal phase and structural stability of the materials. For these reasons, the combined effect of binary $Na_xM'M''O_2$ systems (M', M'' = Ni, Fe, Mn, Co) is expected to obtain higher performance like high operating voltage and reversible capacity, and quite flat potential profiles.[147,148]

From a structural perspective, P2-phase shows better overall electrochemical behavior and stability than O3-phase, as a consequence of low diffusion barrier and high ionic conductivity of the former.[145] Nevertheless, the sodium deficiency makes difficult the application of these materials in full-cell, especially for P2-type, because the cathode is unable to provide its full capacity. Therefore,

activation of the cathode by using different strategies like chemical or electrochemical sodiation, or use of sacrificial agents, is required to exploit its full capacity in SIBs,[149,150] while other approaches, as anode activation, have also been considered.[151]

Na-based layered oxides have attracted a lot of attention at the industrial level, due to their high energy density compared to other cathode chemistries,[148] and the application of O3-type and mixed O3/P2-type has already been patented by Faradion.[18]

Other Cathodes Chemistries

Spinel Oxides: Spinel oxides represent a safer and cheaper alternative to layered oxides, and $LiMn_2O_4$ (LMO) is one of the most employed cathodes for LIBs, firstly proposed by Thackeray.[152] It presents a cubic structure with a $Fd\bar{3}m$ space group, where Mn and Li occupy octahedral and tetrahedral sites, respectively, permitting a 3D network for Li^+ ions diffusion during (de-)insertion.[153] Despite LMO is cheaper than LCO and showing an excellent rate capability, it suffers capacity decay upon cycling, with an irreversible loss of capacity becoming rapid at high temperatures.[154] This phenomenon is related to two causes: (i) Mn^{2+} dissolution, and (ii) Jahn-Teller effect. In the first case, Mn^{2+} is the result of the disproportion of Mn^{3+}, and it is soluble in the electrolyte, leading to loss of the redox center and capacity. In the second case, increasing the concentration of Mn^{3+}, there is a change of symmetry from cubic to tetragonal, which will lead to poor performances.[152] The partial substitution of Mn with Ni in the $LiNi_{0.5}Mn_{1.5}O_4$ (LNMO) provides an effective composition for Mn to stay in the +4 state, thus reducing Jahn-Teller distortion, while still possessing high capacity associated with the high-voltage plateau at 4.7 V.[155] LNMO possesses a specific capacity of 147 mAh g^{-1}, making it an attractive cathode material for next generation batteries.[156] it can also crystallize in two different structures according to the annealing temperature: (i) face-centered cubic phase ($Fd\bar{3}m$ space group), also called "*disordered*" phase, and (ii) the primitive cubic phase ($P4_332$ space group), also called "*ordered*" phase.[157,158] However, LNMO presents issues such as electrode/electrolyte interphase and instability given by Li-rich and Li-poor domains.[157]

Polyanionic compounds (NASICON-type): In contrast with olivine compounds for SIBs, NASICON-type (Na Super Ionic CONductor) materials present a typical robust structure for sodium migration channels and higher ionic conductivity. They have the general formula $Na_xM_2(YO_4)_3$, with $4 \leq x \leq 1$ (M = V, Fe, Ni, Mn, Ti, Cr, Zr; *Y* = P, S, Si, Se, Mo), and suitable characteristic as cathodes for SIBs, as relatively high working potential, remarkable Na^+ conductivity, and thermal stability.[159] Among them, $Na_3V_2(PO_4)_3$ (NVP) has displayed promising features for practical applications,[160] since, thanks to V^{3+} ions, it can act as both anode and cathode. When used as a cathode, two Na^+ ions can be extracted at about 3.4 V vs. Na^+/Na, with a theoretical capacity of 117 mAh g^{-1}, thanks to oxidation

of V from +3 to +4. However, the main issue for NVP is the poor electronic conductivity leading to low specific capacities.[160] To increase the energy density of NASICON-type cathodes a suitable strategy is the introduction of highly electronegative anions (*i.e.* F^-), able to increase their redox potential. Particularly, the fluorinated $Na_3V_2(PO_4)_3F_3$ (NVPF) has proven to be able to deliver a theoretical capacity up to 130 mAh g^{-1} with a suitable high operating voltage of 3.9 V.[161]

Prussian blue analogues: Prussian blue analogues (PBAs) have been extensively studied as promising cathode materials, especially for SIBs, thanks to their low cost, highly reversible phase transition during alkali metal ions (de-)insertion, and excellent redox activity.[162] They have general formula $Na_xM[M'(CN)_6]_y\square_{1-y}zH_2O$, where M and M' are transition metals creating with C≡N groups a 3D open structure, while □ are the vacancies caused by the removal of an $M'(CN)_6$ group and the occupation by coordination or interstitial water. The structure of PBAs can vary between different crystal phases, according to different Na/M/M' ratios, defects, crystal water, and external factors (*i.e.* temperature): monoclinic, rhombohedral, cubic, tetragonal, and hexagonal.[163] Furthermore, crystallite size and morphology can affect both ion diffusion dynamics and the structural evolution mechanism of the materials;[163] accordingly, well-crystallized PBA particles with small dimensions and high specific surface area promote a faster diffusion.[164,165] As their structural evolution during charge/discharge is quite complicated, a defined mechanism has not been established yet.[162] Moreover, energy density, average voltage, and specific capacity of PBAs are related to the amount of interstitial water and vacancies, as well as structure stability and crystallinity, while cycling stability is generally poor and capacity fading is correlated to structure collapse, with dissolution of $M'(CN)_6$ groups in the electrolyte.[166] In these regards, increasing the crystallinity of PBAs is regarded as an effective strategy to achieve increased capacity and prolonged cycle life.[163] Despite the abovementioned issue, added to the possible formation of cyanogen $(CN)_2$ gas during cycling with commercial electrolytes,[167] PBAs are currently used in commercial application, as CATL and Natron use them as cathodes in first generation SIBs.[15,16]

1.4.2 Anode Materials

Anode materials are compounds able to accept Li^+ or Na^+ ions during cell charge (material reduction) and release them during cell discharge (material oxidation), to guarantee the cyclic working of the cell when they are coupled with cathodes. Several materials have been studied for application in LIBs and SIBs considering their cost, safety, sustainability and performance. Indeed, a suitable anode should be able to react with alkali metals at a low working potential with respect to Li^+/Li or Na^+/Na redox couples. Generally, they can be divided into three different classes according to their reaction mechanism: intercalation, alloying and conversion. Each of them presents advantages and

disadvantages, which are summarized in **Table 1.2** and further discussed in the following subsections.[65]

Table 1.2: *Advantages and disadvantages of the three classes of anode materials.*[65]

Mechanism	Advantages	Disadvantages
Insertion/Intercalation	• Stability • Low or negligible volume expansion • Reversibility	• Low specific capacity (ranging from 100 up to 400 mAh g^{-1})
Alloying	• Highest specific capacities (ranging from 700 up to 4000 mAh g^{-1})	• High volume expansion • Instability
Conversion	• High specific capacity (ranging from 500 up to 1000 mAh g^{-1}) • Economically and environmentally sustainable	• Voltage hysteresis • Structural changes

Insertion anodes – Carbon-based

Insertion materials are characterized by a reversible intercalation reaction coupled with a low or negligible volume change. Carbon-based and Ti-based materials are considered insertion anodes, with the former characterized by higher specific capacity (from 200 up to 400 mAh g^{-1}) and lower working potential, while the latter present higher working potential (around 1.5 V) and lower specific capacities.

In these regards, considering the intercalation carbonaceous materials, their characteristics are influenced by surface area, crystallinity, morphology, and spatial orientation of atoms, whereas different levels of graphitization could exist.[168] Carbon and its allotropes received a lot of success in rechargeable batteries due to their large abundance, low cost, tunable electronic and structural properties, excellent reversibility during cycling, ability to form a "protective" passivation film (SEI), and possible preparation from biowaste materials.[61,169,170] Carbon-based materials can be mainly divided into two categories, according to their crystallinity degree and carbon atom stacking (**Figure 1.15**):[171]

- *Ordered carbons:* are characterized by long-range order and included graphite, few layers graphene, and carbon nanotubes.
- *Disordered carbons:* are characterized by no long-range order (no crystallinity) and included hard carbon (HCs) and soft carbon (SCs).

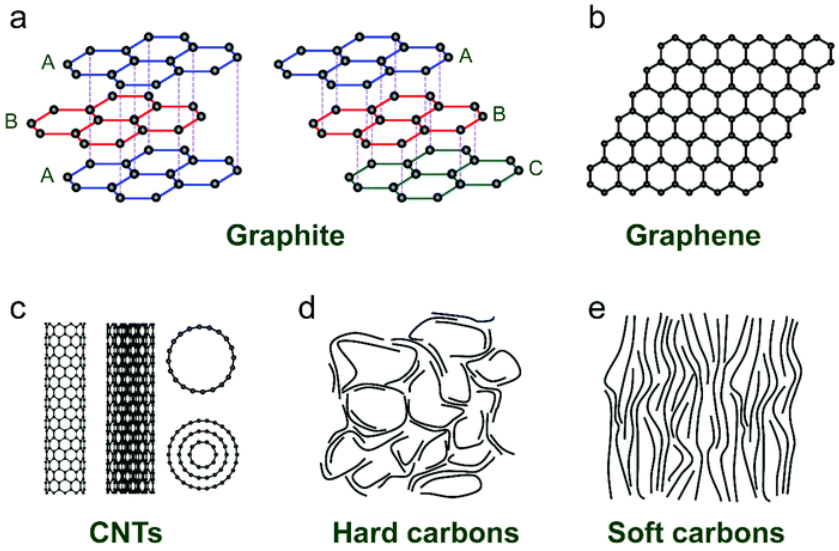

Figure 1.15: *Typical structures of* ***(a)*** *graphite (AB and ABC),* ***(b)*** *graphene,* ***(c)*** *single- and multi-walled carbon nanotubes,* ***(d)*** *hard carbons, and* ***(e)*** *soft carbons.*[171]

In Li-ion systems, graphite is the most used material. Its structure is composed of stacks of sp^2-hybridized graphene layers connected by weak van der Waals forces (interlayer distance of 3.35 Å) and π-π interactions among the delocalized electron orbitals.[172] The layers are stacked in the thermodynamically stable ABAB pattern with hexagonal symmetry, with a small contribution of the less stable ABCABC pattern with rhombohedral symmetry (see **Figure 1.15(a)**).[171] Graphite can store Li^+ ions through stages, reaching a maximum stoichiometry of LiC_6 and a theoretical specific capacity of 372 mAh g^{-1}. Furthermore, thanks to delocalization and weak van der Waals interactions, it possesses high electronic conductivity and preferential Li^+ ion pathways, making it a suitable host material in LIBs.[172] The understanding of alkali ion (de-)intercalation in graphite is significant, but the dynamics of the intercalation processes are still not well understood.[173] Two typical structure models have been proposed to describe the graphite lithiation at different stages: the Rüdorff-Hofmann model (**Figure 1.16(a)**) and the Daumas-Hérold model (**Figure 1.16(b)**), with the former assuming that Li^+ ions alternate occupying the intermediate layers of each carbon layer, while the latter proposing that graphene layers undergo deformation during lithium insertion, facilitating interphase transition.[174] While the Daumas-Hérold model provides a better explanation of the phase transition capability during the process, (de-)intercalation is largely influenced by crystal structure defects, making both models not precise to understand the Li^+ insertion behavior.[175] Alternatively, the widely accepted theory is the one proposed by Yazami and Touzain, in which lithium intercalation

occurs through a concentration-dependent process called "*staging mechanism*", as illustrated in **Figure 1.16(c)**.[174] Each n^{th} stage compound is characterized by a periodic sequence of layers incorporating the intercalant species separated by layers without any intercalant species, where *n* defines the numbers of graphene planes between two intercalated layers. Accordingly, Stage 1 is the highest lithiated state of graphite at ambient conditions.[55]

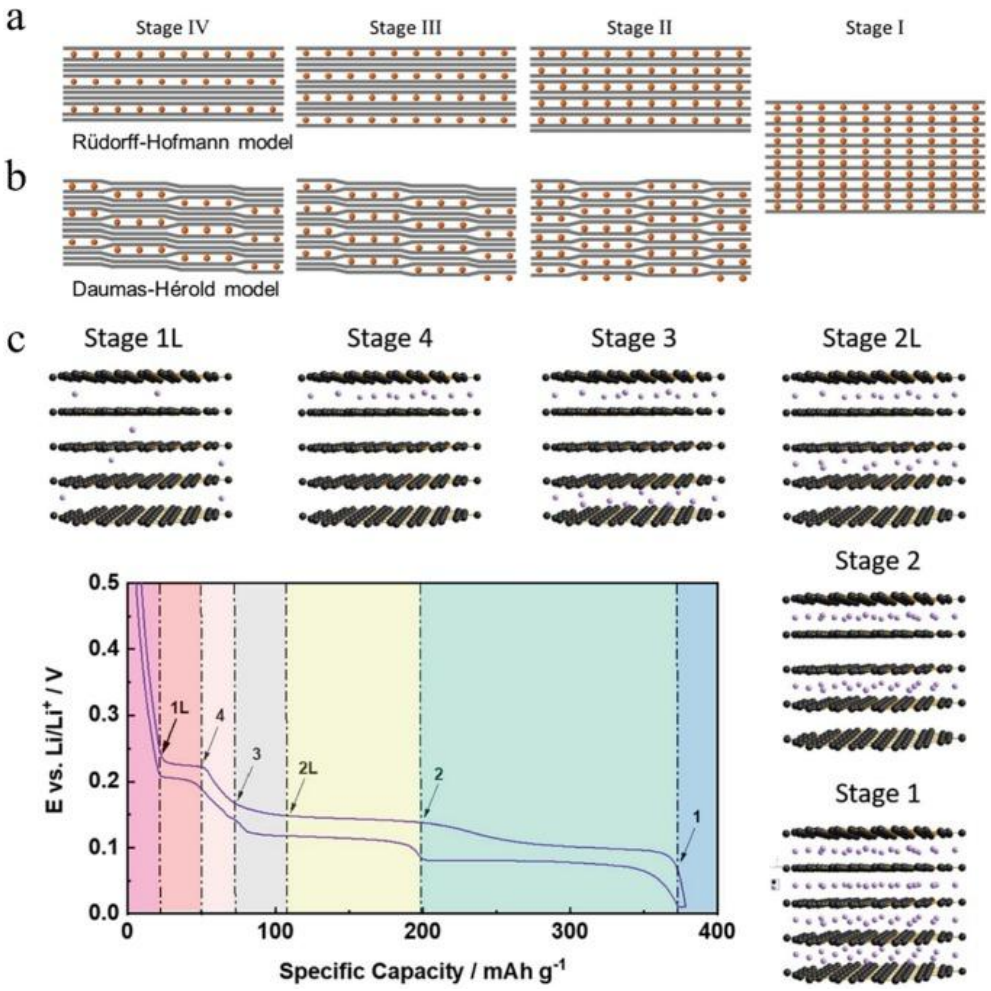

Figure 1.16: *Schematic illustration of the lithiated graphite at different stages.* ***(a)*** *Rüdorff-Hofman model;* ***(b)*** *Daumas-Hérold model;* ***(c)*** *voltage curve of graphite during lithiation following the staging mechanism.*[174]

Upon lithium intercalation into graphite, the different stages can be identified as plateaus (or sloping regions) in the galvanostatic profiles. Initially, the staging process takes place through the formation of a random solid-solution-type intercalation, with Li^+ ions organized in a liquid-like manner (Stage 1L). Subsequently, a phase transition takes place from Stage 1L to Stage 4 and then to Stage 3. The subsequent transition to Stage 2L is temperature dependent, and its structure is not yet completely understood.[176] Upon increasing the lithium content, Stage 2 is formed coupled with an increase in the in-plane ordering, leading, after a first-order transition, to the formation of the completely lithiated Stage 1, accompanied by a flowing of the single planes with respect to each other and by an increase

of the interlayer distance to 3.70 Å. The whole process of lithium intercalation is summarized in the following equations (**Equation 1.5 – 1.8**):[174]

Stage 4 → 3 $LiC_{72} + Li^+ + e^- \rightarrow 2LiC_{36}$ **(1.5)**

Stage 3 → 2 $LiC_{36} + 2Li^+ + 2e^- \rightarrow 3LiC_{12}$ **(1.6)**

Stage 2 → 1 $LiC_{12} + Li^+ + e^- \rightarrow 2LiC_6$ **(1.7)**

Overall $6C_{(graphite)} + xLi^+ + xe^- \rightarrow Li_xC_6$ **(1.8)**

Nevertheless, in carbon materials graphite structure presents ordered and disordered layers, with the latter that can hinder the intercalation of Li^+ between the layers, especially in the higher-order formation process, reducing the actual specific capacity of the anode.[172] A high-temperature method could be adopted to remove these disorderly layer structures.[177] Generally, despite the high stability and reversibility of graphite, its relatively low theoretical specific capacity limits its applications, in particular for high energy density devices (*i.e.* EVs). To increase its specific capacity, ball milling could be a suitable strategy, breaking the C-C bonds, and leading to formation of defects and related amorphization around the particle edges. However, this strategy may lead to a large voltage hysteresis of the material.[178] Furthermore, specific new forms of graphite have been developed with improved performance, especially rate capability, such as meso-carbon microbeads (MCMB) or micro-carbon fibers (MCF).[179]

Graphene is considered a single or few layers of sp^2 hybridized carbon, possessing remarkable properties in terms of reliable thermal conductivity, good electrical conductivity, and superior mechanical properties.[180–182] Its application as anode material is still under development: albeit it has a high theoretical capacity of 744 mAh g^{-1} thanks to the ability to store lithium ions on both sides of the layer (Li_2C_6), graphene layers tend to restack forming amorphous carbon and, at the end, graphite. Moreover, graphene presents elevated irreversibility at the first cycle and a large voltage hysteresis, hindering its practical application as anode for rechargeable batteries.[183] Carbon nanotubes (CNTs) have been reported as possible anode material in many literature works, since their first report in 1991.[184] They consist of one-dimensional carbon nanostructures, with their structure which is similar to a cylinder obtained by wrapping a single (single-walled carbon nanotubes, SWCNTs) or a few (multi-walled carbon nanotubes, MWCNTs) graphene layers. Lithium ions can diffuse into stable sites either on the outer or the inner surface of a single graphene layer, leading to a larger Li^+ uptake than graphite.[185] Moreover, Li^+ ions can be inserted in the interstitial sites of close-packed SWCNT bundles and within the graphene layers of MWCNTs, mechanism that strongly relates the performance with the morphology.[89] Structure defects increase the CNTs capacity, while

leading to an increase of irreversible capacity and voltage hysteresis, as already reported for graphite.[172,185]

Differently from the above-described materials, disordered carbons do not possess long-range order in planes or along the stacking directions. They present sp^2 hybridized carbon networks randomly located and partially linked with sp^3 hybridized carbon. They are classified as hard carbons and soft carbons due to the degree of crosslinking and graphitization.[186] In the former case, crosslinking degree is very high, hindering the movement of sp^2 carbon domains even at high temperatures (3000 °C), thus avoiding the graphitization. On the other hand, soft carbons develop the graphite structure upon thermal treatments, due to the low degree of crosslinking with related improved sp^2 carbon domains mobility. They can be prepared pyrolyzing compounds rich in aromatic functionalities (*i.e.* petroleum, coke), while under the graphitization temperature turbostratic disordered carbons are obtained, presenting lower specific capacities related to inhibited lithium accommodation. In these regards, the research community was more interested in hard carbon materials, which can be obtained by thermal decomposition of organic precursor (*i.e.* glucose, biowaste) under inert atmosphere, resulting in more sustainable and cheaper materials, also considering a possible large-scale production.[171,186] During the pyrolysis, the more evident mass loss takes place at relatively low temperature (250 – 500 °C), mainly ascribed to heteroatoms removal (*i.e.* O, S, N, etc.), while the complete carbonization is reached at temperatures higher than 700 °C.[171] Hard carbons could deliver capacities ranging from 200 up to 800 mAh g^{-1}, depending on several synthetic parameters,[186] revealing a wide range of applications as anode material beyond LIBs, such as in SIBs and potassium-ion batteries (KIBs), as well as carbon matrix for Si anode.[187–189]

Considering the sodium-ion systems, the inability of Na^+ ions to reversibly intercalate to form graphite intercalation compounds (GICs) hinders the use of graphite as anode material for SIBs. Therefore, the higher ionic radius of Na^+ as compared with Li^+ is not the main issue, since larger alkali metal ions (*i.e.* K^+, Rb^+, and Cs^+) have been reported to form GICs.[57,190] On the other hand, Na-based GICs possesses the lowest energetic stability and formation potentials, ascribed to very weak chemical binding ability of Na towards graphite substrate, resulting in poor electrochemical performance (*i.e.* 30 – 50 mAh g^{-1}).[57] To implement the use of graphite as anode for SIBs, glyme-based electrolytes enable the co-intercalation of solvated Na^+ ions, while only limited capacities have been reached.[191]

In these regards, hard carbons represent the most promising choice for application in SIBs as anode material, since they have high storage capacity, low working potential, and cycling stability, thanks to their mechanical properties and porosity, with an interlayer spacing of 3.7 – 4.0 Å, which favors the Na^+ ions into energetically stable sites near defects.[192–194] The structure of HCs is difficult to

describe since they have a quite complex turbostratic structure which depends on employed precursors, local random stacking, pores, voids, interlayer crosslinking, and presence of heteroatoms and folded graphemic domains. However, different models have been proposed over the years, emphasizing different hard carbon properties, while maintaining porosity as a key property.[195] The most employed one is that proposed by Dahn,[196] which tries to link between porosity and structure by assuming that HCs are composed of a combination of pseudo-graphitic micro-crystallites (sp^2 hybridized) and amorphous regions (sp^3 hybridized edges and defects). From an electrochemical perspective, hard carbons are now presenting specific capacities close to those of graphite in LIBs, as a result of many improvements over the years.[186,195] Nevertheless, the Na storage mechanism still remains controversial, given the lack of a unique structural model, creating several debates over sloping or plateau regions of the typical galvanostatic profile of the material.[195]

Alloying anodes

Anodes based on alloying mechanism can store a large amount of alkali ions (**Figure 1.17**) compared to insertion and conversion materials (Li- or Na- rich alloys), exhibiting very high specific capacities (ranging from 700 up to 4000 mAh g^{-1}).[197] Particularly, metals and semimetals of IV and V groups can electrochemically form alloys with Li or, in some cases, other alkali metals (*i.e.* Na) at room temperature,[198,199] as described in **Equation 1.9**:

$$M + xLi^+ + xe^- \rightleftarrows Li_xM \qquad \textbf{(1.9)}$$

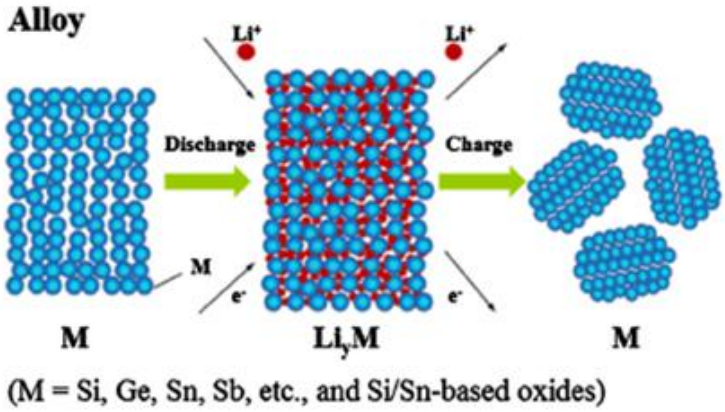

Figure 1.17: *Schematic illustration of alloying reaction mechanism and Li_xM-type alloy formation for LIBs.*[197]

Thanks to their relatively good electronic conductivity, suitable discharge plateaus and operating voltage, alloying anodes are considered the most promising materials for high energy density batteries. The alloying process generally occurs with formation of Li_xM-type (or Na_xM-type) alloy phases with progressively increasing alkali ion content upon uptake, as described in **Equation 1.9**.

Furthermore, the alloying reaction can be classified in two different categories depending on whether a crystal structure change occurs or not: *solid-solution reaction* or *addition reaction*. Particularly, formation of Li/Na alloys with crystalline Si, Sn, Al, and Sb, in which a crystal structure change takes place, belongs to the former, while electrochemical alloying of Li/Na with Mg or amorphous-Si are part of the latter.[200] Alloying anodes can work at relatively low potentials vs. Li^+/Li or Na^+/Na, with related energy densities largely exceeding that of the commercial graphite.[201] This peculiarity, as well as tin and silicon abundance, sustainability, safety and cheapness, carried out an increasing interest in these materials as high-energy anodes for application in LIBs and SIBs. However, some drawbacks hinder implementation and commercialization of alloying materials, such the huge volumetric expansion and contraction of the involved metals/semimetals (up to 300% for Si). This leads to pulverization of the electrode, with consequent loss of the material/current collector contact, and instability of the SEI, resulting in poor performance and cycle life (**Figure 1.18**).[200,202] Furthermore, the radius of the adopted alkali metal has a strong effect on the alloying reaction, with higher deformation and lower capacity for Na-based alloys working at higher potentials.[203,204] Consequently, alloying anodes in SIBs have lower gravimetric and volumetric energy densities compared to LIBs, while the less reductive Na^+/Na potential leads to lower electrolyte degradation at the electrode/electrolyte interphase.[205]

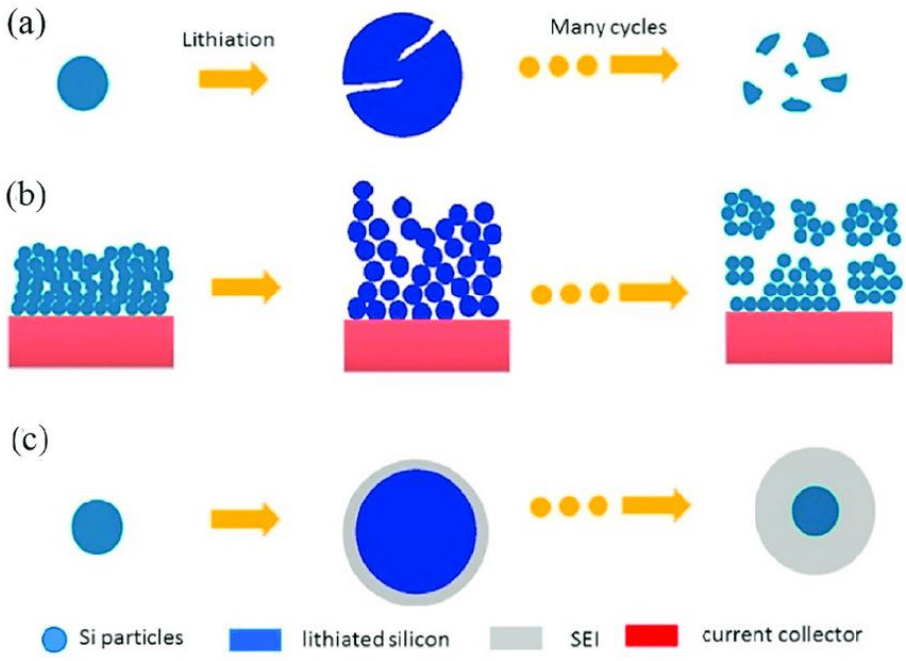

Figure 1.18: *Various failure mechanism of alloying-based anodes (silicon-based) in LIBs:* ***(a)*** *particle pulverization;* ***(b)*** *collapse of the electrode structure with detachment from current collector;* ***(c)*** *repeated generation and instability of SEI.*[200]

Going into more detail in the alloying process, a various number of phenomena can occur: (i) loss of active material due to volume expansion and consequent pulverization, leading to particles isolation

and electrode inactivation, with related lower conductivity; (ii) formation of unstable SEI film on the electrodes and its braking for the subsequent volume changes upon cycling , with related loss of capacity; (iii) occurring of irreversible processes, such as trapping of ions into the host alloy for a slow release kinetics, formation of stable lithiated/sodiated compounds, or aggregation of particles due to heating induced by the pressure generated upon volume expansion, with related effect on irreversible capacity.[200,202]

To mitigate these phenomena, a good approach is to disperse the active materials in a matrix, in order to buffer the volume changes and preserve the electrode integrity. A good matrix has to favor a fast ion exchange and promote the structural stability of the whole electrode, preventing particle aggregation.[199] The materials suitable for use as matrices can be summarized in: (i) inactive/electrochemically inert matrix compounds; (ii) electrochemically active matrix compounds; (iii) electrodes with 3D porous structure; (iv) carbon-based compounds (*i.e.* graphene).[199] Another approach is the reduction of the particle size of alloying anodes at the nanometer scale, leading to a significant improvement in cell performances. Indeed, nanoparticles can better sustain mechanical stress without fracturing, and they also shorten electronic and ionic transport distances, favoring faster diffusion.[199,206]

Considering alloying compounds for LIBs, silicon is the most interesting, thanks to its very high theoretical specific capacity of 3579 mAh g^{-1} and the suitable low charge/discharge potential under 0.4 V vs. Li^+/Li.[207] The alloying reaction produces a compound with a stoichiometry up to $Li_{15}Si_4$ at room temperature, as shown in **Equation 1.10**:

$$4Si + 15Li^+ + 15e^- \rightleftarrows Li_{15}Si_4 \qquad \textbf{(1.10)}$$

At higher temperatures, further lithiation could occur, reaching the highest stoichiometry $Li_{22}Si_5$, with a theoretical capacity of 4200 mAh g^{-1}, as described in **Equation 1.11**:[207]

$$5Si + 22Li^+ + 22e^- \rightleftarrows Li_{22}Si_5 \qquad \textbf{(1.11)}$$

Beyond the quite high theoretical capacity, Si displays other interesting qualities, such as high relative abundance, environmental sustainability, and low cost.[208] Nevertheless, it suffers from a vast volume expansion (up to 400%), which leads to repeated SEI formation/destruction and irreversible capacity loss, also considering that the effect is grater with respect to other materials due to the large amount of Li stored.[208] The use of Si-based alloying anodes in SIBs has not received the same attention as for LIBs, due to cycling irreversibility of the NaSi alloy.[205]

Alternatively to Si, Sn has also received great attention thanks to the possibility of electrochemically react with both Li and Na to form several alloys. The formation of alkali-rich phases can reach

stoichiometries as high as $Li_{22}Sn_5$ in LIBs and $Na_{15}Sn_4$ in SIBs, leading to theoretical capacities of 994 mAh g^{-1} and 847 mAh g^{-1}, as reported in **Equation 1.12** and **Equation 1.13**, respectively:[209]

$$5Sn + 22Li^+ + 22e^- \rightleftarrows Li_{22}Sn_5 \quad \textbf{(1.12)}$$

$$4Sn + 15Na^+ + 15e^- \rightleftarrows Na_{15}Sn_4 \quad \textbf{(1.13)}$$

Similarly to Si, even Sn suffers from volume change upon cycling, which could reach expansions up to 259% for LIBs and 423% for SIBs, thus limiting its performance.[210]

Conversion anodes

Conversion-type compounds follow a reaction in which a transition metal oxide, phosphide, nitride, or sulfide is reduced with Li^+ to give metal nanoparticles and the corresponding lithium (or sodium) compound, as described by **Equation 1.14**:

$$M_aY_x + xnLi^+ + xne^- \rightleftarrows aM^0 + xLi_nY \quad \textbf{(1.14)}$$

A wide range of transition metal oxides, sulfides, phosphides and similar compounds of p-block metalloids have been investigated as possible conversion anodes thanks to their interesting electrochemical properties and relatively low cost.[65,211–214] Conversion anodes can offer a higher specific capacity than insertion materials (ranging from 500 up to 1000 mAh g^{-1}) and a broader range of working potentials vs. Li^+/Li and Na^+/Na (between 0.5 and 1.5 V), the latter related with higher safety with reduced risk of dendrite formation.[215] However, their application is hindered due to the instability driven by the intrinsic structural change of the conversion reaction. Moreover, the voltage profiles of conversion-based anodes are characterized by a large voltage hysteresis which lowers the charge/discharge energy density.[216]

Among the different conversion anodes, binary and ternary oxides of 3d transition metals (*i.e.* Cr, Mn, Fe, Co, Ni, Cu) are the most investigated for both LIBs and SIBs.[216] Particularly, Fe_2O_3 is one of the most studied systems, thanks to its abundance, stability and high capacity of 1011 mAh g^{-1}.[214] Moreover, mixed oxides with more than one electrochemically active metal (AB_2O_4 stoichiometry) have been studied as possible anode in Li-ion and Na-ion batteries,[217] revealing not efficient back conversion to the starting material, with consequent irreversible capacity loss. Additionally, transition metal chalcogenides, phosphides, nitrides and hydrides have also been explored, with sulfides showing interesting properties.[212,216] Indeed, the latter possesses better electrical conductivity compared with oxides, while the dissolution of discharge product leads to low coulombic efficiency and poor cycle life.[216]

1.4.3 Electrolytes

The electrolyte solution is another key component of the cell, and its choice is crucial to obtain good performance of the battery. Electrolytes are the medium through which Li^+ and Na^+ ions migrate from one electrode to the other. Several types of electrolyte solutions have been studied over the last decades, such as liquid- and glyme-based,[45,50] gel and solid polymers,[50,218,219] or solid ceramics.[220] Nevertheless, the most commercially used electrolytes are liquid solutions employing an inorganic salt dissolved in organic solvents. A good electrolyte must satisfy the following requirements:

- Low viscosity.
- Low electronic conductivity ($\sigma_e < 10^{-10}$ S cm^{-1}) to avoid short-circuit in the cell.
- High ionic conductivity ($\sigma_{Li} > 10^{-4}$ S cm^{-1}) to minimize internal resistance.
- Wide voltage range, or rather large electrochemical stability window (ESW).
- Chemical stability and lack of reactivity with the other cell components.
- Sustainability, cheapness, and acceptable stability.

In both LIBs and SIBs polar organic aprotic solvents (especially carbonate-based) are employed instead of water due to their wide ESW, low melting point, and high melting point, characteristics that prevent decomposition of the solution coupled with a large number of anodes and cathodes.[45,221] The most used organic solvents are illustrated in **Figure 1.19**, each one possessing its own dielectric constant and viscosity. The combination is extremely crucial to favor high ionic conductivity, cyclability, and suitable SEI/CEI formation and composition.[11]

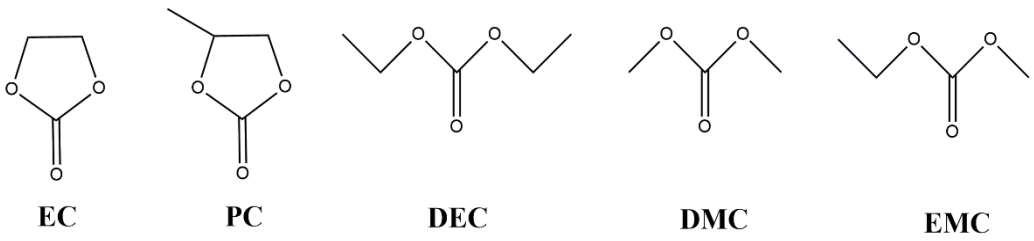

Figure 1.19: *Chemical structures of the most employed carbonate solvents for LIBs and SIBs. In detail: ethylene carbonate (EC), propylene carbonate (PC), diethyl carbonate (DEC), dimethyl carbonate (DMC), ethyl methyl carbonate (EMC).*

In general, a mixture of the above indicated solvents guarantees better performance, by enhancing the conductivity and thermal stability of the single component.[222] Ethylene carbonate (EC) is the most used solvent thanks to its high dielectric constant (89.6).[45]

Considering the salts, there are only a few appropriate species. Indeed, they must have a very bulky negative counter ion, in order to neglect its contribution to the diffusion with respect to Li^+ and Na^+. In these regard, the commonly used lithium- and sodium-based electrolyte salts are

hexafluorophosphates ($LiPF_6$ or $NaPF_6$), tetrafluoroborates ($LiBF_4$ or $NaBF_4$), bis(fluorosulfonyl)imides (LiFSI or NaFSI), and bis(trifluoromethane) sulfonimides (LiTFSI or NaTFSI).[223] Additionally, for SIBs also sodium perchlorate ($NaClO_4$) is widely employed. As described for solvents, more than one salt can be dissolved. This strategy could be used to avoid gas production and improve cyclability at high temperatures.[50] For Li-ion batteries, two electrolytes are highly diffused: a 1M solution of $LiPF_6$ dissolved in a 1:1 v/v mixture of EC:DMC (called LP30), or a 1M solution of the same salt dissolved in 3:7 v/v mixture of EC:EMC. However, in SIBs better performances are achieved with a 1M solution of $NaClO_4$ dissolved in 1:1 v/v mixture of EC:PC or EC:DEC,[223] while in the last years the substitution of sodium perchlorate with $NaPF_6$ is encouraged because of safety concerns.[223] Organic solvents are inclined to decompose at the anode, affecting the electrochemical performance of the cell. Indeed, SEI irreversible formation at the negative side surface is crucial, offering good ionic conductivity and electronic insulation, protecting the electrode surface and avoiding parasitic reactions.[45] Therefore, the nature of the passivation layer is a direct consequence of electrolyte composition: EC is proven to stabilize the SEI, while PC is detrimental in LIBs, since it is co-intercalated in graphene layers causing exfoliation. Nevertheless, PC is required in SIBs because favors suitable solvation energy and charge transfer,[224] despite SEI in Na-ion systems are less stable and partially soluble in carbonate solvents.[225,226] To control SEI formation and avoid its excessive growth, which could block interaction with the anode, an effective strategy is the use of electrolyte additives. They are molecules with the aim of being consumed during the formation of the passivation layer, providing a more stable SEI. The most used additives in both LIBs and SIBs are vinylene carbonate (VC) and fluoroethylene carbonate (FEC).[227,228] Furthermore, especially in sodium half-cells, the use of additives is required to stabilize metal Na used as reference and counter electrodes, favoring potential monitoring and a homogeneous plating/stripping process.[226]

One of the most important drawbacks for the currently employed electrolytes is the flammability of the organic solvents, which could create safety issues, especially if the batteries undergo dendrite formation or thermal runaway.[30,229] An efficient approach to increase the safety and affordability of the batteries is the use of stable and non-flammable electrolyte, adopting end-capped ether called "*glymes*" with $CH_3O(CH_2CH_2O)_nCH_3$ formula and low *n* value (**Figure 1.20**). Glymes are liquid at room temperature and are characterized by high flash point, fast Li^+ and Na^+ ions transport, wide ESW, thermal stability, and compatibility with the commonly used conductive salts, favoring their use as solvents with several anodes and cathodes (*i.e.* LFP, LCO, NMC, graphite, hard carbons) with promising performances.[230–234] However, glyme-based electrolytes reveal low passivation properties, limiting their applicability because of continuous solvent decomposition.[231,235] This

problem may be overcome by using stabilizing additives, like the ones above described or $LiNO_3$, which leads to the formation of a suitable passivation layer.[236] Intensive work has been recently focused studying the intercalation between alkali ions and glyme molecules, along with the study of glyme-based electrolytes exploiting high concentrations of lithium salts, described as solvent-in-salt solutions, revealing superior transport properties, high oxidative and thermal stability, and formation of an improved SEI.[237,238]

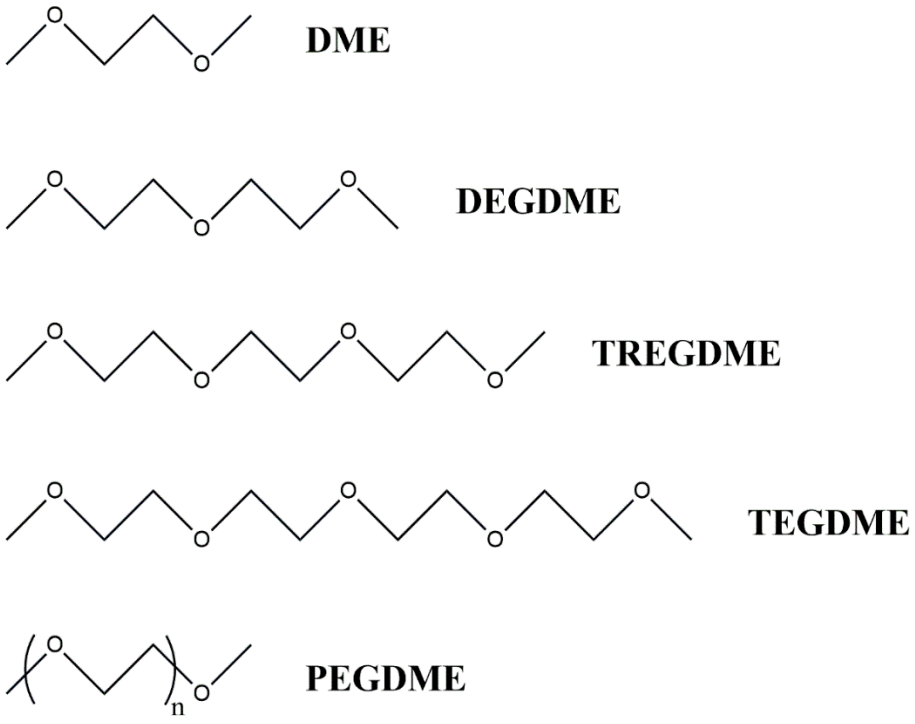

Figure 1.20: *Molecule structure of various glyme solvents. In detail: 1,2-dimethoxyethane (DME, n = 1), diethylene glycol dimethyl ether (DEGDME, n = 2), triethylene glycol dimethyl ether (TREGDME, n = 3), tetraethylene glycol dimethyl ether (TEGDME; n = 4), polyethylene glycol dimethyl ether (PEGDME).*

Solid polymer electrolytes (SPE) are also getting a lot of interest to increase the safety of rechargeable batteries. In particular, SPE based on polyethylene oxide (PEO) exhibit excellent thermal, mechanical, and electrochemical stability, negligible volatility, efficient dendrites suppression, and compatibility with conductive lithium and sodium salts (particularly with LiTFSI and NaTFSI), leading to suitable ion transport characteristics.[239,240] However, the high molecular weight of PEO causes excessive crystallinity at room temperature that requires higher temperatures for application (above 65 °C), when the PEO amorphous state is reached, and adequate ionic conductivity is obtained.[240] Ceramic fillers, *i.e.* TiO_2, Al_2O_3, SiO_2, or ZrO_2, are largely used to promote the polymer amorphous state, while high temperatures (around 60 °C) are still needed.[241–243] Thus, many efforts are required to optimize solid-state polymer electrolytes due to their promising results obtained in lithium batteries exploiting insertion electrodes.[241,243,244]

1.5 Electrodes Processing and Manufacturing

As already described, each component of the battery plays a crucial role in the final application of the devices. Indeed, the electrode processing, by using anodic or cathodic compounds as active materials, and the following manufacturing are key factors to achieve the best battery performances, especially in the upscaling from lab-scale to industrial level.[86,245,246]

In these regards, the slurry formulation represents the starting point to produce high quality electrodes for application in LIBs and SIBs. Generally, electrodes are composed of three main components: the active material (exchanging Li^+ or Na^+ during the redox processes), the conductive agent (typically nanometric carbon such as C65, Super P, carbon black), and the binder (*i.e.* polymeric materials) guaranteeing the adhesion of the slurry to the current collector, while granting interparticle cohesion. Binder and nanometric carbon are employed in small percentages (< 5%), playing a crucial role for the functioning of the device.[247,248] Among the possible different polymers used as binders, polyvinylidene fluoride (PVdF) is currently employed in commercial LIBs, providing good adhesion with the current collector. Furthermore, it is chemically and electrochemically inert towards the common electrolytes in the voltage window at which LIBs/SIBs are operated, possesses good mechanical resistance, and a thermal stability between -40 °C and +150 °C.[249] However, the high costs associated with the necessity to dissolve it, during electrode processing, in toxic and volatile solvents such as N-methyl-2-pyrrolidone (NMP), are undesirable features. In these regards, the use of greener polymers soluble in water, such as carboxymethyl cellulose (CMC), received huge attention, especially when coupled with anodic materials.[250]

To further increase the conductivity of the coatings, especially when low conductive materials are used (*i.e.* olivine cathodes), the addition of a small percentage of different conductive additives represents a valuable choice.[247] The most used are carbon additives such as carbon nanotubes (CNTs) or nanowires (CNWs) or graphene.[88,89,182,185] Indeed, the combined use of various carbon additives enables different conduction pathways, such that carbon black nanoparticles render short-range conduction, while CNTs (or CNWs) provide long-range conduction pathways.[251] Single-walled carbon nanotubes (SWCNTs) are considered ideal conducting agents, owing to their high electrical conductivity (10^6 S m^{-1}), length-diameter aspect ratio (>3500), and excellent mechanical properties (Young's moduli between 270–950 GPa), that could enhance cycling and dimensional stability of electrodes. Nevertheless, large specific surface area of SWCNTs may limit their uniform dispersion in a slurry, causing their aggregation into bundles.[185,252] Considering other possible additives, graphene presents remarkable mechanical properties (Young's modulus 1100 GPa), reliable thermal conductivity (~4000 W m^{-1} K^{-1}), and good electrical conductivity (10^8 S m^{-1}).[180,182] Furthermore, graphene is a promising containment matrix for composite materials, able to withstand

the mechanical stress caused by alloying and conversion materials, thus increasing the electronic conductivity of the whole electrode.[253,254]

To meet the desired specifications for different applications, and for an optimal electrode microstructure, research on the relationship between manufacturing and performance is of paramount importance.[255,256] Indeed, electrode formulation development, slurry processing, and electrode manufacturing play a critical role, especially at the cathode side. In these regards, several parameters could affect the electrode quality and have to be optimized to guarantee satisfactory performance and cell stability, especially when upscaling from lab-scale to larger cell formats.[245,255,257] **Figure 1.21** reports the parameters which plays a crucial role in the electrode manufacturing, such as slurry formulation composition, viscosity, solid content, coating speed, drying temperature, electrode loading, calendering process, density and porosity.[258]

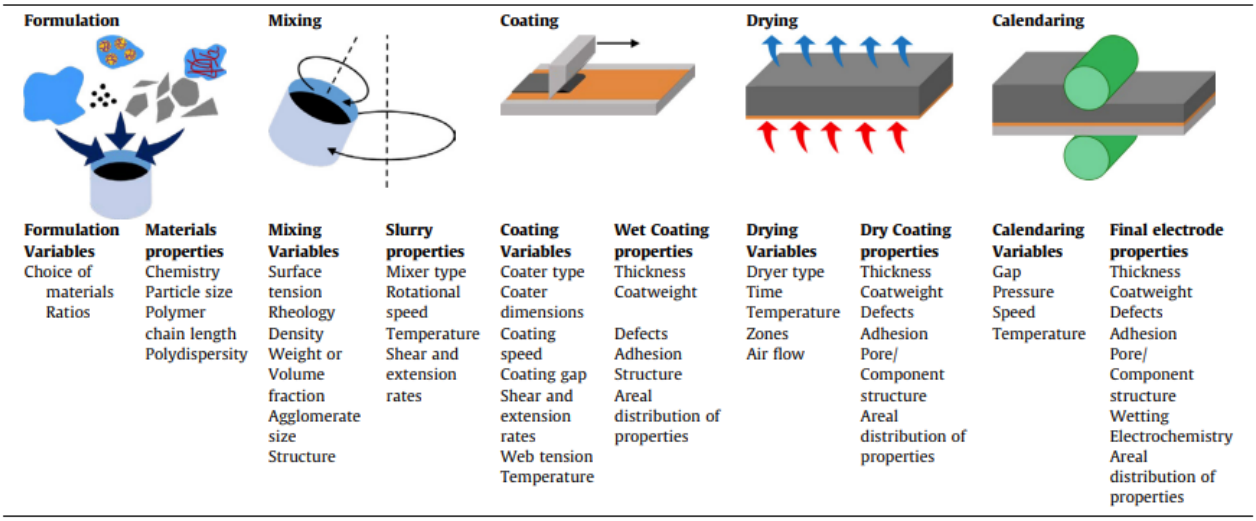

Figure 1.21: *Summary of the parameters involved in the electrode manufacture process.*[258]

The effects of these parameters cannot be studied in isolation. For example, a more intensive mixing (higher speeds, longer time) may more efficiently break up agglomerates, giving a slurry with a more desirable rheology (typically lower viscosity at high shear rates relevant to coating),[258,259] which can be coated at a higher speed. However, high mixing speed could also shear degradation of the binder, causing delamination or cracking of the electrodes during drying or calendering.[258,260]

Overall, the study and the optimization of the chemical and physical parameters involved in the electrode processing and manufacturing is mandatory in order to obtain electrodes with optimal features for application in upscaled devices.[245,261]

1.6 Distribution of Relaxation Time (DRT) Function

Distribution of relaxation time (DRT) is a function which is used to transform a frequency dispersion in the τ-domain.[262] Starting from the work of Ivers-Tiffée,[263] DRT has already been used for characterizations on Li-ion batteries,[264] on fuel-cells,[265] and on solar cells.[266] The transformation into the τ-domain of the impedance data is defined by **Equation 1.15**:

$$Z(\omega_i) = R_\infty + R_p \int_0^\infty \frac{\gamma(\tau)}{1+j\omega_i\tau} d\tau \qquad \textbf{(1.15)}$$

where $Z(\omega)$ is the impedance response, R_∞ is the high-frequency resistance (intercept in the real axis in Nyquist plot), R_p is the polarization resistance, and $\gamma(\tau)$ is the distribution function of relaxation time. Since $\gamma(\tau)$ is a normalized function, from **Equation 1.16**:

$$\int_0^\infty \gamma(\tau) d\tau = 1 \qquad \textbf{(1.16)}$$

Unfortunately, **Equation 1.15** is a Fredholm integral of the first kind and its inversion is an "*ill-posed problem*", *i.e.* its solving can lead to many possible solutions. Specifically, the boundary conditions require that the angular frequency ω tends to zero; however, this requirement is usually not encountered in typical EIS spectra for batteries, as the low-frequency diffusion region diverges from the real axis, and a pre-processing step for the Nyquist plots is required.[262] Indeed, the only two diffusion processes who are DRT-processable are the finite-length Warburg and the Gerischer.[265] Several routes are available to approximate the distribution function: Fourier-transform,[267] Maximum entropy,[268] multiple (*RQ*) fit,[267,269] and Tikhonov regularization.[270–272] In the Fourier-transform method, a window function must be applied which can have significant effect on the DRT shape. Moreover, in the case of Tikhonov regularization and maximum entropy, the adjustment of a particular parameter is necessary to avoid under- or overestimation of the impedance spectra. Common ways to display impedance spectra are Nyquist or Bode plot; however, could be difficult to distinguish two individual processes with time constants or frequency very similar. In these regards, DRT could help to understand the physical processes hiding behind an ac-dispersion. A $(R_1C_1)(R_2C_2)$ circuit with very close time constants ($\tau_2 = 2\tau_1$) is represented as a single arc in the Nyquist plot. However, DRT calculation deconvolutes the processes which appear as two different peaks (**Figure 1.22**), and, more generally for a multiple-feature impedance dispersion, it allows to separate all the (RC) elements into distinct peaks.[262] Particularly, the measurements of each peak position and area can provide useful information about the transport, and interfacial properties of the cell itself.[263,264]

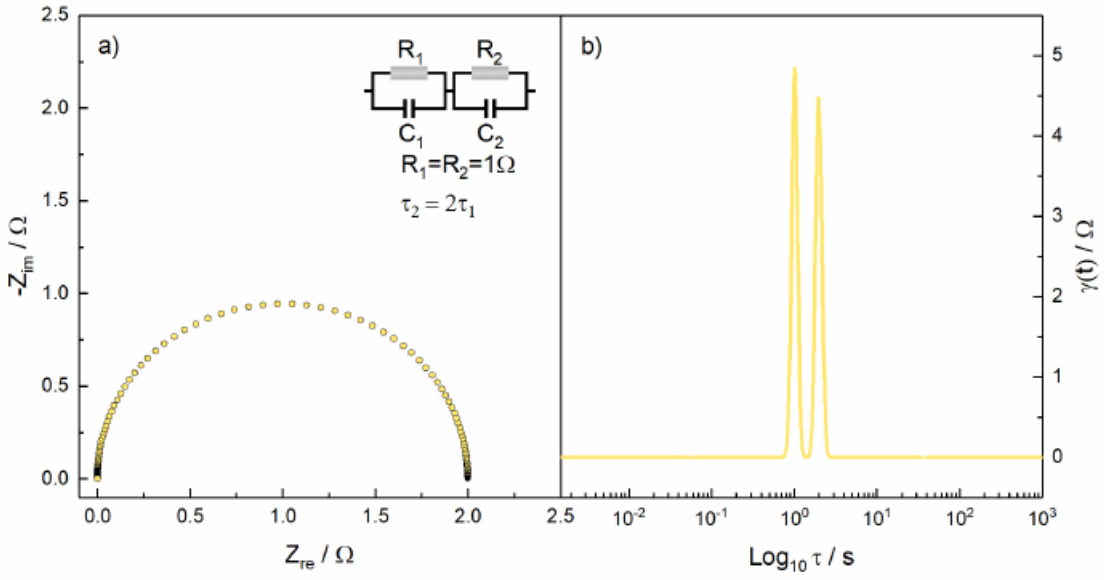

Figure 1.22: (a) *Nyquist plot of a (R_1C_1)(R_2C_2) circuit with $\tau_2 = 2\tau_1$ with* ***(b)*** *corresponding DRT computation of the ac-dispersion.*

Going into detail of the Tikhonov regularization the imaginary part of the impedance can be rewritten as **(Equation 1.17)**:

$$\begin{pmatrix} Z_{i,1} \\ \vdots \\ Z_{i,n} \end{pmatrix} = \begin{pmatrix} \frac{-\omega_1\tau_1}{1+(\omega_1\tau_1)^2} & \cdots & \frac{-\omega_1\tau_n}{1+(\omega_1\tau_n)^2} \\ \vdots & \ddots & \vdots \\ \frac{-\omega_n\tau_1}{1+(\omega_n\tau_1)^2} & \cdots & \frac{-\omega_n\tau_n}{1+(\omega_n\tau_n)^2} \end{pmatrix} \begin{pmatrix} b_1 \\ \vdots \\ b_n \end{pmatrix} \qquad \textbf{(1.17)}$$

However, even small Z_i perturbation will result in large deviations from solution *b*. To avoid that, a regularization parameter λ is introduced in the Tikhonov regularization (**Equation 1.18**):

$$min_b\{\|Ab - Z_i\|_2^2 + \lambda^2\|b\|_2^2\} \qquad \textbf{(1.18)}$$

The solution to the problem is reported in **Equation 1.19**:

$$b = (A^TA + \lambda^2 I)^{-1}A^TZ_i \qquad \textbf{(1.19)}$$

Consequently, too large λ values can result in an underestimation of the DRT function, while a too small λ will result in overestimation and creation of artefact peaks.[272] Indeed, a general rule for the choice of λ does not exist.

DRT is often used as an aid to find a better equivalent circuit model with a physicochemical meaning. For instance, if a peak is related to a charge transfer process, it can be easily spotted by acquiring EIS spectra at different temperatures, following an Arrhenius behavior.[269,273,274]

1.7 Aim of the work

In the present thesis the study of the electrochemical properties of different cathodes for application in both Li-ion and Na-ion batteries is performed, to analyze the suitability of these materials for application and the effect of the electrode processing and cell manufacturing on the final performance of the battery. In these regards, the work is focused on low cost, low toxicity and improved energy densities mixed-olivine cathodes based on iron and manganese. LFP is considered as a Generation 3 *design-to-cost* cathode by the "Strategic Research Agenda for Batteries" of Batteries Europe,[156] and currently employed in commercial batteries, and it lately reached a renewed interest due to their remarkable economic and safety characteristic. Indeed, the study of already commercial mixed olivine cathodes, also considered as Generation 3 *design-to-cost* materials, but not yet employed in commercial batteries, could represent a suitable alternative to obtain new safe, cheap, and stable batteries for application in portable devices and stationary energy storage. Moreover, their possible conversion to obtain Na-based olivine could be implemented as a low-cost alternative for stationary storage. Accordingly, the study of electrode processing and production and of cell manufacturing are key factors to link lab-scale research to industrial production.

Furthermore, the study of layered oxide cathodes combined with alloying anodes in LIBs and SIBs could represent a suitable choice to produce high energy density systems for application in HEVs and EVs. Therefore, also in this case cell manufacturing and, particularly, electrode balancing have a crucial role in the practical application of these devices.

In summary, this work aims to study different cathode chemistries for possible use in LIBs and SIBs addressed to a wide range of possible applications, with particular attention to cathode sustainability, cost, safety, and stability, coupled with the electrodes manufacturing and full-cell balancing to meet upscaling requirements.

2. Structural, Electrochemical and Interfacial Characterization of $AFe_{0.6}Mn_{0.4}PO_4$ (A = Li, Na) Mixed-Olivine Cathodes for Li-ion and Na-ion Batteries

LIBs are the most widely diffused energy storage systems, due to their high energy density and outstanding cycle life.[275] However, the massive use of Li and its compounds for fulfilling this increasing demand poses serious economical and geopolitical concerns, mainly ascribed to the raising price and the local availability of this important alkali metal.[276] A possible solution may be represented by the development of analogue devices using a different and more abundant alkali metal, such as the sodium-ion batteries (SIBs).[47,144] Despite the lower capacity and a higher electrochemical potential than lithium, sodium appears more sustainable due to its abundance and homogeneous distribution on the Earth crust.[74] Furthermore, SIBs exploit a similar reaction mechanism compared to LIBs, thereby possibly facilitating the R&D for alternative energy storage systems based on Na.[277] The economic and environmental issues of transition metals included in layered oxide composition (*i.e.* Co), and possible structural degradation during cell operation, have promoted the use of polyanionic phospho-olivines characterized by remarkable stability, low cost and non-toxicity.[76] Among them, LFP revealed outstanding features, such as high specific capacity (170 mAh g^{-1}),[85,121] relevantly longer cycle life and lower price, despite lower energy density compared to layered oxides, which promoted its commercialization.[77,85] The partial substitution of iron with other transition metals with a higher redox potential, such as Mn into a ‘‘*mixed-olivine*” with general formula $LiFe_{1-x}Mn_xPO_4$, appeared as an adequate strategy to increase the energy density of the olivine cathodes, leading to compounds with a higher potential than LFP, still holding acceptable electronic conductivity, efficient Li^+ transport, and hindered pseudo Jahn-Teller distortion.[82,93,95,97,98,278] For these reasons $LiFe_{1-x}Mn_xPO_4$ cathodes are currently commercial materials.[105]

On the other hand, lithium metal anode may further improve the energy density of the battery; however, safety issues may be related to the possible formation of metal dendrites during lithium deposition/dissolution process.[229,279] Therefore, the use of solid electrolytes exploiting amorphous polymers dissolving lithium salts, such as poly(ethylene oxide) (PEO), has been suggested as a possible choice for achieving a safe use of lithium metal in battery.[280–282] However, PEO have a poor ionic conductivity at temperatures lower than 65 °C due to excessive crystallinity hindering the Li^+ ions transport.[240,243] However, end-capped polyethylene glycol dimethyl ether with MW higher than 1000 g mol^{-1} may be employed to achieve solid polymer electrolytes operating at lower temperature than PEO.[283]

$NaFePO_4$ (NFP) cathode can in principle perform similarly to LFP using the abundant and economically sustainable sodium instead of lithium,[107,151] however with a lower theoretical specific capacity (154 mAh g^{-1}) and potential (3.1 V vs. Na^+/Na), as well as slower kinetics due to the larger and heavier alkali metal.[284] However, a relevant drawback for NFP is represented by the predominant formation of the electrochemically inactive phase with the maricite structure during common synthetic pathways.[110,285] On the other side, electrochemically active triphylite-type NFP has been achieved only through conversion strategies involving electrochemical or chemical de-lithiation of LFP and subsequent sodiation of heterosite $FePO_4$.[111,112] The need for large-scale diffusion of post-lithium materials for energy storage has triggered relevant research for developing NFP electrodes with increased capacity and energy density.[286,287] In analogy with the LFP, a suitable strategy to improve the performances of the NFP is the partial substitution of iron with others transition metals to achieve a mixed olivine version of the electrode.[113,115] In particular, the manganese-to-iron substitution to achieve the $NaFe_{1-y}Mn_yPO_4$ triphylite appears to be one of the most promising pathways to achieve efficient Na^+ insertion/de-insertion electrochemical process into the olivine structure.[115]

Considering the above-described trends for battery materials and polymer electrolytes, **Chapter 2** is focused on the synthesis and characterization of a Fe/Mn-based mixed olivine cathode and its conversion to the sodium analogue, with the study particularly focused on the application of the Li-based olivine in safer Li-metal batteries, and the investigation of Na^+ (de-)insertion mechanism for the Na-based one, with particular attention to diffusion and interfacial properties.

Section 2.1 describes the experimental methods adopted in this chapter.

Section 2.2 reports the synthesis by sol-gel pathway and the full characterization of a $LiFe_{0.6}Mn_{0.4}PO_4$ (LFMP), revealing similar performances with respect to several literature works which report similar compositions achieved with different synthetic strategies.[93,97] The synthesis of LFMP is advantageously monitored by thermogravimetric analysis (TGA) and X-ray diffraction (XRD), while the material is studied in terms of structural, morphological, and electrochemical features in lithium cell with conventional electrolyte. Furthermore, the new electrode is originally investigated in a lithium cell exploiting the solid polymer configuration by employing a composite polymer electrolyte (PEGDME_CPE), which has been previously reported, and revealed excellent properties in terms of Li^+ conductivity, thermal, chemical, and electrochemical stability, and remarkable cycle life in solid polymer lithium battery operating at 50 °C.[219] It is here shown that a LFMP/PEGDME_CPE cell operates at 50 °C with two voltage plateaus centered at about 3.5 and 4 V. The achieved results demonstrate the possibility to achieve new-generation lithium polymer cells characterized by high energy, remarkable stability and, at the same time, suitable safety and environmental characteristics.

In **Section 2.3** the electrochemical conversion of the previously synthesized LFMP cathode to the NFMP analogue is explored. The conversion process is fully monitored by scanning electron microscopy (SEM), energy dispersive X-ray spectroscopy (EDS), X-ray diffraction (XRD), Raman spectroscopy, and inductively coupled plasma–optical emission spectroscopy (ICP-OES), and the electrochemical behavior of the obtained NFMP is studied in sodium cell. The sodium olivine cathode is investigated by means of cyclic voltammetry (CV), galvanostatic intermittent titration technique (GITT), electrochemical impedance spectroscopy (EIS) at different states of charge, with calculation of the distribution of relaxation time (DRT) function, and compared with the lithium analogue. These efforts are aimed at clarifying the analogies and the differences between NFMP and LFMP in terms of alkali ions diffusion coefficient, interphase features, and charge-transfer properties. The achieved results can shed light on reaction kinetics, interfacial properties, and ions diffusion, driving the future improvements of the features of mixed-olivine cathodes for application in Na-ion battery.

Despite the first Mn-doped NFP was already achieved in 2011,[117] only few detailed studies of sodium-based mixed olivine cathodes have been reported in literature, particularly focusing on the degree of Mn substitution,[115] and the associated effect on the structure and on the Na^+ insertion/extraction mechanism.[116] Accordingly, in **Section 2.4** an *operando* X-ray absorption spectroscopy (XAS) analysis on NFMP cathode is reported, to deeply investigate the mechanism of Na^+ (de-)insertion, as well as the actual chemical environment of Fe and Mn centers in the olivine structure. Particularly, the evolution of the oxidation state of the transition metals from the starting LFMP to the converted NFMP is investigated, to assess the hindered reactivity of Mn, also by exploiting *ex-situ* X-ray photoelectron spectroscopy (XPS) analysis. Furthermore, a preliminary investigation of the structural features of the material is performed, to shed light on possible differences compared to the lithium counterpart.

2.1 Experimental Section

Synthesis of $LiFe_{0.6}Mn_{0.4}PO_4$ and preparation of Composite Polymer Electrolyte (CPE)

The olivine cathode (3 g) was prepared by a sol-gel synthesis pathway reported elsewhere for different cathodes.[93,98,288] Lithium dihydrogen phosphate (LiH_2PO_4 99%, Sigma Aldrich) was dissolved in 15 mL of water (solution A), whereas transition metal acetates (iron(II) acetate, $Fe(CO_2CH_3)_2 \geq 99.99\%$, Sigma Aldrich; manganese(II) acetate tetrahydrate, $Mn(CO_2CH_3)_2 \cdot 4H_2O \geq 99\%$, Sigma Aldrich) and citric acid ($C_6H_8O_7 \geq 99.5\%$, Sigma Aldrich) were dissolved in 30 mL of water (solution B). Solution A was added dropwise to solution B to obtain an aqueous solution containing Li^+, transition metal ions (Fe^{2+} and Mn^{2+}), and citric acid in a molar ratio of 1:1:0.3, respectively (solution C), in which

the stoichiometry of the reagents was set to achieve the LFMP material. Solution C was heated at about 60 °C for ~8 h in a silicon oil (Sigma Aldrich) bath under stirring through a hot plate until the formation of a dark gel. The gel was initially dried for 12 h at 120 °C under a dry air flow, and afterwards heated under an argon flow at 350 °C with a rate of 2 °C min^{-1}, held at 350 °C for 3 h, and naturally cooled to room temperature. The precursor was ground in an agate mortar, heated under an argon flow 600 °C with a rate of 2 °C min^{-1}, held at 600 °C for 10 h, heated at 700 °C with a rate of 5 °C min^{-1}, held at 700 °C for 3h, and naturally cooled to room temperature. The achieved material was ground in an agate mortar and the sample was identified by the acronym LFMP_700 (*i.e.* the intermediate olivine). The above sample was subsequently heated under an Ar flow at 850 °C with a rate of 5 °C min^{-1}, held at 850 °C for 1 h, naturally cooled to room temperature, ground in an agate mortar and indicated by the acronym LFMP_850 (*i.e.* the final olivine sample, also indicated as LFMP). All the thermal steps of the synthesis procedure were performed in a tubular furnace (GHA 12/3000, Carbolite).

The CPE was achieved by using solid polyethylene glycol dimethyl ether (PEGDME2000, $CH_3O(C_2H_4O)_nCH_3$, average MW of 2000 g mol^{-1}, Sigma Aldrich), lithium bis(trifluoromethanesulfonyl)imide (LiTFSI, 99.95% trace metal basis, Sigma Aldrich), lithium nitrate ($LiNO_3$, 99.99% trace metal basis, Sigma Aldrich), and fumed silica (SiO_2, average particle size 0.007 µm, Sigma Aldrich) as already described in literature.[219] LiTFSI and $LiNO_3$ were mixed with PEGDME2000 in the ratio of 1 mol of each salt to 1 Kg of polymer, whilst SiO_2 was included by a weight ratio of 10% with respect to the mass of PEGDME2000-lithium salts mixture. The electrolyte film was formed through a semi-liquid slurry of the above-described powder mixed with acetonitrile (ACN, Sigma Aldrich), which was subsequently removed upon several drying steps to obtain a solid membrane indicated using the acronym PEGDME_CPE.

Characterization of Powders

Thermogravimetric measurement was performed to investigate the synthesis process under a N_2 atmosphere employing a heating rate of 2 and 5 °C min^{-1} in the 25 – 600 and 600 – 850 °C temperature ranges, respectively, while thermogravimetric analyses to check the carbon content of the LFMP_700 and LMFP_850 samples were carried out under air flow employing a heating rate of 5 °C min^{-1} in the 25 – 800 °C temperature range. All measurements were carried out through a Mettler Toledo TGA 2 instrument. A reaction mechanism (**Equation 2.1**) involving oxidation of C and Fe in the mixed olivine to form CO_2, Fe_2O_3, $FePO_4$, Li_3PO_4, and $LiMnPO_4$, was assumed for the determination of the carbon content as reported below:

$$xC + yLiFe_{0.6}Mn_{0.4}PO_4 + (0.15y + x)O_2 \rightarrow 0.1yFe_2O_3 + 0.4yLiMnPO_4 + 0.2yLi_3PO_4 + 0.4yFePO_4 + xCO_2 \quad \textbf{(2.1)}$$

Where *x* and *y* (mols) were determined through the following system of equations (**Equation 2.2**):

$$\begin{Bmatrix} xM_C + yM_{LiFe_{0.6}Mn_{0.4}PO_4} = A \times m \\ 0.1yM_{Fe_2O_3} + 0.4y + 0.2yM_{Li_3PO_4} + 0.4yM_{FePO_4} = B \times m \end{Bmatrix} \quad \textbf{(2.2)}$$

Where A and B are the % in weight achieved from TGA measurement (see **Figure 2.3**), for LFMP_700 and LFMP_850, respectively, the values indicated by M_X (g mol^{-1}) represent the molecular weight of the various solids involved in **Equation 2.1**, and *m* (g) is the initial weight of the sample used for the TGA. It is worth noticing that weight losses before 300 °C were attributed to free or absorbed water removal, those after 300 °C to CO_2 evolution, while weight increases after 200 °C to metal oxide formation. The carbon amount (wt.%) in the samples was achieved by **Equation 2.3**:

$$wt.\%C = \frac{xM_C}{xM_C + yM_{LiFe_{0.6}Mn_{0.4}PO_4}} \cdot 100 \quad \textbf{(2.3)}$$

The scanning electron microscope (SEM) images of LMFP_850 were collected using a Zeiss EVO 40 microscope with a LaB_6 thermionic source. Sample stoichiometry was confirmed by energy dispersive X-ray spectroscopy (EDS), collected by the analyzer of the former microscope (X-ACT Cambridge Instrument). Furthermore, ImageJ software was employed to obtain the particle size distribution of the sample. Transmission electron microscope (TEM) analyses were carried out by a Zeiss EM 910 microscope equipped with a tungsten thermionic electron gun operating at 100 kV.

X-ray diffraction (XRD) patterns of both LFMP_700 and LFMP_850 powders spread on a glass sample holder were collected through a Bruker D8 Advance instrument using a Cu K_α source and a graphite monochromator of the diffracted beam. Scans were performed in the 2θ range from 10° to 90° at a rate of 10 s step^{-1} and a step size of 0.02°. Rietveld refinement of the patterns was carried out through the MAUD software,[289] by using the reference parameters of the $LiFe_{0.78}Mn_{0.22}PO_4$ olivine (*Pnma* space group, N. 62, ICSD #193641).[290] The atomic displacement parameters have been forced to have the same value for Fe, Mn, and Li, and for the PO_4^{3-} ions. The weighted-profile (R_{wp}%) and goodness-of-fit (*GOF*) values were < 15 and < 2.0, respectively.

Electrodes preparation and conversion from LFMP to NFMP electrode

LFMP electrodes were prepared by doctor blade casting on aluminum foils (thickness of 20 μm, MTI Corporation). The slurries were achieved by dispersing in a beaker the active material, poly(vinylidene fluoride) (Solef 6020 PVdF), and Super P carbon (Timcal) with an 8:1:1 weight ratio, respectively, in *N*-methyl-2-pyrrolidone (NMP; Sigma Aldrich), and stirring at room temperature

until homogenization (about 2 h). The coated electrode foils were dried for 3 h on a hot plate at 70 °C, cut into the form of disks with a diameter of 10 and 14 mm, pressed with a hydraulic tool (Perkin-Elmer) for 30 s at 6.37 and 3.25 ton cm^{-2}, respectively, and dried for 3 h at 120 °C under vacuum to remove residual traces of water or solvent. The active material loading ranged from 3.5 to 4.5 mg cm^{-2} as normalized to the electrode geometric area (0.785 and 1.54 cm^2 for electrodes with a diameter of 10 and 14 mm, respectively). The NFMP electrodes were achieved throughout galvanostatic de-lithiation of LFMP to $Fe_{0.6}Mn_{0.4}PO_4$ (indicated with the acronym FMP) by charging in Li-cell, and subsequent galvanostatic sodiation by discharging in Na-cell (see below in *Cell Assembly* subsection). Additional carbon coated Al electrodes were prepared by the doctor blade casting procedure above described by using Super P carbon and PVdF binder in the 80:20 wt. ratio, cut into 10 mm disks, and dried for 3 h at 120 °C under vacuum.

Characterization of Electrodes

SEM images of the LFMP, FMP, and NFMP electrodes and EDS spectra were collected using a Zeiss Sigma 300 FE-SEM equipped with Bruker QUANTAX EDX detector. The elemental composition of the samples was determined via ICP-OES technique. HNO_3 (70%, ≥ 99.999% trace metal basis, Sigma Aldrich) and HCl (37%, for analysis-ISO, Carlo Erba reagents) were used without any further purifications. Ultrapure H_2O (18 MΩ cm) was used for the dilution of the samples. The powder recovered from the electrodes (about 4 mg of active material) was digested in 1 mL of aqua regia (HNO_3:HCl 1:3 M ratio) at 120 °C for 1 h by using a Parr 4744 acid digestion vessel (Parr Instrument Company). After cooldown, the solutions were diluted to the proper concentration prior to ICP-OES analysis. An ICP-OES iCAP Pro 11.160 (ThermoFisher Scientific) was used for elemental determination. XRD patterns of LFMP, FMP, and NFMP electrodes leaned on a glass sample holder were collected through the instrumental setup above described in the 2θ range from 15° to 60° at a rate of 10 s $step^{-1}$ with a step size of 0.02°. Rietveld refinement was performed by using the MAUD software,[289] by using the reference parameters of $LiFe_{0.78}Mn_{0.22}PO_4$ (*Pnma* space group, N. 62, ICSD #193641),[290] $Mn_{0.8}Fe_{0.2}PO_4$ (*Pnma* space group, N. 62, ICSD #166750),[291] and $NaMn_{0.93}Fe_{0.07}PO_4$ (*Pnma* space group, N. 62, ICSD #26006)[292] samples for LFMP, FMP, and NFMP, respectively. The atomic displacement parameters have been forced to have the same value for Fe, Mn, alkali metal (Li or Na), and the PO_4^{3-} anions. The weighted-profile *R* factor (R_{wp}%) and goodness-of-fit (*GOF*) parameter values were < 15 and < 1.5, respectively. Raman spectroscopy was performed on the LFMP, FMP, and NFMP electrodes through a Czerny-Turner spectrometer (iHR320 Horiba Scientific) equipped with a diffraction grating of 1800 grooves mm^{-1} and a laser source with λ = 532 nm. X-ray photoelectron spectroscopy (XPS) data were collected on LFMP, FMP; NFMP, and NFMP charged at 4.3 V electrodes at the XPS station of the TEMPO beamline (SOLEIL Synchrotron,

France), using an Al filament. Data were calibrated with the Au emission lines. Sample charging was also accounted for secondary calibration using the C 1s peak of the adventitious carbon (284.8 eV) resulting in a further shift of ~ 1.88 eV applied to all the samples. Before the analysis, FMP and NFMP electrodes recovered after de-lithiation and sodiation processes, respectively, were washed with DMC solvent and dried under vacuum for 30 min.

Cells Assembly

Swagelok-type polypropylene cell, with either two-electrode or three-electrode configuration, and CR-2032 coin-type cells (MTI Corporation) were employed. The Swagelok-type cells were assembled by stacking a 10-mm diameter working electrode, 10 mm-diameter glass fiber disk (Whatman® GF/A) as the separator soaked with the electrolyte, and a 10 mm-diameter disk of either Li or Na as counter electrode. An additional 10 mm-diameter disk of the respective alkali metal was used as the reference electrode to modify the two-electrode to the three-electrode setup. Additional three-electrode Swagelok-type sodium cells were prepared by using a 10 mm-diameter Super P Carbon/PVdF electrode (SP-Al) as cathode, a 10 mm-diameter sodium metal anode, a 10 mm-diameter glass fiber disk (Whatman® GF/B) as the separator, and another 10 mm sodium metal disk as the reference electrode. The coin-type cells were assembled by stacking both 10 and 14 mm-diameter working electrode, 16 mm-diameter glass fiber disk (Whatman® GF/A) as the separator, and 14 mm-diameter counter electrode of either Li or Na. The electrolyte for the Li-cells was a solution of $LiPF_6$ (1 M) in ethylene carbonate/dimethyl carbonate (EC:DMC 1:1 by volume, battery grade, Sigma Aldrich), and for Na-cells a 1 M solution of $NaPF_6$ in ethylene carbonate/propylene carbonate (EC:PC 1:1 by volume, battery grade, Sigma Aldrich) with 2% in weight of fluoroethylene carbonate (FEC, battery grade).[50] For the conversion of LFMP to NFMP, LFMP was initially de-lithiated to FMP in a two-electrode Swagelok-type Li-cell by charging at the constant current rate of C/10 (1C = 170 mA g^{-1}) from the open circuit voltage (OCV, 3V) to 4.6 V, and holding the upper voltage limit until the current reached the limit of C/100 rate to ensure the complete FMP formation. The cell was then disassembled, the electrode collected washed with DMC solvent, dried for 30 min under vacuum, and coupled with sodium metal disk in a new Na-cell. The electrochemical formation of NFMP was subsequently achieved by discharging the Na-cell to 1.8 V at a constant current of C/20 (1C = 154 mA g^{-1}). The NFMP electrode was then recovered, washed with DMC solvent, and dried 30 min under vacuum before use. Additional coin-type control cells with the symmetrical configurations Na/Na, Li/Li, NFMP/NFMP, and LFMP, LFMP were assembled. For all the cells, the applied current and the resulting capacity were calculated from the weight of the pristine LFMP electrodes. All cells were assembled in Ar-filled glove box (MBraun or Jacomex GP-Campus, with H_2O and O_2 content lower than 1 ppm).

Electrochemical tests and ex-situ measurements

Cyclic voltammetry (CV) and electrochemical impedance spectroscopy (EIS) measurements were performed on Li|LFMP and Na|NFMP three-electrode configuration Swagelok cells to investigate the electrochemical process features and the interphase characteristic of the two materials at room temperature (25 °C). CV tests were carried out at a scan rate of 0.05 mV s^{-1} in the 1.8 – 4.3 V vs. Na^+/Na potential range for NFMP, and at a scan rate of 0.1 mV s^{-1} in the 2.0 – 4.6 V vs. Li^+/Li potential range for LFMP. EIS responses were collected after NFMP formation or at the OCV condition of the fresh cell (for LFMP) as well as after 1, 5, and 10 CV cycles at the bias potential of 1.8 V vs. Na^+/Na for NFMP and of 2.0 V vs. Li^+/Li for LFMP, by applying an alternate voltage signal of 10 mV in the 200 kHz – 100 mHz frequency range, with 10 points per decade and logarithmic spacing. The EIS spectra were analyzed through the non-linear least squares (NLLS) fitting method using the RelaxIS3 (rhd instrument) software (only fits with χ^2 values of the order of 10^{-4} or lower were considered).[273,274] An additional CV test was performed within the same potential limits on a Na|NFMP cell by lowering the scan rate to 0.02 mV s^{-1} to achieve higher peak-resolution. Galvanostatic cycling tests for determining battery performances of LFMP and NFMP were conducted at the room temperature (25 °C) using two-electrode Na|NFMP and Li|LFMP Swagelok cells, as well as CR2032 coin-type cells. Considering LFMP, all the cells were cycled in the 2.0 – 4.6 V voltage range at various C-rates, using an additional constant voltage step at 4.6 V until the residual current reached ¼ of the nominal C-rate (that is by adopting the CCCV mode). A rate capability test was performed at increasing current rate by running 5 cycles at C/10, C/5, C/3, C/2, 1C, 2C, and finally lowering back the current to C/10 (1C = 170 mA g^{-1}). Furthermore, galvanostatic measurements with a constant current set at C/10 and C/5 were carried out. To further characterize the LFMP material, a galvanostatic test was run at C/5 by restricting the voltage window to 2.4 -4.4 V with the constant voltage step at 4.4 V. Additional galvanostatic tests, aimed to study the long-term cycling behavior of LFMP, were performed in coin-type lithium cells (14 mm-diameter working electrode) using the current rate of C/5 and 1C. Considering NFMP, a rate capability test was performed by increasing the current rate from C/20 (1C = 154 mAh g^{-1}) to C/10, C/5, C/2, 1C and 2C every 5 cycles and lowering back to C/20 after 30 cycles, in the 1.8 – 4.3 V voltage range. A CCCV test was performed as a strategy to achieve the maximum cell capacity by setting the current at C/5 from 1.8 to 4.3 V and holding the charge voltage at 4.3 V until a current value of C/20 was reached. Additional galvanostatic cycling was performed at 55 °C, and at temperatures increasing from 45 to 50, 55, and 60 °C every 10 cycles at C/5 current rate in the 1.8 – 4.3 V voltage range, by using the CCCV mode at 4.3 V during charge. Linear sweep voltammetry (LSV) was performed using three-electrode Swagelok-type T-cells with SP-Al electrode and EC:PC 1:1 *v/v* 1 M $NaPF_6$ + 2% wt. FEC

as electrolyte at 25, 50, and 65 °C, with a scan rate of 0.1 mV s^{-1} from the OCV condition of the cells to 5.5 V vs. Na^+/Na.

After the galvanostatic tests at C/5 in coin-type lithium cell and in two-electrode Swagelok-type sodium cell, LFMP and NFMP electrodes were recovered, washed with DMC solvent and dried under vacuum for 30 min. Afterward, XRD scans of pristine and cycled electrodes were collected as above described in the 10° - 60° and 15° - 60° 2θ ranges at a rate of 10 s $step^{-1}$ and a step size of 0.02° for LFMP and NFMP, respectively, while SEM images of the pristine and cycled samples were acquired with the abovementioned system for both materials.

The diffusional features of Li^+ and Na^+ ions were investigated in comparison using CV, Galvanostatic intermittent titration technique (GITT), and staircase electrochemical impedance spectroscopy (SPEIS) experiments. CV and GITT were performed using three-electrode Swagelok-type Na|NFMP and Li|LFMP cells, while SPEIS using coin-type cells (10 mm-diameter working electrode). The CV tests were conducted at scan rates of 0.05, 0.10, 0.15, and 0.20 mV s^{-1} in the potential ranges 1.8 – 4.3 V vs. Na^+/Na for NFMP and 2.0 – 4.6 V vs. Li^+/Li for LFMP. GITT experiments were performed after three activation galvanostatic cycles performed at 0.05 C current rate for NFMP (1C = 154 mA g^{-1}) and a 0.1 C current rate for LFMP (1C = 170 mA g^{-1}), in the potential ranges of 1.8 – 4.3 V vs. Na^+/Na and 2.0 – 4.6 V vs. Li^+/Li for NFMP and LFMP, respectively. The titrations were carried out by applying current pulses of 7.7 mA g^{-1} for t = 2107.5 s for NFMP and of 17 mA g^{-1} for t = 1249.5 s for LFMP, followed by potential relaxation steps of 1 h at the open circuit. The GITT operating conditions, in terms of pulse magnitude and duration, have been decided basing on the galvanostatic cycles. SPEIS measurements were performed on both Li|LFMP and Na|NFMP two-electrode cells within one full cycle (3^{rd} cycle) at different states of charge (SoC), during de-lithiation/de-sodiation and lithiation/sodiation, with a sampling interval of about 40 mV. For the measurements, an alternate voltage perturbation of 10 mV was applied within the 200 kHz – 10 mHz frequency range, with 10 points per decade and logarithmic spacing. The calculation of the distribution of relaxation times (DRT) function was performed after subtraction of the low-frequency diffusion region. The fitting procedure through the NLLS method,[273,274] and the calculation of the DRT function were performed by using the software RelaxIS3. The optimization of the λ-factor for the DRT analyses was carried out according to Tikhonov regularization (see **Section 1.6** for further details) by calculating the sum of squared residuals (SSR) vs. λ, assuming a Gaussian distribution.[262,272] In order to separate the contributions of Li and Na counter electrodes from the Li|LFMP and Na|NFMP half-cell responses used for the DRT function calculation, and to assess at the same time the dependency of the charge transfer process on temperature, additional EIS measurements were performed on symmetrical Li|LI, Na|Na, LFMP|LFMP and NFMP|NFMP control cells at 5, 15, 25, and 35 °C. CV, EIS, GITT

measurements and cycling tests were carried out by using a VMP-3 multichannel electrochemical workstation with an integrated frequency response analyzer (Bio-Logic) instrument. Additionally, CV and EIS measurements were also performed with a VersaSTAT MC Princeton Applied Research (PAR, AMETEK), while cycling tests by using a MACCOR series 4000 battery test system.

Ex-situ and Operando X-ray absorption (XAS) measurements

Additional LFMP electrodes were prepared on carbon paper foils (thickness of 110 µm, Toray TP-030) for *ex-situ* XAS measurements with the above-described procedure (see *Electrode preparation* subsection) and cut into the form of disks with a diameter of 9 mm and dried for 3 h at 120 °c under vacuum. The active material loading ranged from 2.5 to 3 mg cm^{-2} as normalized to the electrode geometric area (0.636 cm^2). FMP and NFMP electrodes were achieved as previously described. *Ex-situ* measurements were conducted on LFMP, FMP, and NFMP electrodes sealed in a PET foil with a laminator to avoid contact with air. Self-standing NFMP electrodes (NFMP_SS) were prepared with the following procedure.[293] A 5% wt. solution of sodium carboxymethyl cellulose (CMC) in water was prepared and cast by a doctor blade tool on Cu foil (thickness ~ 15 µm) and dried for 3 h on a hot plate at 90 °C to create a thin layer. The electrode slurry was obtained by dispersing LFMP material, PVdF, and Super P carbon in NMP in the 8:1:1 weight ratio, respectively, and stirring at 25 °C until homogenization (about 3 h). The dispersion was then cast by doctor blade over the CMC thin layer and the obtained coating was dried for 3 h on a hot plate at 70 °C. Subsequently, the coating was immersed in water to dissolve the CMC layer until the complete detachment of the self-standing electrode (LFMP_SS), which was dried to evaporate the excess of water (see **Figure 2.25**), cut into disks with diameter of 14 mm, and dried for 3 h at 120 °C under vacuum to remove possible residual traces of water and NMP solvent. The final active material loading was about 8 mg cm^{-2} as normalized to the electrode geometric area (1.54 cm^2). NFMP_SS electrodes were obtained from LFMP_SS ones through the conversion process above-described in two-electrode ECC PAT-Core EL-Cell by using an 18 mm-diameter glass fiber (Whatman® GF/A) disk as separator and a 16 mm-diameter Li or Na disk as counter electrode. *Operando* XAS measurement was performed by employing a modified CR2032 coin-type cell setup with a Kapton window (diameter of 6 mm) assembled by stacking a 14 mm-diameter NFMP_SS electrode, a 16 mm-diameter glass fiber (Whatman® GF/D) disk as separator soaked with EC:PC 1:1 *v/v* 1 M $NaPF_6$ + 2% wt. FEC solution as electrolyte, and a 14 mm-diameter sodium metal disk as counter electrode. The cell was galvanostatically cycled at 25 °C at the constant current rate of C/20 (1C = 154 mA g^{-1}) through an SP-240 potentiostat/galvanostat (Bio-Logic) instrument to investigate the first cycle. An additional long cycling test was performed by using a CR2032 coin-type cell adopting the same configuration.

XAS measurements were conducted at the SAMBA beamline (SOLEIL Synchrotron, France) in transmission and fluorescence mode at the Mn and Fe K-edges. Spectra were calibrated acquiring Mn and Fe metallic references and aligning the first inflection point to 6539 eV for Mn and 7112 eV for Fe. Data normalization was carried out with the software ATHENA.

LFMP Polymer Cell

A CR2032 coin-type cell was assembled by using the LFMP cathode disk with a diameter of 10 mm as the working electrode, the PEGDME_CPE as the separator, two O-rings (CS Hyde, 23-5FEP-2-50) with an internal diameter of 10 mm and thickness of 127 µm for holding the polymer electrolyte, and a lithium disk with diameter of 10 mm as the counter electrode. The Li|PEGDME_CPE|LFMP cell was examined at 50 °C at the constant current rate of C/5 in the voltage range of 2.4 – 4.4 V. EIS measurements were performed on the above cell by using an alternate voltage signal with an amplitude of 30 mV in the 500 kHz to 100 mHz frequency range, at the OCV after cell conditioning overnight at 70 °C, at 50 °C before cell cycling, and after 107 cycles of the above galvanostatic charge/discharge test. The polymer cell was assembled in Ar-filled glovebox (MBraun, O_2 and H_2O content below 1 ppm), cycled with a MACCOR series 4000 battery test system, and subjected to EIS through a VersaSTAT MC Princeton Applied Research (PAR, AMETEK) instrument.

2.2 Synthesis, Characterization, and Application in Lithium Polymer Battery of $LiFe_{0.6}Mn_{0.4}PO_4$ Mixed-Olivine Cathode

2.2.1 Structural, Morphological and Electrochemical Characterization of LFMP Cathode

The synthesis of the LFMP proceeds with a series of annealing steps under Ar of solid precursors obtained by sol-gel precipitation. **Figure 2.1** depicts the related weight change monitored by TGA during the heating processes (panel **(a)**), and the various isothermal steps (panels **(b-e)**), as well as the corresponding modification of the precursor structure detected through XRD (panels **(f-i)**).

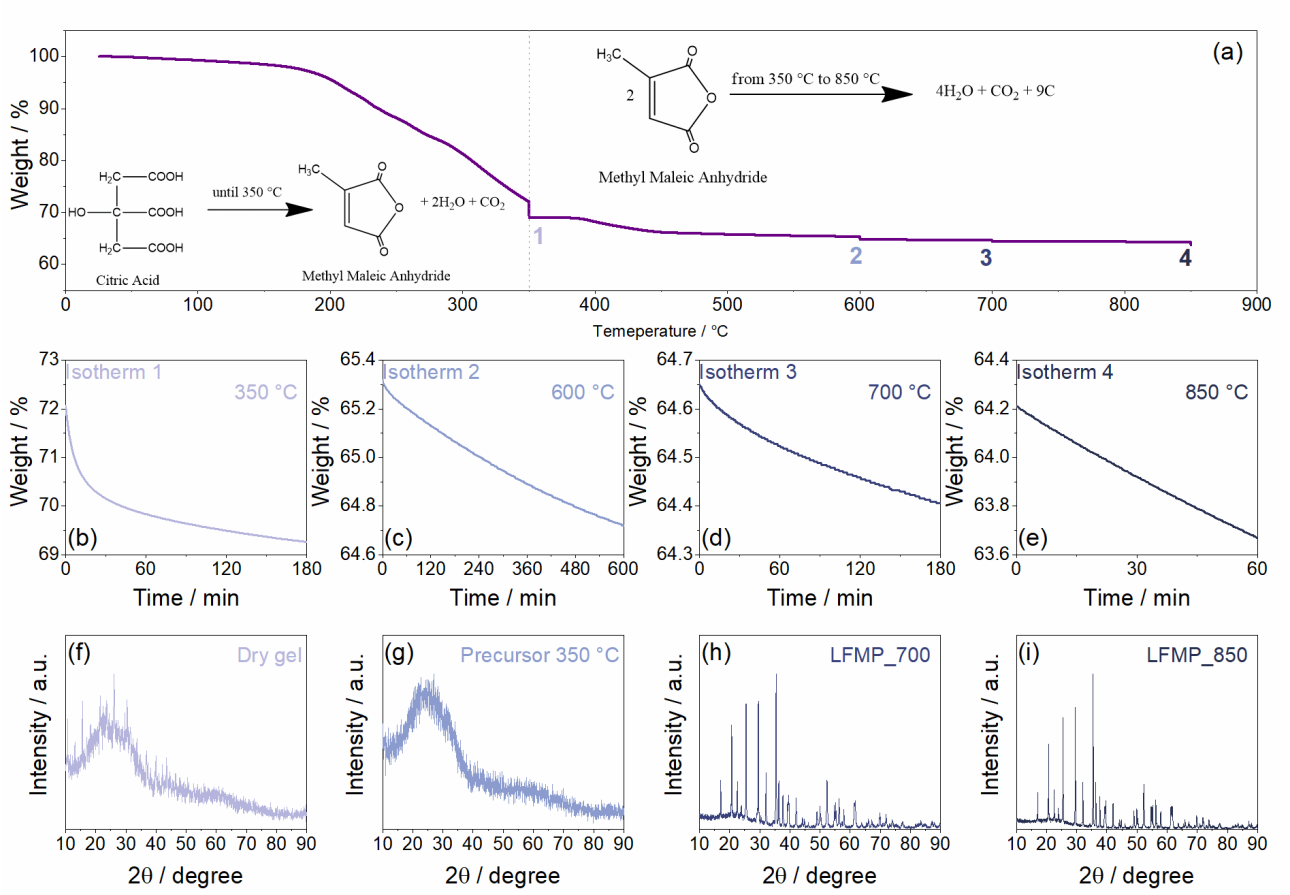

Figure 2.1: ***(a)*** *Synthesis process of the $LiFe_{0.6}Mn_{0.4}PO_4$ olivine cathode evaluated by TGA under N_2, with insets depicting the reactions of the citric acid occurring before (left-hand side) and after (right-hand side) the step at 350 °C, and numbers indicating the isotherm steps adopted at various temperatures. TGA of isothermal steps taking place at* ***(b)*** *350,* ***(c)*** *600,* ***(d)*** *700, and* ***(e)*** *850 °C. XRD patterns of* ***(f)*** *dry gel,* ***(g)*** *precursor at 350 °C,* ***(h)*** *LFMP_700, and* ***(i)*** *LFMP_850.*[98]

The TGA of **Figure 2.1(a)** reveals a first extended weight loss occurring between 150 and 350 °C, likely ascribed to the degradation of the citric acid precursor with formation of methyl maleic anhydride, water and carbon dioxide (see left-hand reaction inset).[294,295] A second weight loss with a lower magnitude compared to the first one occurs at temperatures higher than 450 °C and may be ascribed to the degradation of methyl maleic anhydride to form water, carbon dioxide, and elemental carbon (see right-hand reaction inset).[294] The TGA indicates an overall weight decrease of the precursor extending to about 40% upon the whole annealing process, to finally achieve the thermally stable LFMP olivine cathode.[94,296] Furthermore, isothermal steps at 350 (**Figure 2.1(b)**), 600 (**Figure 2.1(c)**), 700 (**Figure 2.1(d)**), and 850 °C (**Figure 2.1(e)**), applied to achieve the steady state at the end of each annealing stage, reveal significant weight loss only at 350 °C, thus accounting for the stability of the olivine, which is already formed at 700 °C.[296] Indeed, XRD patterns are collected after each synthesis step to evaluate the evolution of the crystalline phase. The XRD of the dry gel (**Figure 2.1(f)**) and of the precursor upon 350 °C (**Figure 2.1(g)**) show the expected amorphous structure, while the crystalline phase grows at 700 °C (LFMP_700, **Figure 2.1(h)**) as above

mentioned, and the final cathode material with the well-defined peaks characteristic of single-phase olivine structure is achieved upon 850 °C (LFMP_850, **Figure 2.1(i)**). The olivine phase formation is confirmed by the peak indexing of XRD patterns of LFMP_700 and LFMP_850 reported in **Figure 2.2(a)** according to the peaks reference diffractogram (ICSD #193641).[290] Additionally, **Figure 2.2** depicts the gaussian fitting of the main peak (2θ = 35.4°) of LFMP_700 (**Figure 2.2(b)**) and LFMP_850 (**Figure 2.2(c)**), in order to obtain the full-width half-maximum (FWHM, degree) and estimate the mean size of the ordered (crystalline) domains (D, Å) by using the Scherrer equation (**Equation 2.4**)[297]:

$$D = \frac{k\lambda}{\beta \cos\theta} \qquad \textbf{(2.4)}$$

Where λ is the wavelength of the X-ray radiations (1.5418 Å for the Cu Kα radiation used herein), k is a dimensionless shape factor, with a value of about 0.9, θ is the diffraction angle of the main peak (17.7°), and β is the FWHM converted to radians by **Equation 2.5**:

$$\beta = \frac{22 * FWHM}{180 * 7} \qquad \textbf{(2.5)}$$

The analysis suggests an increase of D from a value of about 405 Å for LFMP_700 to about 501 Å for LFMP_850, most likely due to partial coalescence of the crystalline domains during the last thermal step. Indeed, the achievement of a suitable structure and the absence of excessive deformations suggest the applicability of the material in Li-ion batteries.[298]

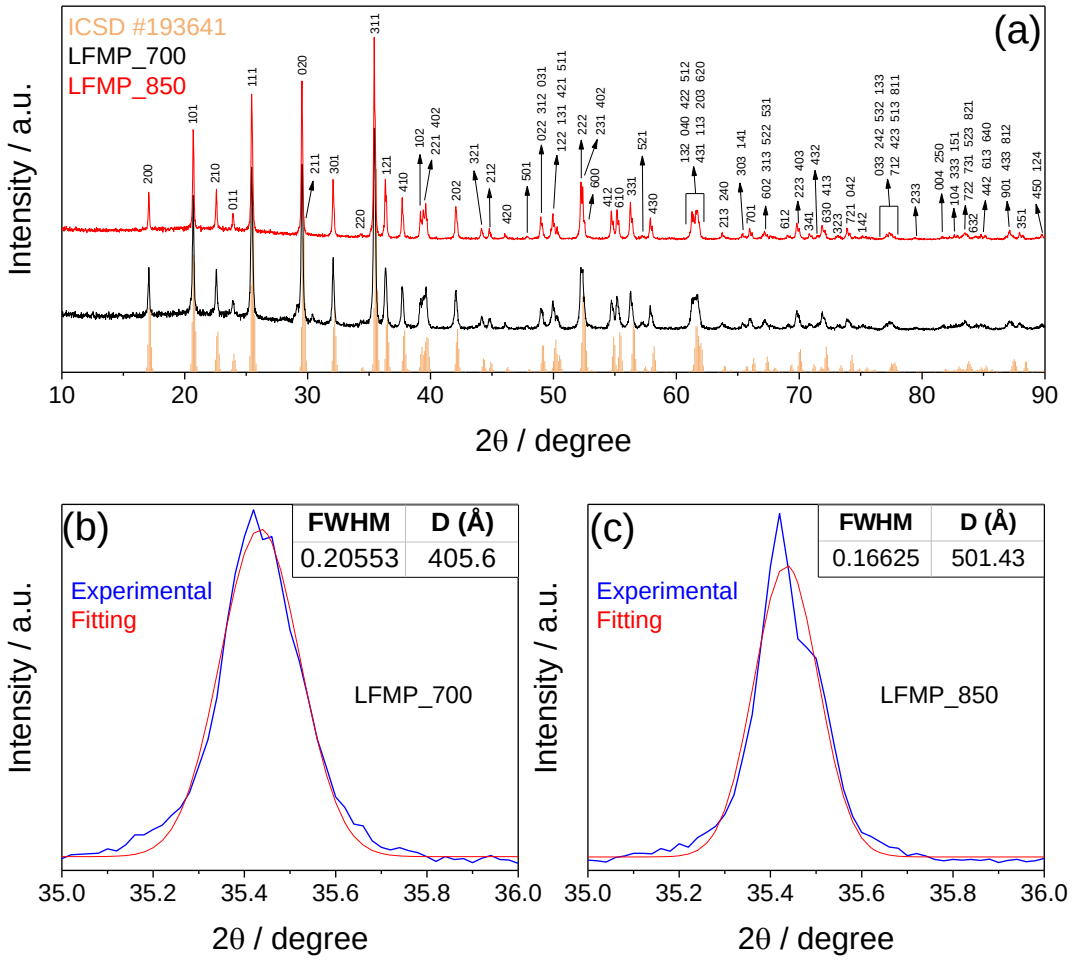

Figure 2.2: ***(a)*** *XRD patterns of LFMP_700 and LFMP_850 indexed according to the peaks of the reference diffractogram (ICSD #193641).* ***(b, c)*** *Main peak at 35.4° of 2θ (blue plot) and fitted one (red plot) for the application of Scherrer equation, including full-width half-maximum (FWHM) and the mean size of the ordered (crystalline) domains (D) for* ***(b)*** *LFMP_700 and* ***(c)*** *LFMP_850.*[98]

To further investigate the structural properties of LFMP_700 and LFMP_850, Rietveld refinement of the diffractograms has been performed, as reported in **Figure 2.3(a)** and **Figure 2.3(b)**, respectively. The experimental XRD patterns (black dots) show, for both LFMP_700 and LFMP_850, an orthorhombic cell unit (*Pnma* space group, table N. 62) without significant content of impurities, according to the reference pattern ICSD #193641 of the olivine lattice, as indeed shown by the refined diffractograms (red line) and the difference profile (blue line).[290] The refinement results reported in **Table 2.1** reveal for the two samples similar values of the cell unit parameters *a*, *b*, and *c*, that is of about 10.4, 6.0, and 4.7 Å, respectively.[76,290,299] Therefore, the samples synthesized herein have a cell volume of about 295.8 $Å^3$ for LFMP_850, which exceeds that of the ICSD reference reported in **Table 2.1** due to the higher Mn fraction achieved in the LFMP_700 and LFMP_850 olivines.[90]

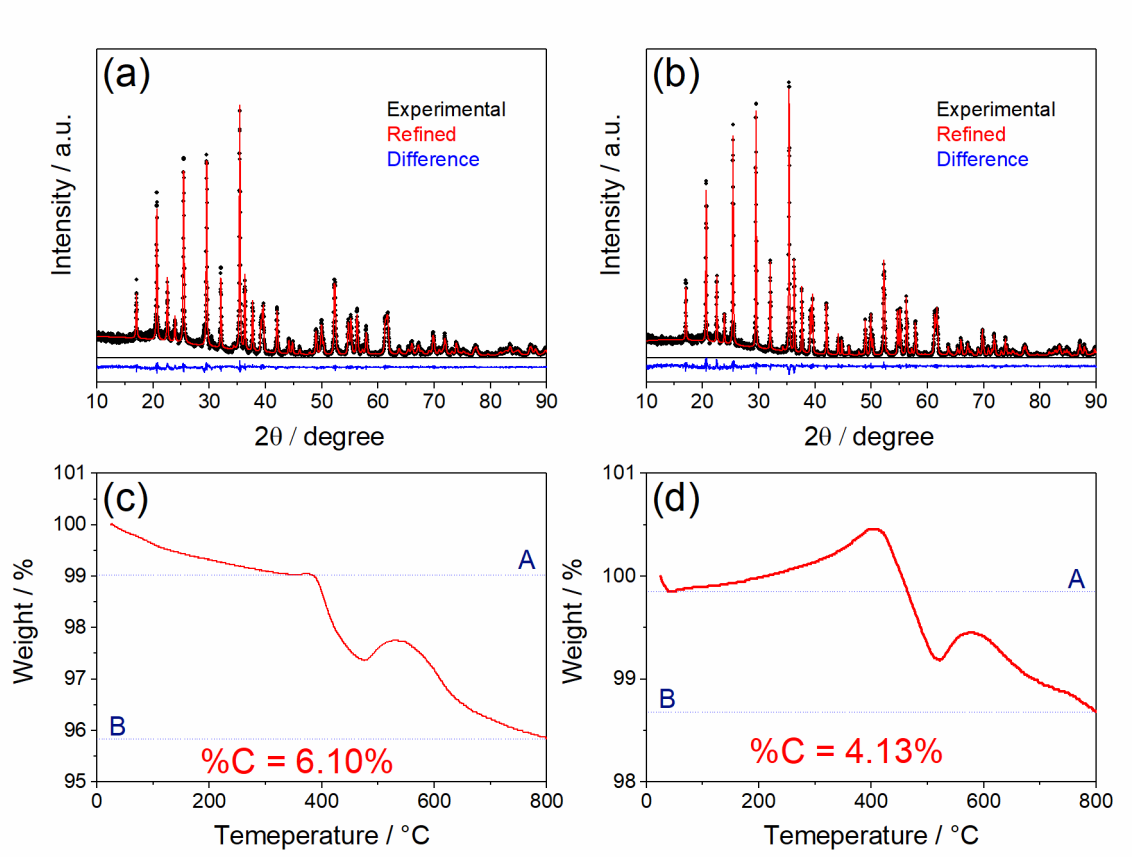

Figure 2.3: *Rietveld refinement of the XRD patterns of* ***(a)*** *LFMP_700 and* ***(b)*** *LFMP_850. In detail: experimental (black dots) and calculated (red line) patterns, difference profile (blue line). Reference ICSD#193641. TGA curves of* ***(c)*** *LFMP_700 and* ***(d)*** *LFMP_850 recorded under air flow, reporting the calculated carbon weight %. Adapted from* [98].

Table 2.1 also reveals an increase of the crystallite size from 95 nm in LFMP_700 to 147 nm in LFMP_850, as most likely due to the expected coalescence of the crystalline domains during the thermal treatment at 850 °C.[299,300] This trend is a further validation of the results obtained by the application of the Scherrer equation to the main peak of the diffractograms (see **Figure 2.2(b, c)**). Despite the increase of the crystallite size may partially hinder the charge transfer, it can actually favor the reversibility of the material, and strongly mitigate side reactions with the electrolyte particularly occurring at the higher potentials.[298] In addition, **Table 2.1** shows values < 2 and < 15 for the GOF and R_{wp}% parameters, respectively, of LFMP_700 and LFMP_850 that can be considered suitable and point out the reliability of the refinement.[301,302] Furthermore, the well-defined structure, the absence of excessive deformations, and the negligible impurity content represent key factors for allowing the efficient operation of the LFMP material in lithium battery.[298]

Table 2.1: *Results of Rietveld refinement of the XRD patterns of Figure 2.3 in terms of lattice parameters, unit cell volume, goodness-of-fit (GOF) parameter and weighted-profile R factor (R_{wp}%) of LFMP_700 and LFMP_850. Reference ICSD#193641.*[98]

Sample	*a* (Å)	*b* (Å)	*c* (Å)	V (Å^3)	Crystallite size (nm)	*GOF*	*Rwp%*
ICSD #193641	10.343	6.022	4.704	293.03	100	/	/
LFMP_700	10.369(4)	6.039(2)	4.709(2)	294.94(3)	95 ± 2	1.33	14.54
LFMP_850	10.378(3)	6.044(2)	4.712(2)	295.80(3)	147 ± 4	1.26	13.89

Another important aspect for the applicability of LFMP in Li cell is represented by the carbon content in the material: indeed, excessive presence of this electrochemically inactive element may jeopardize the energy density of the electrode, instead a too low carbon amount can hinder the reaction kinetics of the intrinsically insulating olivine.[303] Hence, a carbon content ranging from 3% to 5% is expected to allow the most suitable performance of the olivine electrode in Li-cell.[304] This key parameter is herein determined by analyzing the TGA curves from 25 to 800 °C, acquired under air flow, reported in **Figure 2.3(c)** and **Figure 2.3(d)** for LFMP_700 and LFMP_850, respectively. The weight changes are ascribed to the oxidation of the olivine materials to form transition metal oxides, phosphates, lithium oxide, and carbon dioxide as illustrated by **Equation (2.1)** in **Section 2.1**.[103,303] Therefore, according to **Equations (2.2)** and **(2.3)** in **Section 2.1**, the carbon weight ratio in LFMP_700 and LFMP_850 is calculated to be ~ 6% and ~ 4%, respectively. These results suggest optimized synthesis conditions leading to a slight excess of carbon at 700 °C, which is decreased by annealing at 850 °C to fully achieve the ideal target, potentially enabling the best performance of the LFMP olivine material in lithium cell.[103,288]

Figure 2.4 shows the morphological features of final LFMP sample (LFMP_850), investigated by SEM, EDS, and TEM techniques. From here on, LFMP acronym will be referred to LFMP_850 sample, which will undergo electrochemical characterization. The related SEM images at various magnification levels indicate the presence of agglomerates with a size of about 30 µm (**Figure 2.4(a)**), formed by smaller primary particles (**Figure 2.4(b)**) with a submicron diameter (**Figure 2.4(c)**) ranging from 300 to 900 nm. This range is fully confirmed by the analysis of SEM image through ImageJ software, aimed to determine the particle size distribution, with a maximum centered at about 500 nm. This composite morphology can ensure at the same time short diffusion pathway for the lithium ions, and limited side reactions with the electrolyte. Indeed, particles with dimensions of the

order of few hundreds nm allow fast kinetics, while micrometric agglomerates with limited surface area hinder the electrolyte decomposition, particularly at high voltages.[304]

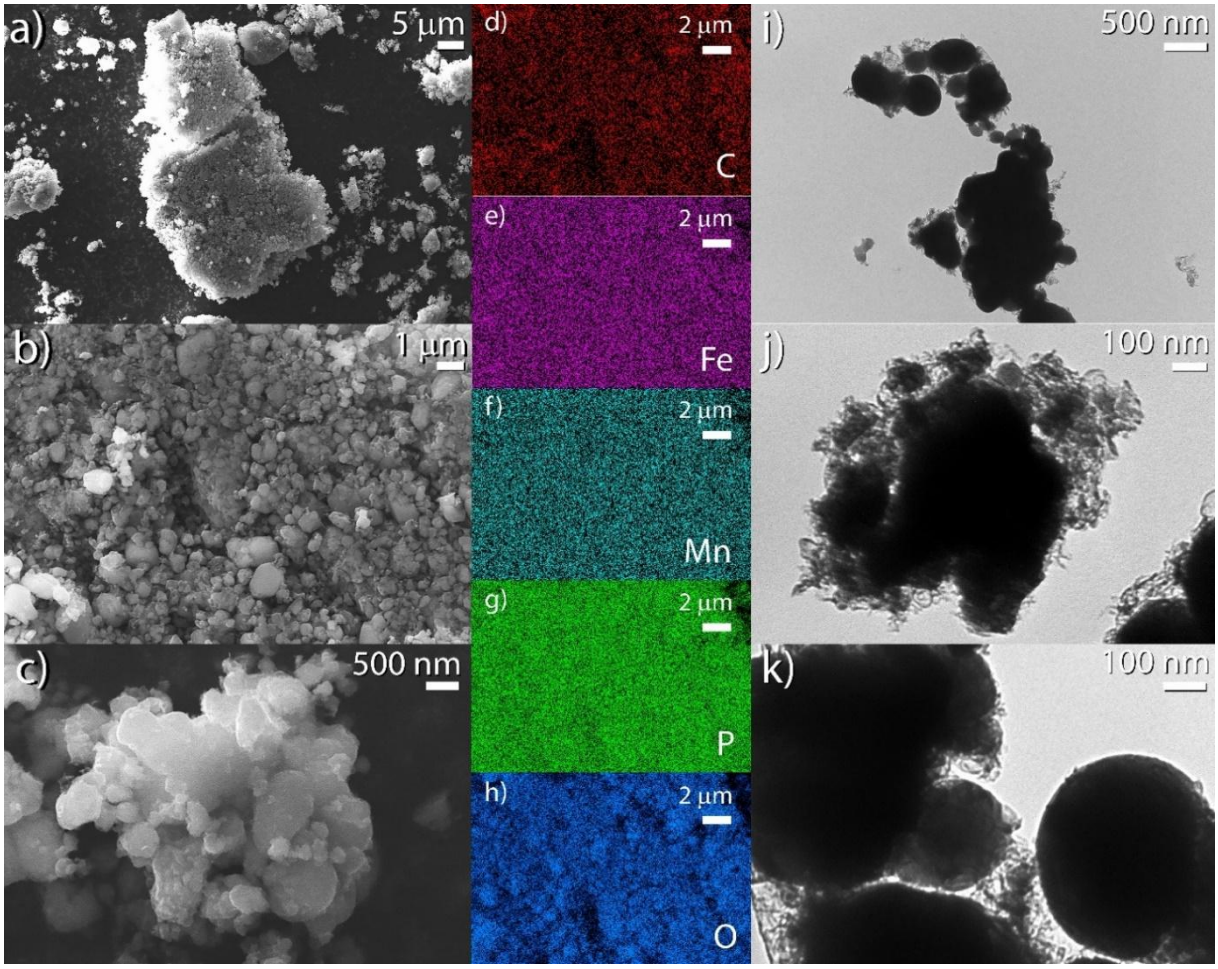

Figure 2.4: *SEM, EDS, and TEM analyses of LFMP powder. In detail:* ***(a–c)*** *SEM images at different magnifications;* ***(d–h)*** *SEM-EDS elemental maps of C, Fe, Mn, P, and O, respectively;* ***(i–k)*** *TEM images at various magnifications.*[98]

The EDS mapping of C (**Figure 2.4(d)**), Fe (**Figure 2.4(e)**), Mn (**Figure 2.4(f)**), P (**Figure 2.4(g)**), and O (**Figure 2.4(h)**) of the material surface detected by SEM suggests a homogeneous distribution of the various elements, and excludes the presence of impurities, in agreement with XRD data (see **Figures 2.2** and **2.3**). Relevantly, the EDS analysis approximately confirms the target stoichiometry of LFMP, with an elemental ratio of Fe and Mn of 0.57 and 0.43, respectively. This result suggests almost full precipitation of the metal precursors during the initial sol-gel step, which is a key factor to achieve the proper olivine structure, and the optimal electrochemical activity of the material. Moreover, the TEM images (**Figure 2.4(i-k)**) confirm the submicrometric size of the primary particles, and evidence the predominance of a spherule-shaped morphology. The TEM reveals the presence of a thin and amorphous material interconnecting the various LFMP domains, which likely represents the conductive carbon matrix detected by TGA (see **Figure 2.3**) deriving from the degradation of the citric acid precursor during synthesis, as previously reported (see complete reaction

in **Figure 2.1(a)**). In this regard, the carbon revealed by TEM in the LFMP olivine and quantified by TGA (~ 4%) appears as a layer extending from about 50 to 100 nm within the active material particles, rather than a homogeneous carbon coating. In summary, both structural and morphological features of LFMP indicate its possible application in efficient energy storage devices characterized by a reversible electrochemical process.[77,305]

The electrochemical process of the LFMP cathode is subsequently investigated in lithium cell by combining CV and EIS, as reported in **Figure 2.5**.

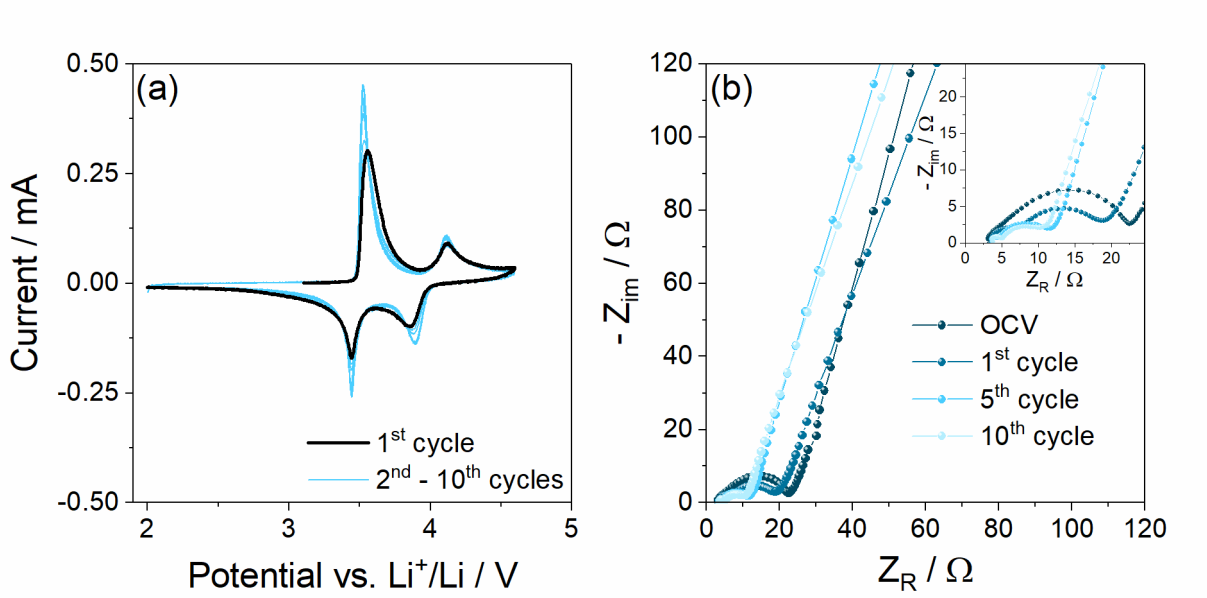

Figure 2.5: (a) *CV and* ***(b)*** *EIS measurements of the Li|LFMP three-electrode cell with a Li reference electrode at 25 °C. CV potential range 2.0 – 4.6 V vs. Li^+/Li; scan rate 0.1 mV s^{-1}. EIS carried out at the OCV of the cell and after 1, 5, and 10 CV scans (inset reports magnification of in the middle-high frequency region); frequency range 500 kHz – 100 mHz; alternate voltage signal amplitude 10 mV.*[98]

The CV response shown in **Figure 2.5(a)** indicates the occurrence of two oxidation processes, corresponding to the peaks centered at about 3.55 and 4.1 V vs. Li^+/Li during the anodic scan and almost completely reversed into two reduction peaks at about 3.45 and 3.9 V vs. Li^+/Li during cathodic scan. Indeed, the peaks at 3.55 and 3.45 V vs. Li^+/Li are ascribed to Fe^{2+}/Fe^{3+} redox couple whilst those at 4.1 and 3.9 V vs. Li^+/Li to the Mn^{3+}/Mn^{2+} one, with de-insertion of Li^+ from LFMP during the anodic scan, and its insertion back into the olivine structure during the cathodic scan.[306] It is worth mentioning that the electrochemical process attributed to the Fe^{3+}/Fe^{2+} redox couple in LFMP occurs at higher potential compared to bare $LiFePO_4$, while that of Mn^{3+}/Mn^{2+} evolves at lower values with respect to $LiMnPO_4$.[99,298] The shift of the transition metal redox potentials is typically observed in mixed olivine materials and is attributed to changes in the ionic character and distance of the M–O bond by substitution.[79,100,278] In particular, a modification in the covalency of the M–O bond and M–O–M interaction has been reported to modify the position of the M^{3+}/M^{2+} redox energy,

thus directly influencing the corresponding redox potential.[100] The CV profile suggests a remarkable reversibility, modest polarization, and a relatively fast kinetics of the electrochemical Li^+ (de-)insertion process for the LFMP electrode.[307] Furthermore, the first cycle of **Figure 2.5(a)** (black line) reveals a slightly higher polarization than the subsequent ones (blue lines), thus indicating an activation process likely attributed to a partial structural reorganization of the material, as well as to the formation of a suitable solid electrolyte interphase (SEI) at the electrode surface.[308] To further clarify this aspect, **Figure 2.5(b)** shows the EIS measurements at the open circuit voltage condition (OCV) of the fresh cell as well as after 1, 5, and 10 CV scans (bias potential 2.0 V vs. Li^+/Li). The Nyquist plots generally reflect the blocking-electrode shape expected at the SOC at which they have been collected, that is the fully discharged state of the cell (*i.e.* at about 3 V vs. Li^+/Li at the OCV, and at 2.0 V vs. Li^+/Li after the CV scans). The plots are characterized by the presence of a medium-high frequency semicircle accounting for the interface, and a low-frequency tilted line representing the cell geometrical capacity.[93] Therefore, the EIS at the abovementioned state of charge may be represented by the equivalent circuit $R_e(R_iQ_i)Q_g$, including a series of: (i) electrolyte resistance (R_e); (ii) one or two parallels each made of a resistance and a constant phase elements (R_iQ_i) accounting for interfacial features (SEI and charge transfer/double layer); (iii) a final constant phase element related to the cell capacitance (Q_g).[273,274]

Table 2.2 reports the interphase resistances calculated by NLLS analysis.[273,274] The data of the table indicate low overall values of the interphase resistance (R_i), which decreases from about 19.5 Ω at the OCV to about 7.5 Ω after 10 voltametric cycles, thus suggesting the formation of an optimal SEI as well as for the previously discussed structural reorganization, which may favor the reaction kinetics and improve the electrode/electrolyte interphase in the lithium cell.[221]

Table 2.2: *Equivalent circuits, interphase resistances (R_1, R_2), and chi-square values accounting for the accuracy (χ^2) of NLLS analysis related to the EIS data of the Li\|LFMP three-electrode cell using a Li reference electrode collected at 25 °C at the OCV, and after 1, 5, and 10 CV cycles in the 2.0 – 4.6 V vs. Li^+/Li potential range. See Figure 2.5 for related CV profiles and Nyquist plots.*[98]

Cell condition	Equivalent circuit	R_1 (Ω)	R_2 (Ω)	$R_i = R_1 + R_2$ (Ω)	χ^2
OCV	$R_e(R_1Q_1)Q_g$	19.5 ± 0.3	/	19.5 ± 0.3	6 x 10^{-4}
After 1 cycle	$R_e(R_1Q_1)(R_2Q_2)Q_g$	4.0 ± 0.1	11.7 ± 0.2	15.7 ± 0.2	4 x 10^{-5}
After 5 cycles	$R_e(R_1Q_1)(R_2Q_2)Q_g$	1.2 ± 0.1	7.2 ± 0.1	8.4 ± 0.1	5 x 10^{-5}
After 10 cycles	$R_e(R_1Q_1)(R_2Q_2)Q_g$	1.4 ± 0.1	6.1 ± 0.1	7.5 ± 0.1	2 x 10^{-5}

The electrochemical performance of LFMP cathode in Li-cell subjected to galvanostatic cycling tests are shown in **Figure 2.6**. The rate capability of the material is evaluated in terms of the voltage profiles (**Figure 2.6(a)**) and the cycling trend (**Figure 2.6(b)**) by increasing the current from C/10 to 2C (1C = 170 mA g^{-1}). The cell reveals the expected shape of the voltage profiles at the various C-rates, characterized by two plateaus at an average voltage of 3.5 and 4 V, ascribed to the Fe^{3+}/Fe^{2+} and Mn^{3+}/Mn^{2+} redox couples, respectively, in agreement with the CV of **Figure 2.5(a)**. Furthermore, the profiles of **Figure 2.6(a)** suggest an increase of polarization by raising the current which leads to the decrease of the capacity from 130 mAh g^{-1} (*i.e.*, about 77% of the theoretical value) at C/10 to about 65 mAh g^{-1} (39% of the theoretical value) at 2C, as indeed expected by the increase of the ohmic polarization. On the other hand, the cycling trend of **Figure 2.6(b)** shows that the initial capacity of about 130 mAh g^{-1} is recovered by decreasing the current back to C/10 after the whole test, thus suggesting a good rate capability and the stability of the LFMP cathode upon the stress caused by raising the currents.[298]

The stability of the electrochemical lithium (de-)insertion process of LFMP in cell is further investigated by repeated charging/discharging at a constant C-rate. The voltage profiles of the test performed at C/10 (**Figure 2.6(c)**) and C/5 (**Figure 2.6(e)**) show the well-defined plateaus described above, and a maximum capacity of about 130 mAh g^{-1} at C/10 and 120 mAh g^{-1} at C/5, in full agreement with the rate capability test. When cycled at C/10, the cell reveals a coulombic efficiency of about 90% at the first cycle which increases and ranges from about 97% to 99% during the subsequent ones, with a capacity retention of about 95% (**Figure 2.6(d)**). Instead, when cycled at C/5 the cell shows an initial coulombic efficiency of about 85%, increasing to about 100% during the subsequent cycles, and a capacity retention of about 90% (**Figure 2.6(f)**). It is worth noting that for the low current cycles at C/10 the coulombic efficiency is considerably low if a possible application in full cell is considered (see **Figure 2.6(d)**).[309] The effect is probably related to the occurrence of parasitic reactions in the cell at low current rates, which could be solved with the optimization of the passivation layer at the electrode/electrolyte interface by using an electrolyte additive (i.e. VC) as described in **Section 1.4.2**.[227,228] Nevertheless, this issue seems to do not affect the performance of LFMP at higher currents, revealing higher coulombic efficiencies. It is worth mentioning that the galvanostatic cycling tests reported in **Figure 2.6** are carried out in T-type cells, which may allow the evaluation of the best performance of the LFMP materials in terms of delivered capacity.

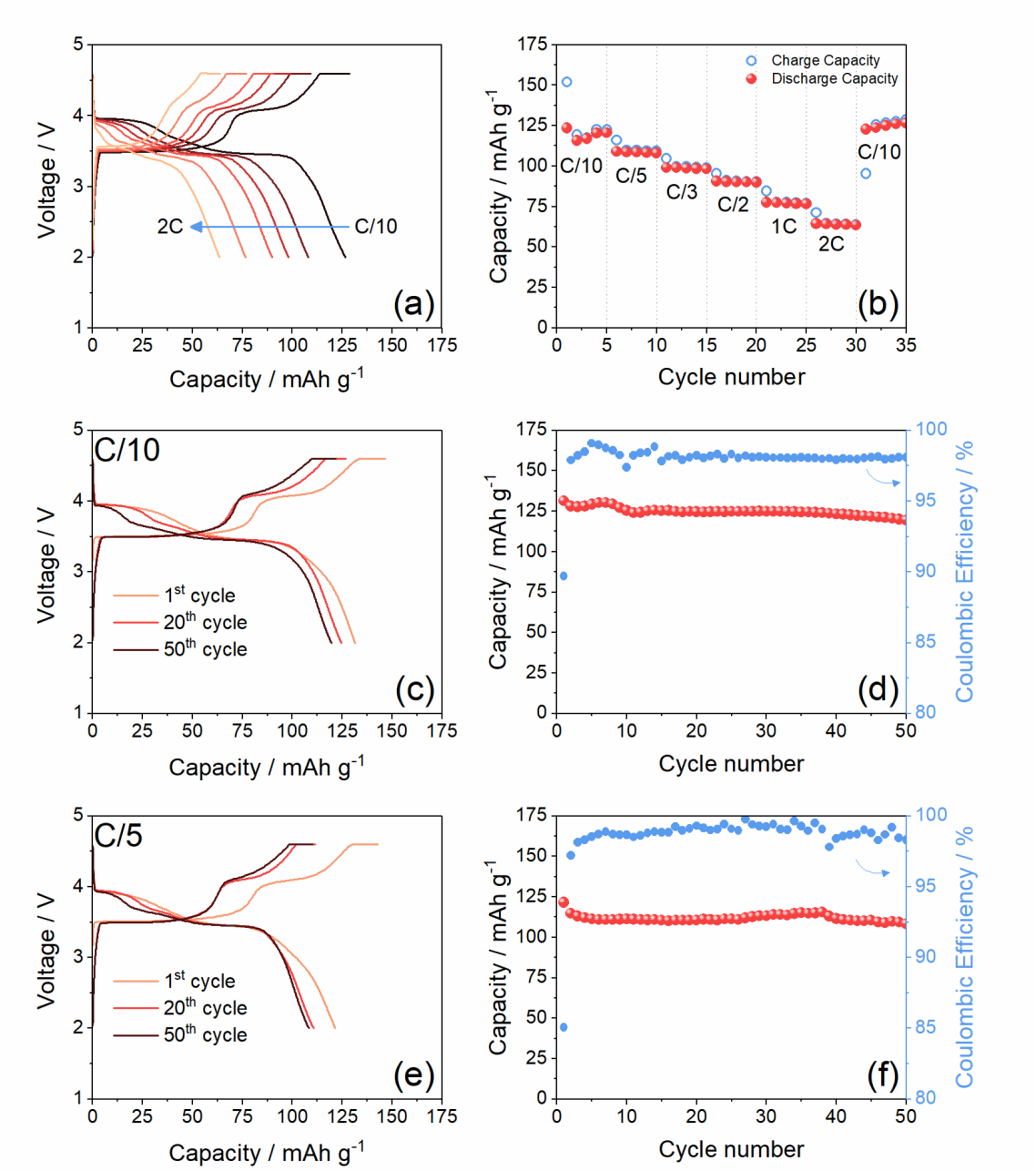

Figure 2.6: *Galvanostatic cycling performances of the Li|LFMP cell at 25 °C. Rate capability in terms of* ***(a)*** *voltage profiles and* ***(b)*** *corresponding cycling trend performed at C/10, C/5, C/3, C/2, 1C, and 2C currents (1C = 170 mA g^{-1}). Electrochemical performance of the cell at the constant current rate of* ***(c, d)*** *C/10 and* ***(e, f)*** *C/5 in terms of* ***(c, e)*** *voltage profiles and* ***(d, f)*** *cycling trends with discharge capacity in the left-hand side y-axis and coulombic efficiency in the right-hand side y-axes. Voltage range 2.0 – 4.6 V with an additional constant voltage step (CCCV mode) at 4.6 V until a finale current of ¼ referred to the nominal C-rate.*[98]

Further cycling tests extended over 300 cycles are performed at higher C-rate of 1C in coin-type cell, to evaluate the cycle life of the LFMP cathode, and the results are reported in **Figure 2.7**.

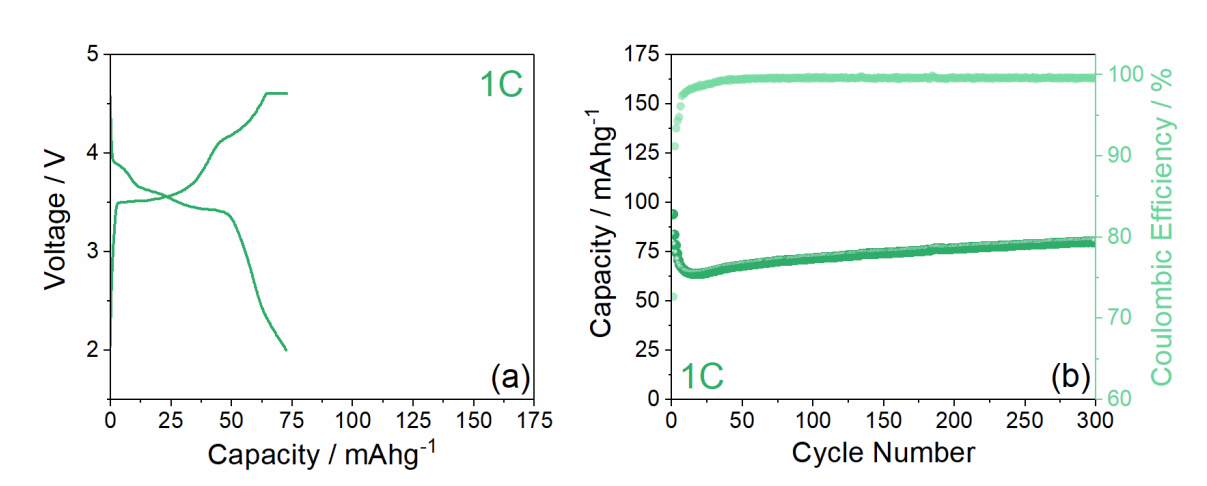

Figure 2.7: *Galvanostatic performance of the Li|LFMP cell at 25 °C at the constant current of 1C (1C = 170 mA g^{-1}) in terms of* ***(a)*** *steady state voltage profile and* ***(b)*** *prolonged cycling trend with discharge capacity in the left-hand side y-axis and coulombic efficiency in the right-hand side y-axes. Voltage range 2.0 – 4.6 V with an additional constant voltage step (CCCV mode) at 4.6 V until a finale current of ¼ referred to the nominal C-rate.*[98]

The cell reveals at the end of the test a voltage signature without significant modifications compared to the typical voltage profile of the olivine (**Figure 2.7(a)**), a coulombic efficiency approaching 100%, and a very stable capacity trend after the initial few cycles (**Figure 2.7(b)**). Indeed, the cell retains 85% of the initial capacity over the 300 cycles investigated herein, thus accounting for the optimal structure and morphology of the LFMP material, which is reflected into a well-reversible Li-(de-)insertion process in battery. Relevantly, the cycling test has very high coulombic efficiency, and excellent retention, thus suggesting the high stability of the sample as expected by the optimal olivine structure obtained.[82,101,102] However, a capacity value lower than the theoretical one (*i.e.*, of ~ 80% at C/10 and ~ 45% at 1C), and a lower rate capability than that of commercial $LiFePO_4$ suggest the need for a further improvement of the synthetic steps.[84] On the other hand, it is remarked that the presence of a second voltage step at about 4 V in LFMP, in addition to the one at 3.5 V typical of the LFP, represents a bonus for increasing the energy density of the material in lithium cell.[76,288] Additionally, the performance of the LFMP cathode are slightly higher compared to other olivines reported in literature and investigated both in liquid and in gel electrolyte, such as $LiFe_{0.5}Mn_{0.5}PO_4$, with a capacity of about 120 mAh g^{-1} at C/10.[278,306] Furthermore, the performance are close to other materials using dopants such as Cr, Ni, Mg, or Ti.[310–313] However, it is highlighted that the simplicity of the adopted approach may actually favor the scaling up of the presented material in terms of cost and sustainability compared to the already cited ones.

The structural and morphological retention of the LFMP electrode upon prolonged cycling in lithium cells is evaluated in **Figure 2.8**.

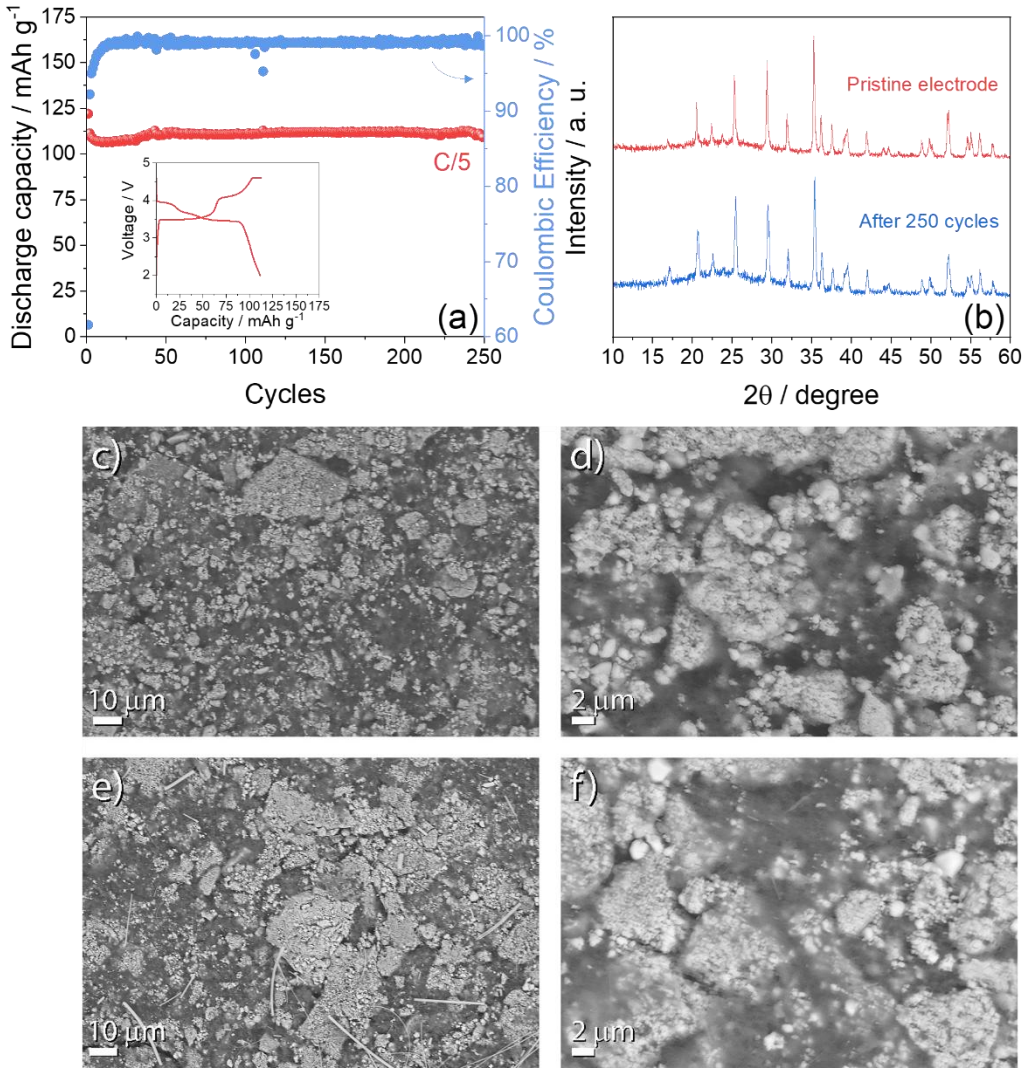

Figure 2.8: (a) *Cycling trend related to galvanostatic test performed at 25 °C at C/5 current (1C = 170 mA g*$^{-1}$*) on a Li|LFMP coin-type cell between 2.0 and 4.6 V with an additional constant voltage step (CCCV mode) at 4.6 V until a finale current of ¼ referred to the nominal C-rate (inset displays a voltage profile collected at the steady state).* ***(b)*** *Comparison between XRD patterns of pristine LFMP electrode (red) and LFMP electrode recovered after cycling test reported in panel* ***(a)*** *(blue). SEM images of* ***(c, d)*** *pristine and* ***(e, f)*** *cycled LFMP electrodes.*[98]

Figure 2.8(a) displays the cycling trend related to a further galvanostatic test carried out at the constant current rate of C/5 in coin-type cell for over 250 charge/discharge cycles (inset shows a related steady-state voltage profile) and reveals an outstanding capacity retention approaching 90%. After the cycling test, the cell is disassembled and the electrode recovered and compared with a pristine LFMP one through XRD analyses (**Figure 2.8(b)**). Hence, the XRD patterns of the pristine and cycled electrode exhibit the same, well-defined, crystalline structure, in full agreement with the one observed in **Figure 2.2(a)** for LFMP_850 powder, thus indicating the retention of the single-phase olivine structure and evidencing the notable stability of the material upon prolonged operation in lithium cell. On the other hand, the morphology of the cycled LFMP electrode is studied by SEM

and compared with a pristine one, as reported in **Figure 2.8(c-f)**. The pristine electrode (**Figure 2.8(c, d)**) shows the expected submicrometric LFMP primary particles aggregated into micrometric secondary particles and homogeneously blend into the electrode film. The particles evidence almost unaltered morphology in the cycled electrode (**Figure 2.8(e, f)**), without relevant reorganization despite long cycling in lithium cell. Furthermore, **Figure 2.8(e, f)** reveals for the cycled electrode the presence of domains with rough morphology dispersed within the primary particles and on the electrode film, which are not observed in the pristine sample, as well as dispersed glass fibers due to the electrolyte separator. The additional domains are likely associated with the formation of a SEI passivation layer during cycling, as already observed.[314] Therefore, the exceptional stability of both structure and morphology of the LFMP electrode further suggests the suitability of this material for application in a novel configuration of lithium cells exploiting olivine-based cathodes operating at raised voltages.

2.2.2 Lithium Polymer Cell Employing LFMP Cathode and PEGDME_CPE Electrolyte

Certainly, the presence of a voltage step over 4 V due to the Mn^{2+}/Mn^{3+} redox couple represents a remarkable advantage of LFMP olivine cathode, and the use of the light lithium metal is a further bonus in terms of energy density. However, the use of this intriguing anode with a liquid electrolyte, such as that typically employed for material characterization (*i.e.* EC:DMC, $LiPF_6$ commonly labeled as LP30), is actually hindered by abovementioned safety reasons related with the flammability of carbonate-based solutions, and possible formation of dendritic structures at the metal surface.[229,279,315] On the other hand, polymer solid-solutions based on PEO may allow the safe use of the Li metal in practical cells; however, a PEO-based electrolyte operates typically at temperature higher than 65 °C and has in this condition an anodic stability limited to about 4 V vs. Li^+/Li.[280–282] Differently, the PEGDME_CPE can operate at 50 °C with anodic stability extending at least over 4.4 V vs. Li+/Li, as demonstrated by previous work.[219] Therefore, the use of alternative PEGDME_CPE electrolyte is here originally introduced in a safe lithium polymer cell with the above investigated LFMP cathode. Prior to polymer cell evaluation, the electrochemical performance of a Li|LP30|LFMP cell at 25 °C in conventional liquid electrolyte is evaluated in the voltage window restricted to 2.4 – 4.4 V, to be used as a benchmark for the Li|PEGDME_CPE|LFMP cell. The results are shown in **Figure 2.9** in terms of voltage profiles (**Figure 2.9(a)**) and charge/discharge capacity with coulombic efficiency (**Figure 2.9(b)**). The Li|LP30|LFMP cell shows the typical two voltage plateaus above described and a capacity of about 95 mAh g^{-1} with a coulombic efficiency of about 81% during the first cycle, increasing to about 100% upon cycling. Furthermore, it displays a retention of 95% over 100 cycles, thus confirming the high stability of the olivine cathode.

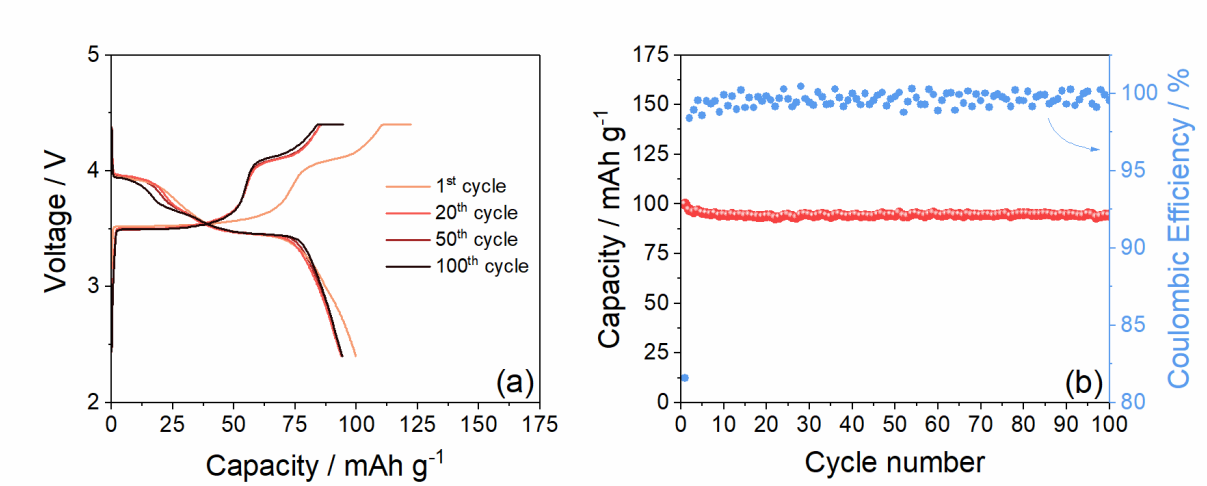

Figure 2.9: *Galvanostatic performance of the Li|LP30|LFMP cell at 25 °C at C/5 current rate (1C = 170 mAh g^{-1}) in terms of* ***(a)*** *steady state voltage profiles and* ***(b)*** *cycling trend with discharge capacity in the left-hand side y-axis and coulombic efficiency in the right-hand side y-axes. Voltage range 2.4 – 4.4 V with an additional constant voltage step (CCCV mode) at 4.6 V until a finale current of ¼ referred to the nominal C-rate.*[98]

Figure 2.10 reports the electrochemical performances in terms of galvanostatic voltage profiles (panel **(c)**) and cycling trend (panel **(d)**) of the Li|PEGDME_CPE|LFMP polymer cell at 50 °C using a current rate of C/5, and a voltage ranging from 2.4 to 4.4 V. Prior to cycling, the cell is heated at 70 °C overnight to achieve a predominantly amorphous state of the polymer, and improve the electrode/electrolyte interphase as demonstrated by the EIS measurement reported in **Figure 2.10(a)**. The corresponding NLLS analysis of the dispersion, reported in **Table 2.3**, is performed by adopting an equivalent circuit $R_e(R_iQ_i)(R_wQ_w)Q_g$, where R_e is the high-frequency intercept accounting for the polymer electrolyte resistance and possible contribution of heterogeneities, (R_iQ_i) represents the middle-to-high frequency semicircle due to the SEI films and charge transfer, (R_wQ_w) is a low-frequency element associated with the Warburg-type Li^+ ion diffusion across the polymer, and Q_g is the constant phase element of the cell geometrical capacity.[273,274] The overall interphase resistance of the polymer at 70 °C, represented by the width of the high-to-middle frequency semicircle of the Nyquist plot, incorporates different contributions including SEI film, charge transfer and heterogeneities.[219] The total resistance of about 275 Ω, including the electrolyte and the interphase, suggests the formation of a suitable SEI film.[219]

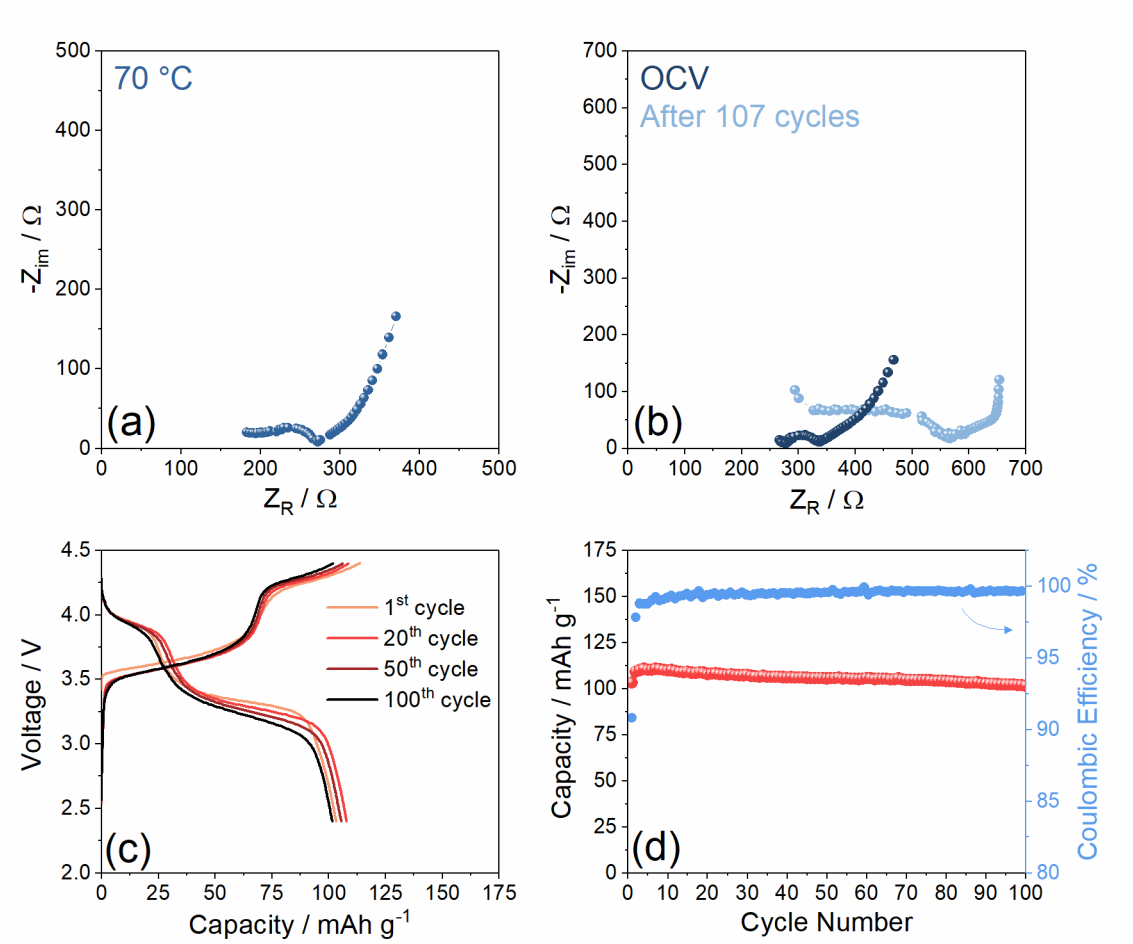

Figure 2.10: *Electrochemical performances of the Li|PEGDME_CPE|LFMP cell. EIS Nyquist plots collected at* ***(a)*** *70 °C at the OCV upon aging overnight and* ***(b)*** *at 50 °C at the OCV condition and after 107 galvanostatic cycles at C/5. Galvanostatic cycling in terms of* ***(c)*** *voltage profiles and* ***(d)*** *cycling trend with discharge capacity in the left-hand side y-axis and coulombic efficiency in the right-hand side y-axes performed at C/5 current (1C = 170 mA g^{-1}). Voltage range 2.4 – 4.4 V. EIS frequency range 500 kHz – 100 mHz; alternate voltage signal amplitude 30 mV. Adapted from [98].*

Subsequently, the cell is cooled down to 50 °C and cycled with a relevant response in terms of stability and efficiency. Indeed, **Figure 2.10(c)** shows the two plateaus with average voltage of 3.5 and 4 V previously described and associated with the $Fe^{3+}/Fe/^{2+}$ and Mn^{3+}/Mn^{2+} redox couples, respectively, with a high reversibility both at the initial stage of the test and after about 100 charge/discharge cycles. It is worth mentioning that this excellent behavior is remarkable, especially taking into account the test conditions (50 °C in a polymeric matrix) and the operating voltage of the cell (extending over 4.4 V). Furthermore, **Figure 2.10(c)** reveals for the cell a more significant slope of the charge/discharge plateaus with respect to the cycling test performed using the liquid electrolyte reported in **Figure 2.9**. This difference may be reasonably ascribed to kinetically limited lithium ions diffusion, both into the polymer matrix and at the electrode/electrolyte interphase.[243] **Figure 2.10(d)** evidences for the polymer battery an initial capacity of about 110 mAh g^{-1}, higher than the value of the cell cycling in the liquid electrolyte at the same C-rate and voltage limits (compare **Figure 2.10(d)** and **Figure**

2.9(b)), because of the higher temperature which typically boosts the reaction kinetics in olivine cathodes.[281,282] The polymer cell reveals a coulombic efficiency of about 90% during the first cycle, which increases to 97% after the second cycle, and approaches 100% at the final stages of the test, with a capacity retention as high as 95% in 100 cycles.

Table 2.3: *Electrolyte resistance (R_e), interphase resistance (R_i), and chi-square value indicating the accuracy (χ^2) of the NLLS analysis using the equivalent circuit $R_e(R_iQ_i)(R_wQ_w)Q_g$ on the EIS data of the Li\|PEGDME_CPE\|LFMP cell collected at 70 °C upon aging overnight at the OCV condition and at 50 °C before and after 107 galvanostatic cycles. See Figure 2.10 for related Nyquist plots.*[98]

Cell condition	R_e (Ω)	R_i (Ω)	$R = R_e + R_i$ (Ω)	χ^2
OCV 70 °C	194 ± 3	81 ± 5	275 ± 6	4×10^{-5}
OCV 50 °C	272 ± 1	58 ± 3	330 ± 3	2×10^{-5}
After 107 cycles	194 ± 34	273 ± 42	571 ± 54	2×10^{-4}

The relevant stability of the polymer cell is ascribed to an optimal electrode/electrolyte interphase which limitedly modifies during cycles, as demonstrated by the EIS measurement before and after 107 cycles (**Figure 2.10(b)**), and by the NLLS results obtained by using the equivalent circuit $R_e(R_iQ_i)(R_wQ_w)Q_g$, as reported in **Table 2.3**. The overall resistance ($R = R_e + R_i$) at the OCV after cooling down the cell at 50 °C (330 Ω) appears higher than that collected in the same conditions at 70 °C, likely due to the higher ionic conductivity of the PEGDME_CPE solid electrolyte at higher temperatures.[219] Therefore, the data of **Table 2.3** reveal an overall resistance with a value increasing from about 330 to about 570 Ω, that is a relatively restricted change, suitable for allowing an efficient and stable operation of the lithium-polymer battery.[316]

2.3 Transport and Interphase Features of a Converted Mixed Olivine Cathode for Sodium-Ion Batteries

2.3.1 Electrochemical Conversion of LFMP to NFMP

The electrochemical behavior during LFMP to NFMP conversion and the related structural changes detected by XRD and Raman spectroscopy are illustrated in **Figure 2.11**.

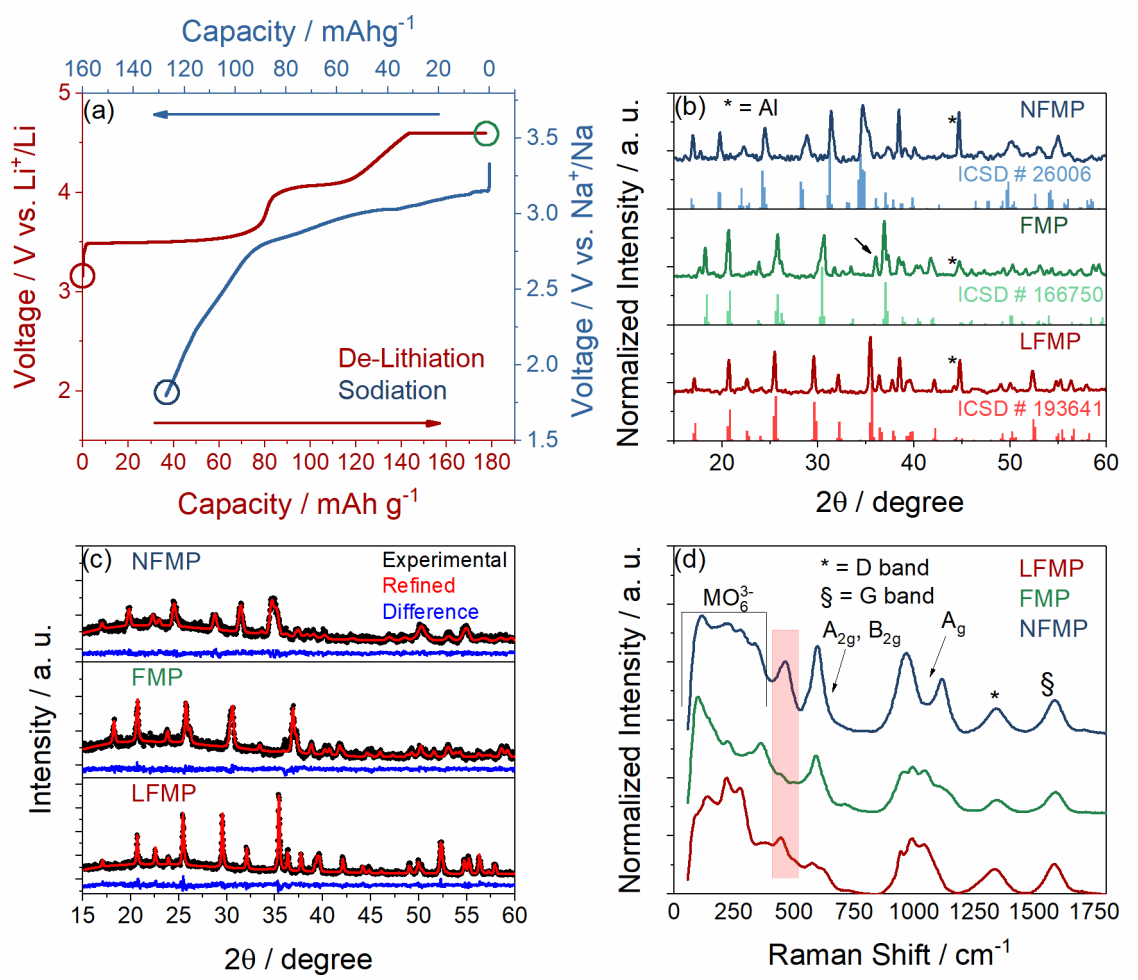

Figure 2.11: *Conversion of LFMP to NFMP.* ***(a)*** *Galvanostatic voltage profiles during de-lithiation of LFMP in Li-cell (red, left-hand y-axes, bottom x-axes) performed at C/10 (1C = 170 mA g^{-1}), and during subsequent sodiation of FMP in Na-cell (blue, right-hand y-axes, top x-axes) at C/20 (1C = 154 mA g^{-1}); circles indicate the SoC of the electrodes corresponding to the subsequent ex-situ studies.* ***(b)*** *XRD patterns of the pristine LFMP electrode (red), de-lithiated FMP electrode (green), and sodiated NFMP electrode (blue) compared to corresponding reference diffractograms.* ***(c)*** *Rietveld refinement of the XRD patterns of LFMP, FMP, and NFMP electrodes. In detail: experimental (black dots) and calculated (red line) patterns, difference profile (blue line).* ***(d)*** *Raman spectra recorded in the 0 – 1750 cm^{-1} range. Highlighted region and indexed peaks allow the transition identification.*[113]

The voltage profile of **Figure 2.11(a)** well reflects the de-lithiation of LFMP to FMP in a Li|LFMP cell, and the subsequent sodiation of FMP to NFMP in a Na|FMP cell. The de-lithiation (red line) proceeds with the expected shape, characterized by the described two plateaus at average voltages of 3.5 and 4 V, ascribed to the Fe^{2+}/Fe^{3+} and Mn^{2+}/Mn^{3+} oxidation processes, respectively, with a delivered capacity close to the theoretical value. The data also evidence the conversion of FMP to NFMP with a capacity of about 140 mAh g^{-1}, which is 91% of the theoretical value, however with a sloping voltage (blue line) possibly affected by polarizations associated with the poor electronic and ionic conductivity of the FMP phase.[87] It is worth noting that the sodiation process reflects the solid-solution behavior at about 3.0 V vs. Na^+/Na associated with the Fe^{3+}/Fe^{2+} reduction with the expected capacity, as already reported for mixed olivines,[115] and pure NFP,[317] and the sloped behavior of the

Mn^{3+}/Mn^{2+} reduction at about 3.5 V vs. Na^+/Na with a lower capacity than that expected from the material stoichiometry. The lower activity of the latter redox process compared to the former one is ascribed to the foreseen hindered kinetics and poor Na^+ diffusivity in the manganese region compared to the iron one. These kinetic limitations are mainly due to relevant Jahn-Teller distortion,[95,116] and to possible Na/Mn antisite mixing, that can lead to cation disorder and to partial formation of the natrophilite structure.[118] Nevertheless, the figure evidences a slight increase of the Fe^{3+}/Fe^{2+} redox potential in the mixed olivine compared with the one exclusively based on Fe, which is promoted by the presence of Mn, as already observed in literature.[100,116] Structure, morphology and composition of the pristine LFMP, the FMP intermediate, and the NFMP material have been investigated by using electrodes collected from the corresponding cells at the SoC indicated by the circles in **Figure 2.11(a)**. The achievement of the conversion is supported by the experimental and reference diffractograms for LFMP (ICSD #193641),[290] FMP (ICSD #166750),[291] and NFMP (ICSD #26006),[292] in **Figure 2.11(b)**, which shows indexable crystalline structure for all the samples with negligible additional peaks, except for that at ~ 44.7° attributed to the aluminum current collector.[318] Moreover, the figure indicates a limited amount of residual LFMP in the converted FMP electrode (arrow in the corresponding diffractogram), thus suggesting a relevant de-lithiation degree in agreement with the electrochemical profile.[291] To further investigate the structural features of the samples, **Figure 2.11(c)** reports a Rietveld refinement of the diffractograms related with electrodes prepared with a high loading, to avoid the appearance of Al current collector peak. The experimental XRD patterns (black dots) show that all the samples are characterized by an orthorhombic cell unit of the olivine lattice (*Pnma* space group, table N.62) without significant impurities, as indeed confirmed by the refined diffractograms (red line) and the almost flat difference profile (blue line).[290–292] The refinement results reported in **Table 2.4** indicate for all the samples a *GOF* < 1.5 and a $R_{wp}\%$ < 15, thus suggesting an acceptable quality.[302] Indeed, $R_{wp}\%$ values higher than 10 are typically associated with XRD measurements carried out on electrode films, in particular upon cycling in cell. This condition can increase the noise of the diffractograms, and consequently the expected square variance factor (R_{exp}) which is strictly correlated with the $R_{wp}\%$.[289,301] Furthermore, the relevant number and the sharpness of peaks in the diffractograms can affect the $R_{wp}\%$ values.[289] Nevertheless, the graphical matching of the experimental points with the refined ones, apart minor differences (see **Figure 2.11(c)**), the low values obtained for the *GOF*, and $R_{wp}\%$ values below 15 despite the phase complexity, can confirm the reliability and the accuracy of the study.[289,301,302]

Table 2.4: *Results of Rietveld refinement of the XRD patterns of Figure 2.11(c) in terms of lattice parameters, unit cell volume, goodness-of-fit (GOF) parameter, and weighted-profile R factor (R_{wp}%) of LFMP, FMP, and NFMP, respectively. References: ICSD #193641 (LFMP); ICSD #166750 (FMP); and ICSD #26006 (NFMP).*[113]

Sample	*a* (Å)	*b* (Å)	*c* (Å)	V (Å^3)	*GOF*	*R*wp%
ICSD #193641	10.343	6.022	4.704	293.03	/	/
LFMP	10.377(3)	6.044(5)	4.712(9)	295.61(9)	1.26	12.36
ICSD #166750	9.657	5.879	4.775	271.15	/	/
FMP	9.613(9)	5.839(1)	4.757(9)	267.09(2)	1.26	12.47
ICSD #26006	10.523	6.312	4.987	331.24	/	/
NFMP	10.446(1)	6.251(4)	4.997(5)	326.35(0)	1.20	11.75

The table also reveals values of the unit cell parameters (*a*, *b*, *c*) respectively of (10.3, 6.0, 4.7 Å) for LFMP, (9.7, 5.9, 4.8 Å) for FMP, and (10.5, 6.3, 5.0 Å) for NFMP.[76,110] These values are compatible with those of the reference diffractograms, and reflect in addition the bigger size of Na in NFMP compared with Li in LFMP, as well as the absence of the alkali ion in the FMP structure.[110,291] Hence, the data show a decrease of the cell volume from ~ 295.6 Å^3 for LFMP, which exceeds the reference one in view of the higher Mn content, to ~ 267.0 Å^3 for FMP as the Li^+ ion is extracted, and a relevant increase to ~ 326.4 Å^3 in NFMP due to the larger Na^+ ion insertion.[290–292] The values achieved for FMP and NFMP are comparable with those of heterosite and triphylite structures, respectively, thus suggesting the formation of the desired phases during the electrochemical conversion process.[110] A further insight on the structural features of LFMP, FMP, and NFMP is achieved by Raman spectroscopy, as reported in **Figure 2.11(d)**. All samples present the characteristic D and G bands of the carbon that coats the electrodes at 1350 and 1600 cm^{-1}, the peaks ascribed to the symmetrical and asymmetrical stretching of the phosphate PO_4^{3-} group with A_g mode centered at ~ 950 and ~ 1000 cm^{-1}, and the other peaks due to the symmetrical and asymmetrical bending of the PO_4^{3-} group with A_{2g} and B_{2g} modes respectively at about 500 and 600 cm^{-1}.[319,320] The most relevant difference between the spectra is observed for the peak centered at about 450 cm^{-1} (highlighted region), associated with lithium or sodium cage modes with translating Li^+ or Na^+ and breathing cage surrounded by O^{2-} ions.[319] As expected, this peak is almost absent in the FMP

spectrum, while it is more intense and resolved in the NFMP spectrum compared with LFMP one.[112,319] Further differences can be observed in the region between 50 and 300 cm^{-1}, which corresponds to the translational motions of the transition metals coupled with the vibrational motion of the MO_6^{3-} network bending.[319,320]

The morphological features and modifications of LFMP (panels **(a-h)**), FMP (panels **(i-p)**), and NFMP (panels **(q-y)**) electrodes are obtained by SEM-EDS analyses reported in **Figure 2.12**.

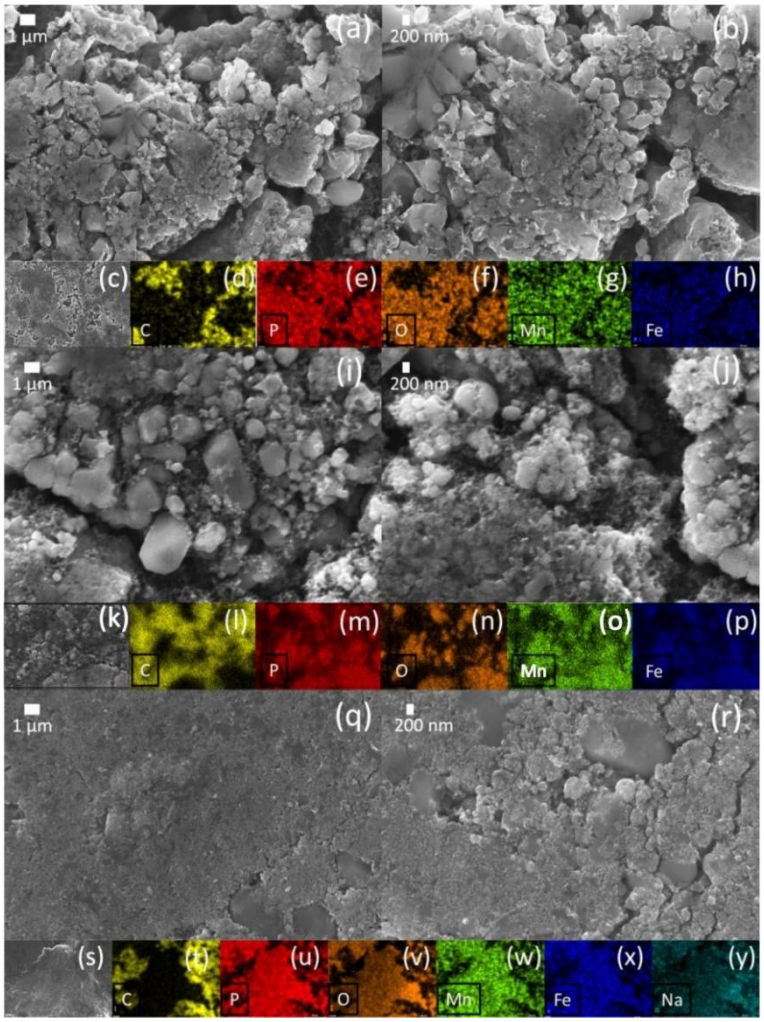

Figure 2.12: *SEM and EDS analyses of* ***(a–h)*** *LFMP,* ***(i–p)*** *FMP, and* ***(q–y)*** *NFMP electrodes. In detail: SEM images at different magnifications for* ***(a–c)*** *LFMP,* ***(i–k)*** *FMP, and* ***(q–s)*** *NFMP; SEM-EDS elemental maps of* ***(d, l, t)*** *C,* ***(e, m, u)*** *P,* ***(f, n, v)*** *O,* ***(g, o, w)*** *Mn,* ***(h, p, x)*** *Fe, and* ***(y)*** *Na for LFMP, FMP, and NFMP, respectively.*[113]

The corresponding SEM images at different magnifications and EDS elemental maps indicate for the three samples the presence of agglomerates of micrometric secondary particles formed by sub-micrometric primary particles homogeneously blended into the electrode film, fully in line with the morphology of LFMP powder reported in **Section 2.2** (see **Figure 2.4**).[98] Furthermore, the EDS maps reveal a homogeneous distribution of the elements for all the samples, excluding the presence

of impurities. **Table 2.5** reports the results of the ICP-OES analysis on the LFMP, FMP, and NFMP electrodes, which confirm the success of the de-lithiation and subsequent sodiation process.

Table 2.5: *Results of ICP-OES measurements in terms of Li, Na, and P concentration and ratio between the alkali metals and phosphorus.*[113]

Sample	Li concentration (ppm)	Na concentration (ppm)	P concentration (ppm)	Li/P ratio	Na/P ratio
LFMP	0.557	0.007	0.566	0.984	0.012
FMP	0.016	0.008	0.268	0.059	0.029
NFMP	0.018	0.400	0.425	0.042	0.941

The table shows sodium traces in LFMP and FMP samples which could be ascribed to possible contamination of the chemicals used for aqua regia preparation with the aim of dissolving the sample. Furthermore, the small lithium fraction detected in the de-lithiated and sodiated phases (*i.e.* ~ 5%) agrees with the small residual peak observed in the diffractograms (see **Figure 2.11(b)**), thus confirming the abovementioned predominant de-lithiation/sodiation degree of the sample.[291] In summary, LFMP, FMP, and NFMP display well-defined morphology and structure, and the data evidence a successful de-lithiation/sodiation process. These optimal characteristics and the uniform distribution of the elements are crucial parameters to enable suitable interphase and satisfactory performance of the NFMP in sodium battery.[317]

2.3.2 Electrochemical Characterization of NFMP

The electrochemical process of the NFMP cathode is investigated in Na-cell by combining CV and EIS as reported in **Figure 2.13**. The CV response (**Figure 2.13(a)**) shows during the first cycle two oxidation peaks centered at 3.1 and 3.9 V vs. Na^+/Na and three reduction peaks centered at about 3.55, 3.0, and 2.8 V vs. Na^+/Na. Indeed, the peaks at 3.1, 3.0, and 2.8 V vs. Na^+/Na are ascribed to the Fe^{3+}/Fe^{2+} redox couple, whilst those at 3.9 and 3.55 V vs. Na^+/Na to the Mn^{3+}/Mn^{2+} one, with de-insertion of Na^+ from NFMP during the anodic scan, and its insertion back into the olivine structure during the cathodic scan.[321] Similarly to Li-based olivine cathodes, the electrochemical process attributed to the Fe^{3+}/Fe^{2+} redox couple in NFMP occurs at higher potential compared to bare NFP, while that of Mn^{3+}/Mn^{2+} evolves at lower values with respect to NFP.[288,321,322] The transition metal redox potential shift, typically observed in mixed olivines, can be attributed to the above-described changes in the ionic character and distance of the M–O bond promoted by substitution.[79,108,116] It is

worth noting that the voltametric profile of NFMP is different from the one expected for pure NFP,[323] since it shows the presence of multiple peaks ascribed to Fe^{3+}/Fe^{2+} during sodiation instead of a single one, which are convoluted during de-sodiation process. Furthermore, the peak associated with the Mn^{3+}/Mn^{2+} shows a low intensity which further decreases after the first cycle during sodiation, thus suggesting an increase of the volume mismatch due to the high Mn content associated with the Jahn-Teller effect of Mn^{3+}.[95]

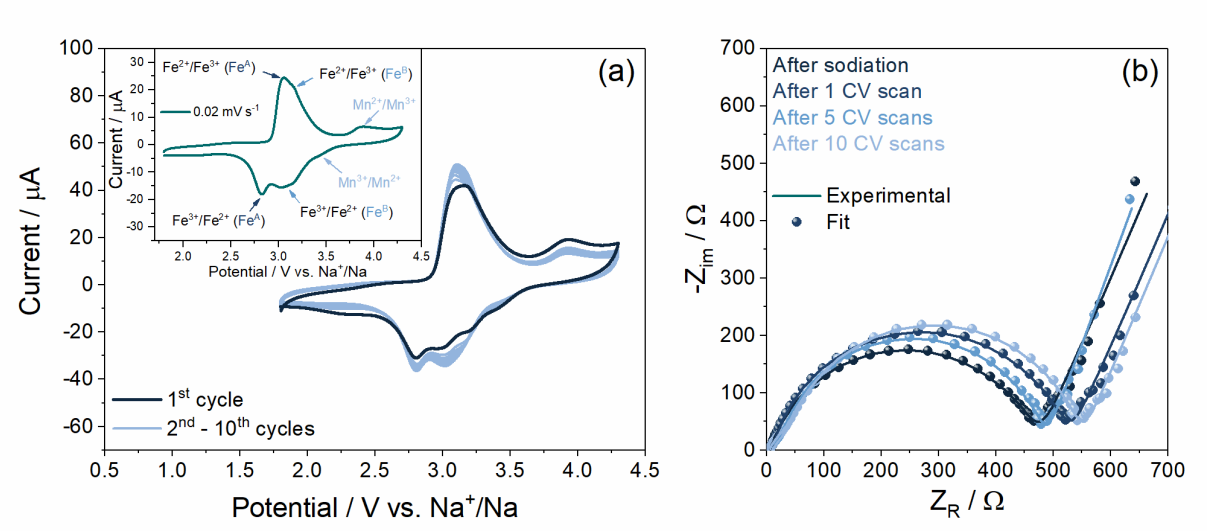

Figure 2.13: (a) *CV profiles and* ***(b)*** *EIS measurements after sodiation of the electrode and after 1, 5, and 10 CV scans of Na|NFMP three electrode cell with a Na reference electrode at 25 °C. Potential range 1.8 – 4.3 V vs. Na^+/Na; scan rate 0.05 mV s^{-1}. EIS frequency range 200 kHz – 100 mHz; alternate voltage signal amplitude 10 mV. Inset in* ***(a)****: CV scan at 0.02 mV s^{-1} scan rate (peaks with related redox couples reactions are indicated). Adapted from [113].*

The slow CV scan performed at 0.02 mV s^{-1} (inset of **Figure 2.13(a)**) increases the peak resolution and facilitates their association with the processes of the various redox couples. Indeed, the CV response indicates the occurrence of two oxidation processes revealed by peaks centered at about 3.05 and 3.16 V vs. Na^+/Na and 3.85 V vs. Na^+/Na during the anodic scan, which are almost completely reversed into two reduction processes with peaks at about 2.82, 3.02, and 3.55 V vs. Na^+/Na during the cathodic scan. The first two convoluted signals can be ascribed to the Fe^{3+}/Fe^{2+} redox couple and the latter to the Mn^{3+}/Mn^{2+} redox couple, respectively. Particularly, the oxidation of Fe^{2+} to Fe^{3+} evolves during charge by a single-phase de-sodiation until $0.6 \leq x \leq 1$ in $Na_xFe_{0.6}Mn_{0.4}PO_4$ (anodic peak at 3.05 V vs. Na^+/Na indexed as Fe^A), and a two-phase reaction including both sodiation and Na^+/vacancies ordering for $x < 0.6$ (anodic peak-shoulder at 3.16 V vs. Na^+/Na indexed as Fe^B), while the reduction of Fe^{3+} to Fe^{2+} occurs during discharge at 2.82 V vs. Na^+/Na (Fe^A) and 3.02 V vs. Na^+/Na (Fe^B). Despite the literature mainly describes the insertion process associated with LFP as a two-phase reaction,[317,323,324] an intermediate phase cannot be completely excluded even for this material. On the other hand, NFP clearly presents two consecutive voltage peaks upon charge at about

2.95 and 3.11 V vs. Na^+/Na merged into a single voltage peak upon discharge at about 2.8 V vs. Na^+/Na, with a three-phase reaction mechanism where an intermediate phase is foreseen, particularly during the charge process.[317] The above-described peak-split for the Fe^{3+}/Fe^{2+} couple, observed also during reduction however with a more complex structure, can be ascribed to the increase of the redox potential in a fraction of Fe sites, promoted by the higher electronegativity of the Mn neighbor.[115,116] Furthermore, the first cycle of **Figure 2.13(a)** (dark blue line) reveals a slightly higher polarization than the subsequent ones, thus suggesting an activation process mostly attributed to a partial structural reorganization of the sample, together with formation of an appropriate solid electrolyte interphase at the anode side and solid polymer interphase at the cathode side (SEI/SPI).[226] The subsequent voltametric cycles in **Figure 2.13(a)** show a well reversible electrochemical process evidenced by the overlapping of the cycles.

The SEI/SPI formation is investigated in **Figure 2.13(b)** by EIS measurements after the sodiation step, as well as after 1, 5, and 10 CV scans (bias potential 1.8 V vs. Na^+/Na) of NFMP in Na-cell, while the related interphase resistance values obtained by NLLS analysis are reported in **Table 2.6**.[273,274]

Table 2.6: *Equivalent circuits, interphase resistances (R_1, R_2), and chi-square values accounting for the accuracy (χ^2) of NLLS analysis related to the EIS data of the Na\|NFMP three-electrode cell using a Na reference electrode collected at 25 °C after sodiation, and after 1, 5, and 10 CV cycles in the 1.8 – 4.3 V vs. Na^+/Na potential range. See Figure 2.13 for related CV profiles and Nyquist plots.*[113]

Cell condition	Equivalent circuit	R_1 (Ω)	R_2 (Ω)	$R_i = R_1 + R_2$ (Ω)	χ^2
After sodiation	$R_e(R_1Q_1)Q_g$	465 ± 2	/	465 ± 2	2 x 10^{-4}
After 1 cycle	$R_e(R_1Q_1)(R_2Q_2)Q_g$	5.1 ± 0.2	513.4 ± 1.2	518.5 ± 1.2	5 x 10^{-5}
After 5 cycles	$R_e(R_1Q_1)(R_2Q_2)Q_g$	19.1 ± 0.5	458.5 ± 1.4	477.6 ± 1.5	5 x 10^{-5}
After 10 cycles	$R_e(R_1Q_1)(R_2Q_2)Q_g$	30.6 ± 0.8	508.9 ± 1.7	539.5 ± 1.9	4 x 10^{-5}

The Nyquist plots reflect the shape associated with a blocking-type behavior of the fully-discharge state of the cell (*i.e.* at 1.8 V vs. Na^+/Na) upon which EIS is collected. Overall, the curves are characterized by the presence of a medium-high frequency semicircle due to the electrode/electrolyte interface, and a low frequency tilted line representing the cell geometrical capacity.[273,274] The EIS response can be represented by the equivalent circuit $R_e(R_iQ_i)Q_g$, including in series the electrolyte resistance (R_e), one or two parallel constant phase/resistance elements (R_iQ_i) mainly accounting for

the SEI/SPI formed at electrodes with marginal charge transfer, and a final constant phase element related with the cell capacitance (Q_g). However, a partial overlapping with a Warburg-type diffusion cannot be excluded.[273,274] The data shown in **Table 2.6** indicate an overall value of the interphase resistance of about 500 Ω, which is higher than the one reported in **Section 2.2** for the lithium counterpart,[98] however in line with that associated to sodium metal interphase.[325] It should be recalled that the growth of surface layer leading to these high values may be typically limited by adding sacrificial substrates such as FEC in the electrolyte,[227] or by using glyme-based electrolytes.[232,234,238] Nevertheless, it is worth noting that in the present case the resistance values undergo very limited variation upon the voltametric scans, thus suggesting the formation of a stable SEI/SPI, in addition to the discussed structural reorganization which may favor the electrochemical reaction of NFMP.

The electrochemical performances of NFMP cathode in Na-cell subjected to galvanostatic cycling tests are shown in **Figure 2.14**.

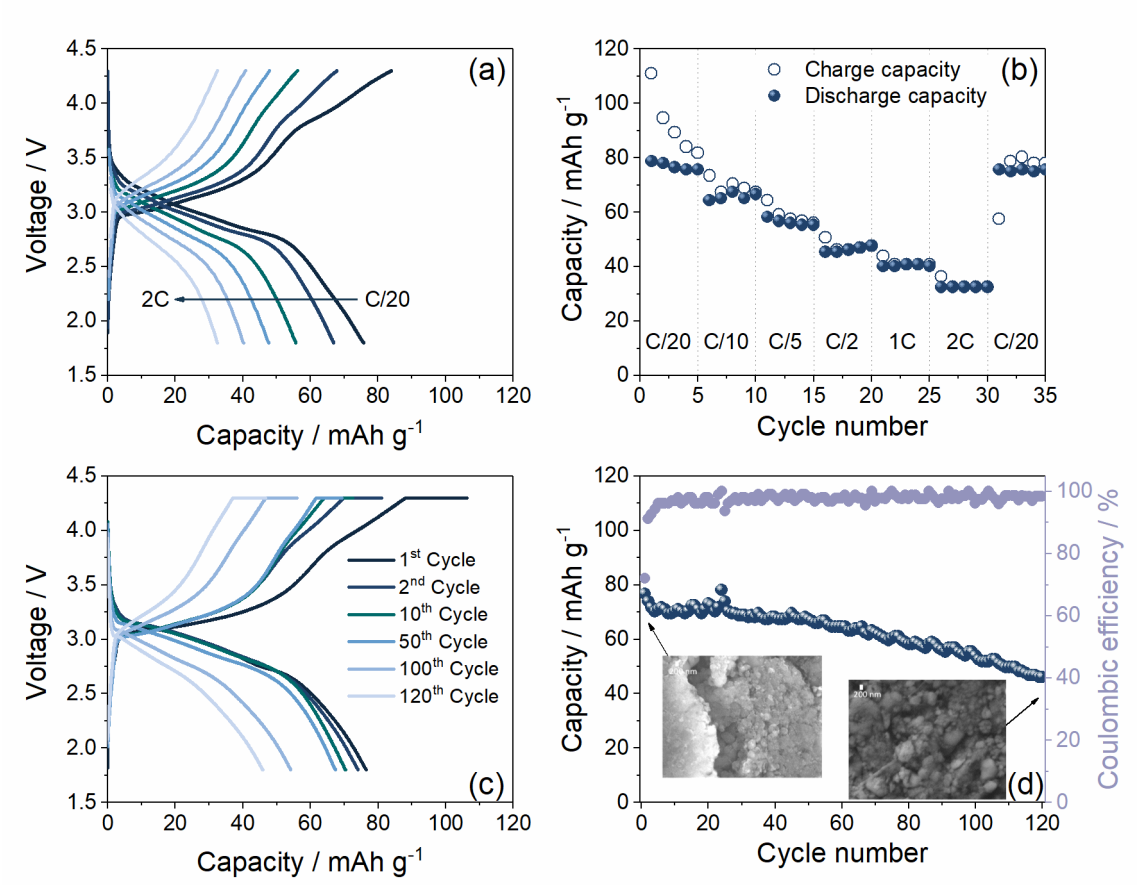

Figure 2. 14: *Galvanostatic cycling performances of the Na|NFMP cell at 25 °C. Rate capability in terms of* ***(a)*** *voltage profiles and* ***(b)*** *corresponding cycling trend performed at C/20, C/10, C/5, C/2, 1C, and 2C currents (1C = 154 mA g^{-1}) in the 1.8 – 4.3 V voltage range. Electrochemical performance of the cell at the constant current rate of C/5 in terms of* ***(c)*** *voltage profiles and* ***(d)*** *cycling trend with discharge capacity in the left-hand side y-axis and coulombic efficiency in the right-hand side y-axes. Voltage range 1.8 – 4.3 V with*

*an additional constant voltage step (CCCV mode) at 4.3 V until a finale current of ¼ referred to the nominal C-rate. Inset in **(d)**: SEM images of the NFMP electrode before and after cycling test. Adapted from [113].*

The rate capability of NFMP is reported in terms of the voltage profiles (**Figure 2.14(a)**) and cycling trend (**Figure 2.14(b)**) by increasing the current from C/20 to 2C (1C = 154 mA g^{-1}). The cell shows at the various C-rates the voltage shape expected by taking into account the CV of **Figure 2.13(a)**, characterized by a solid-state region with three plateaus at an average voltage of 3.0, 3.2, and 3.8 V, associated with Fe^{3+}/Fe^{2+} (Fe^{A} and Fe^{B}) and Mn^{3+}/Mn^{2+} redox couples, respectively. Moreover, the profiles in **Figure 2.14(a)** indicate an increase of polarization by raising the current due to the increase of the ohmic polarization, which leads to the decrease of the capacity from 80 mAh g^{-1} (*i.e.* about 52% of the theoretical value) at C/20 to about 33 mAh g^{-1} (22% of the theoretical value) at 2C. The cycling trend of **Figure 2.14(b)** reveals that the pristine capacity is recovered by decreasing the current back to C/20 after the whole test, thus suggesting the stability of the NFMP cathode upon the stress on the material structure triggered by the raising currents.[288] It is worth nothing that the first charge at C/20 in **Figure 2.14(b)** is characterized by a capacity of about 110 mAh g^{-1} (*i.e.* about 71% of the theoretical value), which is lower than the one obtained after the sodiation of the electrode at the same current in the previous step (*i.e.* about 140 mAh g^{-1} in **Figure 2.11(a)**). The figure also evidences a very modest contribution of the Mn^{3+}/Mn^{2+} redox couple to the overall cell capacity even at low current rate. This behavior may be ascribed to the abovementioned Jahn-Teller distortion promoted by Mn in olivines with high manganese content (*i.e.* $y > 0.2$ in $Na_zMn_yFe_{1-y}PO_4$),[116] which can relevantly hinder the transport of the voluminous sodium ion,[115] promote the strain, and increase the potential hysteresis during oxidation/reduction, thus limiting $Na_zMn_yFe_{1-y}PO_4$ solid solution stability and the performances of the material.[84,116,326] Besides, the complete oxidation of Mn^{2+} to Mn^{3+} requires higher voltages than the theoretical one, in particular with high Mn content, thus leading to possible degradation of the conventional electrolytes.[50] The Na^+/Na (de-)insertion in the olivine lattice may in addition be affected by the split of the Fe^{3+}/Fe^{2+} redox potential promoted by the higher electronegativity of the Mn neighbor,[115,116] while Na and Mn can undergo the abovementioned antisite cation mixing in the structure, with possible formation of the electrochemically inactive natrophilite phase.[118] To investigate the Na/Mn antisite mixing, the crystallographic details and the atomic parameters of NFMP are obtained from Rietveld refinement of **Figure 2.11(c)** and summarized in **Table 2.7**. The table shows a cation disorder of about 8% for NFMP cathode, particularly ascribed to Mn^{2+}, and partially justifies the limited contribution of the Mn^{3+}/Mn^{2+} redox couple to the cell capacity.[117,118,327] It is worth mentioning that the occupancies of M1 and M2 sites vary during the refinement to allow the antisite mixing.

Table 2.7: *Crystallographic details and atomic parameters of the NFMP cathode obtained from Rietveld refinement of Figure 2.11(a).*[113]

Atom	Wycoff position	*x*	*y*	*z*	Occupancy	B_{iso} (Å^2)
Na1	4a	0	0	0	0.918(6)	0.038(7)
Na2	4c	0.2852(6)	0.25	-0.0086(2)	0.084(0)	0.018(8)
Mn1	4a	0	0	0	0.073(3)	0.038(7)
Mn2	4c	0.2852(6)	0.25	-0.0086(2)	0.326(7)	0.018(8)
Fe1	4a	0	0	0	0.009(4)	0.038(7)
Fe2	4c	0.2852(6)	0.25	-0.0086(2)	0.590(6)	0.018(8)
P1	4c	0.1073(4)	0.25	0.4409(1)	1.0	0.033(3)
O1	4c	0.1124(7)	0.25	0.1471(9)	1.0	0.005(6)
O2	4c	0.4675(2)	0.25	0.1609(5)	1.0	0.009(9)
O3	8d	0.1733(6)	0.0609(5)	0.3104(5)	1.0	0.011(1)

A possible strategy to increase the Na^+ extraction/insertion capacity in the olivine lattice is represented by the use of the CCCV mode for charging the cell.[328] Accordingly, a CCCV cycling test has been performed of NFMP in Na-cell at a constant C-rate of C/5, with a constant voltage step at 4.3 V during charge. The related voltage profiles reported in **Figure 2.14(c)** show an increase of the maximum capacity, compared to the corresponding profiles obtained in the rate capability test of **Figure 2.14(a)** (*i.e.* from ~ 60 to ~ 78 mAh g^{-1}). Furthermore, the related cycling trend in **Figure 2.14(d)** evidences a coulombic efficiency of about 72% at the first cycle, which increases and ranges between 98% and 100% during the subsequent ones, with a capacity retention of ~ 87% after 50 cycles and ~ 68% after 120 cycles. It is worth noting that the sudden capacity increase around the 20th cycle, with the corresponding coulombic efficiency oscillation observed in the figure, may be due to a partial activation of the material, which is possibly triggered by the improved electrode wetting achieved upon time evolution. On the other hand, the decrease of the capacity observed at the end of the test is likely ascribed to the limitation of the charge-transfer kinetics promoted by the excessive growth of the SEI/SPI layer upon prolonged cycling, as indeed suggested by the SEM inset in **Figure 2.14(d)** of the NFMP electrode before and after the test.[110]

A more detailed view of the structural and morphological features of the NFMP electrode upon the above cycling test in sodium cell is reported in **Figure 2.15**. Panel **(a)** reports the XRD analysis of the pristine and the cycled electrodes, compared with a reference sample (ICSD #26006).[292]

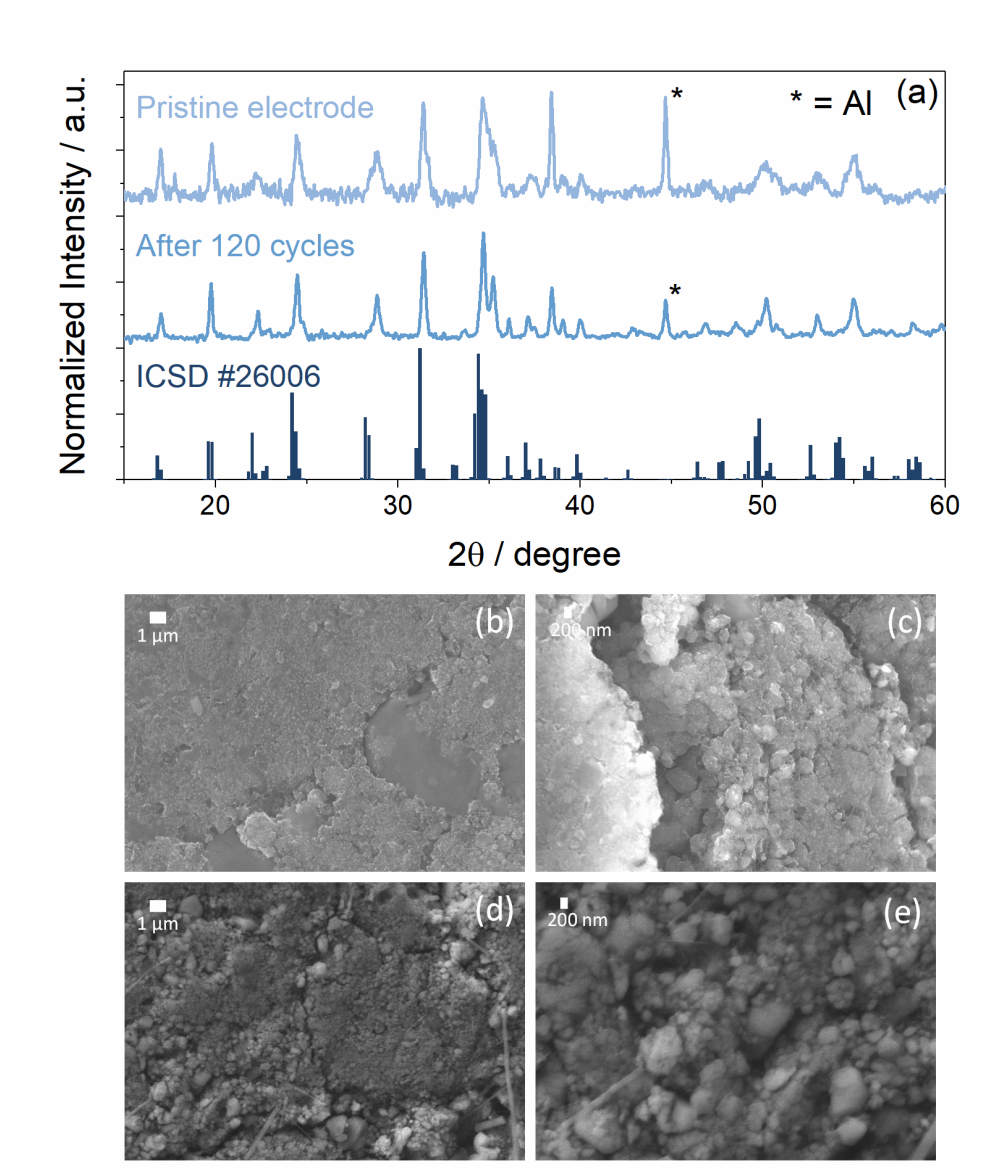

Figure 2.15:(a) *Comparison between the XRD patterns of a pristine NFMP electrode, the NFMP electrode recovered cycling measurement reported in Figure2.14(d), and the reference diffractogram (ICSD #26006). SEM images at different magnifications of* ***(b, c)*** *the pristine and* ***(d, e)*** *the cycled NFMP electrodes.*[113]

The XRD patterns of the electrodes exhibit a defined crystalline structure, in full agreement with the one observed in **Figure 2.11(b, c)** for NFMP without significant modification, thus accounting for a relevant stability of the olivine framework.[292] It is worth noting that the more defined peaks of the cycled electrode are likely ascribed to the different loading of the samples, as indicated by the intensity of the Al current collector peak in the diffractograms. Moreover, the SEM images of the pristine (**Figure 2.15(b, c)**) and cycled (**Figure 2.15(d, e)**) electrodes show the above-described agglomerates of primary sub-micrometric particles aggregated into micrometric secondary particles, without relevant change and reorganization of the NFMP. Additional domains in the cycled electrode, characterized by rough morphology, may be ascribed to the formation of the SEI/SPI,[226,314] as well as to dispersed glass fibers due to the electrolyte separator. Overall, **Figures 2.14** and **2.15** indicate

the stability of both structure and morphology of NFMP upon cycling and its suitability for sodium cells, and suggest further tuning of the material composition in terms of Fe to Mn ratio, to further improve the delivered capacity.

The increase of the Na^+ ion mobility in the olivine framework against the distortion and strain triggered by the Mn^{3+}/Mn^{2+} redox couple at 3.8 V may be actually promoted by increasing the temperature according to an Arrhenius trend. The above improvement of the material conductivity, which may also enhance the reaction kinetics, is typically reflected into a linear increase of the cell capacity by raising the temperature.[329,330] Hence, **Figure 2.16** reports the galvanostatic cycling of the NFMP cathode in sodium cell performed at C/5 rate (CCCV mode), increasing the temperature by 5°C every 10 cycles from 45 to 60 °C. The voltage profiles of **Figure 2.16(a)** selected at 45, 50, 55, and 60 °C present the solid-state region with three plateaus at average voltage of 3.0, 3.2, and 3.8 V previously described, associated with Fe^{3+}/Fe^{2+} and Mn^{3+}/Mn^{2+} redox couples, respectively. It is worth noting that the increase of the temperature leads to the desired rise of the capacity from about 80 mAh g^{-1} at 45 °C to about 110 mAh g^{-1} at 60 °C, with a high stability and efficiency for the tests performed at 45, 50, and 55 °C, according to the trends in **Figure 2.16(b)**. The activation already observed at 25 °C may also be promoted by temperature increase, according to the trend observed in panel **(b)** at 45 and 50 °C. However, the reason for improvement in this case may be found in the increase of the material conductivity following Arrhenius behavior.[325] The values of the maximum capacity obtained by the cell at the different temperatures are reported in **Figure 2.16(c)** as a function of the temperature, and fitted by a straight line with a relevantly high confidence (R^2 = 0.9994). The achieved trend well accounts for the abovementioned effect of the increase of Na^+ ions conductivity into the material framework triggered by the temperature. Despite the test performed at 60 °C achieves the highest value, it also reveals a progressive decrease of the cell capacity and coulombic efficiency, as expected by the more pronounced electrolyte decomposition and growth of electrode/electrolyte interphase at higher temperature.[330–332] To investigate the possible electrolyte oxidation at increased temperature, the anodic electrochemical stability window (ESW) has been measured by LSV at 25, 50, and 65 °C and the results are shown in the inset of **Figure 2.16(c)**. The data reveal the stability of the electrolyte at 25 °C in the 1.8 – 4.3 V vs. Na^+/Na potential range, which is the interval used for cell cycling. Indeed, the full oxidative decomposition of the electrolyte is detected above 4.8 V vs. Na^+/Na at 25 °C. However, the increase of the temperature limits the ESW of the electrolyte to ~ 4.4 V vs. Na^+/Na at 50 °C, and below 4.1 V vs. Na^+/Na at 65 °C. These results confirm the possible electrolyte decomposition at the higher temperatures, possibly resulting into decrease of cell capacity and coulombic efficiency.[331,332] Nevertheless, the interphase stability below

65 °C suggests the compatibility of the electrolyte with the NFMP electrode, as also indicated by the formation of a stable SEI/SPI (see **Figure 2.13** and **Table 2.6**).

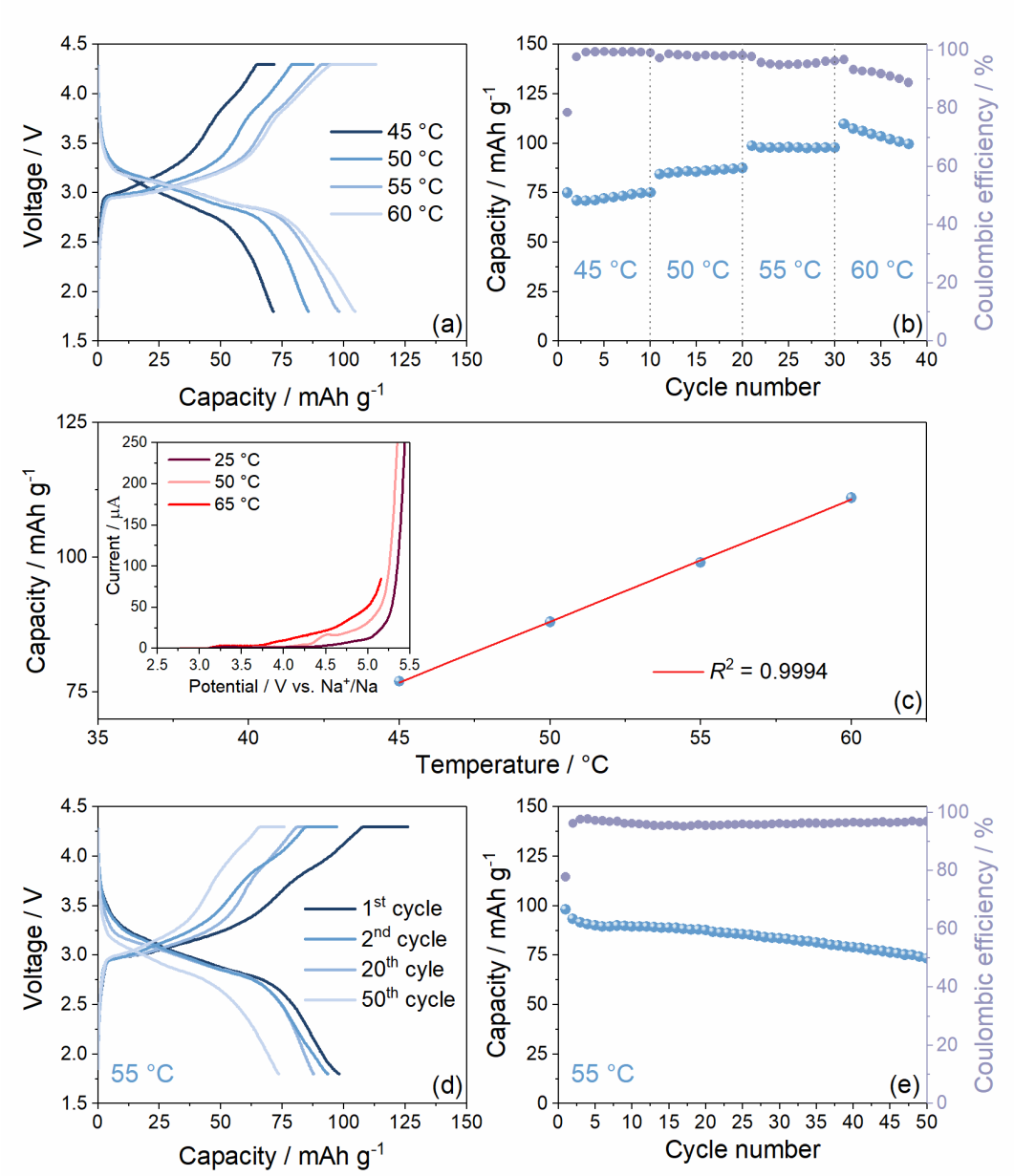

Figure 2.16: *Performance of the Na|NFMP cell at various temperatures. Galvanostatic test performed at C/5 current (1C = 154 mA g^{-1}) in terms of* ***(a)*** *voltage profiles and* ***(b)*** *cycling trend by changing the temperature from 45 to 50, 55, and 60 °C.* ***(c)*** *Linear trend of the maximum specific capacity delivered by NFMP vs. temperature. Inset in (c): LSV measurements of the Na|SP-Al cells for determining the anodic ESW of the electrolyte at 25, 50, and 65 °C. Scan rate 0.1 mV s^{-1}. Galvanostatic test performed at C/5 current in terms of* ***(d)*** *voltage profiles and* ***(e)*** *cycling trend at 55 °C with discharge capacity in the left-hand side y-axis and coulombic efficiency in the right-hand side y-axes. Voltage range 1.8 – 4.3 V with an additional constant voltage step (CCCV mode) at 4.3 V until a finale current of ¼ referred to the nominal C-rate.*[113]

Therefore, the temperature of 55 °C has been chosen for further characterization as a suitable compromise between delivered capacity, high coulombic efficiency, and good retention. **Figure 2.16(d)** reports the galvanostatic voltage profiles of the Na|NFMP cell at 55 °C, while **Figure 2.16(e)** depicts the corresponding cycling trend. The cell shows the plateaus associated with Fe^{3+}/Fe^{2+} and

Mn^{3+}/Mn^{2+}, where the plateau at 3.8 V associated with the latter redox couple presents a more defined shape, thus suggesting a mitigated effect of the Jahn-Teller distortion.[95] Furthermore, the cell reveals a maximum specific capacity of about 100 mAh g^{-1}, a coulombic efficiency of about 78% at the first cycle which increases and ranges from about 97% to 99% during the subsequent ones, and a capacity retention of about 75% after 50 cycles. Overall, the temperature has a beneficial effect on the performances of the cell, which reaches higher capacity, a more defined process associated with the transition metal redox couples without significant strain transformation, and a good coulombic efficiency. Nevertheless, the lower retention and the slightly lower coulombic efficiency compared to the cell cycled at 25 °C (*i.e.* 75% compared to 87% after 50 cycles, and 97% compared to 100%, respectively) suggest a limited decomposition of the electrolyte at 55 °C as discussed above,[332] and the necessity of *ad hoc* tuned electrolyte with a better anodic stability, as well as further improvement of the NFMP electrode to achieve higher performance and stability.[98,317,333]

2.3.3 Ion Transport and Interphase Features of LFMP and NFMP

The understanding of thermodynamics and kinetics plays a key role for evaluating the cycling performances, the ions diffusion and the interfacial properties of mixed olivines.[334] Although the NFMP olivine has the same phase structure as the LFMP olivine (see **Figure 2.11**), they intrinsically differ by the electrochemical process.[108,112,117] According to the data illustrated above, is possible to speculate that the typical phase transformation and ion transport kinetics in NFMP are clearly worse during (de-)insertion of Na^+ in NFMP compared with the LFMP analogue.[98] To further shed light on this aspect and properly evaluate the electrode behavior in sodium cell, hereafter a comparative investigation between NFMP and LFMP is performed, particularly evaluating the difference in the Li^+ or Na^+ ions diffusion coefficient, the equilibrium potential of the ion insertion/extraction, and the charge transfer kinetics of the two materials. It is worth mentioning that the ion transfer occurring at the electrode/electrolyte interphase can be influenced by the different electrolyte media (*e.g.* EC/DMC for lithium and EC/PC for sodium batteries). On the other hand, the impact of the different solvents on the ion migration at the interphase has already been demonstrated using various combinations of substrates and electrolytes, including the carbon-based electrodes in the EC/DEC or EC/EMC media.[331,333] Salt chemistry may also have a concomitant role together with solvent in driving the performance of the Na-battery in terms of ion transport and conductivity. Hence, sodium hexafluorophosphate in the EC:PC solvent has been proven to outperform in SIBs the conventional EC:DMC mixture typically used in LIBs, leading to higher capacity retention and coulombic efficiency, as already mentioned. However, this improvement is typically much more relevant at the anode side, where a thick SEI can be formed.[226] Thickness, composition and stability of the SEI at the SIBs anode are indeed related with to the electrolyte stability towards reduction at low potentials,

and can severely affect the ion transfer.[225] This effect is less pronounced at the cathode side, since SIBs typically operate below the electrolyte oxidation limit. Therefore, the surface layer formed at the higher potentials by marginal oxidation at the cathode surface is thin, in particular using EC:PC solvent mixture which displays enhanced anodic stability at room temperature.[225] Nevertheless, the comparable charge-transfer resistance throughout the whole cycling of the two systems considered herein (LFMP and NFMP) well supports the abovementioned limited influence of the solvent mixture on the achieved results, despite the change of the electrolyte solution.

Figure 2.17 depicts the CV responses at increasing scan rates of LFMP in Li-cell (**Figure 2.17(a)**) and NFMP in Na-cell (**Figure 2.17(b)**).

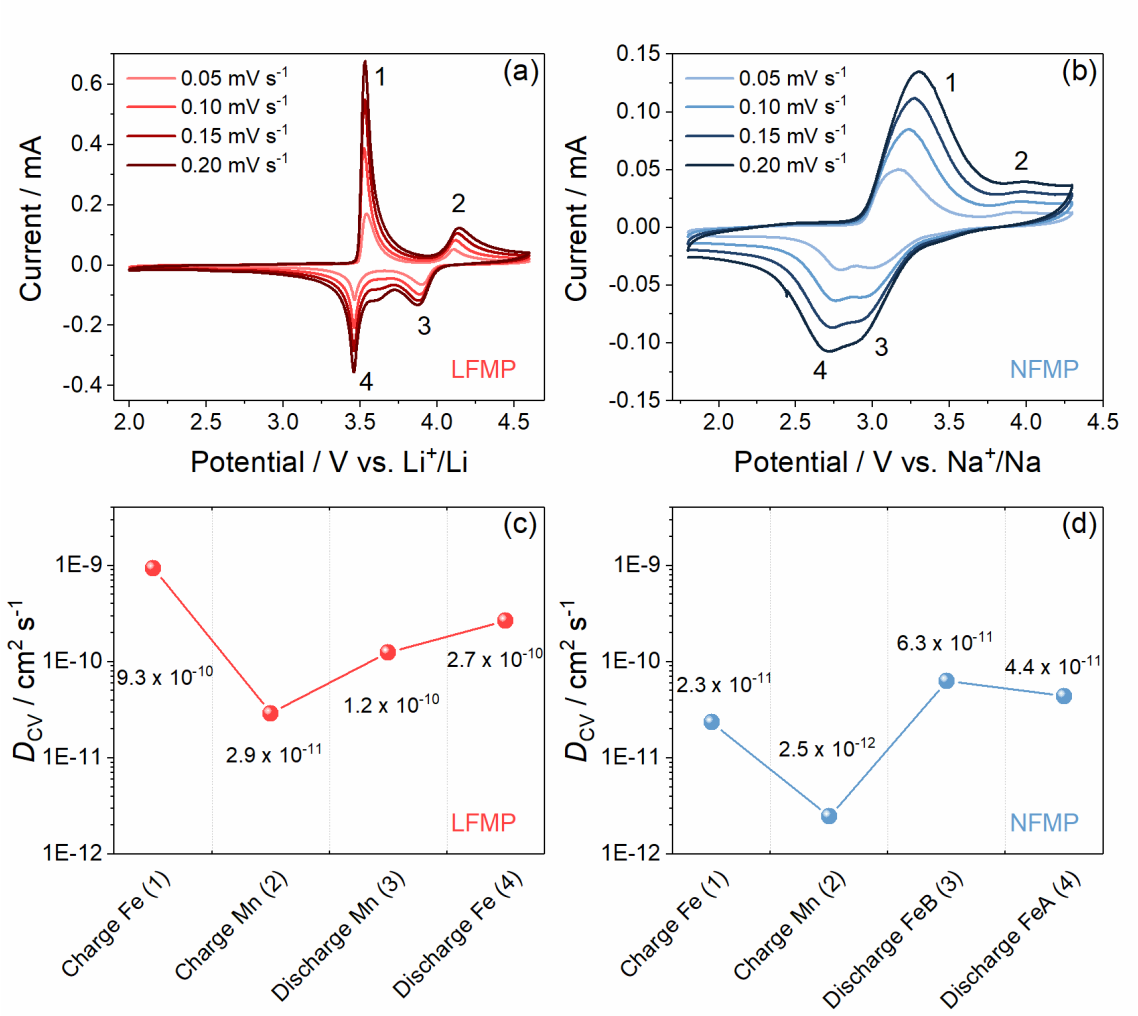

Figure 2.17: *Steady-state CV profiles with indexed peaks of* ***(a)*** *LFMP in LI-cell and* ***(b)*** *NFMP in Na-cell with 3-electrode setup at 25 °C. Scan rates 0.05, 0.1, 0.15, and 0.2 mV s^{-1}. Potential ranges 2.0 – 4.6 V vs. Li^+/Li for LFMP and 1.8 – 4.3 V vs. Na^+/Na for NFMP. Trends of DCV at various SoC for* ***(c)*** *Li^+ in LFMP and* ***(d)*** *Na^+ in NFMP calculated using Equation 2.6.*[113]

The current peak (I_p) increases by rising the scan rate (v), in agreement with a linear trend of I_p *vs.* $v^{1/2}$, thus suggesting lithium or sodium diffusion as rate-determining step of the redox processes. The measured values of CV peak current related with the electrochemical processes of LFMP and NFMP

in Li-cell and Na-cell are reported versus the square root of the scan rate in **Figure 2.18**. The points of the figure follow a linear trend, as expected by the reversible redox processes and confirmed by coefficient of determination (R^2) values.

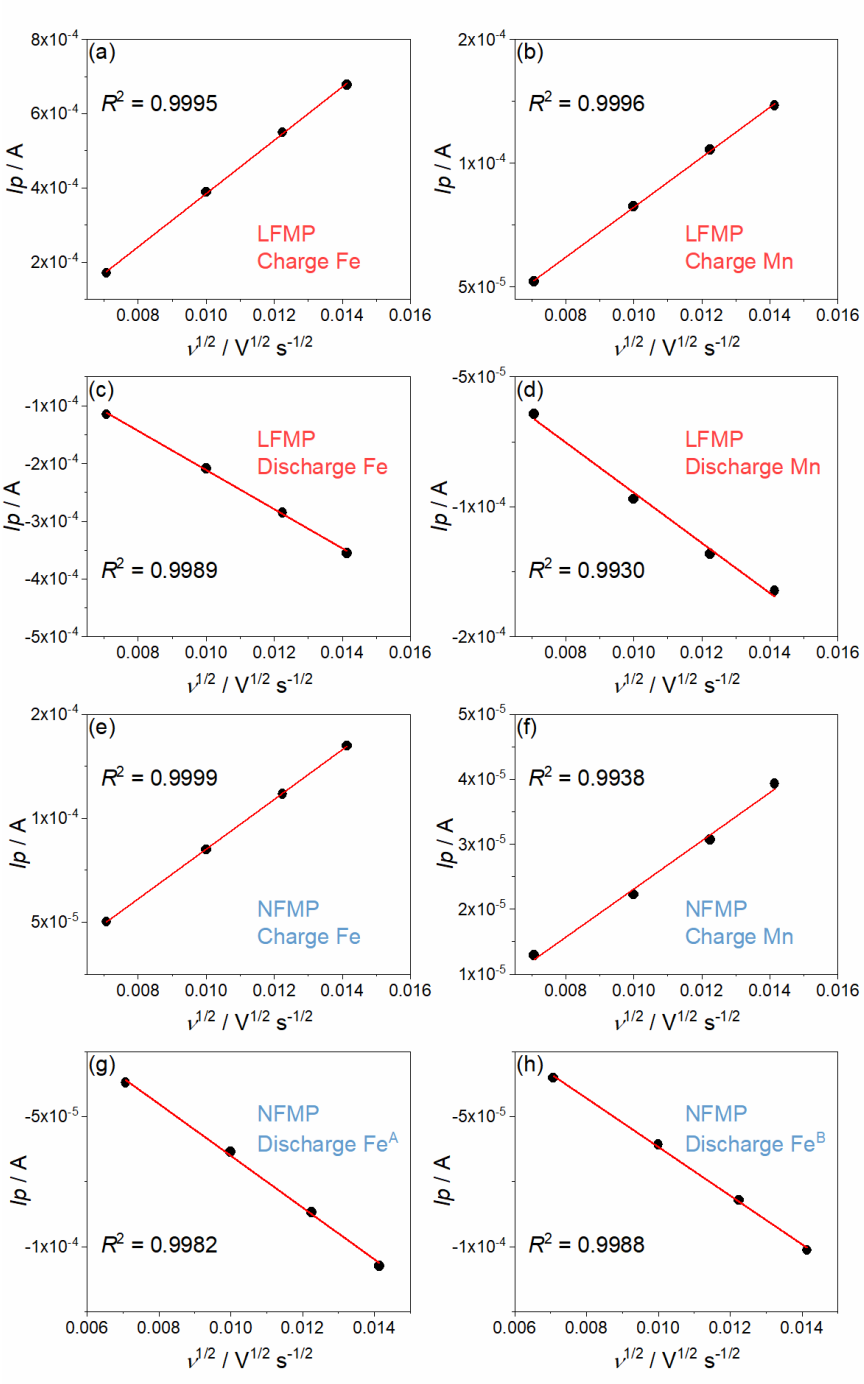

Figure 2.18: *Peak current (Ip, A) vs. square root of scan rate ($\nu^{1/2}$, $V^{1/2}$ $s^{-1/2}$) and related linear fit, with associated coefficient of determination (R^2) values, corresponding to the Fe^{3+}/Fe^{2+} and Mn^{3+}/Mn^{2+} processes within the olivine structure of LFMP and NFMP as determined by CV in Figure 2.17(a) and Figure 2.17(b), respectively.*[113]

The I_p *vs.* $v^{1/2}$ slope values have been used to calculate the Li^+ and the Na^+ diffusion coefficients for LFMP and NFMP, respectively, D_{CV} ($cm^2\ s^{-1}$), according to the Randles-Sevcik equation (**Equation 2.6**):[335]

$$I_p = 0.4463zFAC\sqrt{\frac{zF\nu D_{CV}}{RT}} = 2.686 \cdot 10^5 AC\sqrt{z^3\nu D_{CV}} \qquad \text{with T = 298.15 K} \qquad \textbf{(2.6)}$$

where I_p is the peak current value (A), $z = 1$ is the number of exchanged electrons, F is the Faraday constant (96485 C mol^{-1}), A is the electrodes geometric area (0.785 cm^2), C is the Li^+ or Na^+ concentration within the olivine lattice (mol cm^{-3}), ν is the scan rate (V s^{-1}), R is the gas constant (J K^{-1} mol^{-1}), and T is the temperature (K). The obtained values of the D_{CV} for LFMP and NFMP are shown in **Figure 2.17(c)** and **Figure 2.17(d)**, respectively, and calculated by considering the linear slope previously described in **Figure 2.18** for Fe^{3+}/Fe^{2+} and Mn^{3+}/Mn^{2+} redox couples during charge and discharge processes. It is worth mentioning that during NFMP sodiation process, only the peaks associated with the Fe (Fe^A and Fe^B) are taken into account, since the low intensity of the peak associated with Mn during discharge avoids an accurate determination of D_{CV}.[115] The results of **Figure 2.17(c, d)** indicate a much faster ion transport in LFMP compared to NFMP, with DCV values above 10^{-10} $cm^2\ s^{-1}$ for the former, and in the order of 10^{-12} $cm^2\ s^{-1}$ for the latter. Moreover, the D_{CV} values herein obtained for LFMP are slightly higher than the values already reported in literature for samples prepared by solvothermal reaction, thus indicating that the sol-gel synthesis could be a suitable choice for an enhanced structure.[99,278] Nevertheless, the reported NFMP cathode presents higher values of D_{CV} compared to the ones achieved in literature for pure NFP, thus suggesting a concomitant effect of Na^+ (de-)intercalation features and optimized synthesis on the transport properties.[322,334] The above trends also evidence, for both LFMP and NFMP, a decrease of one order of magnitude of D_{CV} by cell charging and its increase back by discharging, accounting for the remarkably lower ionic conductivity of the de-lithiated/de-sodiated phase of the olivine compared to the lithiated/sodiated one. However, conductivity can be highly enhanced by a fine tuning of the carbon coating in the electrode.[304]

Further determination of Li^+ and Na^+ diffusion coefficients for LFMP and NFMP performed by GITT is reported in **Figure 2.19**, according to the method proposed by Weppner and Huggins.[336] Prior to GITT experiment, three galvanostatic cycles have been performed on LFMP and NFMP, to limit possible effects given by stabilization of the interphase or activation of the material. **Figure 2.19(a, b)** shows the time evolution of the potential during titration (black curves), obtained by applying repeated current pulses followed by potential relaxation steps in three-electrode lithium and sodium cells using LFMP and NFMP, respectively. Small constant currents of C/10 for LFMP and C/20 for

NFMP are used during GITT in order to assume the diffusion process in the surface layer, as proposed by Weppner and Huggins.[336]

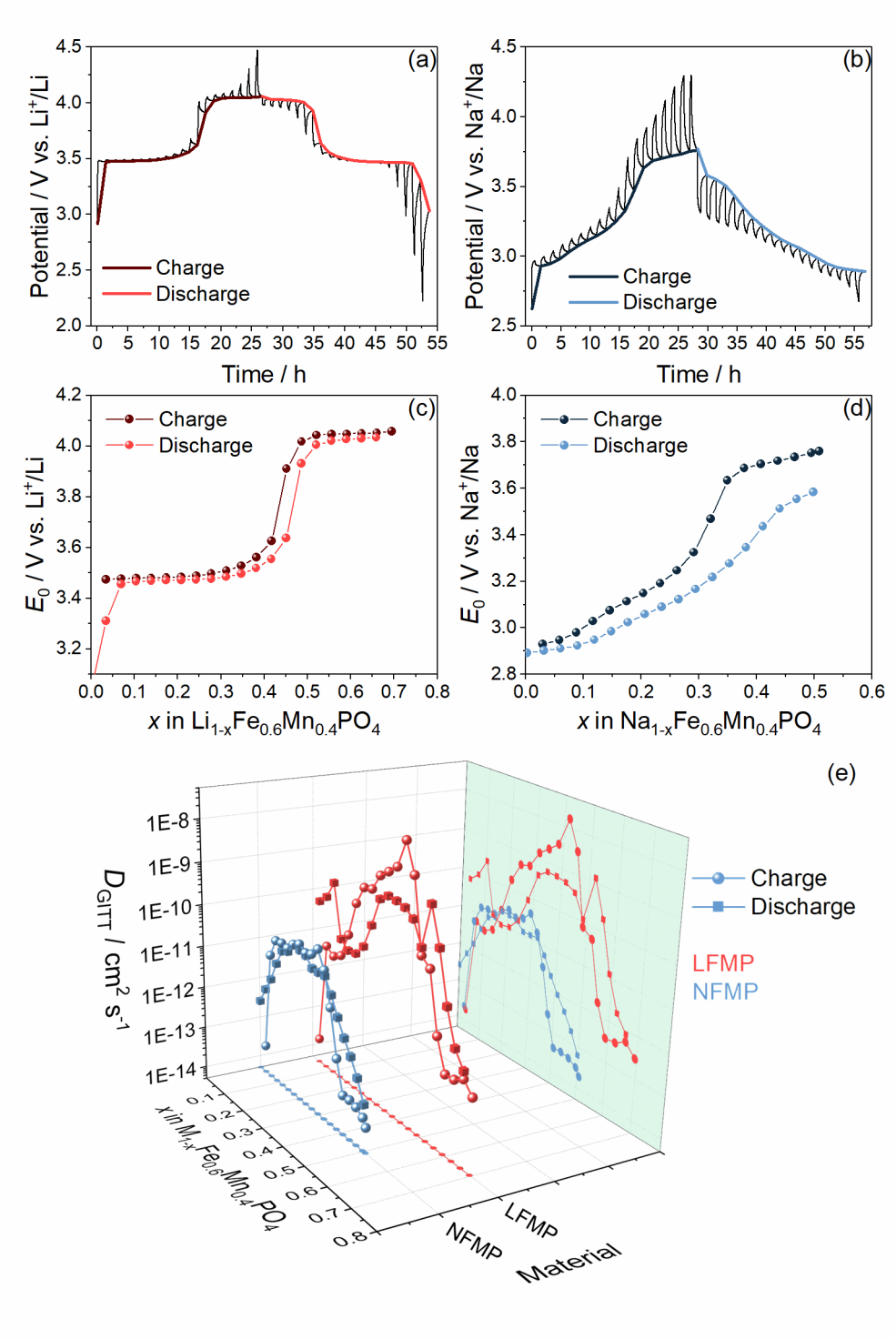

Figure 2.19: *GITT curves in terms of E_0 vs. time of* ***(a)*** *LFMP in Li-cell and* ***(b)*** *NFMP in Na-cell with 3-electrode configuration at 25 °C, with overlapped black curves reporting the overall time evolution of the potential during current pulses and relaxation steps. Trends of E_0 vs. x for* ***(c)*** *LFMP and* ***(d)*** *NFMP determined from GITT.* ***(e)*** *Three-dimensional representation of D_{GITT} vs. x for Li^+ ions in LFMP and Na^+ ions in NFMP calculated using Equation 2.7. Applied current pulses 17 mA g^{-1} for LFMP and 7.7 mA g^{-1} for NFMP. Potential ranges 2.0–4.6 V vs. Li+/Li for LFMP and 1.8–4.3 V vs. Na+/Na for NFMP.*[113]

The same panels show the overlap of the quasi-equilibrium potential profiles (E_0) during charge (dark red and dark blue) and discharge (light red and light blue) for LFMP and NFMP, respectively, after relaxation. The trend of E_0 vs. x (exchanged lithium or sodium degree in $A_{1-x}Fe_{0.6}Mn_{0.4}PO_4$ olivine, with A = Li or Na) reveals a reversible titration extended up to x = 0.69 for LFMP (**Figure 2.19(c)**) and to x = 0.5 for NFMP (**Figure 2.19(d)**) under quasi-equilibrium conditions. The difference of the maximum value of x in NFMP and LFMP is ascribed to a more relevant strain in the olivine structure induced by the bigger Na^+ compared with Li^+, which is reflected into a slower ion diffusion kinetics, mostly because of the abovementioned Jahn-Teller distortion promoted by Mn.[99,116] It is worth noting that the quasi-equilibrium potential hysteresis for NFMP (**Figure 2.19(d)**) is around 120 mV, which is more than 4 times larger than that of LFMP (*i.e.* 30 mV, **Figure 2.19(c)**) at the same alkali ion content. This behavior, already observed for LFP and NFP, is related with a more severe phase transitions stress due to the larger volume change upon sodiation/de-sodiation of the olivine, compared with lithiation/de-lithiation.[334] The Li^+ or Na^+ diffusion coefficients, D_{GITT}, ($cm^2\ s^{-1}$), are obtained using the data of **Figure 2.19** and applying **Equation 2.7**:[336]

$$D_{GITT} = \frac{4}{\pi}\left[\frac{I^0 V_M}{AF}\frac{dE/dx}{dE/dt^{1/2}}\right]^2, \quad t \ll \tau \qquad \textbf{(2.7)}$$

where I^0 (A) is the applied current, V_M is the olivine molar volume (44.53 $cm^3\ mol^{-1}$ for LFMP and 48.21 $cm^3\ mol^{-1}$ for NFMP), A is the electrode geometric area (0.785 cm^2), F is the Faraday constant (96485 C mol^{-1}), and τ is the diffusion time (s). dE/dx is determined by derivation of the titration curves in **Figure 2.19(c, d)**. $dE/dt^{1/2}$ is obtained by linear fit of E vs. $t^{1/2}$ related to each current pulse (with $t << \tau$). **Figure 2.19(e)** represents the D_{GITT} during de-lithiation/lithiation and de-sodiation/sodiation as function of x for LFMP (red) and NFMP (blue). The results evidence the typical trend observed for mixed olivines with a general decrease of D_{GITT} for the de-lithiated/de-sodiated phases at high x,[278] with higher values for LFMP compared with NFMP. This suggests lower mobility of Na^+ than Li^+, as already observed for D_{CV} in **Figure 2.17**. In detail, **Figure 2.19(e)** reveals an initial increase of D_{GITT} by charge to a maximum value of ~ 10^{-9} $cm^2\ s^{-1}$ at x = 0.42 for LFMP and ~ 10^{-11} $cm^2\ s^{-1}$ at x = 0.29 for NFMP, and its subsequent, relevant decrease upon further increasing x to a minimum value of ~ 10^{-13} $cm^2\ s^{-1}$ for LFMP and ~ 10^{-14} $cm^2\ s^{-1}$ for NFMP.

It is worth noting that the diffusion coefficients during the discharge are smaller than the values during the charge, likely due to the insulating character of de-lithiated/de-sodiated olivine. Previous studies indicated much lower D for LFP and NFP compared with LFMP and NFMP, with values ranging from 10^{-17} to 10^{-13} $cm^2\ s^{-1}$ for lithium and from 10^{-19} to 10^{-15} $cm^2\ s^{-1}$ for sodium, depending on the x value as well as on the experimental setup.[322,334,337,338] This discrepancy may be ascribed to the different Li^+/Na^+ (de-)insertion mechanism in LFMP/NFMP compared with LFP/NFP, where the

former foresees two or three interconnected *solid-solution-like* working regions, while the latter has a defined flat plateau.[101,115,116,278] Nevertheless, an intrinsic experimental error of the Li^+ and Na^+ diffusion coefficient determination from GITT data for two-phase materials, ascribed to the solid-solution assumption proposed by Weppner and Huggins, could not be herein excluded.[336] In particular, the Weppner model has been described to provide *D* values for LFP and NFP of about 3 orders of magnitude lower in the two-phase region compared with the single-phase one.[337,338] This difference can be ascribed in part to an intrinsic experimental error on Li^+/Na^+ diffusion coefficient determination, triggered by the characteristic reaction mechanism of the olivines. It is worth mentioning that additional experimental parameters could affect the results of GITT measurements,[339] such as time and number of the current steps, the relaxation time, as well as the electrode film features (*i.e.* uncertainty of surface area, reaction-limitation, inter-particle composition differences, finite size and non-planar geometry). On the other hand, systematic errors derived from composition-dependent overpotentials can be limited by minimizing the current magnitude to support the assumption of semi-infinite behavior also for finite-size spherical particles. In fact, this assumption in planar systems is suitable for very short diffusion time, such as the value herein adopted ($\tau < 0.25$) which is optimized to achieve reliable D_{GITT} value.[339] In this respect, computational studies indicate that the underestimation of the diffusion coefficients in electrodes with flat-shaped potential using GITT can be strongly limited by lowering the thickness to get a more accurate D_{GITT}.[340] Overall, the D_{GITT} values obtained in **Figure 2.19(e)** for LFMP and NFMP are comparable with the ones obtained by CV (**Figure 2.17**), and with those achieved by GITT in other studies focusing on lithium diffusion in mixed olivines.[278] Despite slower ion transport and diffusion leading to a sluggish kinetics, the measurements suggest that the NFMP cathode achieved by electrochemical conversion and the pristine LFMP have a surprisingly similar transport mechanism.

To further understand and compare the interfacial and charge-transfer kinetics of LFMP and NFMP, SPEIS experiments have been performed by running impedance measurements at different SoC every 40 mV, upon full de-lithiation/de-sodiation and subsequent lithiation/sodiation, and the related DRT functions have been calculated (see **Section 1.6** for further details on DRT).[189,265,341] The measurements have been acquired during the 3rd cycle to minimize any bias arising from stabilizations of the interphases or activation of the materials, and a two-electrode coin cell setup has been used to avoid possible inductive contributions given by the reference electrode. The Nyquist plots obtained upon LFMP (de-)lithiation and NFMP (de-)sodiation are reported in **Figure 2.20**. The figure displays the presence of four main features: (i) an intercept to the real axis accounting for the electrolyte resistance; (ii) a high-frequency semicircle accounting for particle-particle and particle-current collector contact resistance, with the associated double layer capacitance; (iii) a medium/low-

frequency semicircle accounting for the interphase and charge-transfer sum resistance of both LFMP/NFMP and Li/Na metal electrodes, coupled to the related capacitances due to surface charge accumulation; (iv) a low-frequency line accounting for solid-state diffusion, changing shape from reflective to transmissive conditions according to the changes in the SoC.[342] NFMP spectra (**Figure 2.20(c, d)**) present higher impedance values with respect to LFMP ones (**Figure 2.20(a, b)**) suggesting a more resistive interphase for the Na-cell compared with the Li one.

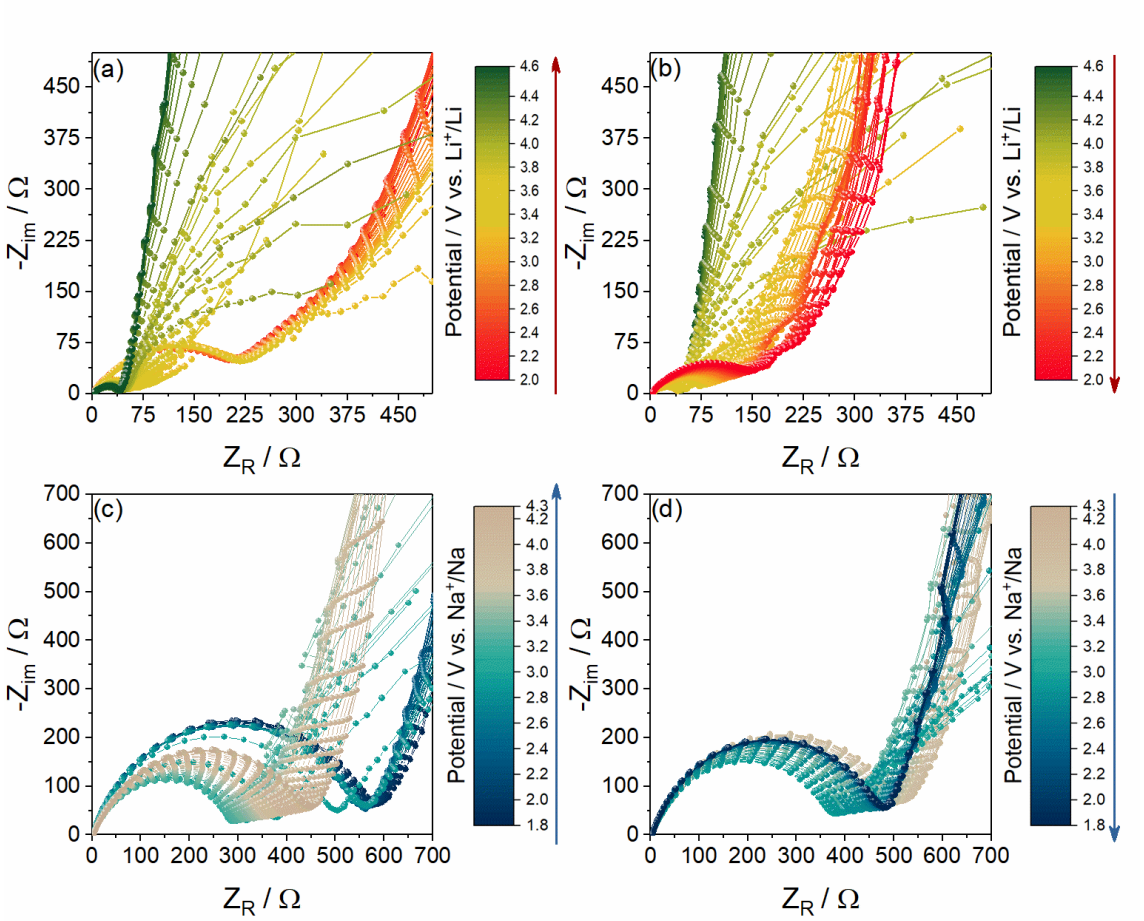

Figure 2.20: *Nyquist plots obtained during* ***(a)*** *de-lithiation,* ***(b)*** *lithiation* ***(c)*** *de-sodiation and* ***(d)*** *sodiation from the SPEIS analyses of LFMP and NFMP electrodes performed at the 3rd cycle. EIS collected every about 40 mV. Potential ranges 2.0 – 4.6 V vs. Li+/Li for LFMP and 1.8 – 4.3 V vs. Na+/Na for NFMP. Frequency range 200 kHz – 10 mHz; alternate voltage signal 10 mV. Adapted from [113].*

As the calculation of DRT from EIS requires the solution of an ill-posed problem, Tikhonov regularization has been here employed.[272] Specifically, the boundary conditions require the impedance spectra to converge towards the real axis, where the angular frequency ω tends to zero; however, this requirement is usually not encountered in typical EIS spectra of intercalation electrodes, as the low-frequency diffusion region diverges from the real axis. As a consequence, a pre-processing step for the Nyquist plots is required.[262,272] Hence, the raw spectra from **Figure 2.20** have been modeled, as a first approximation, to the equivalent circuit $R_e(R_iQ_i)WQ_W$, with particular attention to

the fitting of the low-frequency region.[273,274] In the adopted model, R_e represents the electrolyte resistance (high-frequency intercept with the real axis), in series with three resistances and constant phase elements in parallel, $(R_iQ_i) = (R_1Q_1)(R_2Q_2)(R_3Q_3)$, and a Warburg element with a constant phase element (WQ_W). The above elements respectively account for the contact resistance (R_{cont}) between electrode particles and current collector (high-frequency semicircle), the interphase associated with the SEI/SPI, the charge transfer of the electrodes (medium- and low-frequency semicircles), and the solid-state diffusion (low-frequency tilted line). The fitted low-frequency region, as simulated by the WQ_W elements, has then been subtracted from the overall impedance to obtain the convergence of the spectra to the real axis. Interestingly, the Nyquist plots obtained after removal of the diffusive part (modeled by the equivalent circuit $R_e(R_1Q_1)(R_2Q_2)(R_3Q_3)$) for LFMP in lithium cell (**Figure 2.21(a, c)**) show the appearance of a third semicircle in the low-frequency range, previously not visible due to the partial overlapping by the Warburg diffusion line. The fitted spectra on **Figure 2.21(a)** display upon de-lithiation relatively small changes of the intercept with the real axis and the high-frequency semicircle. The limited variations of R_e and $R_1 = R_{cont}$ confirm the stability of the electrolyte and of the electrode slurry, respectively. On the other hand, a progressive decrease in the diameter of the semicircles at medium- and high-frequencies (R_2 and R_3) is encountered by lithium extraction up to 3.5 V, with a slight increase after 4.2 V. This SoC-dependent behavior is generally consistent with charge-transfer processes occurring at the electrodes' interfaces.[343,344] The related DRT function in **Figure 2.21(b)** deconvolutes the different semicircles into peaks according to their relaxation frequencies,[272] while the small hump centered at $f = 10^{-2}$ Hz (labeled as *) is an artifact due to the removal of the Warburg diffusion. The small peak labeled as *P*1 in the high-frequency range (*i.e.* 10^3 Hz < f < 10^4 Hz) shows slight changes in intensity and frequency throughout the whole cycle, and is therefore consistent with the contribution of the contact resistance (R_{cont}). The peak labeled as *P*2 at high-to-medium frequencies (10^2 Hz < f < 10^3 Hz) shifts to higher frequencies upon de-lithiation and decreases in intensity. Lastly, the *P*3 peak in the low-frequency region (10^{-1} Hz < f < 10^1 Hz) undergoes as initial remarkable decrease in intensity while shifting to higher frequencies (from f = 1 Hz to f = 10 Hz), and then moves back to low frequencies with a slight increase in intensity at the end of the charge. Considering the frequency ranges of *P*2 (R_2 in the equivalent circuit) and *P*3 (R_3 in the equivalent circuit), the two peaks can be associated with the polarizations related to the Li metal counter electrode and the charge-transfer resistance of LFMP cathode, respectively, as already reported in literature for LFP.[344]

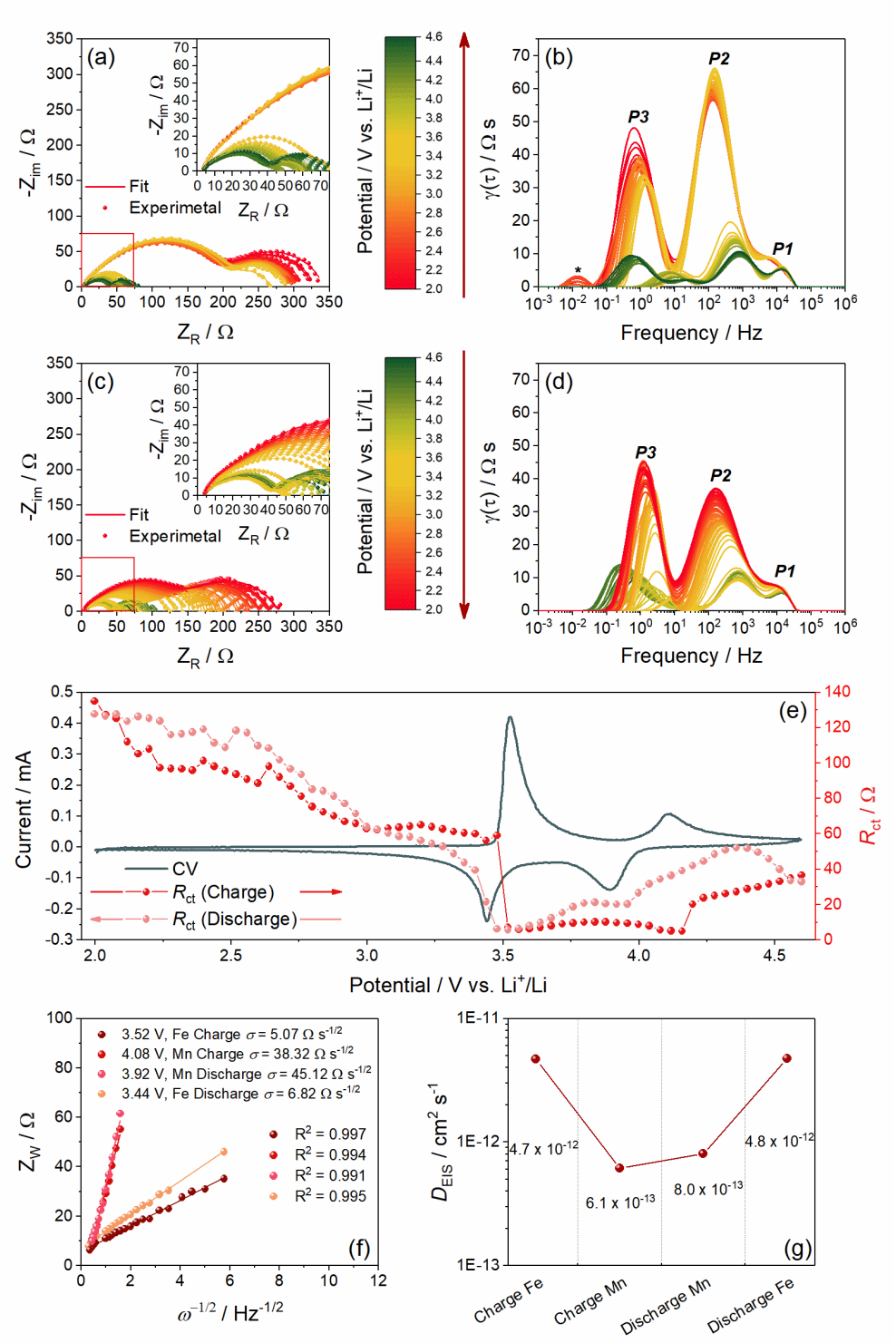

Figure 2.21: *SPEIS analysis of LFMP electrode in Li-cell at 25 °C. Nyquist plots after subtraction of the diffusive contribute and related DRT analyses in terms of γ-factor vs. x with associated peak indexing obtained during* ***(a, b)*** *de-lithiation and* ***(c, d)*** *lithiation process, respectively. Inset in* ***(a)*** *and* ***(c)****: magnification of the high-frequency region.* ***(e)*** *Trend of R_{ct} (right axis) and current (left axis) as a function of electrode potential during CV.* ***(f)*** *Plots of Z_W vs. $x^{-1/2}$ with related linear fits and corresponding R^2 achieved for determination of σ.* ***(g)*** *Values of D_{EIS} determined by using Equation 2.8 for the Nyquist plots of Figure 2.20(a, b) at indicated potentials. EIS collected during the 3rd cycle with sampling interval of about 40 mV, within the 2.0–4.6 V vs. Li^+/Li potential range, in the 200 kHz–10 mHz frequency range and with an alternating voltage signal of 10 mV.*[113]

To unambiguously assign these SoC-dependent peaks to the actual interfacial processes, the DRT functions for symmetrical Li|Li and LFMP|LFMP cells at different temperatures are reported in **Figure 2.22(a)** alongside with that of Li|LFMP half-cell obtained at 2.0 V (*i.e.* lithiated state). In addition, the related sum of square residuals (SSR) vs. λ plots (**Figure 2.22(b)**) and the Arrhenius plots of the areal specific resistance (ASR) (**Figure 2.22(c)**) are used to find out the correlation between resistances and temperature.[345] Indeed, the DRT of the symmetrical cells are calculated to deconvolute the contribution of lithium counter electrode and LFMP. From frequency of the peak and its shifts at different temperatures it is possible to isolate the contribution of charge transfer resistance of the LFMP active material from the other contributions, as reported by peak indexing of **Figure 2.22(a)**. The calculation of the DRT functions is performed according to the optimal λ factor as shown in **Figure 2.22(b)**. To further confirm the peak indexing for the different contributions, in **Figure 2.22(c)** the Arrhenius plots for all the symmetrical cell processes, with the related coefficients of determination, are provided.

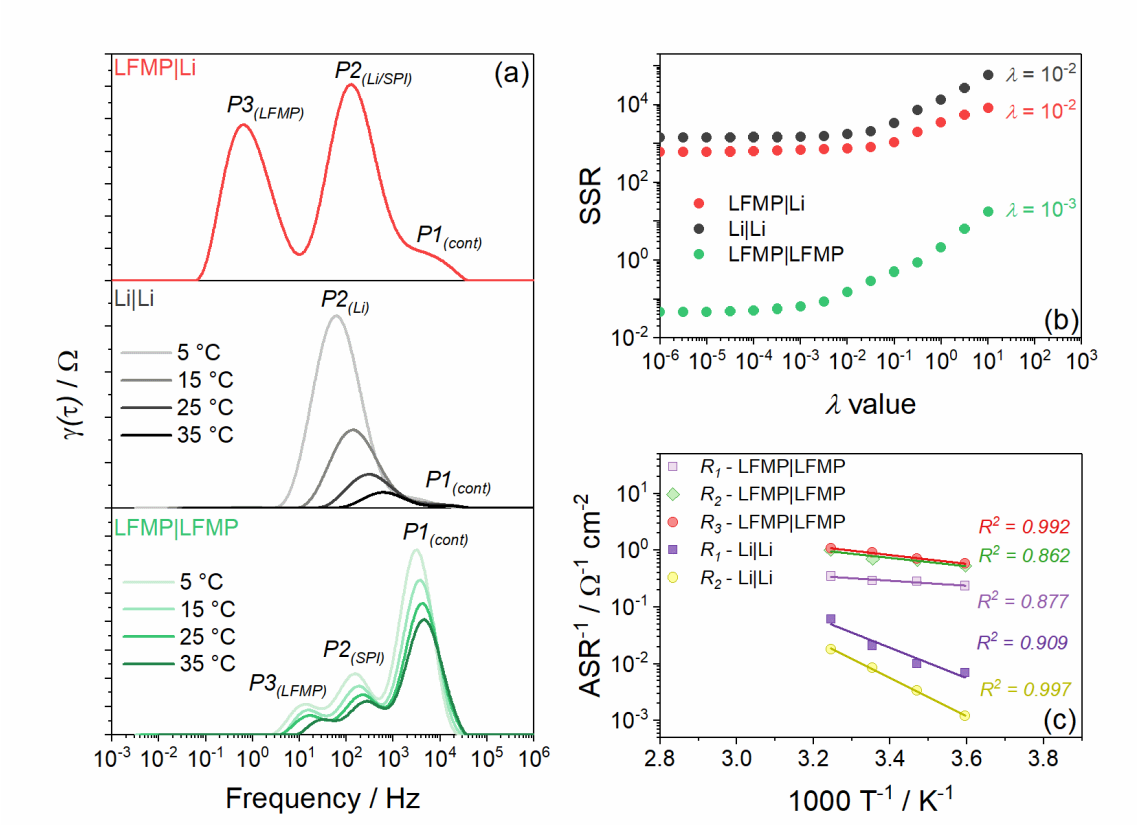

Figure 2.22: ***(a)*** *DRT function with associated peak indexing, and* ***(b)*** *SSR vs. λ plot for Li|LFMP half-cell (red), Li|Li symmetrical cell (grey), and LFMP|LFMP symmetrical cell (green). DRT for Li|Li and LFMP|LFMP cells were obtained at 5 °C, 10 °C, 15 °C, and 25 °C.* ***(c)*** *Arrhenius plot of the ASR values for the symmetrical cells processes with associated coefficient of determination (R^2).*[113]

In agreement with the previous assignment, the *P*1 peak (R_1 resistance) at high frequencies identified in both symmetrical cells is attributed to particle-particle and particle-current collector contact, since

the related resistance ($R_1 = R_{cont}$) displays a linear dependance on the temperature with low coefficient of determination ($R^2 < 0.91$). The two symmetrical cells also exhibit *P*2 peak (R_2 resistance) at medium frequencies, while the related resistance shows a satisfactory linear dependence on the temperature only in the Li|Li one ($R^2 > 0.99$). This trend suggests that *P*2 in the Li|LFMP half-cells includes contributions from the cathodes SPI and the Li counter electrode, with the latter being predominant ($R_2 = R_{Li}$).[343] Instead, the *P*3 peak (R_3 resistance) in the low-frequency region is only observed for the LFMP|LFMP symmetrical cell, and the associated resistance changes linearly with the temperature by a relevant confidence ($R^2 > 0.99$), thus confirming the assignment of the semicircle at low frequencies to the charge-transfer resistance of the LFMP electrode ($R_3 = R_{ct}$).[344] The fitted Nyquist plots upon the lithiation process after removal of the diffusion line (**Figure 2.21(c)**) still display relatively limited changes of R_e and R_{cont}, while the medium- and low-frequency semicircles (R_{Li} and R_{ct}) show a decrease in diameter upon lithium insertion up to 3.5 V and a progressive increase until reaching the lower cut-off. The related DRT functions (**Figure 2.21(d)**) reveal polarizations deconvoluted according to their different relaxation frequencies.[272] The data indicate a *P*1 (R_{cont}) at high frequencies with slight intensity and frequency modifications, while *P*2 (R_{Li}) and *P*3 (R_{ct}) display an almost opposite trend as compared to the de-lithiation process. During the initial stages of the test *P*2 slightly shifts to lower frequencies and increases in intensity, while *P*3 shifts to higher frequencies from $f \sim 1$ Hz to $f \sim 10$ Hz and slightly decreases in intensity. In the final part of the discharge process, *P*2 and *P*3 strongly increase in intensity and reach almost the same frequency as for the initial state at 2.0 V vs. Li^+/Li already observed in **Figure 2.21(b)**.[344] The polarization associated with the charge-transfer of LFMP (*i.e.* R_{ct} in the equivalent circuit and the related *P*3 in the DRT function) is reported as a function of the SoC during the voltammetry cycle in **Figure 2.21(e)**. Interestingly, during the anodic scan R_{ct} gradually decreases from ~ 140 to ~ 60 Ω, suddenly drops to ~ 5 Ω at about 3.5 V as de-lithiation begins, holds this low resistance until ~ 4.2 V where the oxidation of Fe^{2+} and Mn^{2+} ends yielding to large part of the cell capacity, and finally raises to ~ 40 Ω gradually until 4.6V. Moreover, the related *P*3 peak from the DRT functions shifts to higher frequencies, thus suggesting the enhancement of the charge transfer kinetics promoted by lithium extraction from 3.5 to 4.2 V.[99] During the reverse cathodic scan, the R_{ct} shows an initial fluctuation from ~ 35 to ~ 55 Ω and back to ~ 35 Ω upon lithium insertion from 4.6 to 4.2 V, and a subsequent decrease to ~ 20 Ω at 3.9 V and to ~ 5 Ω at 3.5V upon reduction of Mn^{3+} and Fe^{3+}, while the related *P*3 peak increases in frequency as the charge-transfer kinetics improve. Further reduction to 3.3 V leads to a rapid increase of R_{ct} from ~ 5 to ~ 50 Ω, and a gradual rise to ~ 130 Ω until 2.0 V where the scan ends. To further evaluate this behavior, the Li^+ diffusion coefficient in LFMP is achieved using the Warburg coefficient (σ), which is calculated as the slope of the linear plots in **Figure 2.21(f)** of Warburg impedance (Z_W) vs. the

square root of the angular frequency ($\omega^{-1/2}$), using the impedance data taken from **Figure 2.20(a, b)** at potentials associated with the redox couples Fe^{3+}/Fe^{2+} (3.52 and 3.44 V vs. Li^+/Li) and Mn^{3+}/Mn^{2+} (4.08 and 3.92 V vs. Li^+/Li). Therefore, the Li^+ (or Na^+) diffusion coefficient, D_{EIS} ($cm^2\ s^{-1}$), is calculated using **Equation 2.8**:[346]

$$D_{EIS} = \frac{1}{2}\left(\frac{RT}{z^2F^2AC\sigma}\right)^2 \quad \text{with} \quad Z_W = \sigma\omega^{-1/2} \qquad \textbf{(2.8)}$$

Where R is the gas constant (8.314 J K^{-1} mol^{-1}), T is the temperature (K), z = 1 is the number of exchanged electrons, F is the Faraday constant (96485 C mol^{-1}) C is the Li^+ (or Na^+) concentration within the olivine lattice (mol cm^{-3}), and A is the electrode geometric area (0.785 cm^2). The resulting D_{EIS} trend shown in **Figure 2.21(g)** suggests a faster ion transport within the olivine lattice in correspondence with the Fe^{3+}/Fe^{2+} redox process (~ 5 x 10^{-12} $cm^2\ s^{-1}$) than the Mn^{3+}/Mn^{2+} one (6-8 x 10^{-13} $cm^2\ s^{-1}$), as already observed for DCV in **Figure 2.17(c)**. In addition, the D_{EIS} values are smaller than D_{CV} and D_{GITT} (**Figure 2.19(e)**), *i.e.* ~ 10^{-12} $cm^2\ s^{-1}$ compared to 10^{-10} $cm^2\ s^{-1}$ at the same SoC. These differences could be ascribed to the use of different electrochemical techniques (*i.e.* different electrochemical equilibrium conditions depending on the applied signal), which may lead to different actual solid-state diffusion lengths, as mentioned in literature.[278] In detail, the ion diffusion coefficients reflect in fact the different electrochemical equilibrium conditions foreseen by the various electrochemical techniques. Hence, the ion transport is a consequence of the formation of a concentration gradient on the surface layer, which is achieved within potentiostatic conditions according to Nernst equation in CV and EIS.[335,336,339] Therefore, D_{CV} and D_{EIS} could be representative for a theoretical and sensitive setup, which may however differ from the practical operation of the cell. Instead, GITT is a galvanostatic technique, and the related results could be more easily associated with the effective cyclic behavior of the material, as the (de-)insertion processes proceed in the battery. Hence, D_{GITT} may be considered the most representative method for cells under operating conditions.[339,340] Nevertheless, all the diffusion coefficients show comparable trends, especially when comparing D_{EIS} and D_{CV}, thus suggesting the accuracy and reliability of the electrochemical methods adopted herein. Accordingly, the results point out a relevant reversibility of the processes within the mixed olivine, with a relatively fast charge-transfer upon lithiation/de-lithiation.

The SPEIS protocol illustrated for LFMP is repeated hereafter to investigate the interfacial and Na^+ transport properties of NFMP, and the results are reported in **Figure 2.23**, while the Nyquist plots obtained upon the electrochemical process of NFMP in Na-cell are depicted in **Figure 2.20(c, d)**, with analogue features as compared to LFMP.

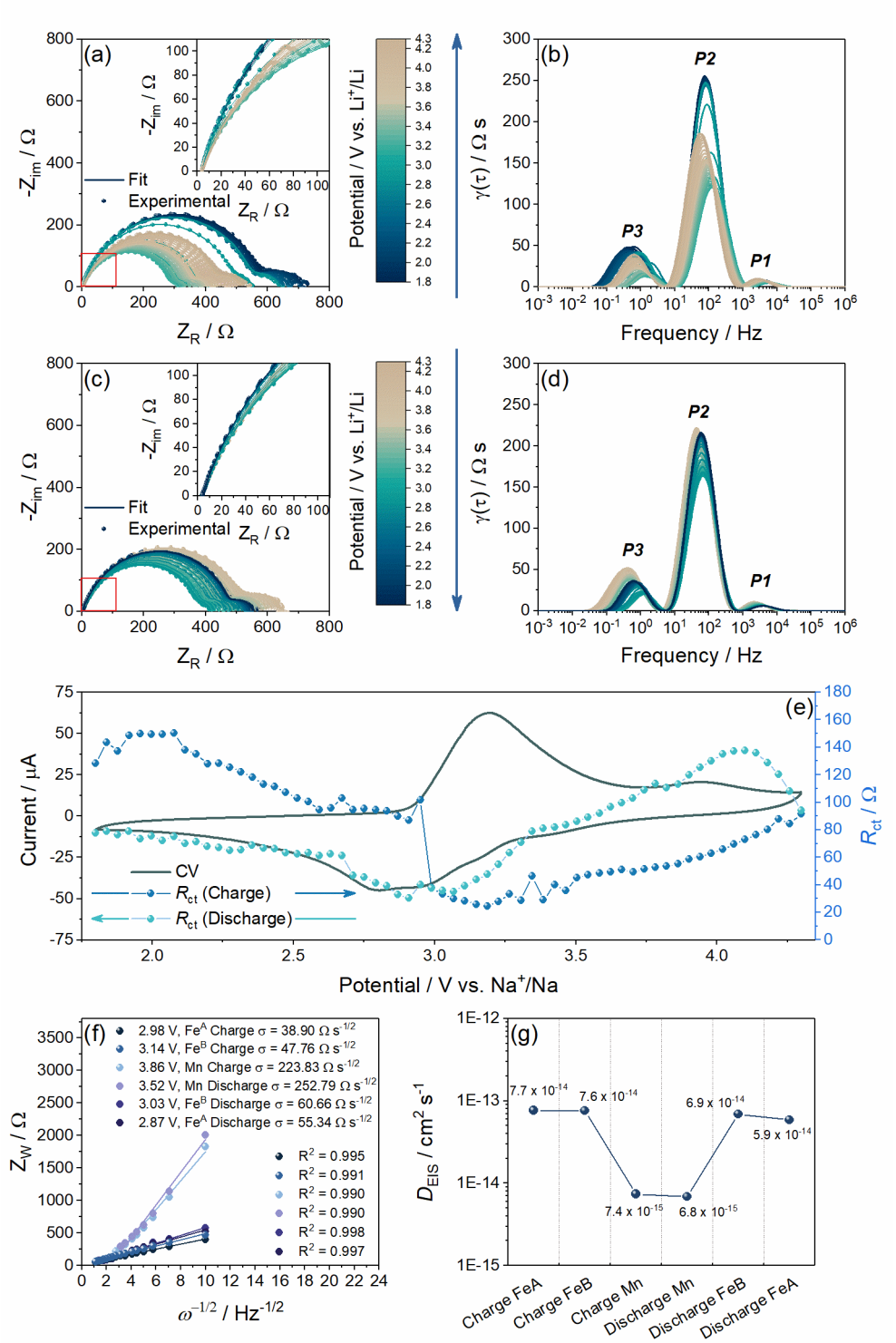

Figure 2.23: *SPEIS analysis of NFMP electrode in Na-cell at 25 °C. Nyquist plots after subtraction of the diffusive contribute and related DRT analyses in terms of γ-factor vs. x with associated peak indexing obtained during* ***(a, b)*** *de-sodiation and* ***(c, d)*** *sodiation process, respectively. Inset in* ***(a)*** *and* ***(c)****: magnification of the high-frequency region.* ***(e)*** *Trend of R_{ct} (right axis) and current (left axis) as a function of electrode potential during CV.* ***(f)*** *Plots of Z_W vs. $x^{-1/2}$ with related linear fits and corresponding R^2 achieved for determination of σ.* ***(g)*** *Values of D_{EIS} determined by using Equation 2.8 for the Nyquist plots of Figure 2.20(c, d) at indicated potentials. EIS collected during the 3rd cycle with sampling interval of about 40 mV, within the 1.8–4.4 V vs. Na^+/Na potential range, in the 200 kHz–10 mHz frequency range and with an alternating voltage signal of 10 mV.*[113]

After pre-processing, with related WQ_W circuit element removal, the fitted spectra upon de-sodiation in **Figure 2.23(a)** (modeled by the equivalent circuit $R_e(R_1Q_1)(R_2Q_2)(R_3Q_3)$) show relatively small changes of R_e and R_1 (equal to R_{cont}), progressive decrease of R_2 and R_3 until 3.0 V, and slight increase after 3.5 V. The sodiation process (**Figure 2.23(c)**) leads to less remarked change of R_2 and R_3, with a decrease upon sodium insertion up to 2.7 V and a subsequent increase until reaching the lower cut-off, while R_e and R_{cont} show limited modifications. The DRT analysis, with deconvolution of the various contributions to polarizations in three main peaks, is reported in **Figure 2.23(b)** during de-sodiation and in **Figure 2.23(d)** during sodiation of NFMP in Na-cell, while the peak assignment is verified by the analysis of the symmetrical Na|Na and NFMP|NFMP cells in **Figure 2.24**, according to the same method adopted for LFMP. Indeed, the figure shows the DRT function (panel **(a)**) with the related SSR vs. λ plot (panel **(b)**). DRT for the symmetrical cells is calculated to deconvolute the contribution of sodium counter electrode and NFMP. The calculation of DRT functions is performed according to the optimal λ factor as shown in **Figure 2.24(b)**. To further confirm the peak indexing for the different contributions, the Arrhenius plot of the ASR values obtained for all the symmetrical cell processes is provided in **Figure 2.24(c)**. As expected, only the fit for R_3 resistance of symmetrical NFMP|NFMP cell (corresponding to $P3$ peak), and for R_2 resistance of the symmetrical Na|Na cell (corresponding to $P2$ peak) presents a linear trend with $R^2 > 0.99$, thus confirming that the associated process is related with charge transfer.[345]

During de-sodiation, **Figure 2.23(b)** evidences that the $P1$ peak related to R_{cont} slightly changes, with frequency values close to LFMP, instead $P2$ (polarization of Na metal, $R_2 = R_{Na}$) $P3$ (charge-transfer resistance of NFMP, $R_3 = R_{ct}$) initially shift to higher frequencies and decrease in intensity, and then move back to the initial frequencies and gradually increase in intensity.[343,344] The DRT functions analysis related with the subsequent sodiation process (**Figure 2.23(d)**) exhibits limited changes of $P1$, and $P2$ and $P3$ with initial intensity decrease and shift to higher frequency, indicating a faster charge-transfer, and subsequent intensity increase while moving back almost to the initial frequency. Interestingly, the frequency shift of $P2/R_{Na}$ and $P3/R_{ct}$ in NFMP upon (de-)sodiation are much less pronounced and the corresponding frequencies reach lower values as compared to those of LFMP. This behavior indicates that the higher ionic radius of Na^+ hinders the charge-transfer kinetics and avoids the shift to the higher frequencies of the processes.[334]

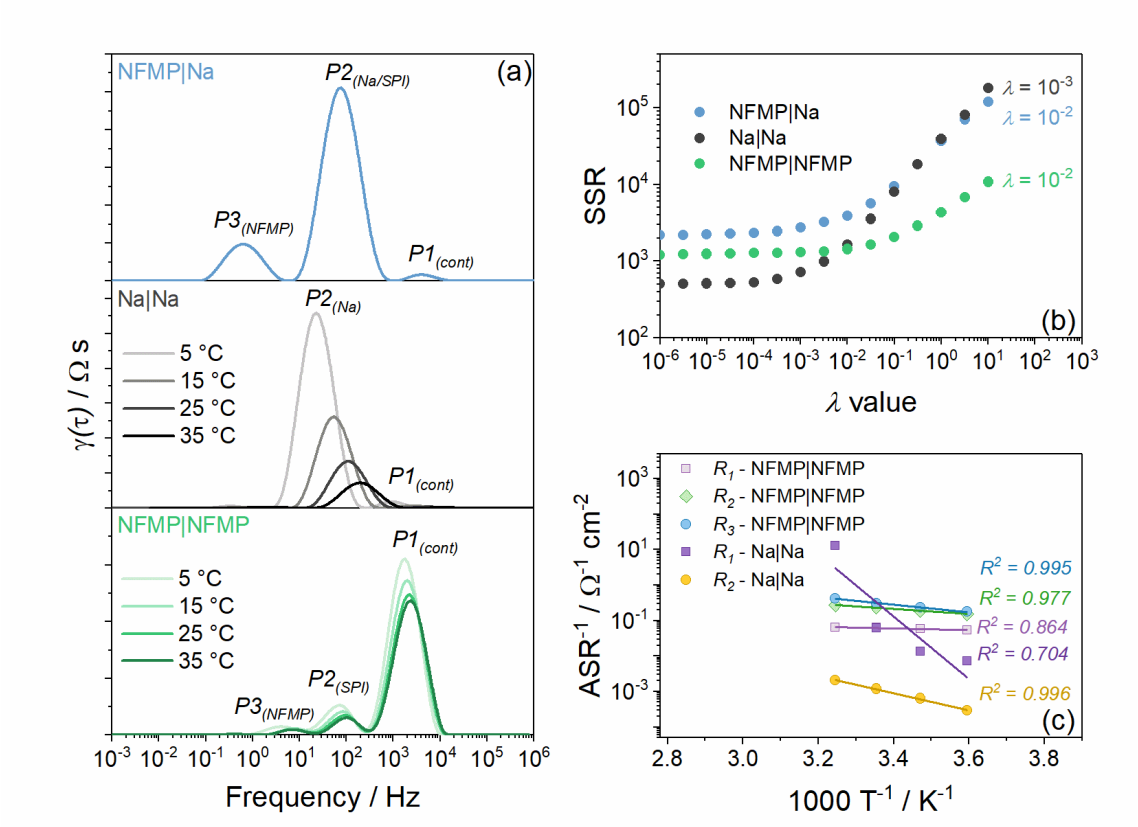

Figure 2.24: ***(a)*** *DRT function with associated peak indexing, and* ***(b)*** *SSR vs. λ plot for Na|NFMP half-cell (blue), Na|Na symmetrical cell (grey), and NFMP|NFMP symmetrical cell (green). DRT for Na|Na and NFMP|NFMP cells were obtained at 5 °C, 10 °C, 15 °C, and 25 °C.* ***(c)*** *Arrhenius plot of the ASR values for the symmetrical cells processes with associated coefficient of determination (R^2).*[113]

Summarizing, the above discussed data suggest once again a more challenging interphase with higher resistance and a limited ion diffusion in NFMP compared with LFMP, mainly due to kinetic issues associated with the larger volume of sodium than lithium, and with the resulting structural frictions within the olivine framework. **Figure 2.23(e)** overlaps R_{ct} of NFMP with the cyclic voltammetry in Na-cell; remarkably NFMP reveals an analogue trend to LFMP, however with a different feature due to the different alkali ion. Indeed, the Mn redox activity appears weakened in NFMP by the increased Jahn-Teller effect,[115,116] and the resistance variation within the potential range of the redox activities is less pronounced. Hence, R_{ct} progressively decreases from ~ 150 to ~ 100 Ω upon charging from 1.8 to 2.9 V, rapidly decreases to ~ 40 Ω at about 3.0 V, maintains almost the same value until ~ 3.5 V, and progressively increases to ~ 100 Ω at the charge cut-off (4.3 V). During the subsequent sodiation, the R_{ct} value initially increases to ~ 140 Ω by discharging until 4 V, then start decreasing gradually until 3.4 V to reach ~ 90 Ω and more rapidly until 3.1 V to ~ 45 Ω, slightly fluctuates from 3 to 2.7 V to a value of ~ 60 Ω, and the increases and holds a value of ~ 70 Ω from 2.6 V to the end of the discharge at 1.8 V. Despite less evident changes compared to LFMP, the trend of R_{ct} described above is consistent with the activation of the processes related to the Mn^{3+}/Mn^{2+} and Fe^{3+}/Fe^{2+} couples

at potentials corresponding to the related peaks in the voltammetry cycle. The Na^+ diffusion coefficient in NFMP is calculated according to the Warburg equation (**Equation 2.8**),[346] using σ achieved from the plots of Z_W vs. $\omega^{-1/2}$ (**Figure 2.23(f)**) from impedance spectra at selected potentials (**Figure 2.20(c, d)**), corresponding to the redox processes associated with Fe (Fe^A at 2.98 and 2.87 V vs. Na^+/Na, and Fe^B at 3.14 and 3.03 V vs. Na^+/Na) and Mn (at 3.86 and 3.52 V vs. Na^+/Na). The D_{EIS} trend in **Figure 2.23(g)** remarks the higher transport properties within the olivine lattice for the Fe^{3+}/Fe^{2+} redox couple than the Mn^{3+}/Mn^{2+} one, which is a trend in line with the data achieved by CV and GITT, however with lower values at comparable SoC, *i.e.* of about 10^{-14} cm^2 s^{-1} for D_{EIS} as compared to 10^{-12} cm^2 s^{-1} for D_{CV} and D_{GITT} (see **Figures 2.17(d)** and **2.19(e)**, respectively).

The results obtained from the interfacial analysis in terms of R_{ct} for the LFMP and NFMP mixed olivines display a similar behavior upon Li^+ or Na^+ (de-)insertion, despite the different reaction kinetics related to the characteristic ion mobility which, in general, favor lithium with respect to sodium.[115,278,334] Hence, the relevant Jahn-Teller distortion promoted by Mn can hinder the transport of the voluminous sodium ion. On the other hand, the decrease of the diffusion coefficient in Mn sites is principally ascribed to the lower ionic conductivity of the de-lithiated/de-sodiated phase of the olivine compared with the pristine one, particularly over the extraction of more than a half of the overall Li^+/Na^+ occurring upon Fe^{3+}/Fe^{2+} redox process.[99]

2.4 Operando X-ray Absorption Study of Na Insertion Mechanism in $NaFe_{0.6}Mn_{0.4}PO_4$ Structure

To deeply investigate the structural dynamics of the NFMP olivine cathode and to facilitate the comprehension of its behavior in Na-cell, X-ray absorption spectroscopy (XAS) has been employed. Particularly, the analysis conducted at the Fe and Mn K-edges could lead to a better understanding of the active material oxidation process and local structural rearrangements, essential for the comprehension of the behavior of single redox couples, as well as of the electronic structure of each element in the NFMP sample during the charge/discharge process.

Considering the few works in literature on sodium-based olivine cathodes,[116,347] and to better understand the behavior of redox couples under operative conditions, *operando* XAS measurements have been performed by using self-standing NFMP electrodes (NFMP_SS), obtained from the lithium analogues, on a Na|NFMP_SS cell. The various steps used for the preparation of LFMP self-standing electrodes (LFMP_SS) employed for the *operando* XAS analysis are summarized in **Figure 2.25** (see **Section 2.1** for further details).[293]

Figure 2.25: *Photographic images of LFMP_SS electrodes during casting procedure:* ***(a)*** *coating of a thin layer of CMC solution onto a copper foil;* ***(b)*** *coating of PVdF-based layer onto the dried CMC film;* ***(c-e)*** *immersion of the coating in water and subsequent dissolution of the CMC layer;* ***(f)*** *final LFMP_SS electrodes.*

Initially a thin layer of CMC was cast onto a Cu foil (panel **(a)**). After drying, a PVdF-based slurry (LFMP active material) was cast over the CMC layer (panel **(b)**) and dried until complete NMP evaporation. After that, the coating was immersed in water to dissolve the CMC layer until the complete detachment of the self-standing electrode from the current collector (panels **(c-e)**), which was subsequently dried to evaporate the excess of water to obtain the final LFMP_SS electrodes (panel **(f)**). This method has already been reported as a valuable choice to obtain suitable electrodes for application in *in-situ* or *operando* measurements.[293,348]

The above-described electrochemical conversion strategy from LFMP (see **Section 2.3**) has been used to achieve NFMP_SS electrodes for XAS measurements. Indeed, **Figure 2.26** reports the voltage profiles corresponding to the electrochemical de-lithiation of LFMP_SS (**Figure 2.26(a)**), performed at the constant current of C/15 (1C = 170 mA g^{-1}), and to the subsequent sodiation of recovered FMP electrode (**Figure 2.26(b)**), carried out at the constant current of C/25 (1C = 154 mA g^{-1}). The galvanostatic voltage profiles and cycling trend of the achieved NFMP_SS electrode are reported in (**Figure 2.26(c)**) and (**Figure 2.26(d)**), respectively. The voltage profiles of **Figure 2.26(a, b)** reflect the de-lithiation of LFMP to FMP and the subsequent sodiation to NFMP, presenting the expected shape described in **Section 2.3** (see discussion of **Figure 2.11(a)**). Particularly, the sodiation process (**Figure 2.26(b)**) is consistent with the solid-solution behavior at about 3.1 V vs. Na^+/Na associated to the Fe^{3+}/Fe^{2+} reduction, coupled with the low activity of the Mn at around 3.5 V vs. Na^+/Na, ascribed to the relevant Jahn-Teller effect and possible Na/Mn antisite mixing, in agreement with the results obtained for the conventional electrodes.[113,115,116] On the other hand, the voltage profiles of self-standing electrodes evidence a slightly higher polarization compared to the conventional ones, probably associated with the higher loading and hindered wettability of the self-standing configuration, despite the lower current rates adopted for the test.[348] Additionally, the electrochemical performance in Na-cell of the achieved NFMP_SS electrode is evaluated to confirm the stability of the self-standing electrodes.

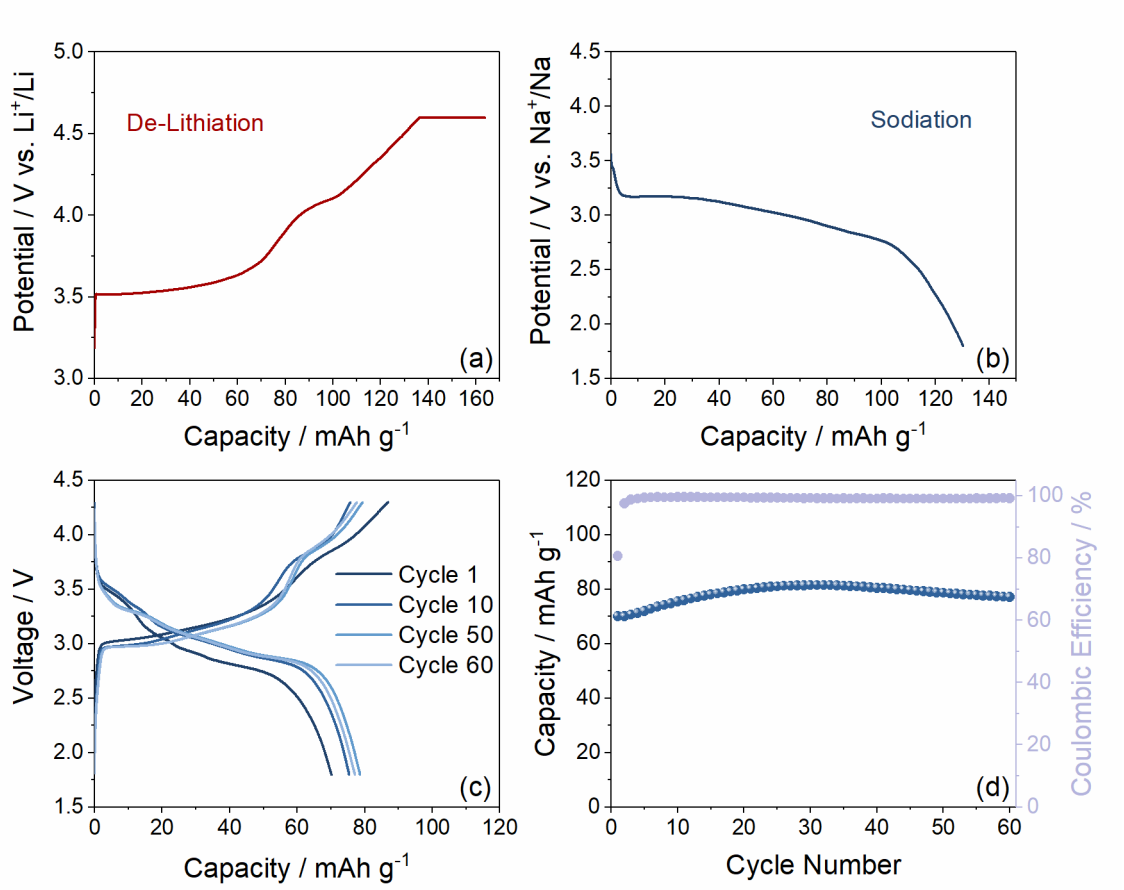

Figure 2.26: *Electrochemical conversion of LFMP_SS to NFMP_SS in terms of galvanostatic voltage profiles during* ***(a)*** *de-lithiation of LFMP_SS in Li-cell performed at C/15 (1C = 170 mA g^{-1}), and* ***(b)*** *during subsequent sodiation in Na-cell at C/25 (1C = 154 mA g^{-1}). Galvanostatic cycling performance of the Na|NFMP_SS cell at the constant current rate of C/20 in terms of* ***(c)*** *voltage profiles and* ***(d)*** *cycling trend with discharge capacity in the left-hand side y-axis and coulombic efficiency in the right-hand side y-axes. Voltage range 1.8 – 4.3 V. Room temperature (25 °C).*

Figure 2.26(c) reveals the expected shape of the voltage profiles characterized by a solid-state region with the three plateaus at average voltages of 3.0, 3.2, and 3.8 V, associated with Fe^{3+}/Fe^{2+} and Mn^{3+}/Mn^{2+} redox couples, respectively. Moreover, the NFMP_SS presents a capacity of about 70 mAh g^{-1} at the first cycle, which increases to reach a maximum value of 80 mAh g^{-1}, value in agreement with the results obtained from the rate capability of **Figure 2.14**. Furthermore, the related cycling trend in **Figure 2.26(d)** reveals a coulombic efficiency of about 80% at the first cycle, which increases and ranges between 98% and 100% during the subsequent ones, with the increase of capacity after the initial cycles probably ascribed to partial activation of the material, triggered by the improved electrode wetting, as already mentioned. Overall, NFMP_SS electrodes show suitable electrochemical features for application in *operando* measurements in terms of both electrode' loading and delivered capacity, comparable to the behavior obtained with conventional electrodes. Moreover, the promising results in the long cycling test could pave the way for the possible

implementation of self-standing configuration for application in new generation Li-ion or Na-ion cells avoiding the use of current collectors.[245]

Prior to *operando* XAS measurements, the *ex-situ* X-ray absorption near-edge spectroscopy (XANES) data have been acquired for LFMP, FMP, and NFMP electrodes coated on carbon paper in both transmission and fluorescence mode at the Mn and Fe K-edges. The data acquired in transmission mode were used to estimate the bulk Mn and Fe valency of the materials, as shown in **Figure 2.27**. As already discussed in literature for olivine cathodes, the Mn and Fe oxidation states can be calculated from the edge energy position.[349,350] For olivines the most accurate edge position is to be taken at the inflection point at a 0.9 fraction of the jump, thus each energy position corresponding to the 0.9 jump was measured. The obtained results were compared with literature data,[349] and the Mn valency was calculated via linear fit of the edge position. It is expected that the increase of a unit of oxidation at the Fe and Mn K-edges should result in a ~ 4 eV edge shift. In these regards, by performing a linear fit of the results on a previously studied olivine cathode,[349,350] a 3.76 eV/unit oxidation was obtained for Mn, with theoretical Mn^0 position at 6540.6 eV, while in the case of Fe a 3.55 eV/unit oxidation with Fe^0 at 7113.76 eV was obtained.

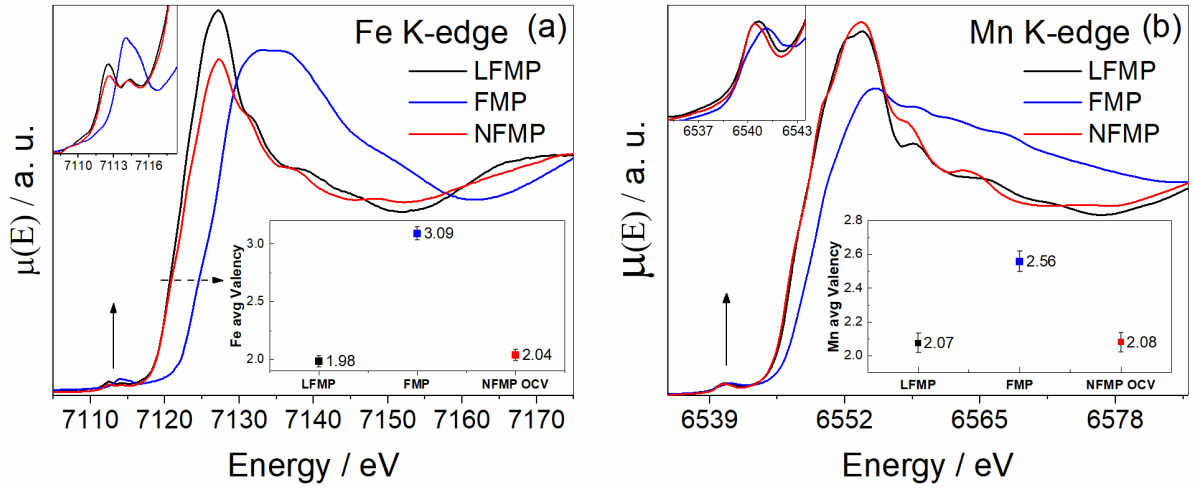

Figure 2.27: *XANES spectra at the* ***(a)*** *Fe and* ***(b)*** *Mn K-edges acquired in transmission mode on sealed LFMP, FMP, and NFMP electrodes. Insets report a zoom on the pre-edge region (top-left inset) and the calculated valencies (bottom-right inset).*

As shown in the figure, a clear blue shift of the absorption edge can be observed for the de-lithiated sample (blue line) in both Fe (panel **(a)**) and Mn (panel **(b)**) K-edges. The presence of a well-defined pre-edge peak at 6540.5 eV in **Figure 2.27(b)** can be attributed to the electric dipole-forbidden transition of Mn 1s electron to an unoccupied Mn 3d orbitals, which is partially allowed, and/or the 3d – 4p orbital mixing that arises from the non-centrosymmetric environment of the slightly distorted MnO_6 octahedra.[351] The pre-edge peak is also shifted and broadened after the de-lithiation, as

expected from the Mn oxidation. The average Mn valency obtained from the edge position is shown in the inset. Both lithiated and sodiated samples are within the experimental error of the theoretical Mn valency of +2 (LFMP = 2.04 ± 0.06, NFMP = 2.06 ± 0.05) while the +1.8 eV shift in the FMP edge position suggests an increase of Mn^{3+}, with an average Mn valency calculated of 2.64 ± 0.07. Hence, the final valency of Mn remains significantly lower than 3, result in excellent agreement with the de-lithiation process previously observed, confirming the sluggish Mn activity also noticed during cycling in Na-cell.[113] On the other hand, the much larger energy shift observed at the Fe k-edge (almost + 4 eV) correlates with the complete oxidation of the bulk iron ions in the sample to the +3 state upon de-lithiation (FMP). After sodiation, all iron completely reduces back to the initial Fe^{2+} state.

To further confirm the values of Mn valency, *ex-situ* XPS measurements were performed on LFMP, FMP, and NFMP electrodes, as well as on an additional de-sodiated NFMP sample (electrode recovered after charging the cell at 4.3 V), and the results are depicted in **Figure 2.28**.

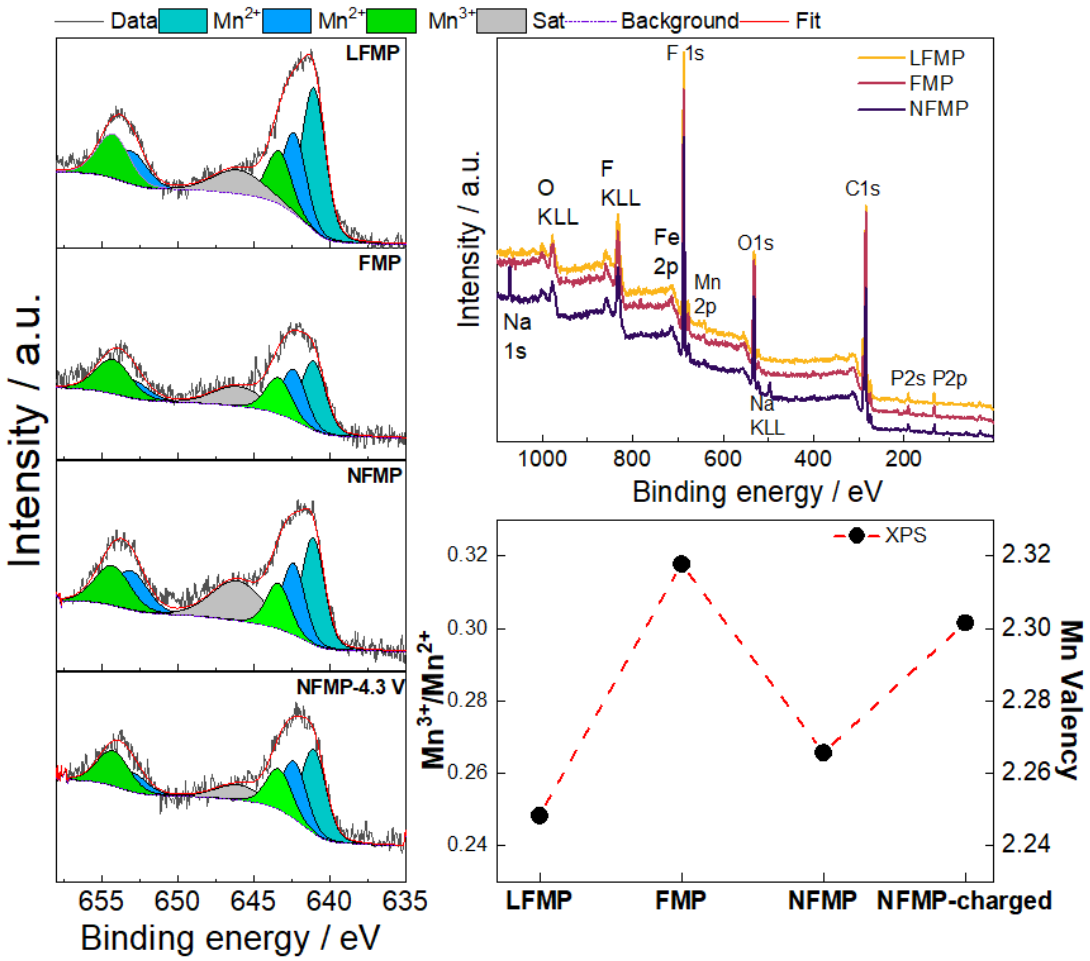

Figure 2.28:*Ex-situ XPS analysis for LFMP, FMP, NFMP, and charged NFMP. In particular: XPS Mn 2p fitted spectra (left), XPS wide scan (top right) and fitting results (bottom right).*

The XPS spectra reveal the strong presence of fluorine ascribed to the PVdF binder and residual traces of electrolyte on the electrodes. A very poor Mn and Fe 2p emission signal was detected, overwhelmed by the high intensity of the neighboring F 1s signal. Particularly for the iron case, the proximity of the F 1s to the Fe 2p distorts and hinders the Fe 2p spectra too much to be properly analyzed. All samples show the expected presence of P, while the presence of Na is confirmed in the sodiated sample. The Mn 2p were fitted following literature data based on mixed olivine electrodes,[352] with 2 Mn $2p^{3/2}$ components for Mn^{2+} at 641 and 641.2 eV (+ 1.2 eV) and a satellite peak at 646 eV (+ 5 eV). The Mn $2p^{1/2}$ components were fitted at a position 12 eV higher than the $2p^{3/2}$ counterparts. The Mn^{3+} component was fixed at + 2.3 eV respect to Mn^{2+}. Even though the change is not drastic, the modulation of the Mn^{3+} relative concentration is consistent with the already observed trend, increasing after de-lithiation (FMP) and subsequent de-sodiation (NFMP charged). These results further confirm the low reactivity of Mn, especially in the sodiated sample; indeed, the complete oxidation to Mn^{3+} probably requires higher voltages, as already evidenced in the previous section.[113]

Operando XAS measurements were performed by adopting the previously studied self-standing NFMP electrode in order to investigate the structural dynamics of the NFMP sample at different states of charge during one galvanostatic cycle as shown in **Figure 2.29**. In particular, the attention has been focused on the correlation with the redox activity of the material. The figure reports the *operando* XAS measurement carried out in fluorescence mode at different state of charge (SoC) on a modified coin cell with a Kapton window using the NFMP_SS electrode as working electrode. **Figure 2.29(a)** reveals the electrochemical response of the first cycle of the cell at the constant current of C/20 (1C = 154 mA g^{-1}), presenting the expected typical voltage profile of mixed-olivine cathodes already described.[113] The panel also shows the points where the XAS spectra have been collected (highlighted in red) at Fe and Mn K-edges, corresponding to different processes occurring for NFMP material. In particular, the spectra were acquired at the OCV condition of the cell, at the two Fe^{2+}/Fe^{3+} oxidation plateaus (at about 2.92 and 3.1 V), at the Mn^{2+}/Mn^{3+} oxidation plateau (at about 3.8 V), and at the upper voltage cut-off at 4.3 V in CCCV mode during charge, as well as after the Mn^{3+}/Mn^{2+} reduction at about 3.3 V, at the Fe^{3+}/Fe^{2+} reduction plateau (at about 2.9 V), and at the lower voltage cut-off at 1.8 V in CCCV mode during discharge.

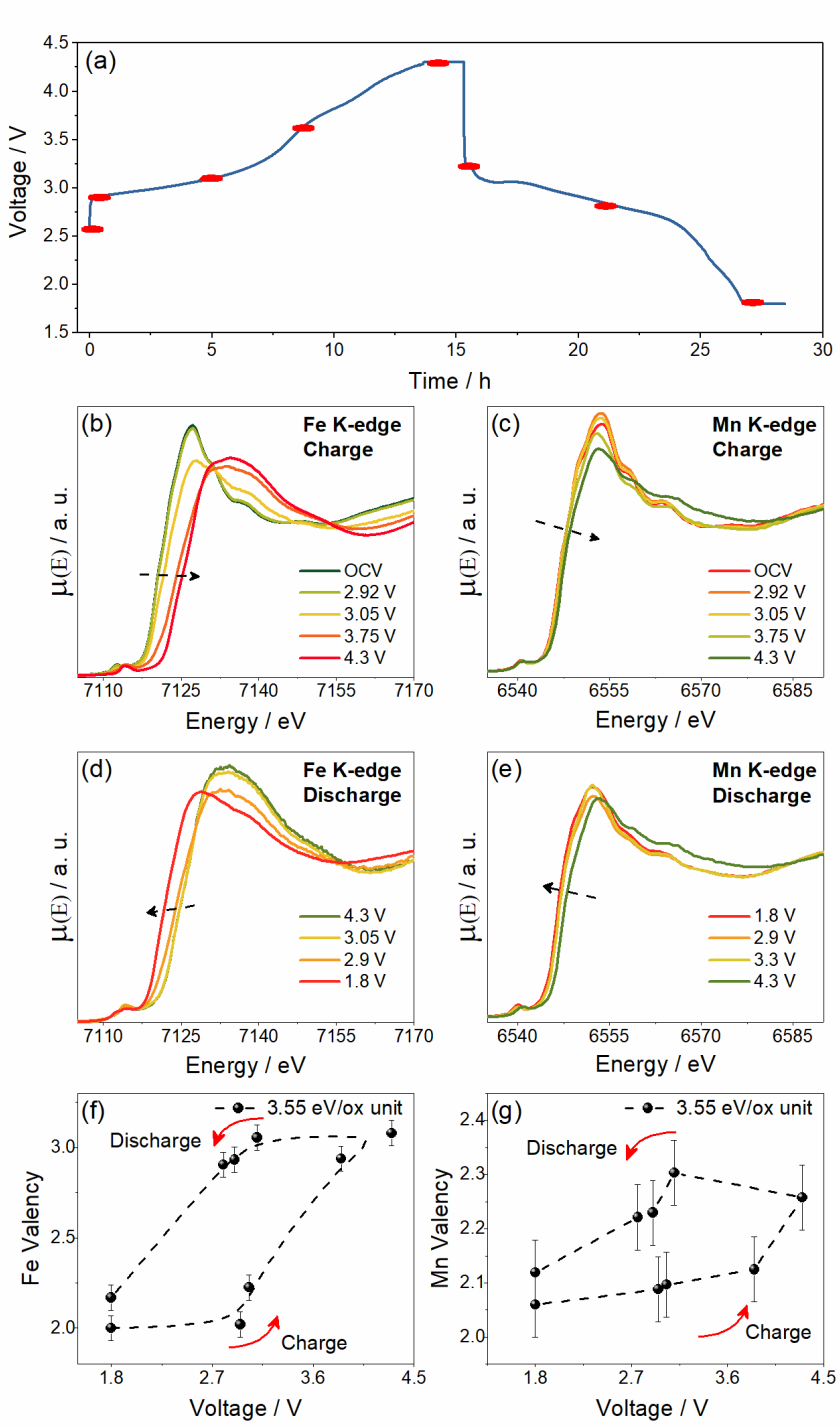

Figure 2.29: *Operando XAS analysis performed on the Na|NFMP_SS cell.* ***(a)*** *Electrochemical response in terms of voltage profile of the first cycle at the constant current rate of C/20 (1C = 154 mA g^{-1}) with highlighted the SoC where XAS spectra have been acquired. Voltage range 1.8 – 4.3 V. XANES spectra collected at* ***(b, d)*** *Fe K-edge and* ***(c, e)*** *Mn K-edge during* ***(b, c)*** *charge and* ***(d, e)*** *discharge of the cell. Metal valency estimated from the edge position for* ***(f)*** *Fe and* ***(g)*** *Mn. The chronological direction of the measurement is highlighted by the arrows. Room temperature (25 °C).*

For the XANES analysis evaluated in **Figure 2.29(b-g)**, the relative increase of the oxidation state was estimated for both edges from the position of the 0.5 jump, since at 0.9 for manganese the formation of another feature is observed. A 3.55 eV/unit of oxidation was estimated for both shifts. As expected from the de-sodiation process occurring during charge, a gradual oxidation of the Fe and

Mn ions could be observed in the spectra of **Figure 2.29(b, c)**, respectively. Considering the Fe K-edge, at the OCV the sample shows a high content of Fe^{2+}. The iron ions within the sample remain unchanged until after the first iron plateau potential; indeed, if at 2.92 V a very modest change of the Fe valence and overall sample structure is observed, with Fe valency barely increases of 0.02 (*i.e.* +2% Fe^{3+}) the blue-shift and intensity decrease of the white line becomes evident at 3.05 V. The inversion of the relative intensities of the two components at the pre-edge (see magnification in **Figure 2.30**) agrees with the prevalence of Fe^{3+} species, as expected in this potential region, with still a relevant presence of Fe^{2+} species. The average Fe valency increases to +2.23 (see **Figure 2.29(f)**). In the high voltage plateau (3.75 V), even though only Mn ions are supposed to react, Fe species are also affected. The further shift and broadening of the white line can be attributed to the decrease of the lattice size upon de-sodiation, in good agreement with what has been observed for the lithium-based olivine.[353] The disappearance of the 7112 eV component supports the complete oxidation of the Fe species to Fe^{3+}, with a valence of + 2.94. At 4.3 V. The further broadening and intensity increase of the white line supports the complete de-sodiation, especially when compared with the spectrum of the FMP electrode (see **Figure 2.27(a)**). At the Mn K edge (**Figure 2.29(c)**), a similar trend is observed, with a gradual, partially reversible shift of the edge position for increasing potential. The moderate increase of the white line and decrease of the pre-edge intensity at the two low voltage Fe plateau suggest an increase of the electron population following the decrease of the lattice size expected during the de-sodiation.[353] The oxidation of Mn^{2+} species at 3.75 V towards Mn^{3+} is clearly shown by the shift of the spectra. As observed at the Fe K-edge, the de-sodiation at 4.3 V results in a further blue-shift and broadening of the white line as well as the pre-edge. However, in this case the overall change in the oxidation state is significantly lower, going from 2.06 at OCV up to 2.26 at the maximum potential (4.3 V), as shown in **Figure 2.29(g)**. This is also evidenced by the comparison with FMP electrode, suggesting a lower degree of oxidation in the *operando* conditions or a more moderate variation of the Mn local coordination upon charge. **Figure 2.29(d, e)** reports the XANES spectra at Fe and Mn K-edges, respectively, during discharge process. At the Fe K-edge, after a moderate decrease of the white line intensity at the Mn reduction plateau (3.3 V), a gradual red shift of the XANES and reappearance of the 7112 eV pre-edge component due to Fe^{2+} species is observed (see **Figure 2.30**). During discharge, the sample Fe valency starts to decrease gradually for potential below 3.1 V, going back to a +2.16 valency at 1.8 V (**Figure 2.29(f)**). The reversibility of the charge/discharge process is observed also at the Mn K edge, where the main reduction occurs at the higher potential plateau (3.3 V), the Fe reduction at 2.9 V and the complete sodium re-intercalation (1.8 V) result in an additional red-shift and re-arrangement of the structure. The overall trend, especially the Fe and Mn valency reported in **Figure 2.29(f, g)**, is a further confirmation of the

complete reactivity of iron in the sodium-based mixed olivines with respect to the hindered reactivity of Mn, as also evidenced, even if at a minor extent, in lithium-based ones.[353,354] Furthermore, the low degree of oxidation from Mn^{2+} to Mn^{3+} (*i.e.* Mn valency from + 2.06 to + 2.26), together with the Jahn-Teller distortion of the oxidized phase, limits the performance of the material in Na-cell, as evidenced in **Section 2.3**.[113]

To better observe the shifts in the XANES spectra, a magnification of the pre-edge at Fe and Mn K-edges during the charge of the cell is reported in **Figure 2.30**, together with the reference spectra of Fe^{2+}, Fe^{3+}, and Mn^{3+}.

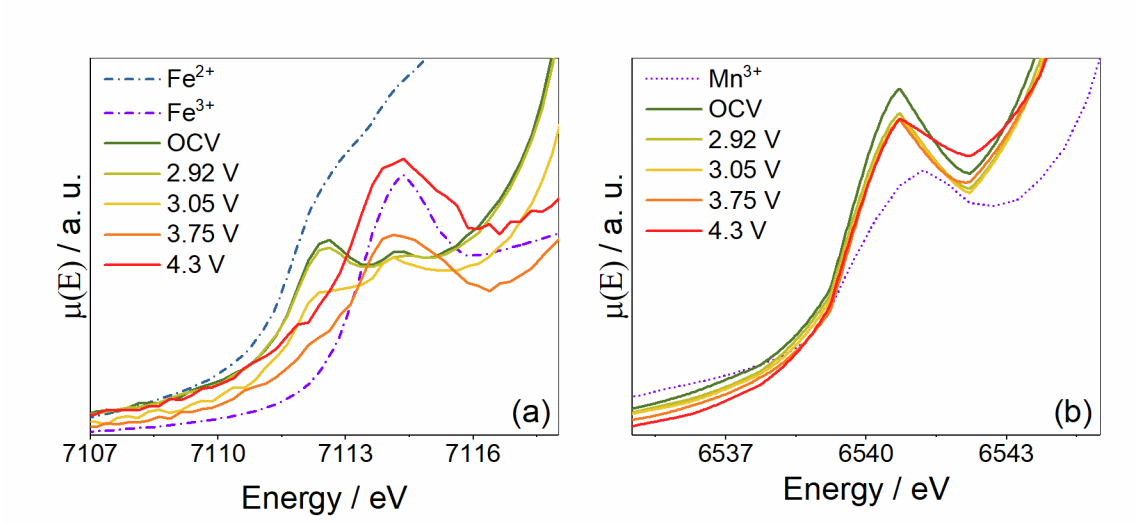

Figure 2.30: *Magnification of the pre-edge of XANES spectra of Figure 2.29(b, c) at the* ***(a)*** *Fe and* ***(b)*** *Mn K-edges, compared with references of known valency (dashed curves).*

The Fe valency can be deduced by the Fe pre-edge intensity, which shows two components around 7112 eV (Fe^{2+}) and 7114 eV (Fe^{3+}). The evolution of the Fe K pre-edge confirms the already described trend, with a gradual shift from 7122.5 to 7114 eV at increasing potential, which correlates with the Fe^{2+} to Fe^{3+} oxidation (as shown by comparison with a reference). On the other hand, the concurrent intensity increase of the pre-edge suggests an increase of the distortion within the FeO_6 octahedra.[355] Furthermore, the lower degree of modification of Mn is confirmed also by the pre-edge behavior, that shows a modest positive shift compared to Fe pre-edge.

To further investigate the local structural rearrangements of the NFMP material during charge, the Fourier-transformed extended X-ray absorption fine structure (FT-EXAFS) spectra collected at both Fe and Mn K-edges are shown in **Figure 2.31**.

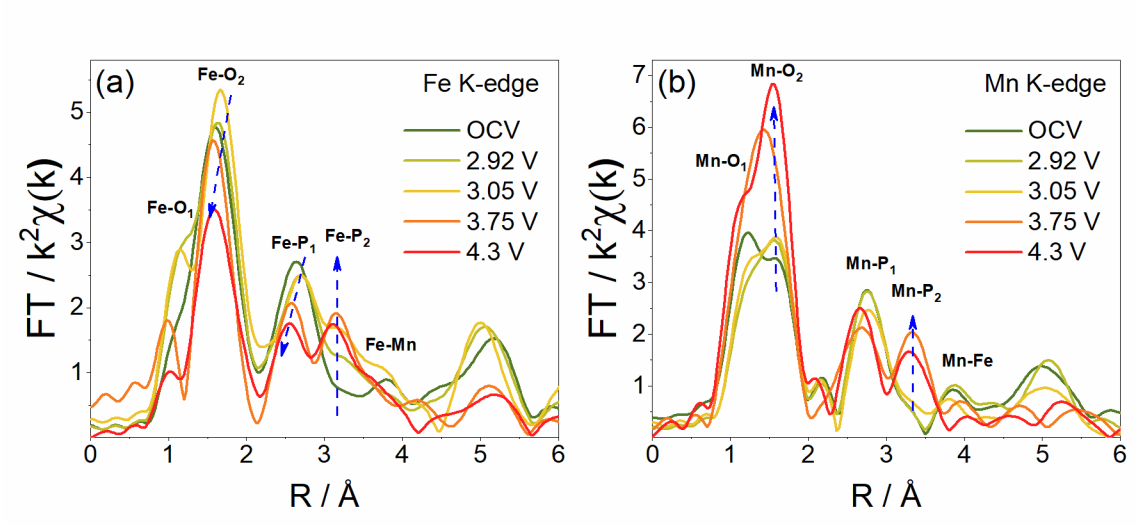

Figure 2.31: *Fourier-transformed EXAFS spectra acquired during the charge process of the Na\NFMP cell at* ***(a)*** *Fe and* ***(b)*** *Mn K-edges.*

The changes observed correlate with the results of previous literature work for $LiFe_{0.75}Mn_{0.25}PO_4$ during de-lithiation.[354] At the Fe K-edge (**Figure 2.31(a)**), a severe modification of the Fe-O shells, with a shortening and intensity decrease of the bond length, could be observed, in agreement with an oxidation accompanied by an increase of the octahedral distortion. The Fe-P1distance decreases in distance and intensity as well, while the Fe-P2 shell, on the other hand, increases in intensity. At the Mn site (**Figure 2.31(b)**), no clear change in Mn-O distance is observed, while an increase in the scattering peak width may suggest higher Debye-Waller factors, as a result of Jahn-Teller distortion. Again, the P2 scattering intensity increases upon de-sodiation. An increase of the scattering intensity may be associated with the Mn anti-site mixing, already observed for these samples, in agreement with the results obtained from Rietveld refinement of the XRD data (see **Table 2.7** in **Section 2.3**).[354,356,357] Although the initial promising information, a proper fit of the results and further analysis are required to confirm these initial outcomes and to fully understand the structural dynamics of the NFMP cathode.

2.5Conclusions

In this chapter the synthesis of a Li-based mixed olivine cathode and the characterization in Li and Na systems has been deeply investigated. In **Section 2.1** the experimental methods adopted in this chapter have been reported.

In **Section 2.2** the synthesis and the full characterization of a cathode material exploiting the olivine structure ($LiFe_{0.6}Mn_{0.4}PO_4$) and benefitting from the simultaneous presence of iron and manganese into a LFMP stoichiometry has been reported. The data indicated the achievement of a material with

a well-defined crystalline structure without any impurity due to a process originally optimized by TGA/XRD investigation during the various thermal steps. A suitable micrometric morphology, the expected stoichiometry, and the advantageous presence of 4 wt.% of carbon allowed a reversible electrochemical process of Fe and Mn redox couples in lithium cell at 3.5 and 4 V vs. Li^+/Li, respectively, with a modest polarization and a relatively low impedance. Furthermore, tests in lithium battery exploiting the conventional electrolyte indicated a maximum capacity of about 130 mAh g^{-1} and an acceptable rate capability from C/10 to 2C rate. Considering the achieved capacity value and the average working voltage of the cells, a theoretical energy density of about 490 Wh kg^{-1} can be estimated for LFMP. Therefore, taking into account inactive components such as battery case, current collectors, and electronics, the LFMP can achieve a practical energy approaching 170 Wh kg^{-1} in lithium-ion cell, and even a higher value in cells using the lithium metal anode. Therefore, a possible step forward for achieving a safe version of the lithium metal battery has been investigated by exploiting the polymer configuration, using an electrolyte based on solid PEGDME and operating at 50 °C. The cell revealed exceptional stability with a capacity of about 110 mAh g^{-1} retained for about 95% over more than 100 charge/discharge cycles. In summary, the results suggest the possible achievement of safe, low cost, and efficient batteries including a new generation of stable olivine cathodes, solid polymer electrolyte, and high-energy lithium metal.

Section 2.3 reported the features and electrochemical behavior of a NFMP sodium-mixed olivine cathode which has been achieved by the electrochemical de-lithiation of the analogue lithium-based electrode proposed in **Section 2.2**, and subsequent sodiation process. The study indicates that LFMP has been successfully converted to NFMP with a well-defined structure without any impurity, as confirmed by XRD, Raman spectroscopy, and ICP-OES. SEM/EDS revealed for NFMP suitable morphology with homogeneous distribution of the elements in the electrode, allowing a reversible electrochemical process of Fe^{3+}/Fe^{2+} and Mn^{3+}/Mn^{2+} redox couples in sodium cell at 3.0, 3.2, and 3.8 V vs. Na^+/Na, respectively. The data also suggested for the mixed olivine based on iron and manganese a different electrochemical reaction mechanism as compared with the pure iron olivine. In fact, CV measurement revealed two redox processes for Fe (Fe^A at 3.05 and 2.82 V vs. Na^+/Na, and Fe^B 3.16 and 3.02 V vs. Na^+/Na) and a single one for Mn (at 3.85 and 3.55 V vs. Na^+/Na) in NFMP, instead of the one centered at about 3.0 V vs. Na^+/Na associated with the Fe^{3+}/Fe^{2+} in NFP observed in literature. Tests in sodium cells of NFMP have shown a maximum capacity exceeding 100 mAh g^{-1} at 55 °C and a satisfactory rate capability from C/20 to 2C rate at room temperature. The achieved capacity values and the average working voltage of the cells suggested possible improvement of the energy density of the material by optimizing the Fe/Mn ratio. Moreover, the comparison of ion transport and interfacial properties of LFMP with NFMP indicated for the latter

slower kinetics and more resistive interphase of the cell, as expected by the higher dimension and reactivity of the Na compared with the Li. Relevantly, the data have shown for NFMP ion transport and charge-transfer behavior analogue to that of LFMP, thus suggesting the actual possibility of exploiting the mixed olivine as an efficient cathode in sodium cell. The ion diffusion coefficients in NFMP and LFMP have been achieved by CV, GITT and SPEIS. The trends of SPEIS confirmed faster transport within the olivine lattice in correspondence with the Fe^{3+}/Fe^{2+} redox processes than the Mn^{3+}/Mn^{2+} one, in line with the data achieved by CV and GITT, however with lower values for D_{EIS} as compared to D_{GITT} and D_{CV}. The achieved results can rationalize the behavior of the mixed olivine in terms of the reaction mechanism and ion transport and shed light on the possibility of achieving a low-cost and environmentally friendly cathode with similar structural stability, ion transport, and interfacial properties compared with lithium olivine. Moreover, NFMP cathode may be improved by further tuning the material composition in terms of Fe to Mn ratio to limit the Jahn-Teller distortion affecting the olivines with high Mn content.

In **Section 2.4** *ex-situ* and *operando* XAS analyses on the achieved NFMP cathode have been described. The study indicated the suitability of the adopted self-standing procedure to achieve NFMP_SS electrodes for application in *operando* measurements, suggesting its possible implementation to use self-standing electrodes in Na-metal cells, with capacity comparable to them obtained for conventional electrodes. The preliminary *ex-situ* XANES analysis on LFMP, FMP, and NFMP electrodes revealed a Mn valency of +2.64 in the FMP sample, suggesting the uncomplete oxidation of Mn, also confirmed by XPS analysis on the same samples. The hindered reactivity of Mn compared to Fe is also evidenced by *operando* XANES spectra acquired during the first charge/discharge cycle, with a less marked blue-shift increasing the voltage and lower values of valency at 4.3 V (+ 2.94 for Fe and + 2.26 for Mn), confirming the hindered Mn reactivity evidenced in **Section 2.3**. Furthermore, the FT-EXAFS spectra acquired during charge revealed an increase of scattering intensity of Mn-O distance, probably associated with antisite Mn/Na mixing as already evidenced in the XRD analysis. In summary, the distortion of NFMP olivine structure has been confirmed by XAS, with low Mn valence which hinders its reactivity and decreases the performance of the material, while further studies are required to achieve a comprehensive understanding of the reaction mechanism.

3. Investigation of Formulation Effect and Manufacturing Process on $LiMn_{0.7}Fe_{0.3}PO_4$ Cathode for Application in Upscaled Li-ion Batteries

As previously described in **Chapter 2**, the economic and environmental issues associated with the critical transition metals employed in layered oxide cathodes, such as cobalt, has recently shifted trajectory towards the use of alternative cathode chemistries such as the polyanionic phospho-olivine cathodes characterized by outstanding thermal and electrochemical stability, non-toxicity, and low manufacturing costs.[76,77,121] Furthermore, mixed olivine cathodes with general formula $LiMn_xFe_{1-x}PO_4$ (LMFP) possess higher energy density than LFP whilst still holding efficient Li^+ transport and hindered pseudo-Jahn-Teller distortion dependent on Mn^{3+},[95,102,105] while their low ionic and electronic conductivity is a major hindrance to achieve good rate performances and long cycle life. Various strategies including transition metal doping, tuning of particle size and morphology have been extensively investigated to accelerate the electron transport and ion diffusion in LMFP cathodes.[358–361] Beside bulk material modifications, the low electronic conductivity of olivines has been reported to be mitigated by carbon-coating at the active material level,[87,362,363] and/or by the addition of different conductive additives at the electrode formulation level, such as carbon nanotubes (CNTs) or nanowires (CNWs), graphene and conductive binders (CPs), in addition to the commonly used nanometric carbon (*i.e.* C65, Super P, carbon black).[88,89,247,364,365]

The combinatorial use of various carbon additives enables different conduction pathways such that carbon black nanoparticles render short-range conduction, while CNTs (or CNWs) provide long-range conduction pathways.[256] Single-walled carbon nanotubes (SWCNTs) are considered ideal conducting agents, which could enhance cycling and dimensional stability of electrodes. Nevertheless, large specific surface area of CNTs may limit their uniform dispersion in a slurry, causing their aggregation into bundles.[89] Improved cell performance at high current rates and cycling stability strongly depends on the ionic and electronic conductivity of the electrodes.[84,366] Carbon additives increase the ionic conductivity, defining with their shape and size the voids and contact between active particles and influencing electrolyte penetration into the electrode.[247] Electronic conductivity of the electrode can also be improved by increasing the electrode density, however, beside a certain threshold, this could also lead to an increased tortuosity impairing ion transport.

As such, to meet the desired specifications for different applications, and for an optimal electrode microstructure, research about manufacturing-performance relationship is of paramount importance, as the final electrode microstructure and design contribute significantly to the cell's performance. In this regard, electrode formulation development, slurry processing, and electrode manufacturing play

a critical role, especially at the cathode side.[255,256] Parameters such as slurry formulation composition, viscosity, solid content, coating speed, drying temperature, electrode loading, density, and porosity must be optimized to guarantee satisfactory electrochemical performances and cell stability, especially when upscaling from lab-scale to larger cell formats, such as single or multi-layer pouch (SLP and MLP, respectively) or cylindrical cells.[245,255,257] The investigation of these parameters is essential to produce reasonably thick electrodes bridging the gap between academic and industrial perspectives and tackling challenges in performance improvement while taking into account realistic and practical conditions.[245,255,261] The comparative assessment of cell performance when transferring the knowledge gained in labs to relevant prototype and production scales has proven to be challenging, especially considering the increased number of publications in the field adopting testing conditions not applicable to industrial requirements.[245,367]

In these regards, in **Chapter 3** manufacturing-performance correlation aspects of electrode design, reporting on a comprehensive analysis of electrode manufacturing parameters and their effect on cell performance, are investigated. Indeed, in **Section 3.1** the experimental methods adopted in the chapter are reported, while in **Section 3.2** the impact of SWCNT addition in commercial $LiMn_{0.7}Fe_{0.3}PO_4$ (LMFP73) electrode formulation is assessed and the effect of various slurry and electrode processing parameters on the overall cell performance at coin cell level and in SLP cells is studied. Different amounts of SWCNT are incorporated in the formulation of LMFP73 coatings (indicated as LMFP73-*X*%SWCNT where X = 0, 0.5, 1, and 2.5). The obtained electrodes are evaluated electrochemically by galvanostatic cycling and analyzed in terms of structural and morphological integrity by cross-sectional scanning electron microscopy (cx-SEM) and bendability tests. The synergy of the mixing strategy, the slurry viscosity and solid content, the coating speed, and the electrode loading in relation to the mechanical and microstructural properties of the electrodes is investigated, to obtain industrially relevant optimal coating parameters for electrodes to be implemented both in lab-scale coin-type full-cells with graphite anode and upscaled SLPs. The results report a systematic optimization of the slurry mixing and coating process as crucial steps of electrode manufacturing and indicate the importance of the manufacturing-performance correlation on the overall cell performance and cycling stability, particularly when transitioning from lab scale to industrially relevant cell formats.

3.1 Experimental Section

LMFP73 powder characterization

The X-ray diffraction pattern of carbon-coated $LiMn_{0.7}Fe_{0.3}PO_4$ (LMFP73, Gelon, 1.5 wt.% of carbon) powder was collected using a Malvern PANalytical Aeris diffractometer (40 kV, 15 mA) with non-monochromated Cu Kα radiation (λ = 1.5408 Å). A Ni Cu Kβ filter, a Soller slit (0.04 rad), a divergence slit (1/4°), and a 13 mm X-ray mask were used on the incident beam side. An anti-scatter (9 mm) and Soller (0.04 rad) slits were used on the diffracted beam side. The scan was performed in Bragg-Brentano mode in the 2θ range from 10° to 75° at a rate of ~ 220 s $step^{-1}$ and a step size of 0.02°. Rietveld refinement of the pattern was carried out through the MAUD software,[289] by using the reference parameters of $Li_{0.97}Mn_{0.77}Fe_{0.23}PO_4$ (*Pnma* space group, N. 62, ICSD #193643).[368] The weighted-profile (R_{wp}%) and goodness-of-fit (*GOF*) values were < 4 and < 2, respectively. Scanning electron microscopy (SEM) images were collected using a Tescan CLARA Ultra High Resolution (UHR-SEM) microscope with a Field Emission gun electron source. Energy dispersive X-Ray spectroscopy (EDS) was carried out through the analyzer of the former instrument (Oxford Instruments UltiMax 170). Analysis was carried out by applying an acceleration voltage of 5–10 kV.

Mixing and electrodes fabrication

50 g of LMFP73-X%SWCNT slurries with different solid contents were prepared by dispersing the active material, poly(vinylidene-fluoride) (PVdF 5130, Solef Solvay), carbon black (C65 Imerys), and SWCNT dispersion (BATT TUBALL™, NMP > 97%, PVdF 2%, dimethyl pyrrolidinone 0.05-0.39%, SWCNT TUBALL™ 0.4%) with a 95:2.5:(2.5-X):X (with X = 0, 0.5, 1, 2.5) weight ratio, respectively, in N-methyl-pyrrolidone (NMP, Sigma Aldrich). SWCNTs presented a length ≥ of 5 µm and a diameter of 1.6 (± 0.4) nm. The SWCNT dispersion was used as received. The formulation details are reported in **Table 3.1** in **Section 3.2**. It is worth mentioning that the actual presence of SWCNTs per formulation ranges from 0.002% to 0.01% for the LMFP-0.5%SWCNT and LMFP2.5%SWCNT formulations, respectively, and that the PVdF content has not been adjusted in the slurry preparation with respect to the amount present in the SWCNT dispersion. PVdF was pre-dissolved in NMP as an 8 wt.% solution. The mixing was carried out by using an Intertronics (Kidlington, UK) Thinky mixer. The slurries were prepared following different mixing strategies described in **Section 3.2** (see **Figure 3.2** and **Figure 3.9(a)**). 50 g of Graphite V-H (BTR)[369–371] slurry with a 55% solid content was prepared by dispersing the active material, carboxymethyl cellulose (CMC, BVH8, Ashland), styrene-butadiene rubber (SBR; BM-451B, Zeon), and C65 with a 95.25:1.5:2.25:1 weight ratio, respectively, in deionized water. CMC and SBR were pre-dissolved

in water as 2.5 wt.% and 40 wt.% solutions, respectively. The mixing was carried out with an Intertronics Thinky mixer. The viscosity of the slurries was measured using a TA Instruments HR20 rheometer equipped with a 40 mm roughened parallel plate and roughened lower plate, and a measuring gap of 500 µm, using a 25 °C constant temperature and a 0.001 – 5000 s^{-1} shear rate range. LMFP73-X%SWCNT electrodes (with X= 0, 0.5, 1, 2.5) were prepared by doctor blade casting on 15 µm aluminum foils (Avotec Steel) using an Erichsen draw down coater with a coating speed of 4 mm s^{-1}. The target electrode loading was 100 g m^{-2} (GSM). Subsequently, LMFP73-0.5%SWCNT electrodes, derived from both mixing strategies (50 g of total slurry), were cast at 2, 4, 6, and 8 mm s^{-1}, to optimize the coating speed, with a target electrode loading of ~ 50 GSM. Finally, optimized electrodes were prepared using 46% solid content, a coating speed of 6 mm s^{-1}, with target loadings of 100, 150, 200, and 250 GSM (100 g of total slurry). All the obtained coatings were dried at 80 °C on a hot plate and calendered at 85 °C (Innovative Machine Corp.) to achieve for all the samples a target density ranged between 2.2 and 2.4 g cm^{-3} (equating to ~ 30-35 % porosity). Graphite electrodes were prepared coating on 10 µm copper foils (Avotec Steel) with a coating speed of 6 mm s^{-1}, dried at 40 °C on a hot plate, and afterwards calendered to a target density of 1.5 g cm^{-3} (equating to ~ 30% porosity). The electrode loadings range from ~ 40 to ~ 105 GSM. Prior to cell assembly, electrodes were cut into disks (diameter of 14.8 and 15 mm for LMFP73 and Graphite, respectively, for CR2032 coin cells, and of 12 mm for Swagelok T-cells) and dried under dynamic vacuum using Glass Oven B-585 (BUCHI UK Ltd) at 120 °C for 12 hours.

Electrodes characterization and cell assembly

Cross-sectional scanning electron microscopy (cx-SEM) performed on the electrodes was collected with the above-described system. Before the measurements, homogeneous cross-sections were obtained using a HITACHI Ion Milling System (IM4000 plus) at an acceleration voltage of 4 kV for 90 minutes. The resistivity of the electrode coatings was obtained by using an HIOKI RM2610 electrode resistance measurement system, with a 46-pin probe. Ten measurements for each sample have been performed to assure the reliability of the data, with related confidence intervals and standard deviations of the means. The mechanical properties of the coatings were studied through a cylindrical Mandrel bend tester (BEVS 1603) using a 2-mm stainless-steel mandrel to observe possible cracks (see **Table 3.3** for damage levels).[372] Two-electrode CR2032 coin cells were assembled using the prepared LMFP73 electrode as the working electrode and lithium metal foil (diameter of 14.3 mm) or Graphite electrode as the counter electrode, with a H2325 Celgard® separator (diameter of 16 mm). The Graphite|LMFP73 full-cells were prepared by using a negative to positive (N/P) areal capacity ratio of 1.1 and 80 µL of electrolyte. Three-electrode Swagelok-type

cells were assembled using LMFP73 as working electrode, lithium metal foil (diameter of 12 mm) as counter and reference electrodes, and two glass fiber Whatman GF/A as separators (diameter of 12.8 for the body and of 12 mm for the upper part). A 1 M lithium hexafluorophosphate ($LiPF_6$) solution in a mixture of ethylene carbonate (EC): ethyl methyl carbonate (EMC) in a ratio of 3:7 (*v/v*%) with 1 wt.% of vinylene carbonate (VC) as additive (Solvionic, France) was used as electrolyte for all electrochemical tests. All cells were assembled in an argon-filled glove box (MBraun) with a H_2O and O_2 content lower than 0.5 ppm.

Electrochemical characterization

Cyclic voltammetry (CV) measurements were carried out on Li|LMFP73-0%SWCNT coin type cells at a scan rate of 0.05 mV s^{-1} in the 2.8 – 4.4 V vs. Li^+/Li potential range. Galvanostatic intermittent titration technique (GITT) experiments were performed using three-electrode Swagelok-type Li|LMFP73-0%SWCNT cell after four activation galvanostatic cycles carried out at 0.1 C current rate (1C = 170 mA g^{-1}) in the potential range of 2.8 – 4.4 V vs. Li^+/Li. The titrations were performed by applying current pulses of 17 mA g^{-1} for 1430 s, followed by potential relaxation steps of 1 h at the open circuit. The operation conditions have been decided based on the activation cycles. Galvanostatic cycles were performed on Li|LMFP73-X%SWCNT (X = 0%, 0.5%, 1%, 2.5%) and on Li|LMFP-0.5%SWCNT (loading 100, 150, 200, 250 GSM) coin type cells at the constant current rate of C/5 (1C = 170 mA g^{-1}) and C/2 after 2 activation cycles at C/10, respectively. Rate capability tests were performed at increasing current rate by running 5 cycles at C/20, C/10, C/5, C/2, 1C, 2C, 5C, 10C, and finally lowering back the current to C/20 for Li|LMFP-X%SWCNT cells, while for Li|LMFP73-0.5%SWCNT cells the measurement was conducted in the same condition using C/10 as the starting and final current. Furthermore, alternate current rate capability tests were performed on LMFP73-X%SWCNT electrodes after 5 activation cycles at C/20 by charging the cell at C/10 and subsequently discharging it at C/5, C/2, 1C, 2C, 3C, 4C, 5C, and 10C. All galvanostatic measurements above described have been conducted in the 2.8 – 4.4 V voltage range. Galvanostatic cycles on the Graphite|LMFP73-0.5%SWCNT coin cell type full-cells were performed at the constant current rate of C/5 (1C = 170 mA g_{cat}^{-1}) after 2 activation cycles at C/10 in the 2.0 – 4.4 V voltage range. The reported results are obtained from the average of at least two measurements for each electrochemical test to confirm the reproducibility and reliability of the data. The GITT measurements were carried out by using a VMP-3 multichannel electrochemical workstation (Bio-Logic), while the CV and the cycling tests were performed by using a battery tester (BCS-805, Bio-Logic). All the electrochemical tests were carried out in a climatic chamber (Binder oven) at 25 °C.

Single layer Pouch (SLP) cells assembly and testing

SLP cells were assembled in a dry room, with a dew point lower than -40 °C, using a 33.2 cm^2 LMFP73-0.5%SWCNT electrode with a loading of 200 GSM as cathode and a 35 cm^2 Graphite electrode as anode, stacked between a H1609 Celgard® separator. Aluminum and nickel-plated copper tabs of dimensions 0.2 x 8 x 60 mm (Cambridge Energy Solutions Ltd.) were used at the cathode and anode side, respectively. The stack was then sealed in aluminum laminate pouch bag material then vacuum filled with a slight excess of calculated amount of electrolyte of ~ 0.6g (5 g Ah^{-1} consisting of the same solution above indicated). Cells were compressed between two Perspex plates with a layer of precision thickness polyurethane foam positioned on top and at the bottom of the cell to evenly distribute compression pressure across the electrode stack. Prior testing, cells were rested for 5 hours inside a Binder climatic chamber at 25 °C. Galvanostatic cycles were performed at a constant current rate of C/2 (1C = 150 mA g_{cat}^{-1}) after 2 activation cycles at C/5 between 2.0 – 4.4 V voltage range and using an N/P ratio of 1.1. All cycling tests were performed using a Bio-Logic battery tester at 25 °C.

3.2 Results and Discussion

The structure and morphology of the carbon-coated commercial LMFP73 active material was evaluated and reported in **Figure 3.1**. Carbon-coating allows for enhanced electronic conductivity while mitigating potential interfacial side reactions with the electrolyte.[98,362] **Figure 3.1(a)** shows a detailed structural investigation of the sample by XRD. Rietveld refinement of the sample reveals phase purity of the LMFP73 material characterized by an orthorhombic cell unit (*Pnma* space group, table N. 62), aligning well with the reference pattern of the olivine lattice (ICSD #193643).[368] The refinement results reported in **Table 3.1** show comparable values of the cell unit parameters *a*, *b*, and *c* between LMFP73 and the reference sample, of about 10.4, 6.1, and 4.7 Å, respectively. Furthermore, the unit cell volume of LMFP73 is of about 298.5 $Å^3$, slightly lower respect to the ICSD reference due to a minor Mn fraction present in the olivine under study.[290,368] The accuracy and the reliability of the refinement are confirmed by the goodness-of-fit parameter (*GOF*) and weighted-profile *R* factor (R_{wp}%), values of < 2 and < 4 respectively as provided in **Table 3.1**.[289,302] **Figure 3.1(b, c)** depicts the morphological properties of the LMFP73 powder, investigated by SEM. The related SEM images, obtained at different magnifications, reveal the presence of agglomerates of submicrometric primary particles with a size of about 400 nm. Such submicrometric particles can

guarantee short diffusion paths for Li^+ ions transport and limit the side reactions with the electrolyte.[98,362]

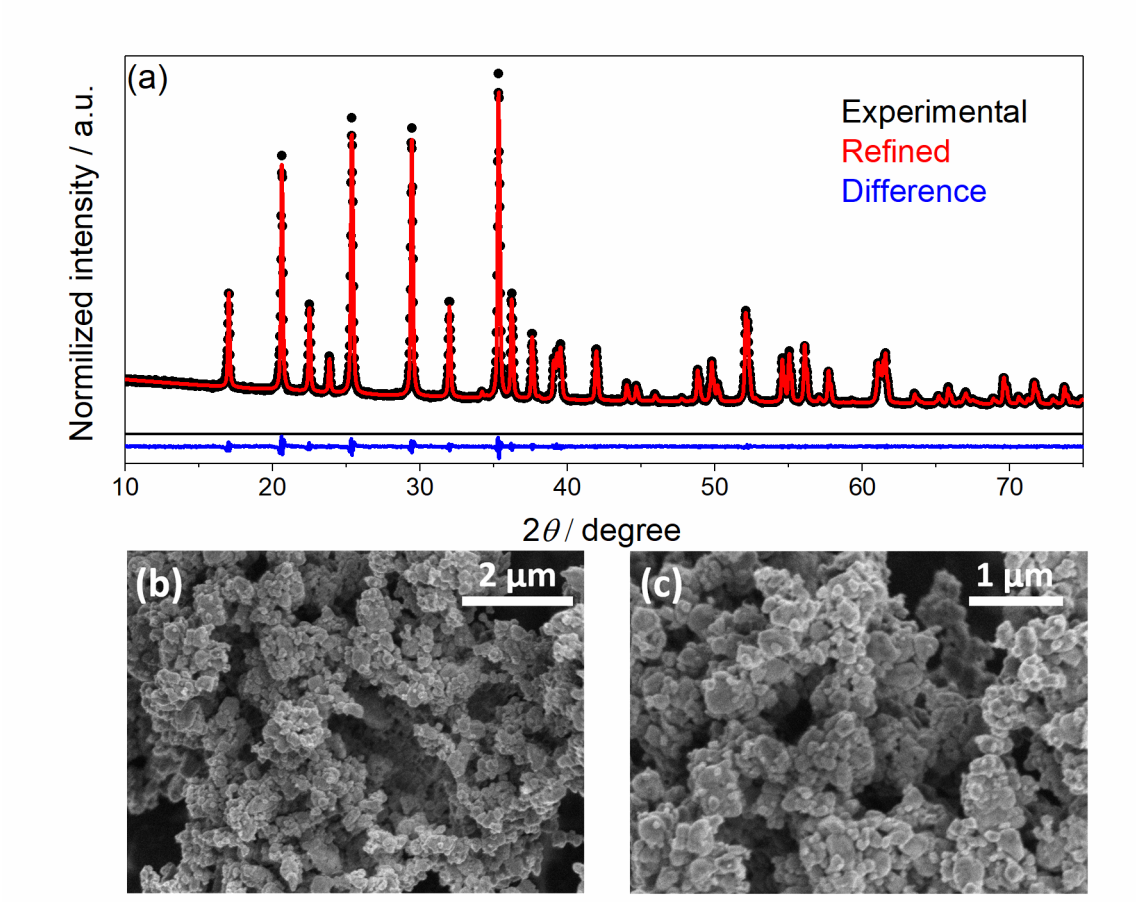

Figure 3.1: ***(a)*** *Rietveld refinement of the XRD patterns of LMFP73 active material powder. In detail: experimental (black dots) and calculated (red line) patterns, difference profile (blue line).* ***(b–c)*** *Scanning electron microscopy (SEM) images at different magnifications of the LMFP73 active material powder.*[86]

Table 3.1: *Results of Rietveld refinement of Figure 3.1(a) in terms of lattice parameters, unit cell volume, molar volume, goodness-of-fit (GOF) parameter, and weighted-profile R factor (R_{wp}%) of the LMFP73 active material powder. Reference ICSD #193643.*[86]

Sample	*a* (Å)	*b* (Å)	*c* (Å)	*V* (Å^3)	V_M (cm^3 mol^{-1})	*GOF*	R_{wp}%
ICSD #193643	10.420	6.080	4.734	299.93	45.16	/	/
LMFP73	10.408(4)	6.070(5)	4.724(7)	298.5(3)	44.94	1.70	3.91

The molar volume (V_M) of the olivine cathode reported in **Table 3.1** was calculated from the unit cell volume through **Equation (3.1)**:

$$V_M = \frac{V_{cell}\,(cm^3) * N_A}{Z} \qquad \textbf{(3.1)}$$

where N_A is the Avogadro's number (6.022×10^{23} mol^{-1}), V_{cell} is the unit cell volume, and Z is the number of formula units in the unit cell (Z = 4). Molar volume is used in the determination of the diffusion coefficient of the LMFP73 cathode (see **Equation (2.7)** and discussion of **Figure 3.5**).

3.2.1 Investigation of the Impact of SWCNTs Content inLMFP73 Electrodes

Conductive agents are often employed to mitigate the low electronic conductivity of olivine-based cathodes. The use of CNTs as a conductive agent for cathode presents several advantages compared to other carbon additives. The high length-diameter aspect ratio for CNTs compared to other additives allows for instance a lower weight doping level to achieve long range connectivity and contiguous pathways for electrons.[185] This is beneficial both in reducing the weight of inactive materials in the electrode composition and in lowering costs. Hereafter, different amounts of pre-dispersed SWCNTs in a solution of NMP and PVdF (denoted as SWCNT dispersion) as conductive additive is employed. **Table 3.2** reports a summary of the different electrode formulations investigated and the resulting slurry properties including composition, solid content and viscosity (see **Section 3.1** for further details).

Table 3.2: *Mixing parameters and properties of LMFP73 slurries with different amount of SWCNT in terms of percentage of mixing materials, solid content of the slurry, and viscosity of the slurry at 10 s^{-1} shear rate (see Figure 3.2(b) for corresponding viscosity trend).*[86]

Sample	Mixing material	Percentage	Solid content (SC)	Viscosity (Pa s)
LMFP-0%SWCNT	LMFP73	95 %	48%	6.6
	8% PVdF solution	2.5 %		
	C65 Imerys	2.5 %		
	SWCNT dispersion	–		
LMFP-0.5%SWCNT	LMFP73	95 %	48%	6.7
	8% PVdF solution	2.5 %		
	C65 Imerys	2 %		
	SWCNT dispersion	0.5 %		
LMFP-1%SWCNT	LMFP73	95 %	48%	7.7
	8% PVdF solution	2.5 %		
	C65 Imerys	1.5 %		
	SWCNT dispersion	1 %		
LMFP-2.5%SWCNT	LMFP73	95 %	43.5%	5.6
	8% PVdF solution	2.5 %		
	C65 Imerys	–		
	SWCNT dispersion	2.5 %		

All the investigated formulations incorporated 95% active material to match standards in commercial cells.[246,256,261] Different amounts of SWCNT dispersion were added in replacement of C65 carbon additive. The solid content target during formulation development was 48%, which was achieved for all slurries except for LMFP-2.5%SWCNT. Indeed, the rheology of cathode slurries is highly dependent on the carbon black network. Here, a lower solid content was achieved, indicating that high content of SWCNT dispersion limits higher solid contents due to an increased viscosity. This is related to the PVdF contained in the SWCNT dispersion, which may result in a reduction of the shear rate, and thus a reduction in the mixing efficiency.[249,373] The formulations shown in **Table 3.2** were used to prepare different slurries with the mixing strategy schematized in **Figure 3.2(a)**. In the first step, LMFP73 active material and C65 carbon additive were added into a pot and mixed for 5 mins at 2000 rpm. The addition of PVdF, SWCNT dispersion, and initial NMP solvent amount followed. After mixing for 5 mins at 2000 rpm, the remaining NMP was added to achieve the targeted solid content and mixed for 5 mins at 2000 rpm. This mixing strategy was chosen as a starting point to investigate the impact of SWCNT addition, and further optimization will be discussed later.

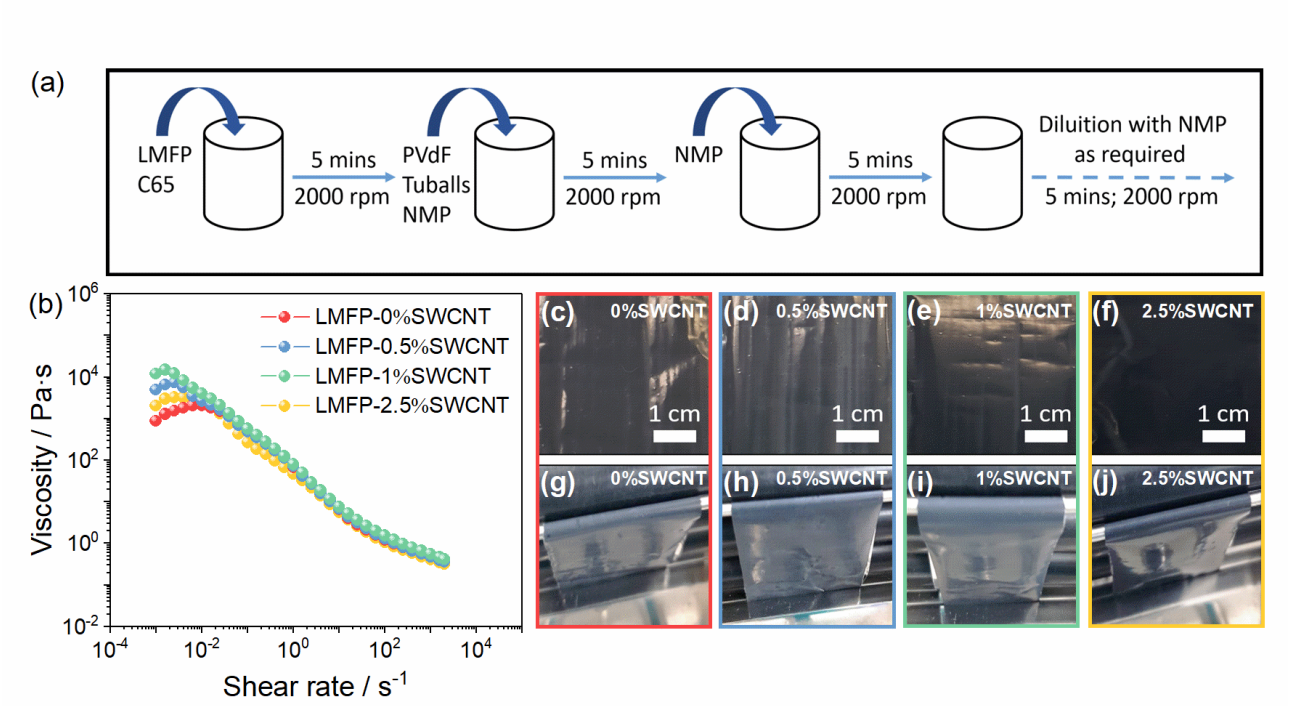

Figure 3.2: ***(a)*** *Schematic representation of the mixing strategy (see parameters reported in Table 3.2).* ***(b)*** *Trend of viscosity vs. shear rate of the slurries with different amount of SWCNT. Photographic images of the obtained* ***(c–f)*** *calendered coatings and* ***(g–j)*** *coating sheets subjected to cylindrical mandrel bend test. In detail:* ***(c, g)*** *LMFP-0%SWCNT,* ***(d, h)*** *LMFP-0.5%SWCNT,* ***(e, i)*** *LMFP-1%SWCNT, and* ***(f, j)*** *LMFP-2.5%SWCNT. Adapted from [86].*

The viscosity of the obtained slurries was investigated with the trends of viscosity vs shear rate reported in **Figure 3.2(b)**. The tabulated viscosity values at a shear rate of 10 s^{-1} are reported in **Table 3.2**. All the samples followed a similar flow viscosity trend displaying a shear-thinning behavior with

an initial flat plateau at low shear rates that correspond to the zero-shear viscosity followed by a decrease in shear viscosity at high shear rates.[374] This behavior generally allows prevention of sedimentation or slumping with breakdown of agglomerates at low shear rates with a subsequent thin down allowing good processability of the slurry flow in the coater.[261,374] The obtained viscosity of all the samples averaged ~ 6.65 Pa·s ±0.86 satisfactory for electrode processing.[374] Subsequently, the coatings were prepared with a coating speed of 4 mm s^{-1} and a target loading of about 100 GSM. **Figure 3.2(c-f)** illustrates photographic images of the coatings after calendering to ~ 30 % porosity. All coatings presented inhomogeneous streaks along the surface, formed as a result of poor particle dispersion and possible formation of C65 or SWCNTs aggregates, due to difficult carbon additives initial homogenization in the adopted strategy. Furthermore, the difficult dispersal of nanometric carbon could also affect the dispersion of LMFP73, resulting in poor dispersion of bigger particles leading to inhomogeneity across the electrodes.[375] It is worth noting that the SWCNTs content does not significantly change the quality of the electrodes, except for the LMFP73-2.5%SWCNT sample, which appears to have an improved quality, associated with the lower solid content in the slurry. This ultimately indicates the flaws in the employed mixing strategy and its possible effect on the overall electrode performance, suggesting the necessity to design an improved mixing strategy that can be effectively scaled up. In this regard, the optimization of several parameters, such as coating speed, mixing time, change of steps of procedure, to favor the carbon dispersion, are required to improve electrodes quality.[258] It is indeed important to consider that the rheology of the slurry strongly affects the coating behavior and the shear rate of the slurry during coating, thus the viscosity of the slurries needs to be optimized considering the coating shear rate.[373,375] Furthermore, the mechanical properties of the coatings were evaluated by using a cylindrical mandrel bend tester, and the photographic images are shown in **Figure 3.2(g-j)**. **Table 3.3** describes the different levels of the bend test, going from no electrode damaging (level 1) to high presence of cracking (level 4).[372] When using a mandrel size of 2 mm diameter, all coatings were shown to have strong adhesion to the aluminum current collector with no signs of delamination or cracking (classified as level 1).

Table 3.3: *Description of cylindrical mandrel bend test levels.*[86]

Level	Description
1	No damage to electrode and no flaking
2	Minor damage to electrode and no flaking (1 – 3 cracks)
3	Moderate damage to electrode and no flaking (> 3 cracks)
4	Moderate to severe damage to electrode and/or flaking (major cracks/flaking)

The electronic conductivity of the coatings was also measured with a HIOKI RM2610 device, and the results are reported in **Table 3.4**. The volumetric resistivity for a coating (ρ_V) and the interface resistance between a coating and the current collector (R_{int}) can be calculated by the instrument via a finite volume model. The total through-plane resistance (R_T) was calculated from the values tabulated in **Table 3.4** using **Equation (3.2)**:

$$R_T = (\rho_V * s_C) + R_{int} \quad \textbf{(3.2)}$$

where s_C is the coating thickness. Subsequently, the through-plane conductivity (σ_T) can be calculated from the obtained R_T values.

Table 3.4: *Results of electrode resistance, resistivity, and conductivity measurements of LMFP73 coatings with different amount of SWCNT in terms of electrode composite layer volume resistivity (ρ_V), interface resistance between the composite layer and the current collector (R_{int}), with related standard deviation (SD), calculated total through-plane resistance (R_T) (see Equation (3.2)), and calculated through-plane conductivity (σ_T), with corresponding coating thickness (s_C).*[86]

Sample	ρ_V (Ω cm)	SD	R_{int} (Ω cm^2)	SD	R_T (Ω cm^2)	s_C (µm)	σ_T (S cm^{-1})
LMFP-0%SWCNT	25.2 ± 1.6	1.8	5.2 ± 1.4	2.3	5.32 ± 0.91	44	8.27x10^{-4}
LMFP-0.5%SWCNT	5.9 ± 0.2	0.3	2.8 ± 0.5	0.8	2.82 ± 0.43	44	1.56x10^{-3}
LMFP-1%SWCNT	3.9 ± 0.5	0.6	1.1 ± 0.2	0.4	1.12 ± 0.21	43	3.84x10^{-3}
LMFP-2.5%SWCNT	5.5 ± 0.2	0.2	2.5 ± 0.1	0.2	2.52 ± 0.13	43	1.71x10^{-3}

The results show low overall values of R_T for all the samples, attributed to an effective calendering process, which improves the contact between the particles in the electrodes and the current collector and leads to a denser particle arrangement and a better bonding between the conductive additive and the active material.[376,377] This results in a subsequent decrease in the interface resistance, as already reported for olivine cathodes.[256,377,378] Nevertheless, the through-plane conductivity (σ_T) increases as the SWCNT content increases up to 1%, to then slightly decrease for the LMFP73-2.5%SWCNT sample which presents no C65 additive. It is worth noting that the conductivity of the coating containing 2.5%SWCNT is higher than that of the coating with only C65 (*i.e.* LMFP73-0%SWCNT), which indicates the enhanced effectiveness of SWCNTs as compared to C65 when it comes to electronic conductivity.[378] Nevertheless, the overall increased resistance observed in the presence of high amounts of SWCNT (2.5%) can arise from the mixing strategy used, resulting in particle

agglomeration linked to the strong inter-tube attraction among CNTs, thus leading to localized electrical disconnections within the electrode.[251,379–381] This clearly highlights the advantage of having both SWCNTs and C65 in the electrode formulation, which allows the building of a three-dimensional conduction framework in the electrode.

The structural integrity and homogeneous distribution of the electrode components of the prepared coatings were investigated by examining electrode cross-sections using SEM coupled with EDS as illustrated in **Figure 3.3**.

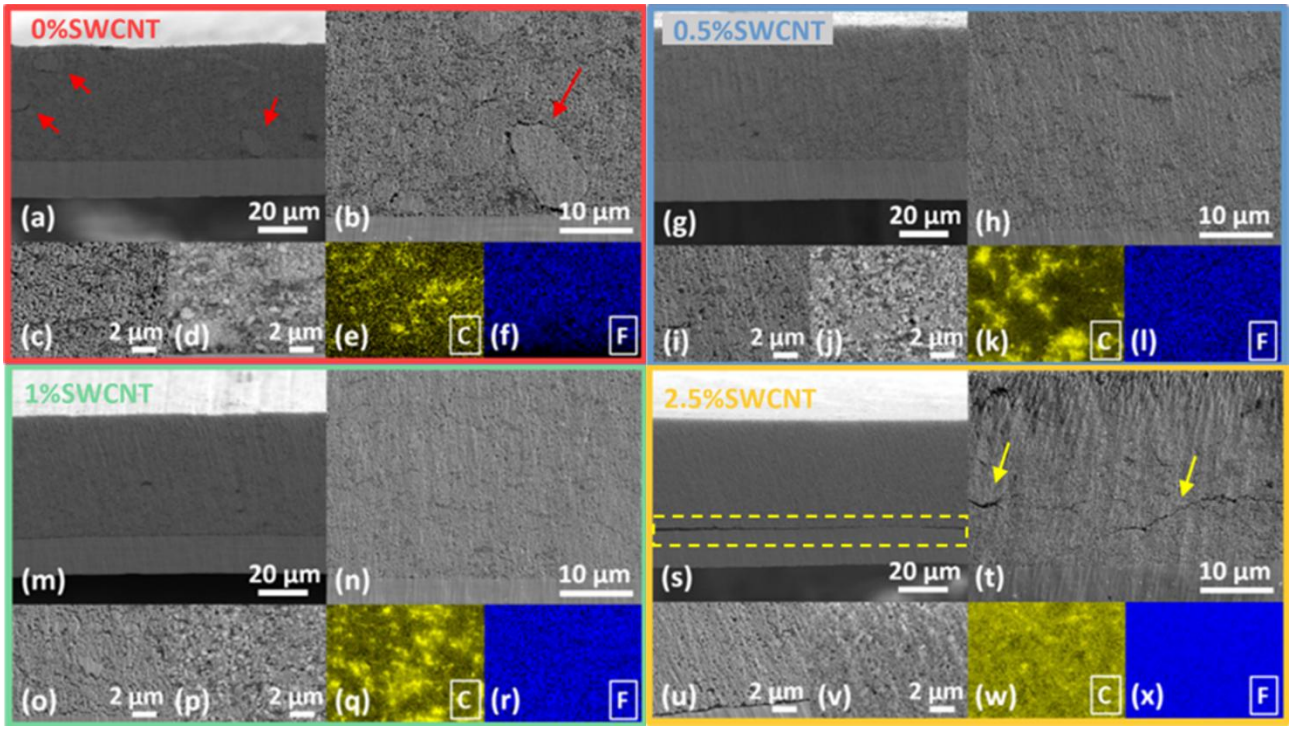

Figure 3.3: *Cross-sectional SEM and correlated EDS analyses of LMFP73 coatings with different amount of SWCNT. In detail: cx-SEM images at different magnifications of* ***(a–d)*** *LMFP-0%SWCNT,* ***(g–j)*** *LMFP-0.5%SWCNT,* ***(m–p)*** *LMFP-1%SWCNT, and* ***(s–v)*** *LMFP-2.5%SWCNT with related SEM-EDS elemental maps of* ***(e, k, q, w)*** *C and* ***(f, l, r, x)*** *F, respectively. Adapted from* [86].

The cross-sectional images of the electrodes containing 0%SWCNTs reveal the presence of particle agglomerates, resulting in large particles clusters across various parts of the electrode as indicated by the red arrows in **Figure 3.3(a, b)**. With the addition of SWCNTs to the formulation a more homogenously distributed mixture was obtained indicating the synergistic effects of using both C65 and CNTs. Carbon agglomerates are also highlighted in the EDS images (**Figure 3.3(e)**) of the lower magnification SEM images (**Figure 3.3(c)**). EDS carbon maps with higher magnifications, reported in **Figure 3.4(b, c)**, illustrate a more continuous conductive network between the active material particles across the electrode as compared to the electrodes containing 0%SWCNTs (**Figure 3.4(a)**), where regions of no carbon network are encountered, as highlighted by the white arrows. Indeed, electrodes containing 0.5 and 1 % SWCNTs show carbon agglomerates (brighter regions) associated

with the strong clustering tendency of CNTs (see C maps in **Figures 3.3** and **3.4**). However, for the electrodes with 2.5% SWCNTs (**Figure 3.3(s-t)**), the presence of electrode cracking (indicated by the yellow arrows) and a partial detachment from the current collector (see **Figure 3.3(s)**) was observed. The complete removal of C65 and the exclusive use of SWCNTs in the formulation results in a reduction of point-to-point contact, which is typically observed between carbon black (*i.e.* C65) and active material particles, and an increase in line-to-line contact between CNTs leading to an overall poorer contact between the electrode particles and/or to current collector.[251,252] In addition, the EDS carbon map shown in **Figure 3.3(w)** and **Figure 3.4(d)** illustrates the accumulation of carbon on the electrode surface proving poor conductive network throughout the electrode. This carbon accumulation could be related to segregation and sedimentation of heavier particles, probably ascribed to the additional amount of PVdF binder included in the slurries by adding increasing amounts of SWCNT dispersion, which also contains PVdF. This is also evidenced by the EDS fluorine map reported highlighting an increase of fluorine content from 0%SWCNT to 2.5%SWCNT (see **Figure 3.3** panels **(f, l, r, x)**, respectively).[249] This behavior further limits the ion/electronic transport and rate performance, especially in high loading electrodes.[261]

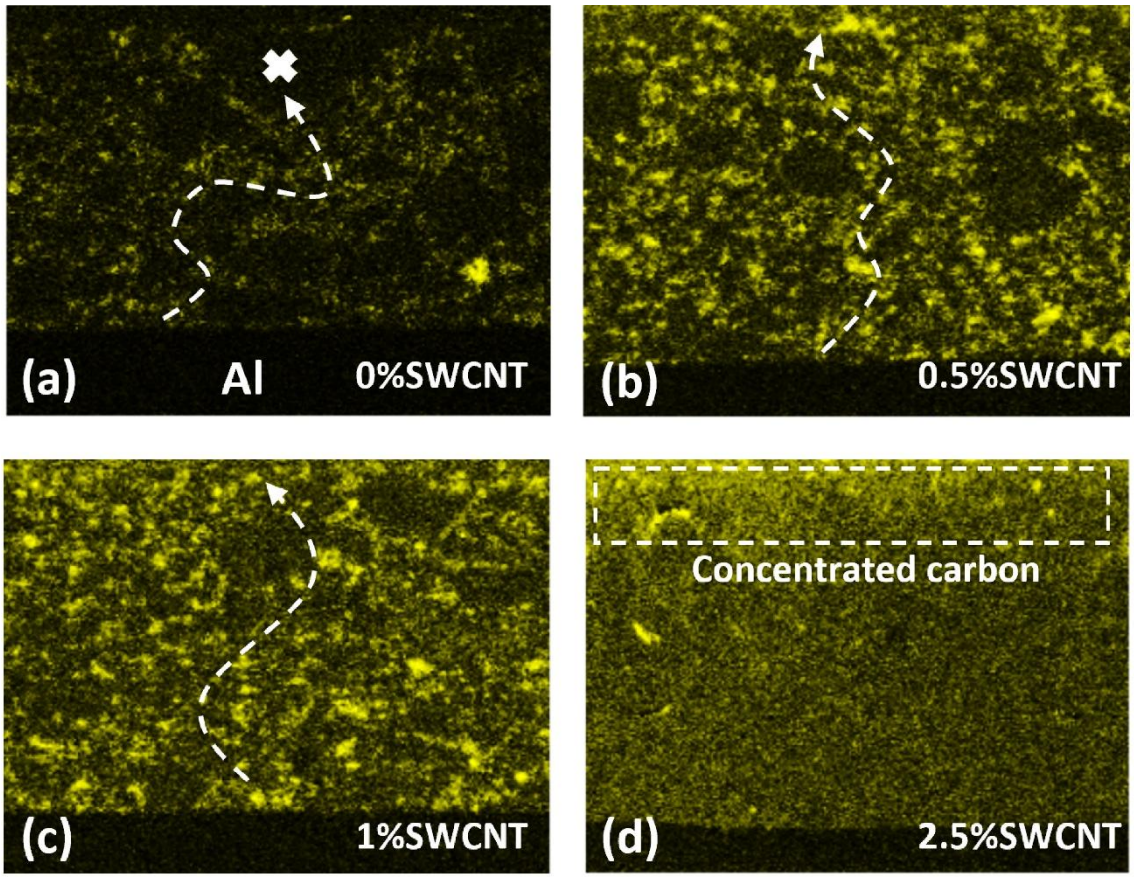

Figure 3.4: *Magnification of SEM-EDS elemental maps of carbon of LMFP73 coatings with different amount of SWCNT (see Figure 3.3). In detail:* ***(a)*** *LMFP-0%SWCNT,* ***(b)*** *LMFP-0.5%SWCNT,* ***(c)*** *LMFP-1%SWCNT, and* ***(d)*** *LMFP-2.5%SWCNT.*[86]

Overall, the preliminary evaluation of the prepared electrode coatings suggests the need to further optimize the slurry and electrode processing parameters to improve the distribution between active material, conductive additive and binder system in the electrode. However, to better understand the manufacturing-performance relationship, electrochemical testing of the prepared coatings was conducted to evaluate the effect of varying SWCNT dispersion contents and their deriving electrode properties on their electrochemical response. **Figure 3.5** and **Figure 3.6** report the electrochemical response of the prepared LMFP electrodes.

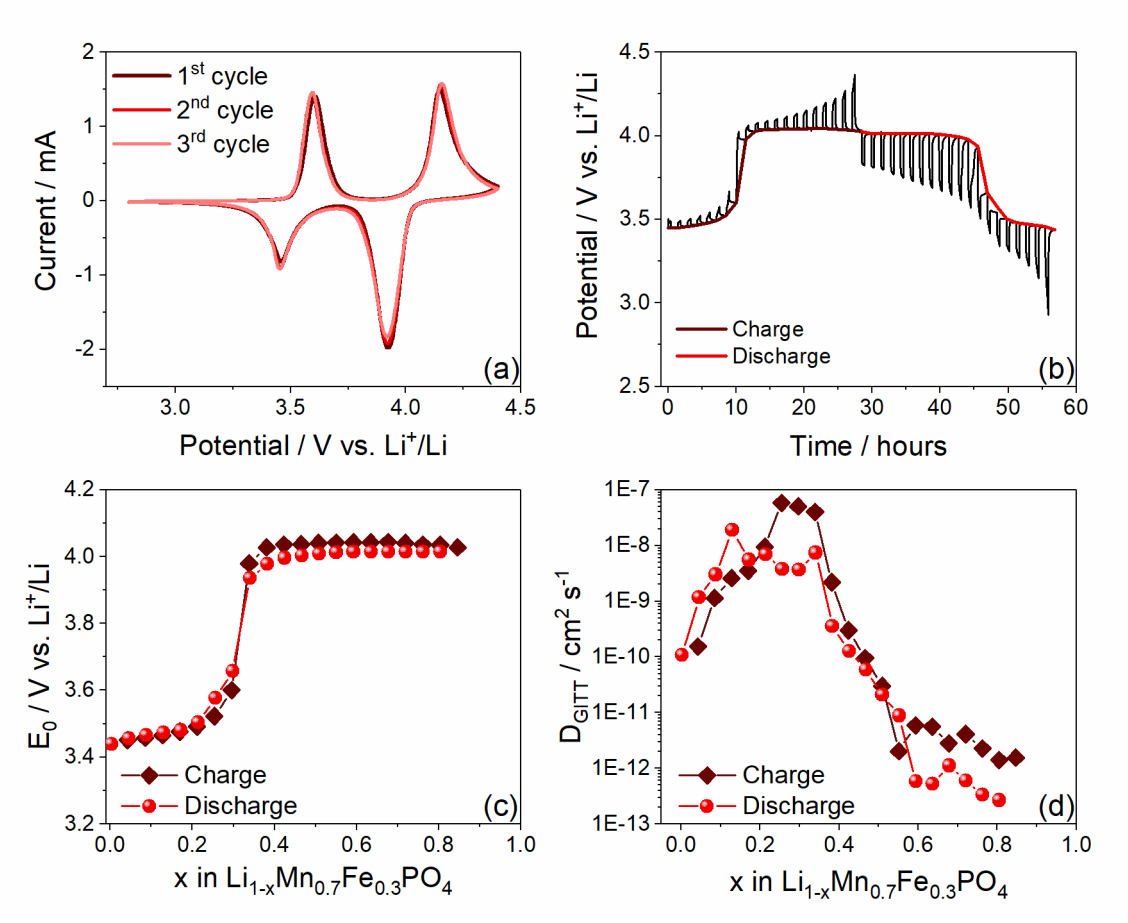

Figure 3.5: *Electrochemical characterization of LMFP73-0%SWCNT in Li half-cell at 25 °C.* ***(a)*** *CV profiles at 0.05 mV s^{-1} scan rate. Potential range 2.8 – 4.4 V vs. Li^+/Li.* ***(b)*** *GITT curve in terms of E_0 vs. time, with overlapped black curve reporting the overall time evolution of the potential during current pulses and relaxation steps.* ***(c)*** *Trend of E_0 vs. x determined from GITT curve.* ***(d)*** *Trend of D_{GITT} vs. x for Li^+ ions calculated using Equation (2.7). Applied pulses current: 17 mA g^{-1}; potential range 2.8 – 4.4 V vs. Li^+/Li. Adapted from [86].*

As a representative standard system, electrodes containing 0%SWCNTs were first used to benchmark the electrochemical processes using CV and GITT. **Figure 3.5(a)** shows the voltammogram of the LMFP73-0%SWCNT electrode exhibiting the characteristic anodic peaks centered at 3.6 and 4.15 V vs. Li^+/Li indicating the oxidation (de-lithiation) process, and the cathodic peaks centered at 3.45 and 3.9 V vs. Li^+/Li indicating the reduction (lithiation) process. The peaks at 3.6 and 3.45 V vs. Li^+/Li are ascribed to the Fe^{3+}/Fe^{2+} redox couple, while those at 4.15 and 3.9 V vs. Li^+/Li are attributed to

the Mn^{3+}/Mn^{2+} redox activity in LMFP73. It can be noted that the Fe and Mn redox couples are observed at slightly higher and lower potentials, respectively, compared to the bare $LiFePO_4$ and $LiMnPO_4$, aligning well with previous reports on mixed olivine cathodes and with the results obtained in **Chapter 2**.[79,98,298,307] Furthermore, the CV curves reveal considerable reversibility, modest polarization, and fairly fast Li^+ (de-)insertion kinetics process for the LMFP73 material.[307] To further investigate the ion transport kinetics, Li^+ diffusion coefficient was determined, according to the method proposed by Weppner and Huggins.[336] Prior to the experiment, four galvanostatic cycles were performed to allow interphase stabilization and minimize material activation effects. **Figure 3.5(b)** depicts the time evolution of the potential during titration (black curve), obtained by applying repeated current pulses/potential relaxation steps. A constant current of C/10 (1C = 170 mA g^{-1}) is used to assume the diffusion process in the surface layer, as evidenced in the Weppner and Huggins procedure.[336] The figure also shows the overlap of the quasi-equilibrium potential profiles (E_0) during charge (dark red) and discharge (light red) after relaxation. The trend of E_0 vs. x (exchange lithium degree in $Li_{1-x}Mn_{0.7}Fe_{0.3}PO_4$) is reported in **Figure 3.5(c)** and shows a reversible titration extended up to x = 0.84 under quasi-equilibrium conditions, which confirms high electrochemical activity and the beneficial effect of iron incorporation in $LiMn_{1-y}Fe_yPO_4$ phase on the Li^+ reversible exchange ability.[95,113] The Li^+ diffusion coefficient, D_{GITT} (cm^2 s^{-1}), was calculated using the data reported in **Figure 3.5(c)** and applying **Equation (2.7)**,[336] already reported and discussed in **Section 2.3**. **Figure 3.5(d)** reports the D_{GITT} during (de-)lithiation as a function of x for LMFP73. The results show the typical trend commonly reported for mixed olivine cathodes with a general decrease of diffusion coefficients for the de-lithiated phase at high x.[113,278] In particular, the figure depicts an initial increase of D_{GITT} in charge to a maximum value of ~ $5x10^{-8}$ cm^2 s^{-1} at x = 0.3, followed by a sharp decrease as x increases to a minimum value of ~ 10^{-12} cm^2 s^{-1}. Furthermore, D_{GITT} during discharge (lithiation) are slightly smaller than the values obtained during charge, likely due to the insulating character of the de-lithiated phase. Overall, the obtained D_{GITT} values for LMFP73 are slightly higher but comparable with those achieved in **Section 2.3** and other studies focusing on mixed olivines, suggesting favorable Li^+ diffusion kinetics.[113,278]

The effect of SWCNT dispersion amount on the electrochemical performance of LMFP73 electrodes was evaluated in Li half-cells, using 1 M $LiPF_6$ in EC:EMC (3:7 *v/v*%) with 1 wt.% VC containing electrolyte and 100 GSM electrode loading. The corresponding data are reported in **Figure 3.6**. Rate capability tests of the four samples were carried out by increasing the current from C/20 to 10C (1C = 170 mA g^{-1}) as shown in **Figure 3.6(a)**. All samples exhibited an initial capacity of about 150 mAh g^{-1} (88% of the theoretical value) that was reduced to about 2 mAh g^{-1} at 10C. However, an excellent recovery of the initial capacity was observed in all the samples as the current was reduced back to

C/20 after the consecutive cycles, indicating good rate capability and the stability of LMFP73 material upon the stress caused by high current loads.[366] Moreover, at high currents (above 1C), the electrodes containing 0.5% and 1% SWCNTs outperformed the bare electrodes without SWCNTs exhibiting higher capacity retention. Indeed, electrodes containing exclusively 2.5% SWCNTs (no C65 additive) resulted in poor performance at such higher rates as compared to electrodes with both C65 and SWCNT additives, in agreement with the conductivity data and the SEM cross-sectional analysis reported in **Table 3.4** and **Figure 3.3**, respectively.

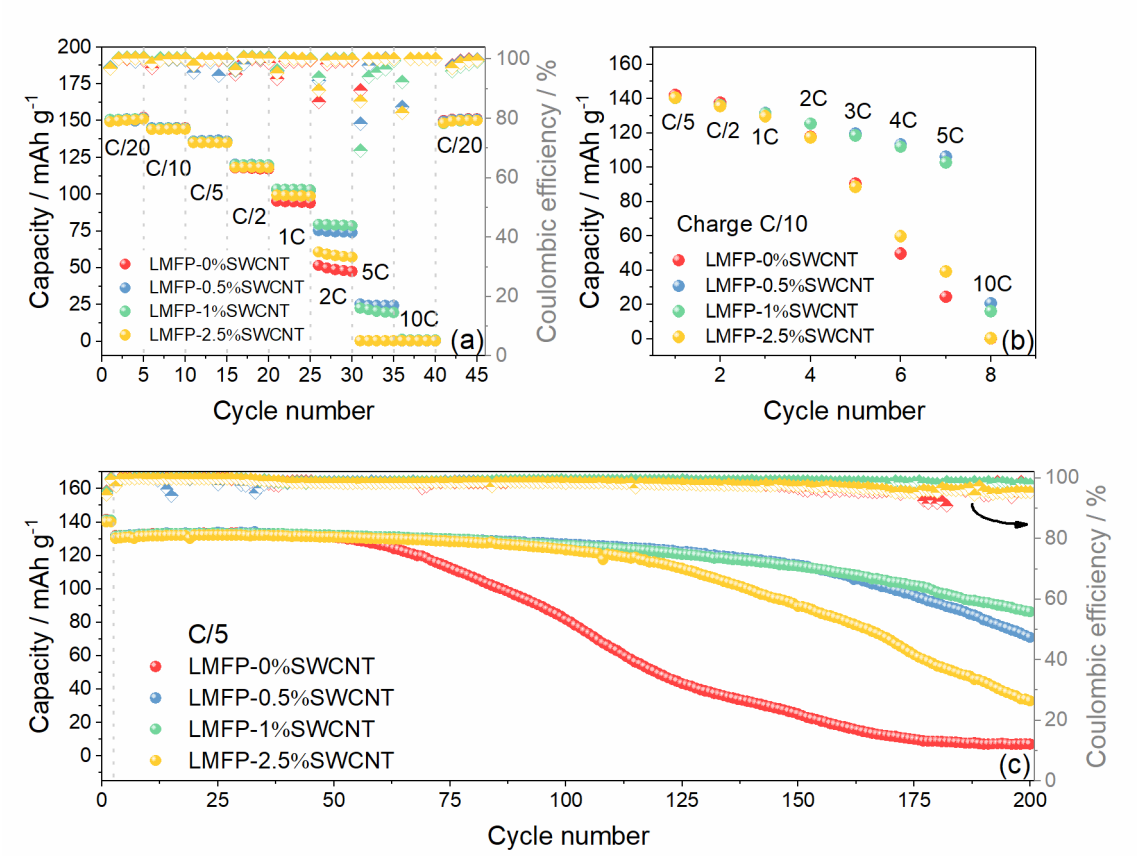

Figure 3.6: *Electrochemical characterization of LMFP73 coatings with different amount of SWCNT in Li half-cell at 25 °C. Cycling trend of* ***(a)*** *rate capability test performed at C/20, C/10, C/5, C/2, 1C, 2C, 5C, and 10C currents (1C = 170 mA g^{-1}) with discharge capacity in left-hand side y-axes and coulombic efficiency in right-hand side y-axes,* ***(b)*** *alternate current rate capability test performed charging the cell at C/10 and discharging it at C/5, C/2, 1C, 2C, 3C, 4C, 5C, and 10 C currents, and* ***(c)*** *prolonged galvanostatic test performed at the constant current rate of C/5 after 2 activation cycles at C/10 with discharge capacity in left-hand side y-axes and coulombic efficiency in right-hand side y-axes. Voltage range 2.8 – 4.4 V. Adapted from [86].*

To further investigate the effect of SWCNTs on the performance, an alternative rate capability test was performed in which the cell is charged at C/10 and discharged with increasing current loads up to 10C. **Figure 3.7** reports the voltage profiles corresponding to the electrodes obtained with the four formulations suggesting an increase in polarization as a consequence of current increase which lead to a decrease of discharge capacity from 140 mAh g^{-1} at C/5 for all the samples to about 20 mAh g^{-1}

at 10C for 0.5% and LMFP73-1%SWCNTs. Electrodes with 2.5%-SWCNT show a prominent degradation over cycling at increasing rates.

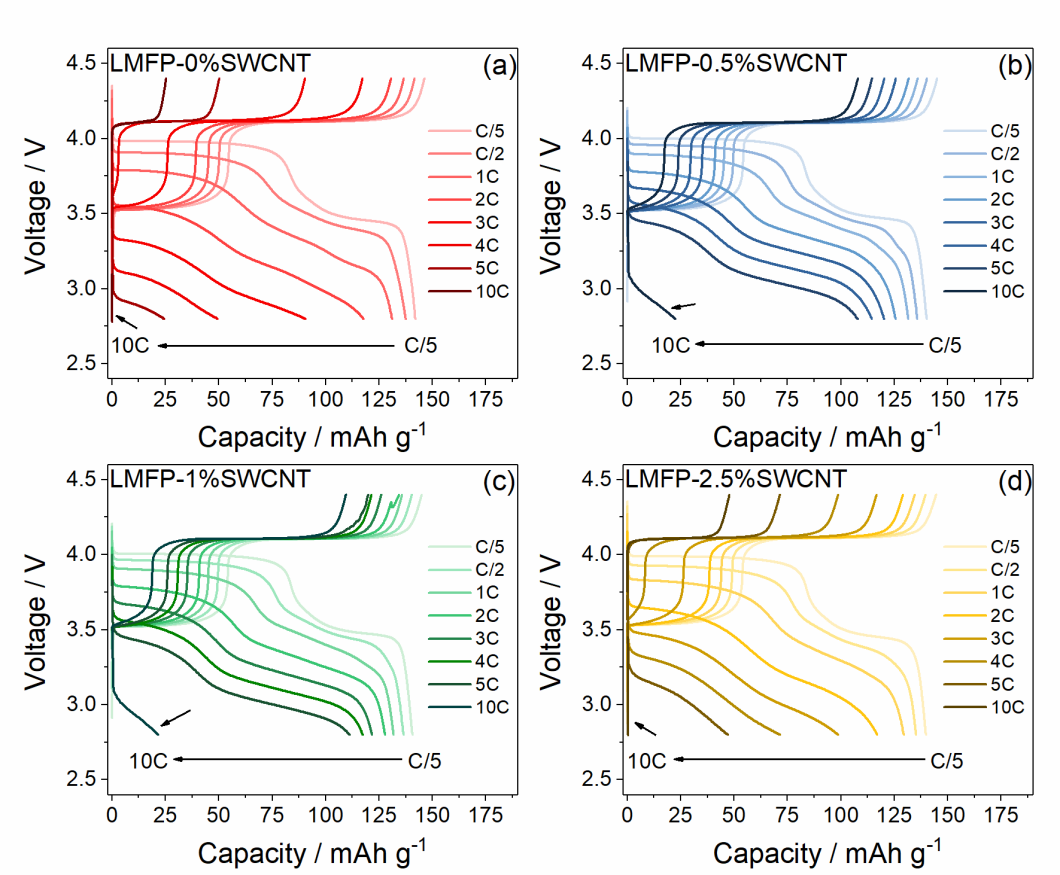

Figure 3.7: *Galvanostatic voltage profiles of LMFP73 coatings with different amount of SWCNT corresponding to cycling trends in Figure 3.6(b) performed charging the cell at C/10 and discharging it at C/5, C/2, 1C, 2C, 3C, 4C, 5C, and 10 C (1C = 170 mA g^{-1}), with arrows indicating the discharge profile at 10C. Voltage range 2.8 – 4.4 V. Test conducted at 25 °C.*[86]

The cycling trend shown in **Figure 3.6(b)** is further evidence of the beneficial effect of SWCNT incorporation, with the 0.5% and 1% SWCNTs containing electrodes maintaining discharge capacity values higher than 100 mAh g^{-1} up to 5C current. The stability of the electrochemical lithium (de-)insertion process is investigated by galvanostatic cycling at a constant rate of C/5 after 2 activation cycles performed at C/10. The corresponding voltage profiles (see **Figure 3.8**) reveal the expected shape for all the samples characterized by two well-defined plateaus at an average voltage of 3.55 and 4.1 V, ascribed to the Fe^{3+}/Fe^{2+} and Mn^{3+}/Mn^{2+} redox couples, respectively, in agreement with the CV of **Figure 3.5(a)** emphasizing that CNTs serve mainly as conductive additives without direct participation in the electrochemical process. Furthermore, the profiles show a maximum capacity of about 130 mAh g^{-1}, in full agreement with the rate capability results.

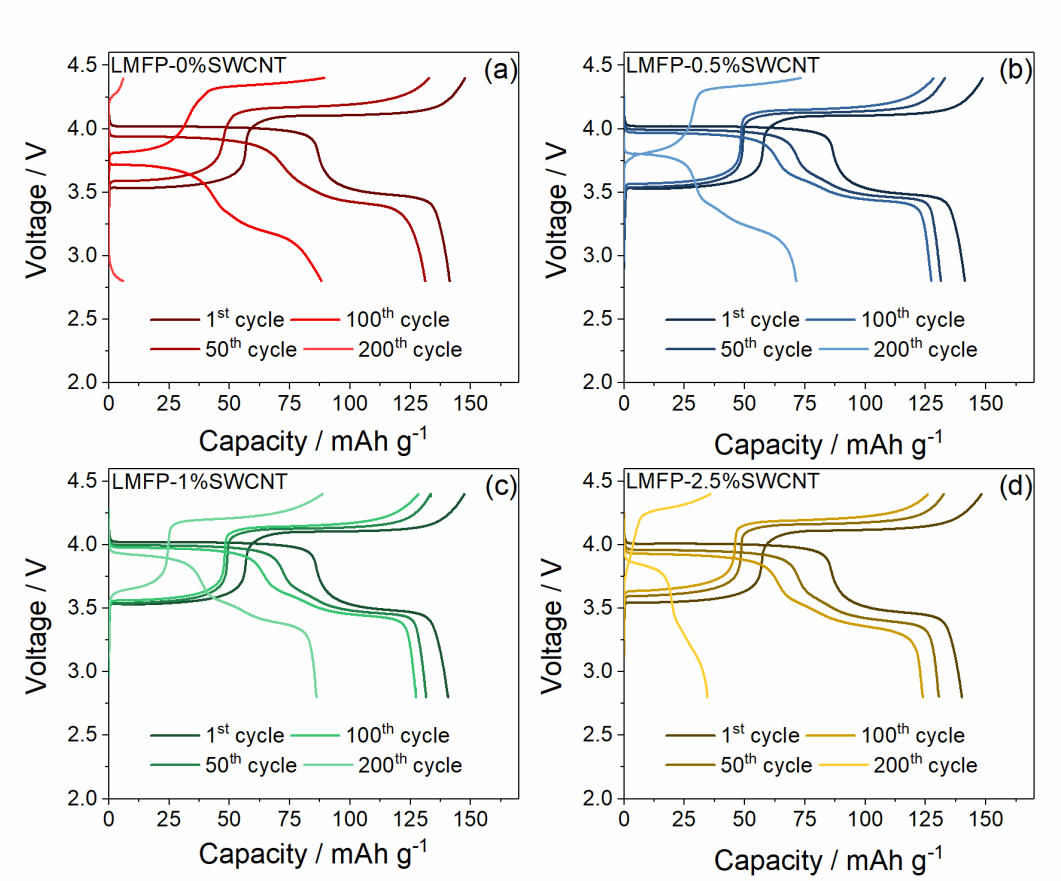

Figure 3.8: *Selected voltage profiles of LMFP73 coatings with different amount of SWCNT corresponding to cycling trends in Figure 3.6(c) performed at the constant current rate of C/5 (1C = 170 mA g^{-1}) after 2 activation cycles at C/10. Voltage range 2.8 – 4.4 V. Test conducted at 25 °C.*[86]

The cycling trend reported in **Figure 3.6(c)** shows different cycling stability for the different coatings. In particular, all samples present the same capacity trend up to about 75 cycles, from when the 0%SWCNT containing electrodes show a very rapid decrease in capacity up to complete deterioration. This is likely associated to the lower electronic conductivity and the poor mixing dispersion during electrodes processing, as evidenced earlier.[105] It is worth noting that the 2.5%SWCNT electrodes cycle longer, with capacity decays observed after about 125 cycles, indicating further the advantage of using solely CNTs rather than only C65.[382] Furthermore, the cells with intermediate amount of SWCNTs, *i.e.* LMFP73-0.5%SWCNT (blue dots) and the LMFP73-1%SWCNT (green dots), reveal better stability, with the latter one exhibiting an improved retention of about 67% after 200 cycles. Moreover, all the cells report coulombic efficiency of about 96% in the first activation cycle which further increases and reaches about 99% in the subsequent ones. The results of the formulation effect on LMFP73 cathode suggests LMFP73-0.5%SWCNT and LMFP73-1%SWCNT as the most promising candidates for further applications, with the latter presenting slightly higher conductivity and prolonged cycling stability than the former. Nevertheless, both electrodes reach 80% of the initial capacity retention, considered as a threshold value of state of

health,[245] after 170 cycles. Considering economic benefits of including less inactive materials and the satisfactory electrochemical performance, the 0.5%SWCNT formulation was selected over the LMFP73-1%SWCNT for further optimization studies.[245,246]

3.2.2 Investigation of the Impact of Slurry and Electrode Processing Parameters

The effect of the slurry mixing and coating parameters were investigated with the LMFP73-0.5%SWCNT electrode formulation optimized above. To improve the quality of the slurry mixing and resultant electrode coatings, the mixing procedure was modified by altering the sequence of slurry component addition while mixing (denoted as Mixing #2, **Figure 3.9(a)**) and compared with the previous mixing strategy (denoted as Mixing #1, see **Figure 3.2(a)**) at 50% solid content. The modified mixing strategy, labeled as Mixing #2, includes an additional mixing of C65 in NMP, to further improve carbon distribution within the mix and avoid particle agglomeration, thus improving slurry processability.[256] In detail, C65 and the first part of NMP were added into a pot and mixed for 5 mins at 2000 rpm. LMFP73 and the second part of NMP were then added and mixed for 5 mins at 2000 rpm. This was then followed by the addition of PVdF, SWCNT dispersion, and the third part of NMP, then by mixing for 5 mins at 2000 rpm. The addition of remaining NMP was done in single or multiple steps, followed by mixing for 5 mins at 2000 rpm to achieve the target solid content. The viscosity vs. shear rate profiles of the mixes prepared by the two procedures (**Figure 3.9(b)**) presented similar trends, exhibiting viscosity values of 7.8 Pa·s at 10 s^{-1} in both cases. The slightly higher viscosity values, compared to the one obtained previously for the LMFP73-0.5%SWCNT formulation (see **Table 3.2**), are due to the higher solid content adopted with Mixing #2. Further, the slurry coating speed was investigated to improve the homogeneity of the electrode coatings.[258] The electrode loadings achieved with various coating speeds were plotted and compared as shown in **Figure 3.9(c)**. It is worth noting that coatings prepared at various speeds via Mixing #1 exhibited slightly higher electrode loadings compared to the analogous coatings prepared with Mixing #2, which can be attributed to the flaws in Mixing #1, resulting in the non-homogenous dispersion of particles and larger variations in electrode loading (see **Figure 3.9(d-k)**). Even though the electrode loadings prepared with both mixing strategies follow a linearly increasing trend with an increase in coating speed, considering a target loading of 50 GSM, the coatings prepared with Mixing #2 at 6 mm s^{-1} achieved an electrode loading closer to the target and were selected for further process optimizations.

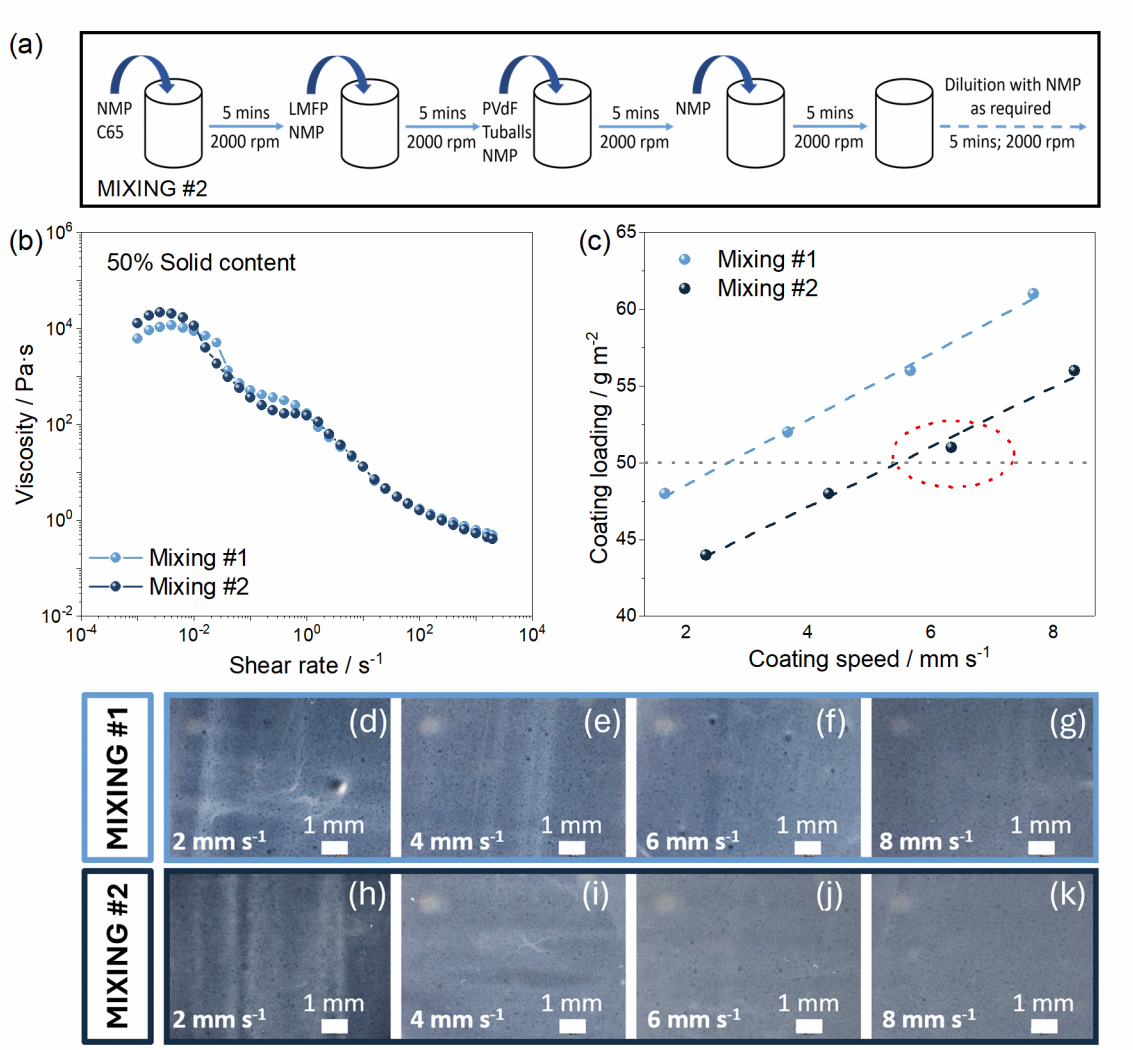

Figure 3.9: *Processing and manufacturing optimization of LMFP-0.5%SWCNT in terms of mixing and coating parameters.* ***(a)*** *Schematic representation of Mixing #2 procedure.* ***(b)*** *Trend of viscosity vs. shear rate of the slurries obtained from the two mixing strategies.* ***(c)*** *Trend of coating loading vs. coating speed of the samples obtained from the two mixing strategies. Optical microscope images of coatings obtained using* ***(d–g)*** *Mixing #1 and* ***(h–k)*** *Mixing #2 casted at different speeds. In detail:* ***(d, h)*** *2 mm* s^{-1}*,* ***(e, i)*** *4 mm* s^{-1}*,* ***(f, j)*** *6 mm* s^{-1}*,* ***(g, k)*** *8 mm* s^{-1}*.* [86]

Furthermore, the optical microscopy images of the calendered coatings prepared with Mixing #1 and Mixing #2 are shown in **Figure 3.9(d-g)** and **Figure 3.9(h-k)**, respectively. The coatings prepared with Mixing #2 exhibited improved homogeneity associated with an efficient dispersion of the slurry components, while particle agglomerates and streaks were evidently observed in the coatings prepared with Mixing #1. The effect was more evident for slower coating speeds. Indeed, the electrodes prepared with the lowest coating speed (*i.e.* 2 mm s^{-1} and 4 mm s^{-1}) for both Mixing #1 (panels **(d, e)**) and #2 (panels **(h, i)**) revealed inhomogeneous areas evidenced by brighter lines visible in the images. Instead, the electrodes prepared with coating speeds of 6 and 8 mm s^{-1} via Mixing #2 (panels **(j, k)**) exhibited improved homogeneity without defects observed on the electrodes' surface. All the coatings analyzed displayed good bendability with a mandrel size of 2 mm diameter, as

demonstrated in **Figure 3.10(a-h)**, indicating the absence of flaking and damage to the electrodes (level 1, see **Table 3.3**).

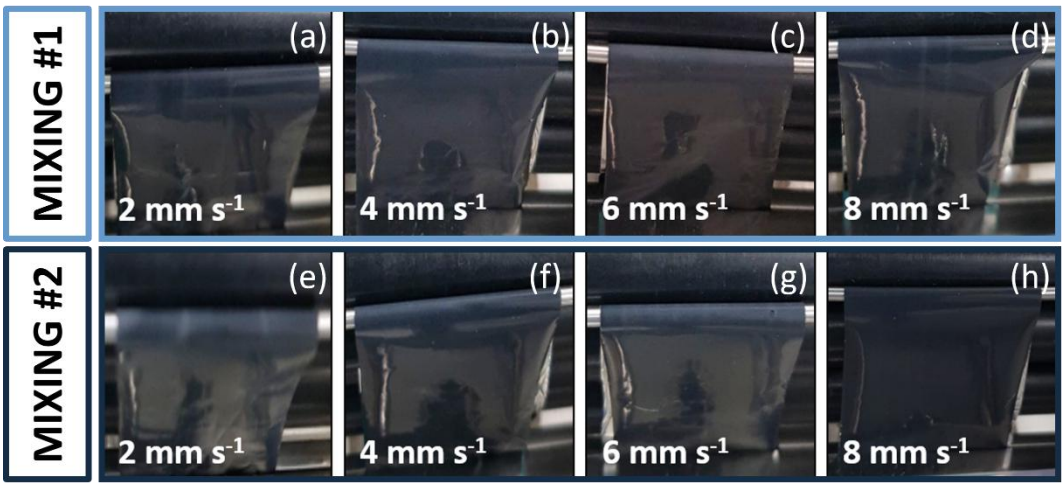

Figure 3.10: *Photographic images of* ***(a–d)*** *Mixing #1 and* ***(e–h)*** *Mixing #2 coating sheets casted at different speeds subjected to cylindrical mandrel bend test. In detail:* ***(a, e)*** *2 mm* s^{-1}, ***(b, f)*** *4 mm* s^{-1}, ***(c, g)*** *6 mm* s^{-1}, ***(d, h)*** *8 mm* s^{-1}.[86]

As solid content represents a critical parameter in formulation development studies, affecting rheology, mixing efficiency and homogeneity of the slurries, further studies were conducted to evaluate its effects.[255] To determine the impact of solid content, the mixing strategy and the coating speed of the formulations were fixed as previously optimized (Mixing #2, 6 mm s^{-1}) and three different solid contents, *i.e.* 40%, 50%, and 60%, for the LMFP73-0.5%SWCNT formulation were investigated. **Figure 3.11(a)** reports the viscosity trends of the three electrode formulations, where a higher viscosity is observed for the formulation with 60% solid content and comparatively lower viscosities are observed as the solid content goes down to 40%. The observed viscosity values for 40%, 50%, and 60% solid content are 2.1, 12.9, and 72.2 Pa·s respectively at 10 s^{-1}, highlighting the importance of slurry viscosity to guarantee good processability of the electrode coatings, particularly at higher solid contents.[374] The photographic images of the calendered electrode coatings (**Figure 3.11(b-d)**) with a target electrode loading of 50 GSM and their corresponding mandrel bend test (**Figure 3.11(e-g)**) exhibit severe surface inhomogeneity at 60% solid content (panel **(d)**) compared to 40% and 50% (panels **(b)** and **(c)**, respectively), ascribed to the improper mixing and agglomeration of the slurry components at higher solid content. All the electrode samples exhibit good bendability with a 2 mm mandrel, owing to the low target electrode loading (50 GSM) as observed previously.

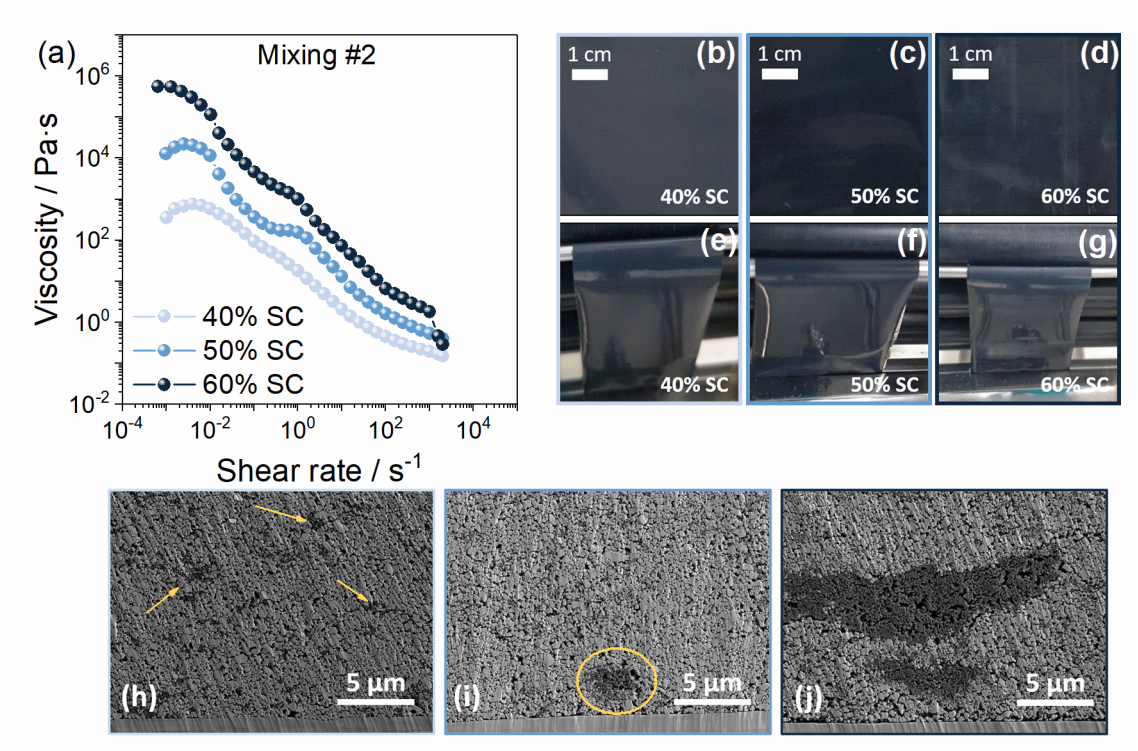

Figure 3.11: *Effect of solid content in formulation optimization of LMFP-0.5%SWCNT slurries. Mixing #2, coating speed 6 mm s^{-1}.* ***(a)*** *Trend of viscosity vs. shear rate of the slurries prepared with the three selected solid content. Photographic images of* ***(b–d)*** *electrode coatings and* ***(e–g)*** *coatings subjected to cylindrical mandrel bend test. In detail:* ***(b, e)*** *40% SC,* ***(c, f)*** *50% SC,* ***(d, g)*** *60% SC. cx-SEM images of* ***(h)*** *40% SC,* ***(i)*** *50 % SC, and* ***(j)*** *60% SC electrodes.*[86]

Further, the quality of the electrode coatings with varying solid content was evaluated by assessing the cx-SEM images of the electrodes recorded after calendering. The electrode obtained with 60% solid content exhibited significantly large darker areas (panel **(j)**), ascribed to the agglomerates of SWCNTs resulting from inefficient mixture of the slurry components. The electrode coatings with 40% solid content revealed evident discontinuities consisting of voids and cracks (panel **(h)**, indicated with yellow arrows). This is due to weak inter-particle cohesion and lack of optimal adhesion between the particles and the current collector, ascribed to the dilute and flowy liquid-like slurry at low solid contents.[256] At 50% solid content, the electrode exhibited the best surface homogeneity without any crack formation (panel **(i)**) compared to 40% and 60% solid contents. However, small, less occurring areas of non-homogenously distributed carbon were observed in the electrode (highlighted in yellow), suggesting the requirement for further solid content optimization. The best compromise of viscosity, optimal mixing and particles cohesion was identified when adopting 46% solid content retaining a processable viscosity of 6.8 Pa·s at10 s^{-1}.

The electrochemical performance of the optimized LMFP73-0.5%SWCNT electrodes was evaluated, in comparison with the results obtained with electrodes produced before optimization (see **Figure 3.2**

for details). The results of the comparison in terms of morphological and electrochemical features are reported in **Figure 3.12**.

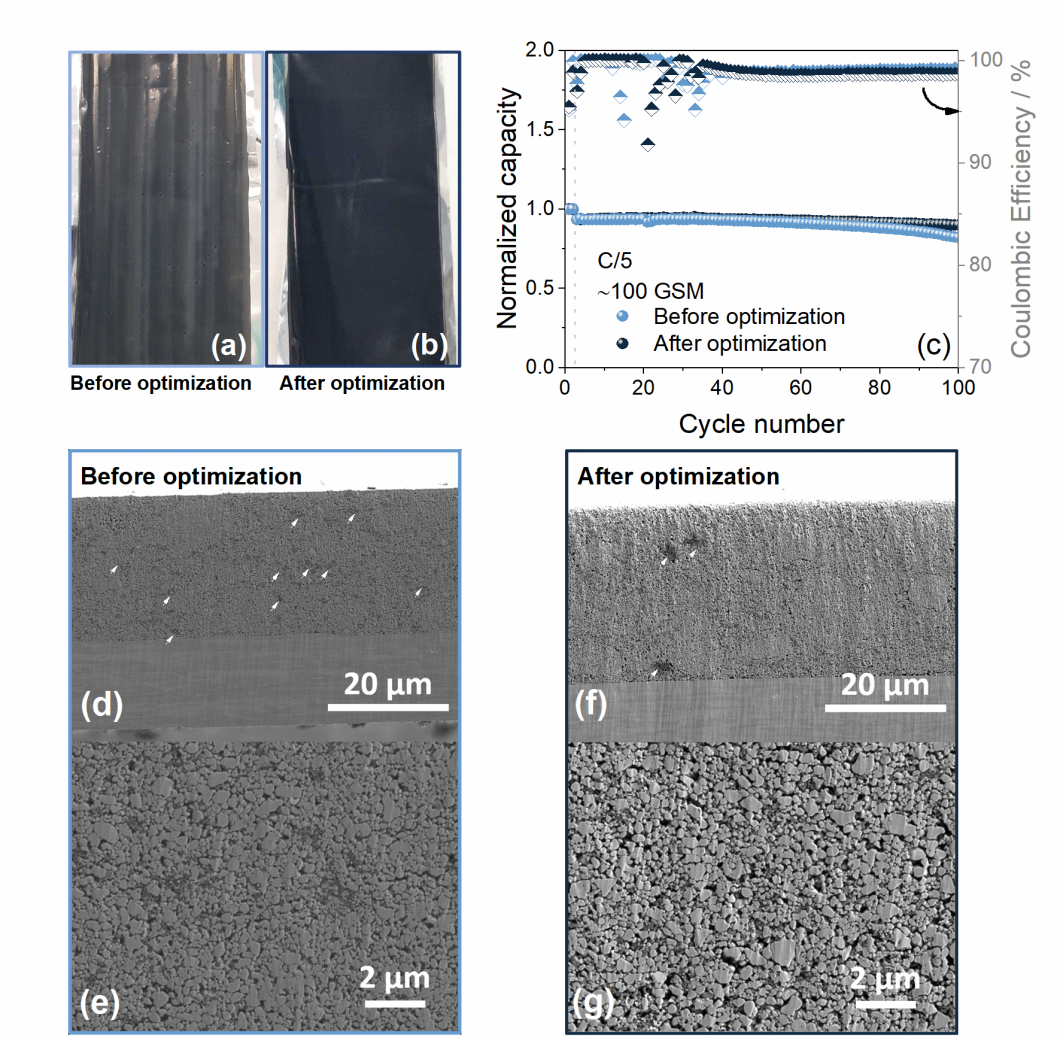

Figure 3.12: *Comparison of LMFP-0.5%SWCNT coatings properties before and after optimization. Photographic images of coating sheets* ***(a)*** *before and* ***(b)*** *after the optimization process.* ***(c)*** *Electrochemical performance in Li-cell at 25 °C in terms cycling trend of prolonged galvanostatic test performed at the constant current rate of C/5 (1C = 170 mA g^{-1}) after 2 activation cycles at C/10 with normalized discharge capacity in left-hand side y-axes and coulombic efficiency in right-hand side y-axes. Voltage range 2.8 – 4.4 V. cx-SEM images of the electrodes at different magnification* ***(d, e)*** *before and* ***(f, g)*** *after the optimization process.*[86]

The photographic images of the coatings before and after optimization, shown in **Figures 3.12(a)** and **3.12(b)**, respectively, reveal an evident improved quality of the electrodes. Defect-free coatings were attained with the optimized mixing procedure against the surface inhomogeneity characterizing the coating obtained with the first mixing strategy. However, this difference was not clearly reflected at the microstructural level or in the electrochemical response observed in coin cells. The cycling trend of the electrodes in half-cells is reported in **Figure 3.12(c)**, with normalized capacities to avoid the possible capacity discrepancies due to small variations of electrode loadings (gravimetric capacity at the first cycle is 141 mAh.g^{-1} and 145 mAh g^{-1} for the electrodes before and after optimization,

respectively). The electrodes exhibit similar capacity retention until 80 cycles (88% and 95% before and after optimization, respectively), with a coulombic efficiency of 95% in the first activation cycle further increased from about 97% to 99% during the subsequent cycles. It is worth mentioning that the low coulombic efficiencies observed are attributed to an unstable solid-electrolyte interphase (SEI) at the lithium metal electrode and that higher efficiencies are expected in full coin-cell, as it will be shown later. In addition, between cycles 20-40 destabilized efficiency was observed, that may be ascribed to possible gas evolution inside the cells.[229] Moreover, the cx-SEM images of the coatings before (panels **(d, e)**) and after (panels **(f, g)**) optimization depict a similar morphology of the electrodes, without the presence of significant cracking or inhomogeneity. The electrodes obtained before optimization showed several small agglomerations of particles (some of them highlighted by white arrows in **Figure 3.12(d)**), while the electrodes obtained after optimization showed a reduced number of agglomerates, however with larger areas. While the differences observed at coin cell level may be considered minor, it is important to consider that the electrochemical performance would be significantly impacted if evaluated in large-format cells employing electrodes prepared with the first mixing strategy. This highlights the challenges and complexity involved in scaling up electrode production. Inhomogeneous electrodes may indeed strongly affect cell performance, especially of cylindrical cells, which require larger and longer homogeneous electrodes.[245,257,367]

3.2.3 Investigation of the Impact of Electrode Loading and Upscaling to Single Layer Pouch Cells

The optimized LMFP73-0.5%SWCNT formulation and Mixing strategy #2 at a coating speed of 6 mm s^{-1}, and 46% solid content were adopted to produce electrodes with higher loadings up to 250 GSM. The corresponding electrochemical responses were evaluated at coin cell level, as reported in **Figure 3.13**. The electrodes' mechanical properties were evaluated through cylindrical mandrel bend test, and the corresponding photographic images are reported in **Figure 3.13(a-d)**. The coatings exhibited lower bendability at higher electrode loadings, as expected. The electrode coating with 100 GSM (panel **(a)**) showed good bending features with no flaking or damage (level 1, see **Table 3.3**), while the 250 GSM coating (panel **(d)**) revealed severe cracking and flaking (level 4, see **Table 3.3**). The poor mechanical features can affect the structural integrity of electrodes leading to cracking, delamination, and poor electrical contact, which can significantly hinder the electrochemical performances and reduce the cycle life, negating the benefits achieved with increased active material content.[372]

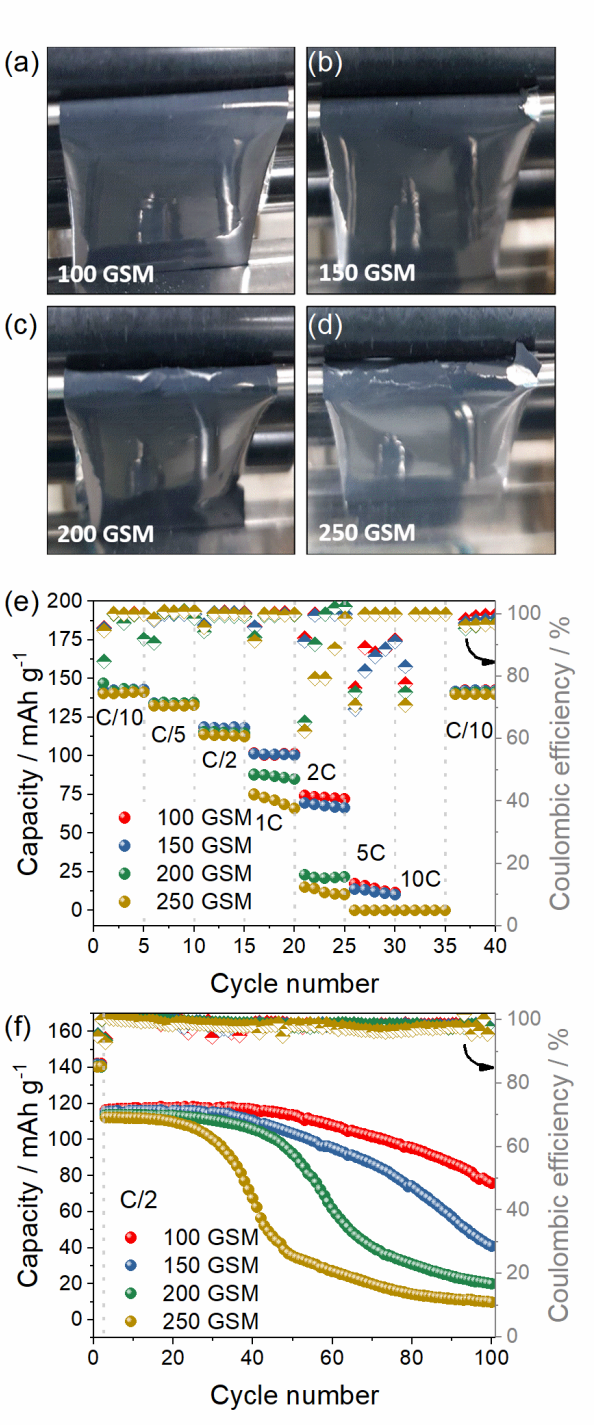

Figure 3.13: *Mechanical and electrochemical characterization in Li half-cell at 25 °C of LMFP-0.5%SWCNT electrodes with different loadings.* ***(a–d)*** *Photographic images of coating sheets subjected to cylindrical mandrel bend test:* ***(a)*** *100 GSM,* ***(b)*** *150 GSM,* ***(c)*** *200 GSM,* ***(d)*** *250 GSM. Cycling trend of* ***(e)*** *rate capability test performed at C/10, C/5, C/2, 1C, 2C, 5C, and 10C currents (1C = 170 mA g^{-1}) and* ***(f)*** *prolonged galvanostatic test performed at the constant current rate of C/2 after 2 activation cycles at C/10 with discharge capacity in left-hand y-axes and coulombic efficiency in right-hand y-axes. Voltage range 2.8 – 4.4 V.*[86]

The electrochemical responses of the prepared LMFP73-0.5%SWCNT high-loading electrodes were evaluated in Li half-cells by galvanostatic cycling, with results shown in **Figure 3.13(e, f)**. Rate capability tests were carried out by progressively increasing the current from C/10 to 10C (1C = 170 mA g^{-1}) and finally switching back to C/10, as reported in **Figure 3.13(e)**. The corresponding voltage

profiles are provided in **Figure 3.14**. Well-defined voltage plateaus ascribed to Fe^{3+}/Fe^{2+} and Mn^{3+}/Mn^{2+} redox couple were observed at lower current rate for all the samples retaining 140 mAh g^{-1} at C/10, however an increased ohmic polarization was evident at higher currents leading to a complete loss of capacity at 10C in all the cells.

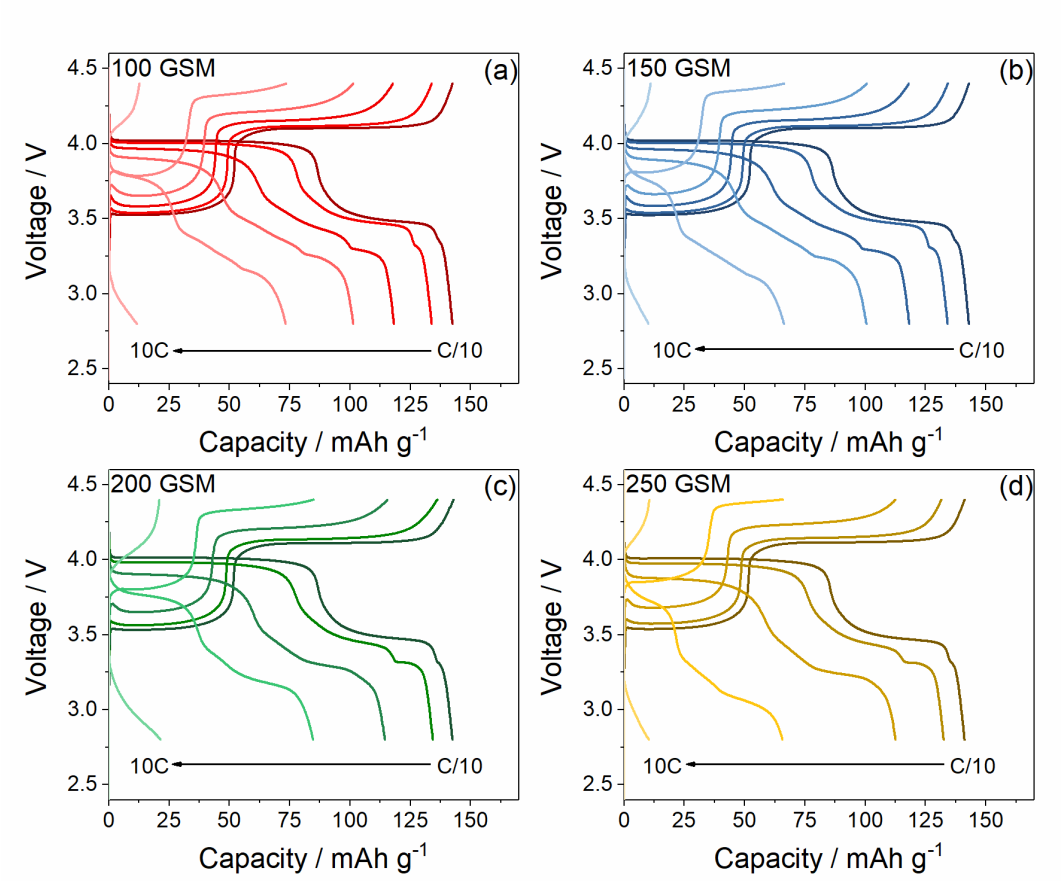

Figure 3.14: *Galvanostatic voltage profiles of LMFP-0.5%SWCNT electrodes with different loadings corresponding to cycling trends in Figure 3.13(e) performed at C/10, C/5, C/2, 1C, 2C, 5C, and 10C current rates (1C = 170 mA g^{-1}). Voltage range 2.8 – 4.4 V. Test conducted at 25 °C.*[86]

The cycling trend in **Figure 3.13(e)** reveals the recovery of the initial capacity of about 140 mAh g^{-1} when lowering back the current at C/10. On the other hand, the cells containing the heavier cathodes showed lower capacity at the high current rates starting from 1C, thus suggesting lower stability caused by the stress of raising the currents, also ascribed to the possible deterioration of the electrodes.[366,382,383]

The stability of the electrochemical Li^+ (de-)insertion process was further investigated by galvanostatic cycling at a constant current rate of C/2, after two activation cycles at C/10 with the corresponding voltage profiles reported in **Figure 3.15**. As expected from the mechanical bend test results, the lower loading electrode (*i.e.* 100 GSM) showed improved cyclability and capacity retention (*i.e.* 70% after 100 cycles, **Figure 3.13(f)**), while increased loading led to faster deterioration

and capacity fade.[372] On the other hand, all the cells present coulombic efficiency of about 94% at the first activation cycle, which increases and reaches 99% in the subsequent ones.

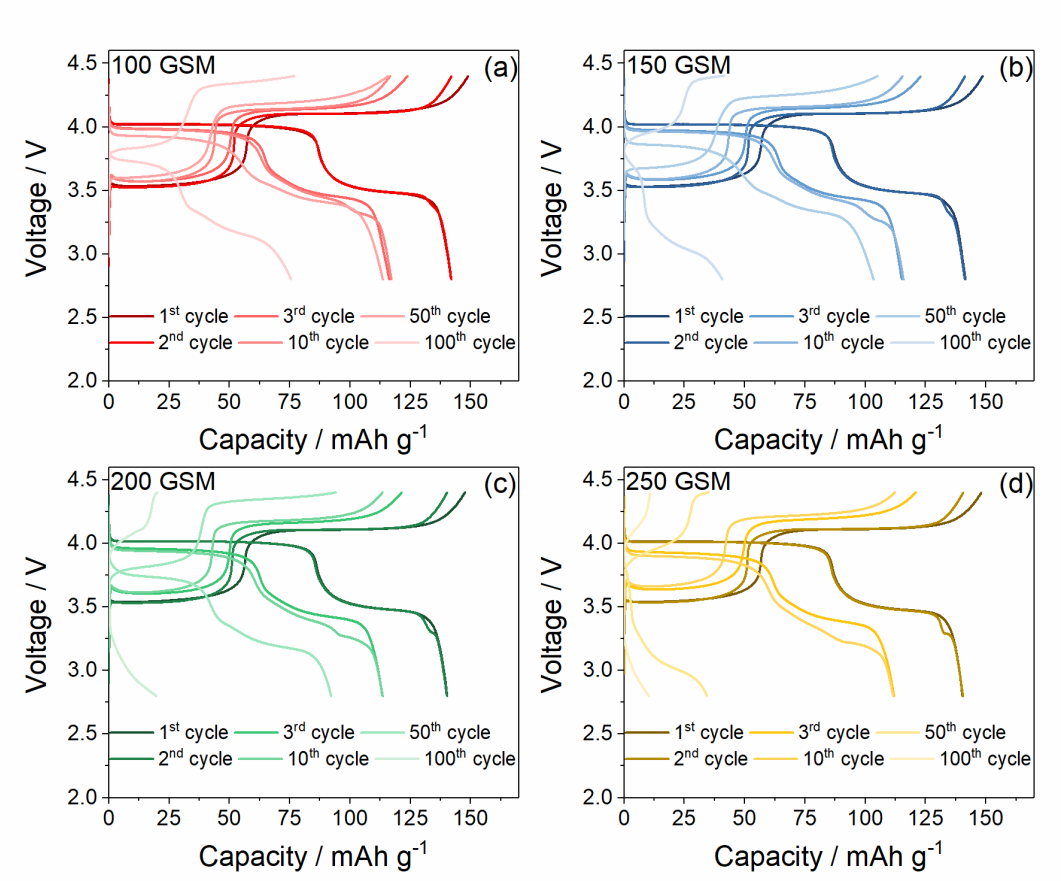

Figure 3.15: *Selected voltage profiles of LMFP-0.5%SWCNT electrodes in Li half-cells with different loadings corresponding to cycling trends in Figure 3.13(f) performed at the constant current rate of C/2 (1C = 170 mA g^{-1}) after 2 activation cycles at C/10. Voltage range 2.8 – 4.4 V. Test conducted at 25 °C.*[86]

While 250 GSM is a substantial electrode loading, it is also worth considering that the low stability of the heavier electrode in half-cell configuration could be also affected by the presence of lithium metal, which may favor possible side reaction and electrodes degradation that could instead be reduced in full-cell configuration.[279] In this regard, the electrochemical performance of all the cells prepared with LMFP73-0.5%SWCNT samples with different loadings were tested in coin-type full-cells by using graphite as anode material and a constant current of C/5 as referred to the cathode (1C = 170 mA g_{cat}^{-1}). The negative to positive areal capacity ratio (N/P) was settled at 1.1 for all cells and the results are reported in **Figure 3.17**. The gravimetric capacity upon cycling for the different mass loadings is reported in **Figure 3.17(a)** (corresponding voltage profiles are reported in **Figure 3.16**), while the areal capacity is reported in **Figure 3.17(b)**. The voltage profiles reflect the combination of the respective cathode and anode signatures, thus leading to a behavior fully in line with the one related to LMFP73 half-cells, characterized by two voltage plateaus at about 3.4 and 4 V ascribed to Fe^{3+}/Fe^{2+} and Mn^{3+}/Mn^{2+} redox couples, respectively. Furthermore, the profiles reveal a maximum

gravimetric capacity of about 135 mAh g^{-1} for all the samples, aligned with the rate capability results of the Li half-cells (see **Figure 3.13(e)**).

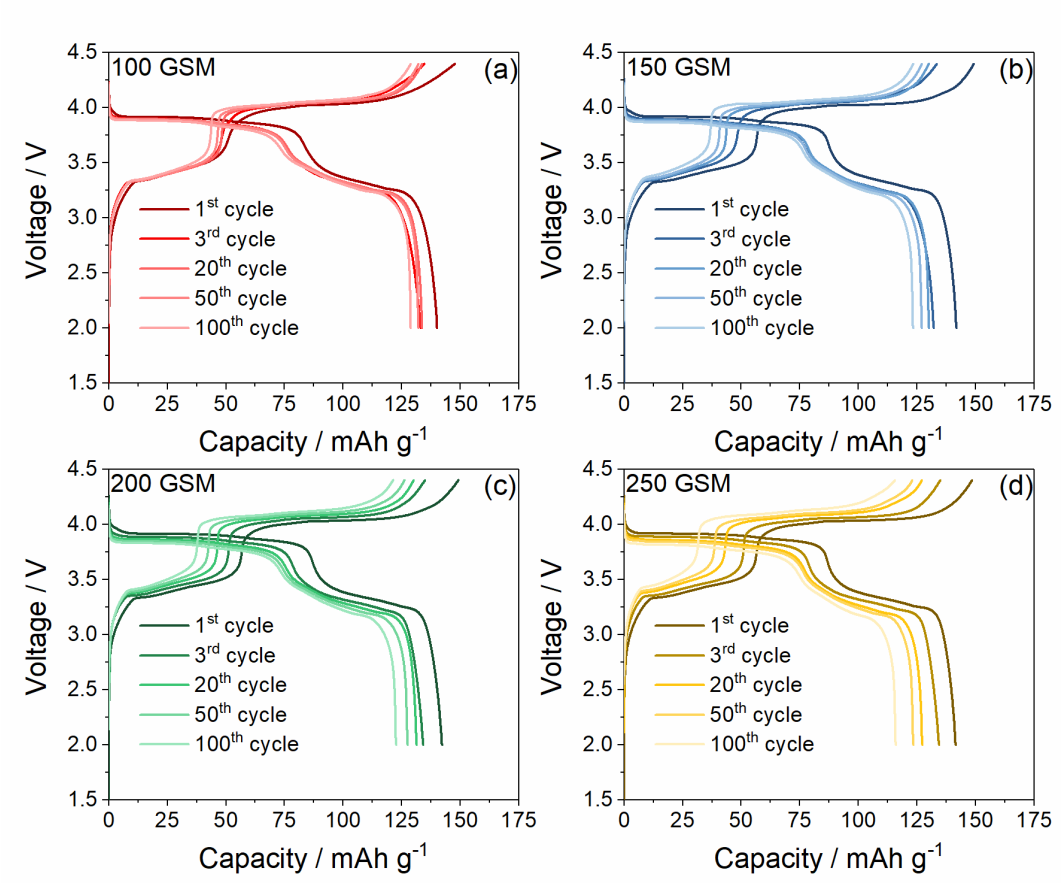

Figure 3.16: *Selected voltage profiles of Graphite|LMFP-0.5%SWCNT full-cells with different cathode loadings corresponding to cycling trend in Figure 3.17(a) performed at the constant current rate of C/5 (1C = 170 mA g_{cat}^{-1}) after 2 activation cycles at C/10. Voltage range 2.0 – 4.4 V. Test conducted at 25 °C.*[86]

The cycling trend of the full-cells (**Figure 3.17(a)**) reveals similar stability for all the samples, confirming the improvement of the electrochemical response of heavier electrodes when avoiding the use of Li metal.[279] In particular, the cells exhibit remarkable coulombic efficiency of about 99.8% after activation cycles, with a maximum capacity retention of 96% for the cell adopting 100 GSM electrodes after 100 cycles. However, the cells containing electrodes with loadings of 200 and 250 GSM also show remarkable capacity retention of 89% and 86%, respectively. Furthermore, heavier electrodes exhibit higher areal capacity (**Figure 3.17(b)**) with values approaching 2.75 and 3.25 mAh cm^{-2} for the 200 and 250 GSM samples, respectively. Obtaining high areal capacities with satisfactory cycling stability is of outmost importance for the successful scaling up of cell prototype. Indeed, the industrially relevant loadings herein investigated also enable the matching with anodes presenting realistic loadings.[309,384]

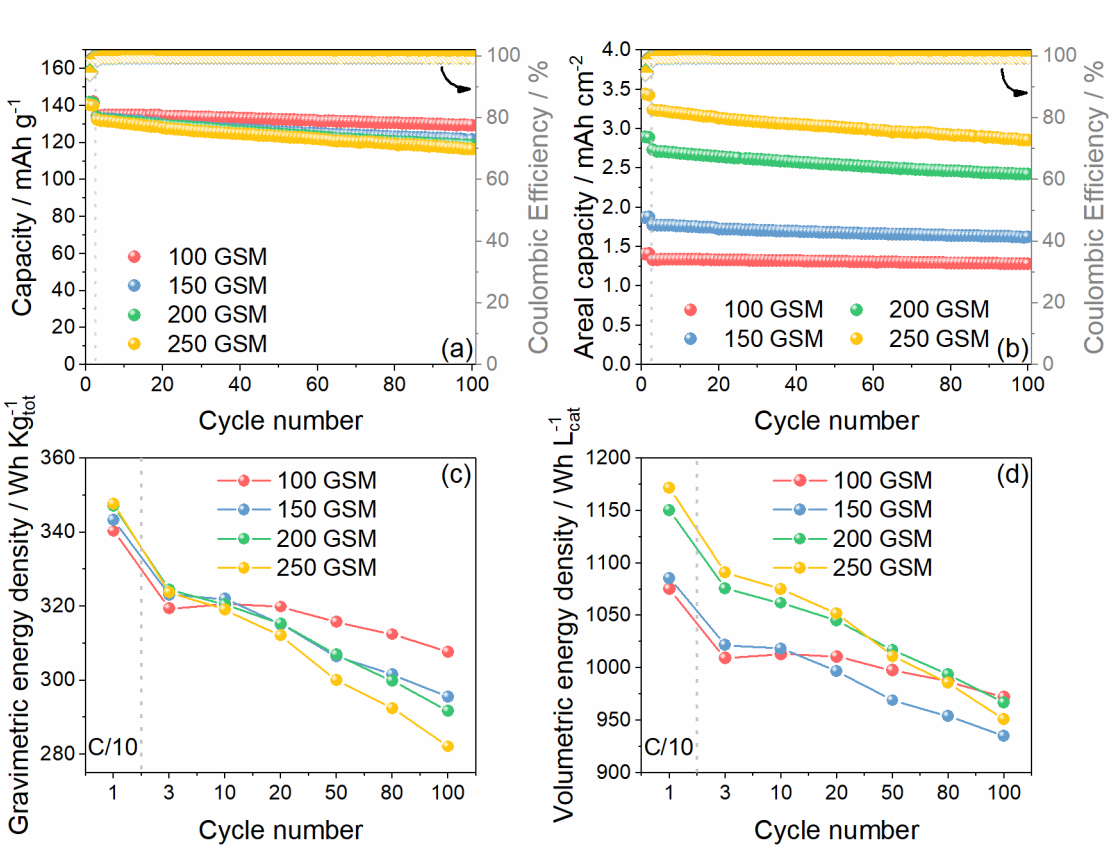

Figure 3.17: *Electrochemical response of Graphite|LMFP-0.5%SWCNT coin cell-type full cells with different cathode loadings at 25 °C. Cycling trend of prolonged galvanostatic test performed at the constant current rate of C/5 (1C = 170 mA g_{cat}^{-1}) after 2 activation cycles at C/10 with* ***(a)*** *gravimetric and* ***(b)*** *areal discharge capacity in left-hand side y-axes and coulombic efficiency in right-hand side y-axes. Voltage range 2.0 – 4.4 V. Trend of calculated* ***(c)*** *gravimetric and* ***(d)*** *volumetric energy density for different selected cycles.*[86]

Gravimetric (**Figure 3.17(c)**) and volumetric (**Figure 3.17(d)**) energy densities were calculated integrating the capacity as a function of the cell voltage for selected cycles dividing by the total mass of the coatings (anode + cathode, neglecting the current collectors) and by the volume of the cathode composite layer, respectively. At the electrode level, the cells reveal high initial gravimetric energy density (of about 325 Wh Kg_{tot}^{-1}) for all the samples, which decreases as the cycles progress, due to the associated loss of capacity and different retention. Moreover, the volumetric energy density follows the same trend, with higher initial values of about 1090 Wh L_{cat}^{-1} for the cells adopting the higher areal loading. Particularly, the energy density herein obtained is higher than others achieved in literature at the active material level for LFP and mixed olivine cathodes.[98,241,256] Furthermore, the energy density achieved for the full cell is also comparable with the ones obtained in configurations employing cathodes with higher working voltage (i.e. $LiCoO_2$, $LiNi_{0.8}Mn_{0.1}Co_{0.1}O_2$),[385,386] confirming the manufacturing-performance correlation in the improved results, also compared with higher energy density systems. It is worth noting that the gravimetric energy density of the entire cell should be lower, as the contribution of the other components (*e.g.*

current collectors, electrolyte, and cell casing) on the total weight are not considered.[387] Nevertheless, the optimized electrode fabrication process developed has enabled satisfactory results also for high areal capacity electrodes, revealing the possibility to implement high loading cathodes in full-cells with low losses in capacity retention and energy density when compared to lower loading cathodes. However, considering the lower structural stability of the 250 GSM cathodes, to mitigate potential detrimental issues upon cycling,[384] electrodes with 200 GSM loading were chosen as a suitable choice for the upscaling of the cell into single layer pouch (SLP) cell formats.

Figure 3.18 reports the electrochemical response for SLP cells cycled at a constant current of C/2 referred to the cathode (1C = 150 mA g_{cat}^{-1}), after 2 activation cycles at C/5. 0.1 Ah SLPs were obtained with an N/P ratio of 1.1 by using 0.6 g of electrolyte per cell.

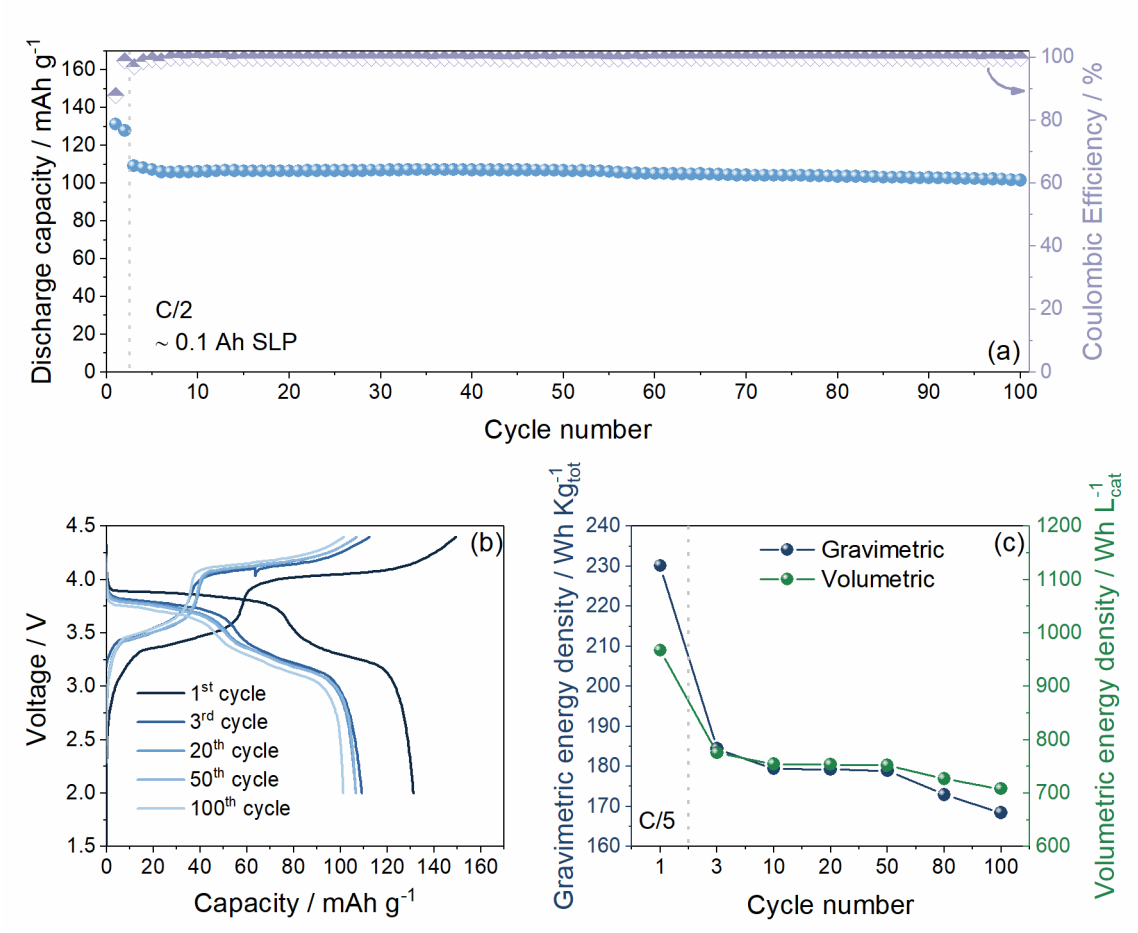

Figure 3.18: *Electrochemical characterization of Graphite|LMFP-0.5%SWCNT single layer pouch cell 25 °C.* ***(a)*** *Cycling trend and* ***(b)*** *selected voltage profiles of prolonged galvanostatic test performed at the constant current rate of C/2 (1C = 150 mA* g_{cat}^{-1}*) after 2 activation cycles at C/5, with discharge capacity in left-hand side y-axes and coulombic efficiency in right-hand side y-axes. Voltage range 2.0 – 4.4 V.* ***(c)*** *Trend of calculated gravimetric and volumetric energy density for different selected cycles.*[86]

The cycling trend (**Figure 3.18(a)**) reveals remarkable cycling stability with a capacity retention of 93% after 100 cycles. Coulombic efficiency values of 97.1% are recorded after the first activation

cycles, stabilizing to a value of 99.8% after 10 cycles. The voltage profiles (**Figure 3.18(b)**) reveal the same features described above for full coin-cells, with the presence of two well-defined voltage plateaus. Furthermore, the profiles exhibit a maximum capacity of about 110 mAh g^{-1} after activation, in full agreement with the rate capability data of the Li half-cells (**see Figure 3.13(e)**). However, considering the higher current rate adopted for the test, the gravimetric and volumetric energy densities (**Figure 3.18(c)**) of the cell are lower than the one reported for coin cells in **Figure 3.17(c, d)** (about 185 Wh Kg_{tot}^{-1} compared to 320 Wh Kg_{tot}^{-1}), despite showing comparable trends. This suggests the possible need of optimization of the SLP cell assembly steps, including improved electrode alignment and optimized electrolyte amount.[246,261,384] Indeed, it is worth noting that the electrochemical response is also cell-format dependent.[309] SLPs for instance allow for degradation processes to occur in a more practical cell environment. An example is represented by gas evolution, which may not affect substantially coin cell cycling, while may be more evident in upscaled cell formats. In addition, while the reported results focus on the manufacturing-performance correlation, it is also important to consider that the electrolyte adopted has not been optimized. As a consequence, degradation mechanisms, including potential manganese dissolution or instability of the SEI, are still occurring in the developed cells. These processes are expected to be more relevant with increased loading and surface area of the anode exposed to the electrolyte. A comprehensive structure-property correlation study of the materials employed in battery research is of paramount importance, to lead and guide performance optimization from a manufacturing point of view. A combination of these approaches is necessary to successfully translate research results from lab to industrial relevant scales, bridging the gap between academic research and industrial production.[245,367]

3.3 Conclusions

The impact of the addition of SWCNTs to LMFP73 electrode formulation has been herein evaluated, in addition with the study of the influence of electrode processing parameters to the overall cell performance in lab-scale and industrially relevant SLP cells. The results identified LMFP-0.5%SWCNT and LMFP73-1%SWCNT as the most promising formulations for enhancing the electronic conductivity of the olivine cathode, showing low electronic resistivity, suitable electrode morphology, with homogeneous components distribution and good structural stability. Given the economic advantage of minimizing inactive components in electrodes, the 0.5%SWCNT formulation was further studied to explore the effects of mixing protocol, coating speed, viscosity, and solid content on electrochemical performance. Mixing protocol #2, a coating speed of 6 mm s^{-1}, and 46% solid content led to improved results. Additionally, the influence of electrode loading on cyclability

was assessed using optimized electrodes in both Li half- and full-cells. While lower-loading electrodes (100 GSM) demonstrated higher cycling stability, high-loading electrodes (250 GSM) showed an initial capacity of 130 mAh g^{-1} when cycled in Li half-cells at C/5, with reasonable rate capability up to 2C, though with limited stability, likely due to Li metal/electrolyte interphase instability. Full-cells with graphite anodes showed greater stability compared to half-cells, with the 200 GSM sample offering the best balance in terms of mechanical properties, areal capacity (2.75 mAh cm^{-2}), and energy density (~320 Wh Kg_{tot}^{-1}). As a result, the 200 GSM cathode was chosen for 0.1Ah SLP cell implementation, achieving a capacity of 110 mAh g^{-1} with 93% retention after 100 cycles, though with lower energy density than in coin cells. These findings provide practical methods and processing parameters to bridge the gap between academic and industrial perspectives in electrode performance evaluation under practical conditions. The critical role of the manufacturing-performance relationship on cell performance and cycling stability is also underscored, particularly when scaling up from lab-scale to industrial cell formats.

4. Investigation of Full-Cells Balancing Employing Layered Oxide Cathodes and Alloying-Based Anodes

The massive diffusion of ground-breaking technology described in Chapter 1 actually triggered a rapid development of EVs and posed concerns on the present systems due to challenging market requirements such as the long driving autonomy, high safety level, and an adequate price.[81,388] According to the cathode optimization, the typical $LiCoO_2$ layered material has been almost fully replaced by multi-metal oxides of the same structure, such as the above described NMC, in which the expensive and toxic cobalt is partially or totally substituted with other transition metals, thus achieving further bonuses including adequate operating voltage, specific capacity, and thermal stability of the de-lithiated phase.[127–130] Despite the remarkable performance of widely employed NMC333 and NMC811 electrodes,[130,131] the layered oxides still suffer from capacity decay upon prolonged cycling and possible safety issues due to phase changes involving material delamination and oxygen loss at the charged (de-lithiated) state.[132,389] The side reaction during the first cycle has also been reported as one of the main issues of voltage hysteresis during subsequent cycles, in particular in Li-rich layered oxides, which causes instability of the structure during redox processes.[133] Various strategies have been adopted to enhance the NMC stability, such as metal doping, acid treatments, and partial substitution of cobalt with aluminum which may represent a viable approach due to the stabilizing effect of Al already observed for the α-$NaFeO_2$-type layered structure.[135,137,138,140,390]

A viable alternative to Li-ion systems could be represented by Na-ion analogues, despite the exploitation of the *rocking-chair* mechanism, which can effectively move the lithium ion from cathode to anode for storing energy and back to get power, appears relevantly more complex in the sodium environment than lithium.[65,144] Indeed, one of the most diffused and efficient cathodes for Na-cell is represented by the mixed Na/transition-metal layered oxide, which can be sodium deficient or sodium rich, with O2, P2, P3 or P3' structures.[56,147,149,391] Moreover, they suffer from the same structural instability compared to the Li-based ones, reflected in a reorganization from P2 to O3-type structure that inhibits the cell performance.[56,392] This variety of configurations requires a sodium metal anode to compensate the alkali metal content into the cathode structure.[393]

Considering the anode side, Li-alloy composites including Si,[207] Sn,[304,394] Sb,[395] and SiO_x,[158,396] attracted the interest of the scientific community due to the higher capacity delivered than the conventional graphite.[397] Furthermore, the combination of the substituted layered cathodes and Li-alloy anodes is an attractive strategy to enhance the energy content and environmental compatibility of LIBs,[398,399] despite still open issues of possible irreversible charge at the first cycle of the cathode,

ascribed to structural reorganization by oxidation,[400] and relevant irreversibility of the anode at the first discharge, due to matrix modifications and SEI formation.[158] This behavior posed intrinsic issues on the direct combination of the electrodes in an efficient Li-ion cell, without ad-hoc designed pre-activation procedures including preliminary electrochemical or chemical lithiation, particularly at the anode, before their use.[314,400]

This problem is also related to Na-ion systems employing layered oxide cathodes, which mandatory foresees the adequate pre-storing of Na-reservoir in anodes, particularly alloying-based.[390,401–403] Among the alloying materials suitable for this activation process in Na-ion cells, Sn and Sb revealed the most promising features; indeed, the high conductivity of metallic Sn and Sb can allow either the typical electrochemical sodiation, or a more scalable and appealing pathway in which Na-metal alloying is directly achieved by mechanochemical treatments.[60,65,151,199]

In these regards, **Chapter 4** is focused on original procedures for full-cell balancing by employing layered oxide cathodes and alloying-based anodes to achieve proof-of-concept Li- and Na-ion batteries with high energy density thanks to the adopted chemistry. The experimental methods adopted in the chapter are reported in **Section 4.1**.

The possible irreversibility on cathode or anode side may lead to the loss of the cell balance in terms of negative to positive (N/P) ratio, affecting both delivered capacity and cycling stability in the final cell. Accordingly, in **Section 4.2** a multi-metal substituted $LiNi_{0.2}Co_{0.2}Al_{0.1}Mn_{0.45}O_2$ (LNCAM) layered cathode for Li-ion batteries is synthetized and thoroughly characterized for direct application in full Li-ion battery using a pristine carbon-coated SiO_x anode (SiO_x-C) without any further treatment of the electrodes before use in cell. Therefore, the remarkable irreversible capacity observed in the LNCAM cathode during the first charge, due to its specific composition, is advantageously exploited to balance the intrinsic SiO_x-C anode irreversibility, thus allowing a preliminary control of the full-cell behavior by adequately selecting the N/P ratio. This novel combination, and the alternative approach adopted to achieve Li-ion full-cells with promising performances, may allow the exploitation of alternative materials with physical-chemical characteristics different than those of diffused electrodes in the commercially available LIBs.

Considering the sodium-ion systems, in **Section 4.3** a direct mechanical treatment of a Sn-C anode for application in a full Na-ion cell using the $Na_{0.48}Al_{0.03}Co_{0.18}Ni_{0.18}Mn_{0.47}O_2$ (NCAM) layered cathode is explored. The anode can operate in Na-cell according to the alloying mechanism with an initial irreversibility exceeding 50% of the steady state value, instead, the cathode can deliver in half-cell an initial charge limited to only 60% of the maximum capacity. The compensation of the initial sodium deficiency at the cathode side and of the initial irreversibility of the anode is originally exploited by a pre-treatment process of the Sn-C anode, consisting of mechanical capillary contact

with sodium metal. Tuning the contact time and pressure allowed the achievement of various degrees of anode sodiation. The most suitable condition is then adopted to get adequate Na_xSn-C anode for the application in the full-cell with the selected NCAM cathode. Despite being still preliminary, these outcomes suggest the mechanical pre-sodiation as a well-suitable approach to scale up the Na-ion battery and achieve a sustainable energy storage.

4.1 Experimental Section

Synthesis of cathode (LNCAM and NCAM) and anode (SiO_x-C and Sn-C) materials

$LiNi_{0.2}Co_{0.2}Al_{0.1}Mn_{0.45}O_2$ material (LNCAM) was synthetized through a co-precipitation method already reported in literature.[391,404] Aluminum nitrate nonahydrate ($Al(NO_3)_3 \cdot 9H_2O$, Sigma Aldrich, ≥ 98%), cobalt(II) nitrate hexahydrate ($Co(NO_3)_2 \cdot 6H_2O$, Sigma Aldrich, ≥ 99%), nickel(II) nitrate hexahydrate ($Ni(NO_3)_2 \cdot 6H_2O$, Sigma Aldrich, ≥ 98.5%), and manganese(II) nitrate tetrahydrate ($Mn(NO_3)_2 \cdot 4H_2O$, Sigma Aldrich, ≥ 97%) were dissolved in deionized water (100 mL) to form a solution with Al/Co/Ni/Mn molar ratio of 0.1:0.2:0.2:0.45. Then, a 0.5 M solution of NaOH pellets (≥ 98%, Sigma Aldrich) in deionized water (212 mL) was added dropwise to the nitrate solution. The nitrate-NaOH solution using a 50 mol% excess of NaOH with respect to nitrate was stirred for 12 h to precipitate a hydroxide precursor which was filtered, washed with deionized water and ethanol until a pH of 7, dried overnight at 70 °C in oven, and calcinated for 12 h at 120 °C (heating rate of 2 °C min^{-1}) in a dry air flow. Afterward, the hydroxide precursor was ground in an agate mortar with lithium hydroxide hydrate ($LiOH \cdot H_2O$, ≥ 98%, Sigma Aldrich) in the 1:1 molar ratio and the resulting mixture was pelletized and calcinated under a dry air flow at 500 °C (heating rate of 5 °C min^{-1}) for 5 h to obtain the material indicated as LNCAM500. The LNCAM500 precursor was ground in an agate mortar, pelletized and calcinated under a dry air flow at 1000 °C (heating rate of 5 °C min^{-1}) for 6 h to obtain the LNCAM1000_6h material, which was then ground, pelletized and calcinated under a dry air flow at 1000 °C (heating rate of 5 °C min^{-1}) for 12 h to obtain the final cathode indicated as LNCAM.

$Na_{0.48}Al_{0.03}Co_{0.18}Ni_{0.18}Mn_{0.47}O_2$ (NCAM) was synthetized through the already described co-precipitation method,[391,404,405] by dissolving nitrate precursors of Al, Co, Ni, and Mn in deionized water to obtain a solution with a Al/Co/Ni/Mn molar ratio of 1:2:2:4.5. The corresponding hydroxide was precipitated from the solution using NaOH, filtered, washed with deionized water, and dried. This precursor was mixed with NaOH in 1:1 molar ratio, calcinated at 500 °C, grinded, pelletized, and calcinated again at 1000 °C in a dry air flow.

The SiO_x-C and Sn-C anode materials were synthesized through a gel-resorcinol-formaldehyde (GRF) procedure previously described in literature.[396,406] For Sn-C, resorcinol was mixed with formaldehyde and sodium carbonate as catalyst to obtain a dark orange hydrogel, which was aged, ground, washed with water and then immersed in tert-butyl alcohol and filtered. Afterwards, the particles were mixed overnight with the organometallic tin source tributylphenyltin (TBPT), recovered, placed in an oven under Ar-H_2 (5%) flux, and heated at 700 °C for 2 h. For SiO_x-C, resorcinol was added to formaldehyde at room temperature and tetraethyl orthosilicate (TEOS) was dissolved in the homogeneous mixture. The achieved solution was heated at 70 °C and a 1 M solution of HCl (2 mL) was added dropwise to catalyze the formation of a pink gel, which was aged 24 h at room temperature, cut into pieces, washed with ethanol to remove residual HCl, and annealed at 1000 °C for 10 h under Ar-H_2 (5%) flow. The obtained SiO_x-C powder was finally ground in an agate mortar. All the thermal steps of the synthesis procedures were performed in a GHA 12/3000 (Carbolite) tubular furnace.

Characterization of Powders

Scanning electron microscopy (SEM) images of the LNCAM sample were acquired by a Zeiss EVO 40 microscope with a LaB_6 thermionic source. Energy dispersive X-ray spectroscopy (EDS) was performed on the SEM images via an X-ACT Cambridge Instruments analyzer to record elemental maps and estimate the LNCAM stoichiometry. The elemental composition of the sample was also determined via inductively coupled plasma-mass spectrometry (ICP-MS) technique. 100 mg of LNCAM were digested in 5 mL of aqua regia (HNO_3:HCl 1:3 molar ratio) at 120 °C for 1 h by using a Parr 4744 acid digestion vessel (Parr Instrument Company). After cooldown, the solution was diluted to the proper concentration prior to the ICP-MC analysis. HNO_3 (70%, ≥ 99.999% trace metal basis, Sigma Aldrich) and HCl (37%, for analysis-ISO, Carlo Erba reagents) were used without any further purifications. Ultrapure H_2O (18 MΩ cm) was used for the dilution of the sample. An ICP-MS Agilent 7500 (Agilent Technologies inc.) equipped with a 3 MHz quadrupole was used for metal determination. X-ray diffraction (XRD) patterns of the LNCAM500, LNCAM1000_6h and LNCAM materials were collected by performing scans in the 2θ range from 10° to 90° at a rate of 10 s $step^{-1}$ with step size of 0.02° through a Bruker D8 Advance instrument using a Cu Kα source and a graphite monochromator of the diffracted beam. Rietveld refinement of the LNCAM pattern was carried out through the MAUD software.[289] by using the reference parameters of the $LiNi_{0.4}Co_{0.15}Al_{0.05}Mn_{0.4}O_2$ layered oxide ($R\bar{3}m$ space group, N. 166, ICSD #166715).[140] The refinement was carried out by fixing atom occupancies to the values estimated by EDS and ICP and the isotropic atomic displacement parameters were set to the same value for Al, Mn, Co, and Ni upon the refinement. Raman spectroscopy was performed on the LNCAM powder through a Czerny-Turner spectrometer

(iHR320 Horiba Scientific) equipped with a diffraction grating of 1800 grooves mm^{-1} and a laser source with $\lambda = 532$ nm.

Electrode preparation

The electrode slurries were prepared by dispersing the active material (LNCAM, NCAM, SiO_x-C or Sn-C), polyvinylidene fluoride (PVdF 6020 Solef®) binding polymer and carbon black (Super P carbon, Timcal) mixed by the 8:1:1 wt. ratio in *N*-methyl-2-pyrrolidone (NMP, Sigma Aldrich) and were stirred at room temperature until homogenization (about 2 h). The slurries were cast by a doctor blade tool on either aluminum carbon-coated foils (thickness ~ 20 µm, MTI Corporation) for LNCAM and NCAM or scratched copper foils (thickness ~ 30 µm, MTI Corporation) for Sn-C and SiO_x-C. The electrode tapes were dried for 3 h on a hot plate at 70 °C, cut into disks with diameter of either 10 mm or 14 mm, and dried again for 3 h at 110 °C under vacuum to remove possible residual traces of water and NMP solvent. Prior to vacuum drying, LNCAM and NCAM electrodes were pressed with a Hydraulic press (Silfradent) for 30 s at 115 bar. The final active material loading ranged from 4 to 4.5 mg cm^{-2} for LNCAM, from 1.2 to 1.8 mg cm^{-2} for SiO_x-C, and from 1.5 to 2.5 mg cm^{-2} for both NCAM and Sn-C, as normalized to the electrode geometric area (either 0.785 or 1.54 cm^2 for electrodes with a diameter of 10 mm or 14 mm, respectively). Carbon/PVdF electrodes coated on Al foil (thickness ~ 15 µm, MTI Corporation), labeled as SPC-Al, were prepared by the doctor blade casting procedure described above using Super P carbon and PVdF binder in the 80:20 wt. ratio, cut into 10 mm disks, and dried at 110 °C for 3h under vacuum. Sn-C electrodes were sodiated via capillary contact between the material and sodium metal: the Sn-C electrode was placed in contact with a sodium metal disk wetted with a 1M solution of sodium perchlorate ($NaClO_4$) dissolved in propylene carbonate (PC, battery grade, Sigma-Aldrich) with 3% in weight of fluoroethylene carbonate (FEC, battery grade, Solvionic) and attached on a Petri dish. Subsequently, a 1 kg weight was stacked on the electrode and the system was allowed to chemically react until the target time was reached (1 h, 2 h, 6 h, 10 h, 14 h, respectively).

Cells assembly

Two-electrode Swagelok T-type half-cells were assembled by stacking a 10 mm-diameter working electrode (LNCAM, NCAM, pristine or sodiated Sn-C or SiO_x-C), a 10 mm-diameter Li (MTI Corporation) or Na (Sigma Aldrich, 99%) metal disk as counter electrode and a 10 mm-diameter glass fiber Whatman® GF/D disk as the separator. Three-electrode Swagelok T-type lithium half-cells were prepared with the same configuration by using an additional 10 mm-diameter lithium metal disk as reference electrode at the top side of the T-cell. An additional three-electrode Swagelok T-type lithium cell was prepared using a 10 mm-diameter SPC-Al electrode as working electrode, a 10 mm-

diameter lithium metal counter electrode, a 10 mm-diameter Celgard 2400 as the separator, and an additional 10 mm lithium metal disk as reference electrode. CR2032 coin-type lithium half-cells (MTI Corporation) were assembled by using the LNCAM working electrode and a lithium metal counter electrode both with diameter of 14 mm separated by a 16 mm-diameter glass fiber Whatman® GF/D disk. Three-electrode Swagelok-type sodium full-cells were assembled by stacking a NCAM cathode, a 2 h sodiated Sn-C anode, one glass fiber Whatman® GF/D separator, and an additional sodium metal disk as reference electrode placed at the top side of the T-cell. The full-cells were prepared by using negative to positive (N/P) capacity ratios of 1.1, as determined by considering mass loadings and specific capacities of the two electrodes. Three-electrode Swagelok-type lithium full-cells were assembled by stacking a LNCAM cathode, a SiO_x-C anode, one glass fiber Whatman® GF/D separator, and an additional lithium metal disk as reference electrode. An additional CR2032 coin-type full-cell was assembled by using a 14 mm-diameter LNCAM cathode, a 14 mm-diameter SiO_x-C anode, and one 16 mm-diameter glass fiber Whatman® GF/D separator. The SiO_x-C|LNCAM full-cells were prepared by using N/P capacity ratios of 0.98 or 0.84 (for three-electrode cells), and 0.91 (for coin-type cell), as determined by taking into account mass loadings and specific capacities of the two electrodes at the first charge of a full-cell, that is, 300 mAh g^{-1} for cathode first de-lithiation and 810 mAh g^{-1} for anode first lithiation. Hence, electrode loadings of 1.53 mg_{anode} cm^{-2} and 4.21 $mg_{cathode}$ cm^{-2} was used for N/P = 0.98, 1.26 mg_{anode} cm^{-2} and 4.05 $mg_{cathode}$ cm^{-2} for N/P = 0.84, and 1.75 mg_{anode} cm^{-2} and 5.19 $mg_{cathode}$ cm^{-2} for N/P = 0.91. In every lithium cell configuration, a solution of $LiPF_6$ (1 M) in ethylene carbonate/dimethyl carbonate (EC:DMC 1:1 by volume, battery grade, Sigma Aldrich) was used as electrolyte, while in every sodium cell configuration a 1M solution of $NaClO_4$ in PC + 3% wt. FEC was employed. The sodiated Sn-C electrodes were used without any other treatment before assembling the cells. All cells were assembled and sealed inside an Ar-filled glovebox (MBraun, O_2 and H_2O content lower than 1 ppm).

Electrochemical tests

A preliminary linear sweep voltammetry (LSV) was performed to evaluate the EC:DMC 1:1 *v/v* 1 M $LiPF_6$ electrolyte anodic stability in lithium battery using a three-electrode T-type cell with SPC-Al electrode at a scan rate of 0.1 mV s^{-1} from the OCV condition of the cell to 6 V vs. Li^+/Li. Cyclic voltammetry (CV) was performed using a three-electrode Li|LNCAM half-cell at a scan rate of 0.1 mV s^{-1} in the 2.5 – 4.9 V vs. Li^+/Li potential range, while electrochemical impedance spectroscopy (EIS) was collected at the open circuit voltage (OCV) condition of the cell as well as after 1, 5, and 10 CV cycles by applying an alternate voltage signal of 10 mV in the 500 kHz – 100 mHz frequency range. The galvanostatic cycling measurements were performed on CR2032-type Li|LNCAM half-cells; initially three cells were cycled at the constant current rate of C/20 (1C = 298 mA g^{-1}) in the

voltage ranges of 2.5 – 4.4 V, 2.5 – 4.8 V, and 2.5 – 4.9 V by adopting the constant-current constant-voltage (CCCV) mode, that is, by setting an additional constant voltage step during charge at either 4.4 V, 4.8 V, or 4.9 V, respectively, until a current value of ¼ of the initial C-rate was reached. Furthermore, a rate capability test was performed by increasing the current rate from C/10 to C/8, C/5, C/3 and 1C every 5 cycles and lowering back to C/10 after 25 cycles in the 2.5 – 4.8 V voltage range adopting the CCCV mode at 4.8 V during charge. Two additional half-cells were galvanostatically cycled at the constant current rate of either C/10 or C/5 between 2.5 and 4.8 V by using the CCCV mode at 4.8 V during charge. The pristine and sodiated Sn-C electrodes were galvanostatically cycled in two-electrodes T-type Na|Sn-C half-cells at the constant current of 15 mA g^{-1} in the 0.01 – 2.0 V voltage range. Additional galvanostatic cycling was performed at the same current rate in two-electrodes T-type Na|NCAM half-cell in the 1.4 – 4.6 V voltage range. Full SiO_x-C|LNCAM cells were galvanostatically cycled at the constant rate of C/10 (1C = 298 mA g_{cat}^{-1}) in the 1.5 – 4.8 V voltage range by adopting the CCCV mode at 4.8 V during charge. EIS measurements were performed on the three-electrode SiO_x-C|LNCAM cells at the OCV condition and after 1 and 10 galvanostatic cycles by using an alternate voltage signal of 30 mV in the 500 kHz – 100 mHz frequency range at 1.5 V bias potential. Full Sn-C|NCAM cells were galvanostatically cycled at the constant current of 15 mA g_{cat}^{-1} in the 1.0 – 4.5 V voltage range by adopting the CCCV mode at 4.5 in charge. EIS measurements were carried out on the three-electrode Sn-C|NCAM cell at the OCV condition and after 1, 8, and 10 galvanostatic cycles by superimposing an alternate voltage signal of 30 mV in the 500 kHz – 100 mHz frequency range at 1V bias potential. All the Nyquist plots recorded by EIS were analyzed through non-linear least squares (NLLS) fitting method by using the RelaxIS3 software (rhd instruments), and only fits with χ^2 value of the order of 10^{-4} or lower were accepted.[273,274] The distribution of relaxation times (DRT) functions were calculated after subtracting the low-frequency diffusion region, by using the software RelaxIS3. The λ-factor for the DRT analysis was optimized according to Tikhonov regularization, by calculating the sum of squared residuals (SSR) vs. λ, and assuming a Gaussian distribution.[262,272] CV and EIS were carried out by a VersaSTAT MC Princeton Applied Research (PAR, AMETEK) instrument, while the charge/discharge cycling tests were performed by a MACCOR series 4000 battery test system. All the data were recorded at the room temperature (25 ◦C).

Electrode characterization and ex-situ measurements

Ex-situ XRD patterns of pristine and activated Sn-C electrodes, leaned on a glass sample holder and sealed with Kapton tape, where collected with the abovementioned system by performing scans in the 2θ range from 27° to 47° at a rate of 4 s $step^{-1}$ with a step size of 0.02°. SEM images of the pristine and chemically sodiated (14 h) Sn-C electrodes and EDS elemental maps were collected through a

Zeiss Sigma 300 FE-SEM equipped with Bruker QUANTAX EDX detector. Raman spectroscopy was performed on micrometric Sn powder (< 45 μm particle size, 99.8% trace metal basis, Sigma-Aldrich), pristine and sodiated Sn-C electrodes, by using the above-described instrument. For Raman analysis all the samples were placed into a sealed sample holder in Ar atmosphere. *Ex-situ* XRD measurements were performed on LNCAM electrodes retrieved from two-electrode T-type half-cells upon either 1 or 2 charge/discharge cycles at C/20 in the 2.5 – 4.9 V voltage range by adopting the CCCV mode at 4.9 during charge. XRD scans were performed as described in the 10° - 60° 2θ range at a rate of 10 s step $^{-1}$ and a step size of 0.02°. *Ex-situ* SEM images of pristine and cycled Sn-C and NCAM electrodes retrieved from a Sn-C|NCAM full-cell were collected as above described. Before the analyses, all the electrodes, recovered either chemical activation or cell cycling, were washed with DMC solvent and dried under vacuum for 30 min.

4.2 Reciprocal Irreversibility Compensation of Layered Oxide Cathode and Silicon Oxide Anode in Proof-of-Concept Li-ion Battery

4.2.1 Structural, Morphological, and Electrochemical Characterization of LNCAM Cathode in Lithium Batteries

XRD measurements are performed on LNCAM, as well as on the LNCAM500 and LNCAM1000_6h precursors, to investigate the structure of the samples, as reported in **Figure 4.1**. The data of the reference diffractogram $LiNi_{0.4}Co_{0.15}Al_{0.05}Mn_{0.4}O_2$ (ICSD #166715) are added to allow the indexing of the most relevant peaks.[140] The XRD patterns reveal broad and asymmetric peaks for the LNCAM500 precursor which become narrower and more defined upon treatment at 1000 °C with the formation of the LNCAM1000_6h sample. Thus, the final LNCAM cathode shows a well-defined (003) main reflection at 2θ = 18.72° as well as the (101), (006), (012), (104), (018), and (110) planes at 2θ = 36.67°, 37.82°, 38.32°, 44.46°, 64.48°, and 65.44°, respectively.[407] Indeed, the growth of the crystalline phase by the subsequent thermal steps and the final formation of the P3-type layered structure is achieved in the final LNCAM. Moreover, the progressive definition of the (006)/(012) peaks couple at 37.82°/38.32° and the (018)/(110) one at 64.48°/65.44° indicates the consolidation of the hexagonal ordering of the LNCAM layered structure, which is confirmed by a *R* value of about 0.51, where *R* is defined as the $(I_{006}/I_{102})/I_{101}$ intensities ratio.[408]

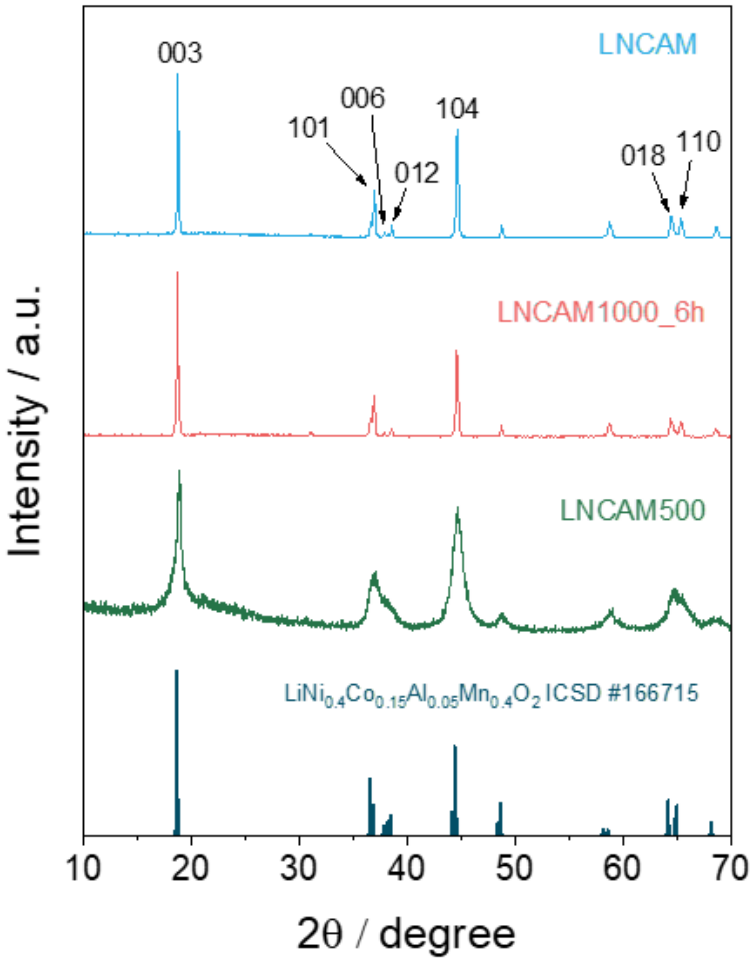

Figure 4.1: *XRD patterns of the LNCAM500, LNCAM1000_6h, and LNCAM materials, reference data of* $LiNi_{0.4}Co_{0.15}Al_{0.05}Mn_{0.4}O_2$ *(ICSD #166715) are reported for comparison and peaks indexing.*[390]

Additional structural insights are provided by the Rietveld refinement of the LNCAM XRD pattern in **Figure 4.2(a)** carried out by constraining the atom occupancy according to the EDS/ICP results (see **Table 4.2**). The refined diffractogram (red dots) confirms a trigonal cell unit (hexagonal $R\bar{3}m$ space group, table N. 166) without significant content of impurities, as also suggested by the difference profile.[140] The lattice parameters determined by refinement, that is, *a*, *c*, *c/a*, and cell volume, are reported in **Table 4.1** and compared with those of the $LiNi_{0.4}Co_{0.15}Al_{0.05}Mn_{0.4}O_2$ (ICSD #166715) reference.[140,408,409] The LNCAM shows slightly different *a* and *c* values leading to a higher cell volume of 102.32 $Å^3$ compared to the 101.99 $Å^3$ of the reference, likely due to the higher content of Mn.[410] Furthermore, **Table 4.1** reveals a *c/a* ratio of about 4.95, which indicates a well ordered structure of the sample,[411] and a 003/104 peaks intensity ratio (I_{003}/I_{104}, see **Figure 4.1** for peak indexing) exceeding 1.5, thus suggesting a low degree of cation mixing, in particular for the Ni^{2+} occupancy in the Li^+ sites, and likely an enhanced Li^+ ions mobility within the cathode.[411] The accuracy of the Rietveld refinement is suggested by a goodness-of-fit (*GOF*) parameter and weighted-profile *R* factor (R_{wp}%) values lower than 2 and 20, respectively.[301,302]

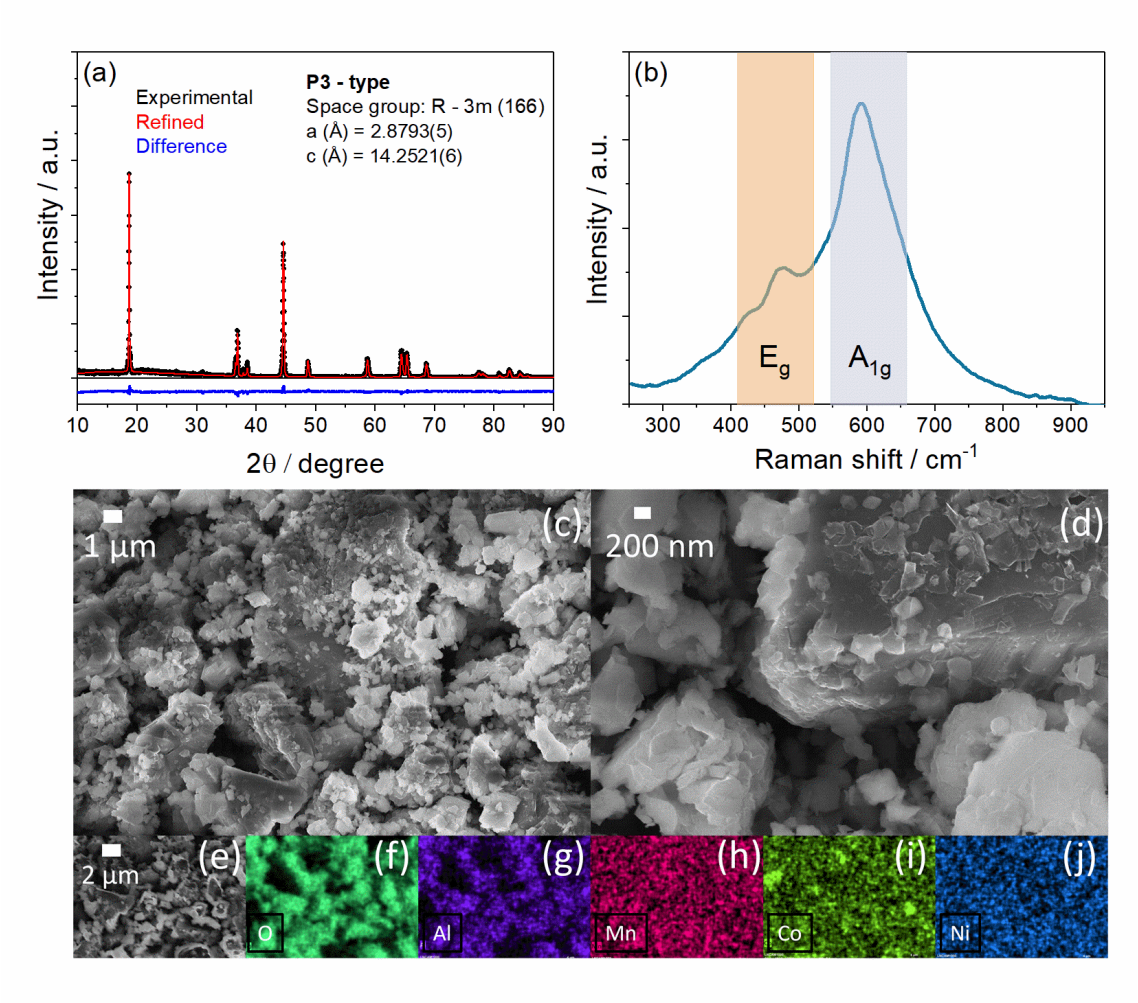

Figure 4.2: *Characterization of the LNCAM material.* ***(a)*** *XRD and corresponding Rietveld refinement showing experimental pattern (black dots), calculated pattern (red line) and difference profile (blue line);* ***(b)*** *Raman spectrum recorded in the 250 – 950 cm^{-1} range. Highlighted regions report transitions identification.* ***(c, d)*** *SEM images at different magnifications;* ***(e-j)*** *SEM-EDS analyses with elemental maps of* ***(f)*** *O,* ***(g)*** *Al,* ***(h)*** *Mn,* ***(i)*** *Co and* ***(j)*** *Ni. Adapted from* [390].

Table 4.1: *Results of Rietveld refinement in terms of lattice parameters, unit cell volume, c/a parameters ratio, I_{003}/I_{104} intensities ratio, good-of-fit parameter (GOF), and weighted-profile R factor (R_{wp}%) of LNCAM. Reference ICSD #166715.*[390]

Material	*a* (Å)	*c* (Å)	*c/a*	V (Å^3)	I_{003}/I_{104}	*GOF*	R_{wp}%
ICSD #166715	2.872	14.273	4.969	101.99	1.848	/	/
LNCAM	2.879(3)	14.252(1)	4.949(8)	102.32(5)	1.517(6)	1.50	17.18

The Raman spectroscopy performed on LNCAM in **Figure 4.2(b)** further confirms the layered structure by exhibiting two main peaks around 476 cm^{-1}, related to the symmetric stretching vibration of the M–O bond (E_g symmetry), and at 590 cm^{-1}, assigned to the O–M–O bending vibration (A_{1g}

symmetry).[412,413] The morphology of the LNCAM cathode material is investigated by SEM-EDS analysis, as reported in **Figure 4.2(c-j)**. The SEM images of the powder show flakes with size ranging from 3 to 25 µm characterized by a layer morphology (**Figure 4.2(c)**) stacked into submicrometric primary particles with nanometric thickness (**Figure 4.2(d)**). The corresponding EDS elemental maps acquired on SEM imaging (**Figure 4.2(e)**) of O, Al, Mn, Co, and Ni (**Figure 4.2(f-j)**, respectively) display a homogeneous distribution of the elements, without relevant impurities. However, the elemental mapping in **Figure 4.2(i)** evidence the presence of more intense Co X-ray signals inferred from few regions suggesting a slight Co segregation and crystalline agglomeration in the sample already observed for similar materials.[414] The EDS analysis allow the determination of a $LiNi_{0.18}Co_{0.2}0Al_{0.09}Mn_{0.43}O_2$ stoichiometry (**Table 4.2**) which well approaches the one designed during synthesis (*i.e.* $LiNi_{0.2}Co_{0.2}Al_{0.1}Mn_{0.45}O_2$), thus suggesting the successful incorporation of the transition metals into the material.[404] A similar result, reported in **Table 4.2**, is obtained by ICP-MS measurement that likely confirms the material stoichiometry discussed above.

Table 4.2: *Results of EDS and ICP-MS measurements in terms of Average atomic %, EDS stoichiometric coefficient, concentration (ppb), and ICP-MS stoichiometric coefficient for Li, Ni, Co, Al, Mn, and O.*[390]

Element	Average atomic %	EDS stoichiometric coefficient	Concentration (ppb)	ICP-MS stoichiometric coefficient
Li	/	/	64.16	1.00
Ni	6.11	0.18	95.15	0.18
Co	6.76	0.2	99.33	0.18
Al	2.96	0.09	33.92	0.14
Mn	14.93	0.43	211.4	0.42
O	69.24	2.00	/	/

In summary, LNCAM displays defined layered structure and morphology with uniform distribution of the elements that are crucial parameters to enable the formation of a suitable electrode/electrolyte interphase in lithium cell and satisfactory cycling behavior,[415] since irregular layer stacking or excessive aggregation may hinder the Li^+ ions diffusion in the material framework.[407]

Prior to testing the cell applicability of the LNCAM electrode, the anodic electrochemical stability window (ESW) of the electrolyte (*i.e.* EC:DMC 1:1 *v/v* 1 M $LiPF_6$) was checked as reported in **Figure 4.3**. The LSV shows a small increase of the current around 5 V vs. Li^+/Li, while the full oxidative decomposition of the electrolyte was detected only at around 5.2 V vs. Li^+/Li. The obtained results are in agreement with various literature reports on the adopted electrolyte,[228,416,417] and confirm its stability for the study in lithium cell of the layered cathode within the voltage ranges employed below.

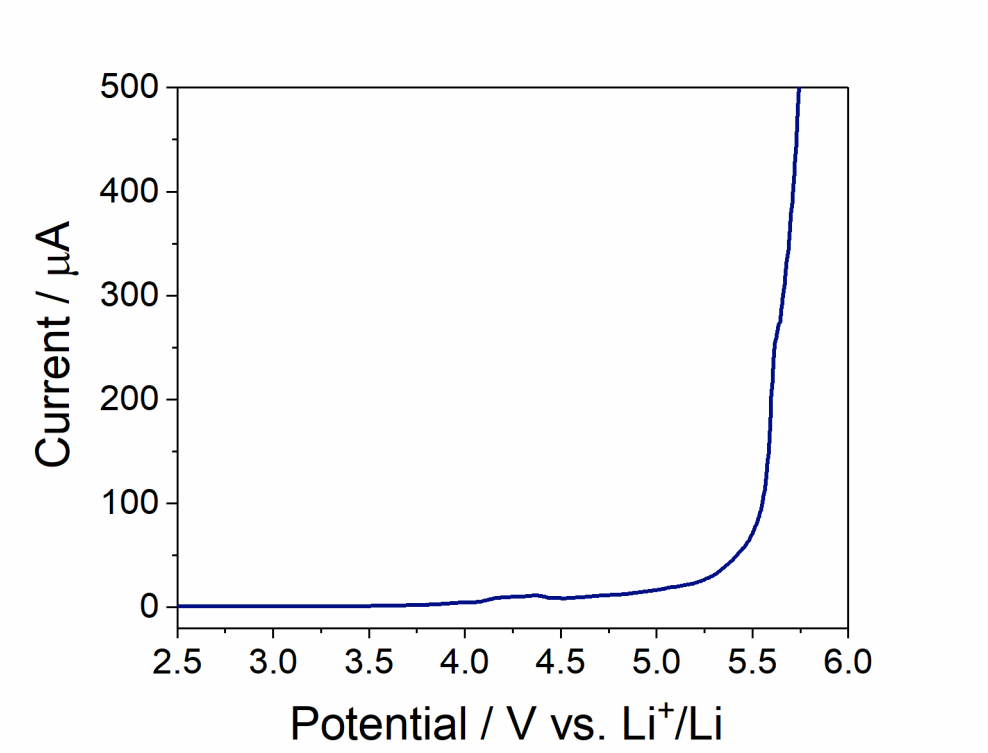

Figure 4.3: *LSV of the Li|EC:DMC 1:1 v/v 1 M $LiPF_6$|SPC-Al cell for determining the anodic electrochemical stability window (ESW) of the electrolyte. Scan rate 0.1 mV s^{-1}.*[390]

The electrochemical process of the LNCAM cathode is subsequently investigated in lithium half-cell by combining CV and EIS measurements, as reported in **Figure 4.4**. The CV response (**Figure 4.4(a)**) shows during the first cycle two oxidation peaks centered at 4.0 V and 4.6 V vs. Li^+/Li, and a single reduction wave merged at about 3.8 V vs. Li^+/Li. The above irreversible oxidation peak at 4.6 V vs. Li^+/Li is likely ascribed to partial oxygen loss due to structural rearrangement with possible phase modification of the cathode and concomitant partial electrolyte degradation,[418] in particular the decrease of Co–O and Ni–O distances due to oxidation of the transition metals, and negligible changes in Mn–O distance which holds Mn^{4+} oxidation state.[419] Nevertheless, the charge and discharge signals at 4.0 and 3.8 V vs. Li^+/Li, respectively, are associated with the reversible (de-)intercalation of the Li^+ ions into the layered structure.[420] The irreversible lithium extraction, related to the additional oxidation peak at the first cycle centered at about 3.4 V vs. Li^+/Li, may be ascribed to the presence of impurity traces in the electrolyte (*e.g.* water or other solvents) as well as to possible

side Ni^{2+}/Ni^{4+} oxidation process as suggested by literature reports.[133] However, the vanishing of the above peak during reduction and in the subsequent cycles suggests the formation of a suitable SEI layer at the electrode surface.[421] During the subsequent voltammetry cycles, the electrochemical process reversibly evolves with a single oxidation peak at 3.9 V vs. Li^+/Li reflected into the corresponding reduction signal at 3.7 V vs. Li^+/Li. The slight shift of the oxidation process to lower potential upon the first cycle further suggests a favorable reorganization of the material structure, while the modest polarization certainly indicates the formation of a suitable SEI at the electrode surface.[421,422]

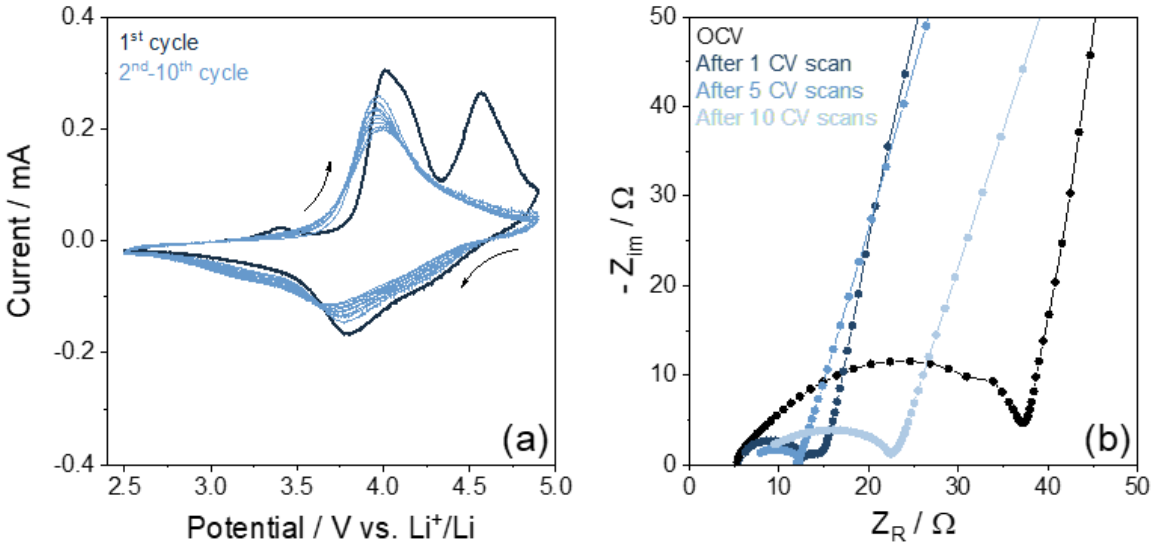

Figure 4.4: (a) *CV and* ***(b)*** *EIS measurements performed on the Li|LNCAM three-electrode cell using a Li reference electrode. CV potential range 2.5 – 4.9 V vs. Li^+/Li; scan rate 0.1 mV s^{-1}. EIS carried out at the OCV of the cell and after 1, 5 and 10 cycles; frequency range 500 kHz – 100 mHz; alternate voltage signal 10 mV.*[390]

This aspect is additionally investigated by EIS measurements performed at the OCV condition of the cell as well as after 1, 5, and 10 CV scans at the fully discharged state of the cell (*i.e.* 2.5 V vs. Li^+/Li), as shown in **Figure 4.4(b)**. The reported Nyquist plots are analyzed by NLLS method, and the results are reported in **Table 4.3**.[273,274] The graphs in **Figure 4.4(b)** display a semicircle in the medium-high frequency region accounting for the Li^+ ion exchange through the electrode/electrolyte interphase, and a low-frequency, almost vertical tilted line representing the cell geometrical capacity.[423] Therefore, the EIS can be represented by the $R_e(R_iQ_i)Q_g$ equivalent circuit where R_e is the electrolyte resistance determined by the high-frequency intercept in the corresponding plot, the (R_iQ_i) elements reflect the main semicircle with a total resistance due to the charge transfer at the electrode/electrolyte interface and the SEI layer at the electrodes surface, while Q_g is a constant phase element related the cell capacitance.[273,274]

Table 4.3: *Equivalent circuits, interphase resistances (R_1, R_2), and chi-square values accounting for the accuracy (χ^2) of NLLS analysis related to the EIS data of the Li|LNCAM three-electrode cell collected at 25 °C at the OCV condition, and after 1, 5, and 10 CV cycles in the 2.5 – 4.9 V vs. Li^+/Li potential range.*[390]

Cell condition	Equivalent circuit	R_1 (Ω)	R_2 (Ω)	$R_i = R_1 + R_2$ (Ω)	χ^2
OCV	$R_e(R_1Q_1)Q_g$	32.3 ± 0.5	/	32.3 ± 0.5	6×10^{-4}
After 1 CV scan	$R_e(R_1Q_1)(R_2Q_2)Q_g$	7.6 ± 0.1	1.8 ± 0.1	9.4 ± 0.1	2×10^{-5}
After 5 CV scans	$R_e(R_1Q_1)Q_g$	5.2 ± 0.2	/	5.2 ± 0.2	3×10^{-4}
After 10 CV scans	$R_e(R_1Q_1)Q_g$	16.2 ± 0.2	/	16.2 ± 0.2	1×10^{-4}

After one cycle, the splitting of the SEI and charge transfer related features is clearly evidenced, thus allowing the fit of the two separate contributions, as detailed in **Table 4.3**. The table also reveals a trend by which the initial total resistance at the OCV of 32 Ω decreases to about 5 Ω after 5 cycles and stabilizes at 16 Ω at the end of the test. This behavior well supports the abovementioned formation of a suitable SEI and the favorable structural rearrangement of the cathode that may boost the reaction kinetics in lithium cell and enhance the corresponding performance.[409]

The LNCAM is evaluated in **Figure 4.5** by galvanostatic cycling in lithium half-cell performed by increasing the charge voltage cut-off from 4.4 V (panels **(a, b)**) to 4.8 V (panels **(c, d)**) and to 4.9 V (panels **(e, f)**) at the constant current rate of C/20 (1C = 298 mA g^{-1}) in order to verify the effects of the irreversible oxidation on cell response and stability. As expected by the CV previously discussed in **Figure 4.3**, the cycling test with the voltage range restricted between 2.5 V and 4.4 V (**Figure 4.5(a, b)**) shows at the first cycle (inset of **Figure 4.5(a)**) only the single-step charge and discharge processes centered around 4.0 V ascribed to the Li^+ (de-)intercalation process. On the other hand, the first cycle reveals a remarkably higher charge specific capacity (207 mAh g^{-1}) compared to discharge (106 mAh g^{-1}) due to the abovementioned cathode structural rearrangement and partial electrolyte decomposition which appear affecting the cell even with a charge cut-off limited to 4.4 V. The subsequent cycles in **Figure 4.5(a)** reveal a highly reversible charge/discharge process, which is confirmed by the cycling trend in **Figure 4.5(b)** with a stable discharge capacity of 106 mAh g^{-1} retained for over 96% at the end of the test, and a coulombic efficiency raising from 50% at the first cycle over 98% at the steady state. Despite the stability, the specific capacity delivered by LNCAM in the 2.5 – 4.4 V voltage range barely exceeds 1/3 of the theoretical value (298 mAh g^{-1}), which may possibly limit its practical application in fields in which high energy density is requested.[424,425]

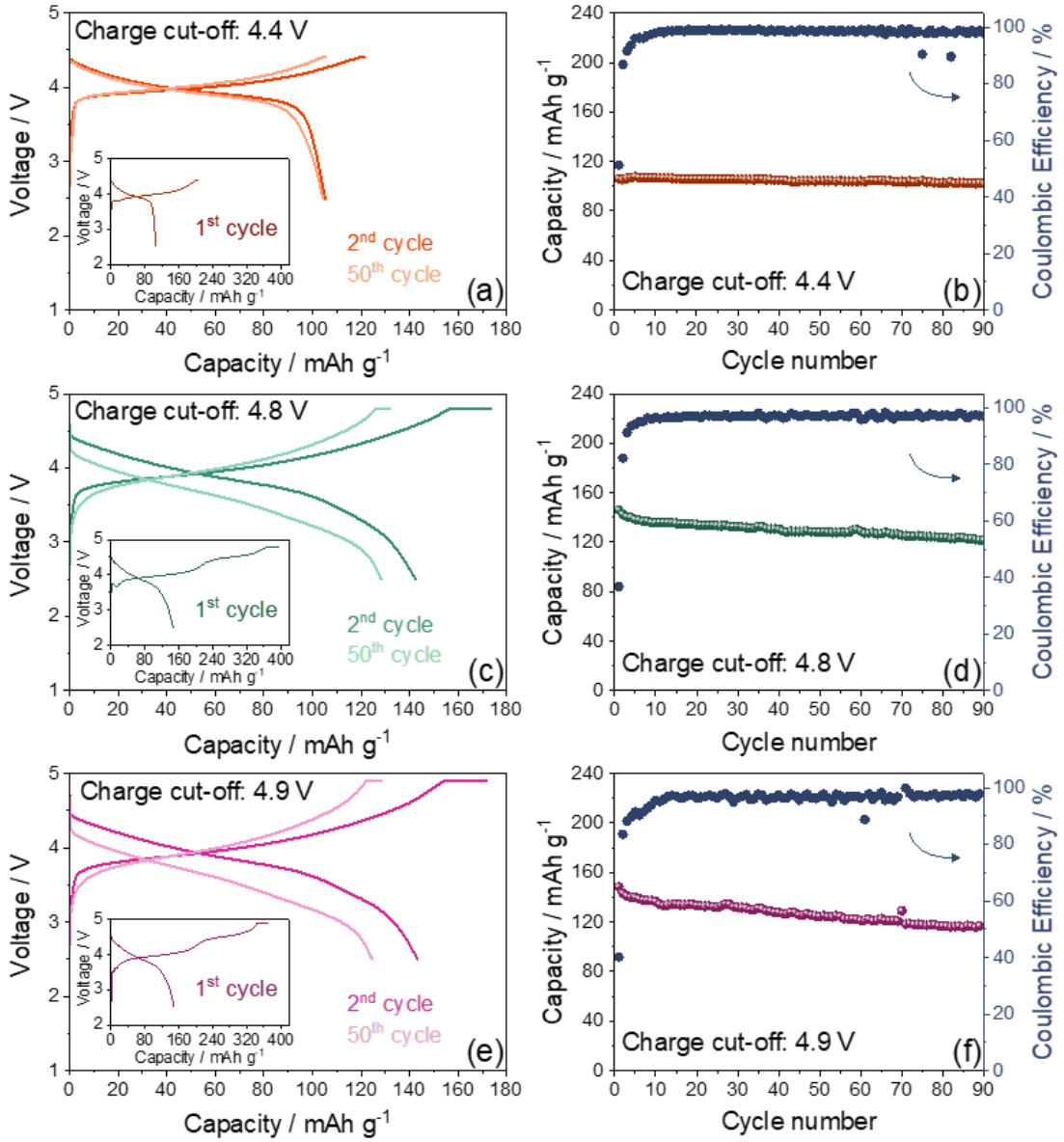

Figure 4.5: *Galvanostatic cycling performances of the Li|LNCAM cell at 25 °C at the constant current rate of C/20 (1C = 298 mA g^{-1}) in terms of* ***(a, c, e)*** *voltage profiles (insets show first cycle) and* ***(b, d, f)*** *discharge capacity trend reporting coulombic efficiency on right y-axes. Voltage ranges:* ***(a, b)*** *2.5 – 4.4 V,* ***(c, d)*** *2.5 – 4.8 V, and* ***(e, f)*** *2.5 – 4.9 V, with an additional constant voltage step at either 4.4 V, 4.8 V, or 4.9 V, respectively, held until a current value of ¼ of the nominal C-rate is reached (CCCV mode).*[390]

The cycling tests performed by using the wider voltage ranges of 2.5 – 4.8 V (**Figure 4.5(c, d)**) and 2.5 – 4.9 V (**Figure 4.5(e, f)**) show during the first cycle (insets in panels **(c)** and **(e)**, respectively) irreversible oxidation processes leading to charge capacity values of 397 mAh g^{-1} at 4.8 V and 370 mAh g^{-1} at 4.9 V, reflected into respective discharge capacities of 146 mAh g^{-1} and 148 mAh g^{-1}; this behavior confirms the irreversibility evidenced in CV profiles (see **Figure 4.4(a)**). The slightly higher capacity observed at the first cycle charging process in the 2.5 – 4.8 V voltage range in comparison with the 2.5 – 4.9 V voltage range is related to the irreversible oxidation process ascribed to electrolyte with partial oxygen loss from cathode.[418] This process may be also influenced by the amount of the

active material in the electrode, particularly affecting the electrolyte oxidation, which may slightly differ in the various samples taken into account. In spite of the excessive oxidation capacity observed during the first cycle, the cells of **Figure 4.5(c, e)** surprisingly exhibit the typical sloped profiles centered at 3.9 V, a discharge capacity approaching 150 mAh g^{-1}, and a well improved reversibility during the subsequent cycles. On the other hand, the increase of the charge cut-off from 4.8 to 4.9 V clearly affects the capacity decay of the cell, as evidenced by the cycling trends reported in **Figure 4.5(d, f)**, respectively. This behavior may be related to charging compensation of the irreversible oxygen loss and possible Ni reduction process at the first cycle accompanied by hysteresis.[133] Indeed, the cell cycled between 2.5 V and 4.8 V shows a capacity retention of 83% and a coulombic efficiency that increases from 37% at the first cycle to about 98% at the end of the test, while the cell tested between 2.5 V and 4.9 V reveals a retention of 77% and initial coulombic efficiency of 40% raising to 98% at the end of the test. Considering the comparable delivered capacity and the better retention achieved by adopting the 2.5 – 4.8 V voltage range compared to 2.5 – 4.9 V, the former is considered a suitable compromise to achieve satisfactory energy and stability which are key factors for the successful application of the layered oxide cathode in lithium-ion batteries.[397] In addition, the relevant side oxidation of the first cycle (efficiency ~ 40%), which usually represents a severe issue for battery application, may be exploited to compensate the typical irreversibility affecting the Li-alloy materials as will be demonstrated hereafter. It is worth mentioning that the LNCAM delivers a capacity ranging from 110 to 150 mAh g^{-1}, depending on the voltage cut-off, which is actually lower than the one delivered by commercial NMC (typically of about 190 mAh g^{-1}). The lower capacity value is ascribed to the inert Al used for stabilizing the P3-type structure,[140] and the Jahn-Teller distortion attributed to the high amount of Mn instead of Co in the electrode formulation.[426] Despite the lower capacity, the substitution of the toxic and expensive Co with Al and Mn leads to a notable reduction of the economic and environmental impact of the electrode.

Prior to further testing in cell, the effects on the layered structure of the severe irreversibility affecting LNCAM at high voltage are investigated by performing *ex-situ* XRD on electrodes retrieved from lithium cells after 1 and 2 cycles at C/20 between 2.5 and 4.9 V. **Figure 4.6** displays the comparison between the XRD of the pristine and cycled LNCAM electrodes in the 10° – 60° range (panel **(a)**) and provides additional focus of the (003) plane in the 17° – 20° 2θ region (panel **(b)**) and the (104) reflection between 43° and 46° (panel **(c)**).

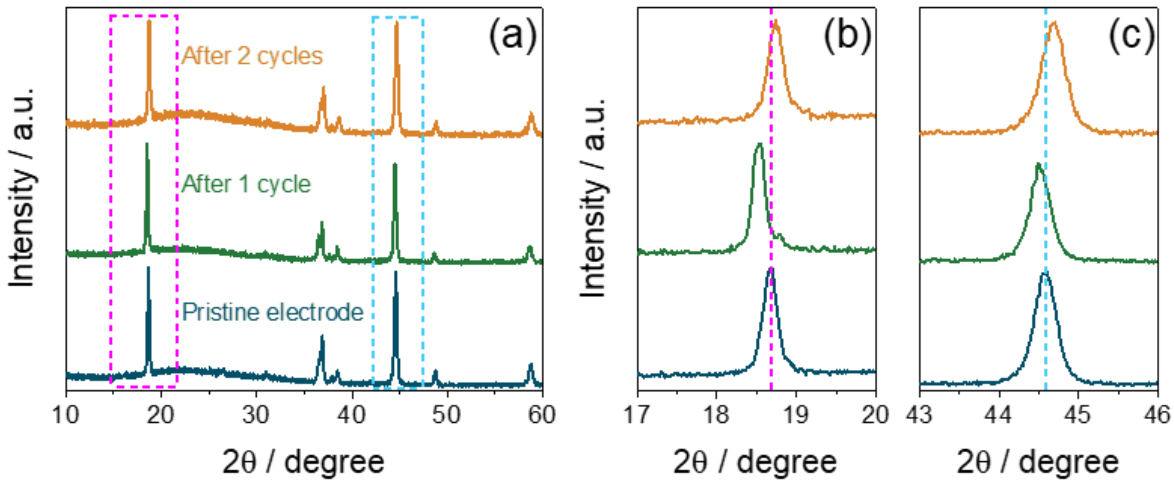

Figure 4.6: (a) *XRD patterns of the LNCAM electrode at the pristine state and after 1 and 2 charge/discharge cycles in lithium cell at the constant current rate of C/20 (1C = 298 mA g^{-1}) between 2.5 and 4.9 V, with an additional constant voltage step at 4.9 V held until a current value of ¼ of the nominal C-rate is reached (CCCV mode).* ***(b, c)*** *Magnification of the* ***(b)*** *17° – 20° and* ***(c)*** *43° – 46° 2θ regions.*[390]

Figure 4.6(a) confirms the retention of the layered structures in the cycled electrodes ($R\bar{3}m$ space group, table N. 166)[140] which show the same diffraction peaks, along with a broad and weak signal extending from about 15° to 30 ° ascribed to the conducting carbon fraction in the electrode composition. This experimental result justifies the evolution of the characteristic (de-)intercalation profile of the layered cathode, even upon the first cycle irreversibility, as well as the relevant cell stability. Interestingly, the magnification of the 17° – 20° 2θ region in **Figure 4.6(b)** reveals the shift of the (003) plane from 18.68° at the pristine condition to 18.54° after 1 charge/discharge cycle and then to 18.74° after 2 cycles in lithium cell. A similar trend can be observed for the (104) reflection in the magnified 43° – 46° 2θ region in **Figure 4.6(c)**, which moves from 44.58° at the pristine state to 44.50° and to 44.70° upon 1 and 2 cycles, respectively. The shift of the (003) and (104) reflections well supports the abovementioned structural variation for the LNCAM material upon cycling in lithium cell with possible partial oxygen loss and aluminum insertion defective sites.[140,425,427] However, a contribution to the cell irreversible capacity of the side reaction with the electrolyte, leading to the SEI layer formation at the electrode/electrolyte interphase, cannot be neglected.[405]

The cycling performance of the LNCAM at higher current rates is also evaluated by additional galvanostatic charge/discharge measurements within the optimal 2.5 – 4.8 V voltage range, and the results are shown in **Figure 4.7**.

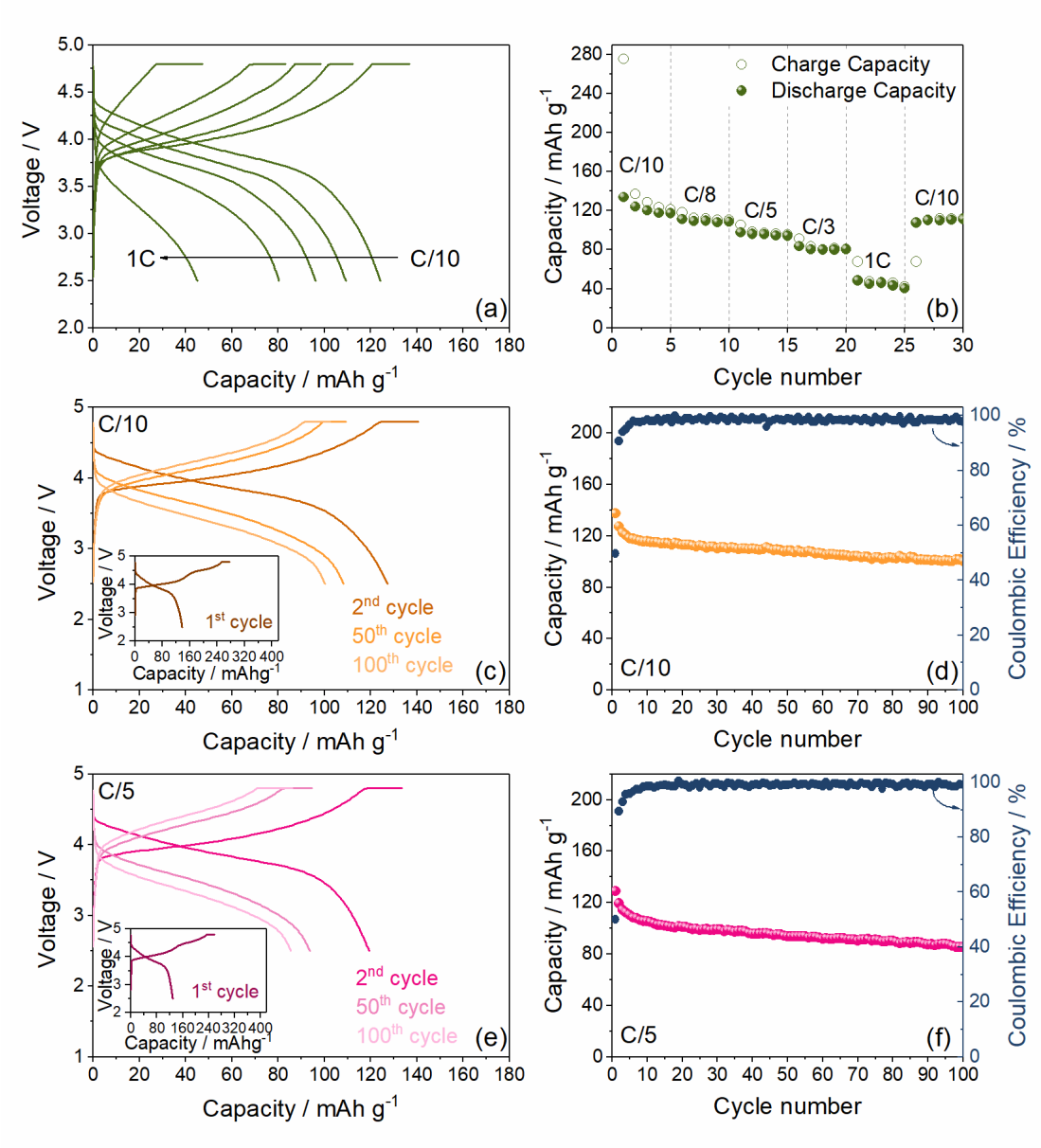

Figure 4.7: *Galvanostatic cycling performance of the Li|LNCAM cell at 25 °C. Rate capability test in terms of* ***(a)*** *voltage profiles and* ***(b)*** *corresponding cycling trend by using C/10, C/8, C/5, C/3 and 1C current rates (1C = 298 mA g-1). Electrochemical performance at the constant current rate of* ***(c, d)*** *C/10 and* ***(e, f)*** *C/5 in terms of* ***(c, e)*** *voltage profiles (insets show first cycle) and* ***(d, f)*** *discharge capacity trend reporting coulombic efficiency on right y-axes performed in the 2.5 – 4.8 V voltage range with an additional constant voltage step at 4.8 V held until a current value of ¼ of the nominal C-rate was reached (CCCV mode). Adapted from* [390].

The figure displays the rate capability test performed on the Li|LNCAM cells by increasing the current rate from C/10 to 1C (1C = 298 mA g^{-1}) in terms of selected voltage profiles (**Figure 4.7(a)**) and capacity trend (**Figure 4.7(b)**). The cell shows the single-step charge/discharge reversible process already observed in **Figure 4.5**, with increasing polarization from C/10 to 1C as expected by the ohmic drop promoted by the current increase. The corresponding cycling trend reveals an initial discharge capacity of 134 mAh g^{-1} at C/10, which stabilizes at 117 mAh g^{-1} after 5 cycles, and values of 109, 96, 80, and 46 mAh g^{-1} at C/8, C/5, C/3 and 1C, respectively. Lowering back the C-rate to

C/10 after 25 cycles leads to a capacity of about 110 mAh g^{-1}, that is 82% of the initial value, which suggests a moderate stability of the LNCAM upon the stress triggered by the progressive raise of the current.[410] Prolonged galvanostatic cycling tests are reported in panels **(c-f)** to determine the cycle life of the LNCAM material at constant C-rates of C/10 (**Figure 4.7(c, d)**) and C/5 (**Figure 4.7(e, f)**). Both cells show the expected irreversible double-plateau during charge at first cycle (insets of panels **(c)** and **(e)**), and exclusively the reversible Li^+ (de-)intercalation in the subsequent cycles with more remarkable slope compared to the tests at C/20 (see **Figure 4.5**), due to the higher currents.[428] Maximum discharge capacities of 137 mAh g^{-1} and 129 mAh g^{-1} are respectively achieved at C/10 (**Figure 4.7(d)**) and C/5 (**Figure 4.7(f)**), retained over 73% and 66% after 100 cycles. As expected, low coulombic efficiency of about 50% is achieved both at C/10 and C/5 during the first cycle, which subsequently increases and reaches values of 98% and 99%, respectively, at the end of the test. The promising performance exhibited by the LNCAM cathode, also compared with other materials employing similar transition metals,[137,381,386,412] may be possibly improved upon optimization of the synthetic process in order to enhance the stability of the layered structure, mitigate the irreversible oxidation process, and limit the capacity decay.

4.2.2 Investigation of Proof-of-Concept SiO_x-C|LNCAM Full-Cells with Different N/P Ratios

As previously mentioned, the initial relevant irreversibility of the cathode can be potentially exploited to compensate similar side processes occurring during the first discharge of Li-alloying anodes such as silicon or tin, which are typically promoted by excessive volume changes, electrolyte reduction, and partial lithiation of the electrode matrix.[80] Indeed, pre-activation processes including direct contact with lithium metal (chemical strategy)[304] and/or preliminary cycling in lithium half-cell (electrochemical strategy)[429] are usually necessary prior to application in full Li-ion cell, in order to prevent parasitic reactions that would compromise the anode/cathode balancing. However, these efficient pre-activation procedures are still within a R&D stage mainly adopted for laboratory prototype cells.[121,314,430] In these regards, hereafter the mentioned additional processes are avoided, and a silicon oxide anode (coated by 70% wt. of carbon, SiO_x-C)[396] is directly combined with the developed layered cathode in a full Li-ion cell by advantageously tuning the N/P ratio estimated from the respective irreversible capacity. The N/P ratios were calculated by taking into account mass loadings and specific capacities of the two electrodes at the first charge of a full-cell including the irreversible part, that is 300 mAh g^{-1} for first cathode de-lithiation and 810 mAh g^{-1} for first anode lithiation (see **Section 4.1** for further details).

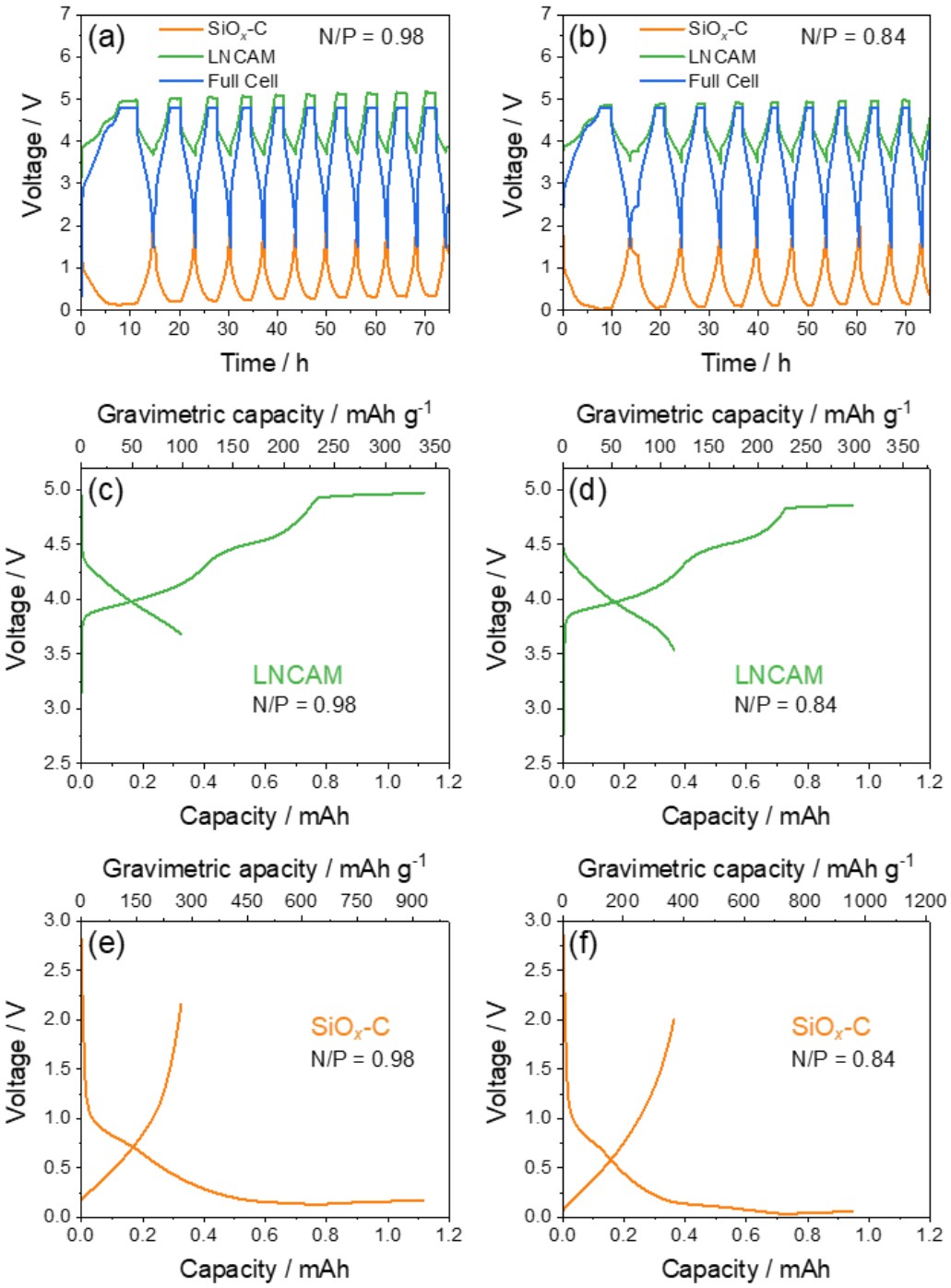

Figure 4.8: ***(a, b)*** *Time evolution of the SiO_x-C anodes and the LNCAM cathodes voltage concomitantly collected by using a Li reference and of the corresponding SiO_x-C|LNCAM full-cells cycled at C/10 (1C = 298 mA g_{cat}^{-1}) with N/P ratio of either* ***(a)*** *0.98 or* ***(b)*** *0.84;* ***(c-f)*** *first cycle in terms of voltage vs. capacity (mAh, bottom x-axes) and gravimetric capacity (mAh g^{-1}, top x-axes) related to* ***(c, d)*** *LNCAM cathodes and* ***(e, f)*** *SiO_x-C anodes in the full-cells with N/P ratio of either* ***(c, e)*** *0.98 or* ***(d, f)*** *0.84. Voltage range 1.5 – 4.8 V with an additional constant voltage step at 4.8 V held until a current value of ¼ of the nominal C-rate was reached (CCCV mode). Room temperature (25 °C).*[390]

As reported in **Figure 4.8**, a higher cathode content does not lead to lithium deposition, which is instead expected at much lower potential. Rather, the excess of cathode causes the irreversible

electrolyte reduction at the anode side during the first cycle of the full-cell with formation of a stable SEI and holds the alloying material at sufficiently low potential to allow battery operation during the subsequent cycles. **Figure 4.8** depicts the electrochemical behavior of two SiO_x-C|LNCAM full-cells cycled at the constant current of C/10 as referred to the cathode (1C = 298 mA g_{cat}^{-1}), using N/P ratio of either 0.98 or 0.84 calculated as indicated above. The cells' responses are reported in terms of the voltage trend versus time of the full-cells (**Figure 4.8(a)** and **Figure 4.8(b)** for N/P of 0.98 and 0.84, respectively), as well as of the signals of the cathode (**Figure 4.8(c, d)**) and the anode (**Figure 4.8(e, f)**), which are concomitantly recorded by using an additional lithium electrode as reference. The measurement clearly exhibits, for the SiO_x-C|LNCAM full-cells, voltage profiles reflecting the combination of the respective cathode and anode signatures, and suggests a reciprocal compensation of irreversible capacities during the first charge, thus leading to a subsequent discharge fully in line with the one related to the Li|LNCAM half-cell (compare voltage profiles of panels **(c, d)** with insets of **Figure 4.7(c)**). Furthermore, the cathode side shows initial discharge capacity and cut-off remarkably depending on the N/P ratio with values of ~ 100 mAh g^{-1} at ~ 3.7 V in the cell using N/P of 0.98 (**Figure 4.8(c)**), and ~ 115 mAh g^{-1} at ~ 3.5 V in the one using N/P of 0.84 (**Figure 4.8(d)**). The charge/discharge profiles of the full-cell with N/P ratio of 0.98 (**Figure 4.8(a)**) display more pronounced alteration. In fact, the working voltage of the electrodes is increased upon cycling more than the cell with N/P of 0.84 (**Figure 4.8(b)**). This difference suggests a better reciprocal compensation of the irreversible capacity ascribed to LNCAM and SiO_x-C through N/P of 0.84 compared to 0.98. In detail, the LNCAM cathode in the cell with N/P = 0.98 (panel **(c)**) delivers irreversible charge capacity of 338 mAh g^{-1} (1.12 mAh) at a final voltage cut-off of 4.971 V, while the cathode in the cell with N/P = 0.84 (panel **(d)**) displays irreversible charge capacity of 299 mAh g^{-1} (0.95 mAh) at 4.858 V cut-off. The respective SiO_x-C discharge capacities and voltage cut-off in the full-cell are of 933 mAh g^{-1} (1.12 mAh) at 0.170 V (N/P = 0.98, panel **(e)**) and 960 mAh g^{-1} (0.95 mAh) at 0.056 V (N/P = 0.84, panel **(f)**). Thus, as mentioned before, the results reveal that the use of a N/P ratio of 0.98 is insufficient to allow a full Li-alloying process of the anode during first charge of the corresponding Li-ion cell with consequent low utilization of SiO_x-C as indicated by the relatively high final reduction voltage (*i.e.* 0.170 V). Instead, the lower anode content achieved by setting up a N/P of 0.84 increases the utilized fraction of the alloying material, as indeed evidenced by the final voltage cutoff of the SiO_x-C (*i.e.* 0.056 V) achieved by full-cell charge. The first discharge of the full-cell further supports the improvement achieved by setting up a N/P of 0.84 which leads to capacity of 113 mAh g^{-1} at 3.534 V cutoff for LNCAM (panel **(d)**) and 364 mAh g^{-1} at 2.009 V for SiO_x-C (panel **(f)**) with respect to 97 mAh g^{-1} at 3.681 V and 275 mAh g^{-1} at 2.163 V, respectively, for N/P of 0.98 (panels **(c, e)**).

Figure 4.9 reports the cycling behavior extended to 10 cycles of the above full SiO_x-C| LNCAM cells in terms of gravimetric capacity calculated with respect to the active cathode mass, delivered at C/10 with N/P ratio of either 0.98 (**Figure 4.9(a, c)**) or 0.84 (**Figure 4.9(b, d)**). The voltage profiles related to the cell with N/P = 0.98 (**Figure 4.9(a)**) show a higher irreversible charge capacity at the first cycle compared to the cell with N/P = 0.84 (**Figure 4.9(b)**), that is, 279 mAh g^{-1} and 258 mAh g^{-1}, respectively, reflected in subsequent discharge capacity of 99 mAh g^{-1} and 115 mAh g^{-1} and corresponding coulombic efficiency of 35% and 44%. Moreover, the cell with N/P ratio of 0.98 shows a more relevant capacity loss with a value of 60 mAh g^{-1} upon 10 cycles and lower final coulombic efficiency of 76% compared to the cell with N/P ratio of 0.84 that delivers a capacity of 73 mAh g^{-1} and coulombic efficiency of 87% at the end of the test. The voltage profiles displayed in **Figure 4.9** show a polarization resulting from the combination of the sloped behavior of anode and cathode, as already mentioned in **Figure 4.8**, thus suggesting an effective reciprocal compensation of the irreversible capacity at the first cycle despite a further effort is required to fully optimize the cell. These data confirm once more a better utilization of LNCAM and SiO_x-C by setting up a N/P of 0.84 in agreement with the behavior of the single electrodes discussed in **Figure 4.8**.

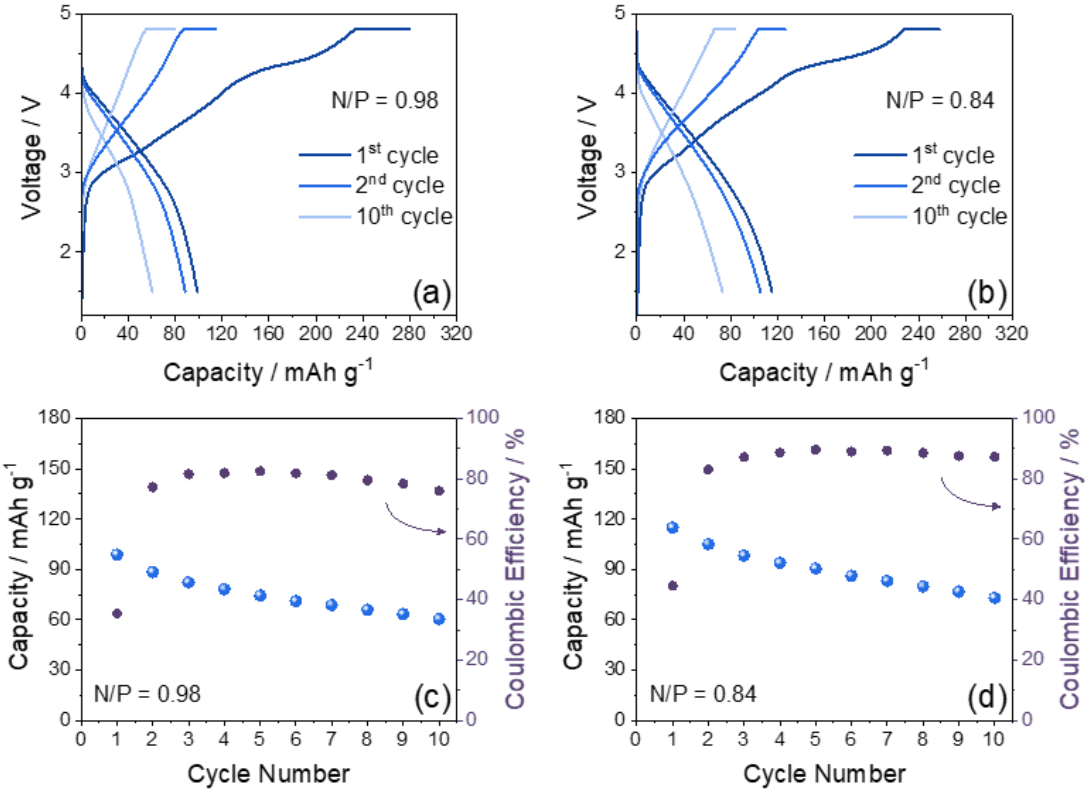

Figure 4.9: ***(a, b)*** *Voltage profiles and* ***(c, d)*** *capacity trends (right y-axes show coulombic efficiency) of the SiO_x-C\|LNCAM full-cells with N/P ratio of either* ***(a, c)*** *0.98 or* ***(b, d)*** *0.84 cycled at the constant current rate of C/10 (1C = 298 mA g_{cat}^{-1}). Voltage range 1.5 – 4.8 V with an additional constant voltage step at 4.8 V held until a current value of ¼ of the nominal C-rate was reached (CCCV mode). Room temperature (25 °C).*[390]

To further investigate the cycling behavior prolonged to 50 cycles of the SiO_x-C|LNCAM system, a coin-type full-cell with N/P of 0.91 was tested, and the results are shown in **Figure 4.10**. The cell shows high irreversible charge capacity at the first cycle, that is 294 mAh g^{-1}, and discharge capacity of 104 mAh g^{-1}, with corresponding coulombic efficiency of 35%. Subsequently, the cell delivers a capacity of about 80 mAh g^{-1} during the initial cycling stages, which stabilizes at about 70 mAh g^{-1} after 20 cycles retained until the end of the test, with a coulombic efficiency approaching 85%. Therefore, the excess of the cathode in the SiO_x-C|LNCAM cell may represent a viable strategy to improve the cycling behavior. In fact, the cell with a N/P ratio of 0.91 delivers capacity and efficiency values close to the ones obtained for the cell with N/P with 0.84 (**Figure 4.9(b, d)**). These data suggest the need of further optimization of the electrode balancing to achieve a higher capacity.[413] Moreover, a capacity retention of about 70% after 50 charge/discharge cycles could represent a promising result in terms of stability of the cell, despite enhanced synthesis pathway for the LNCAM material and optimized cell may lead to performance of practical interest.[158,403,413]

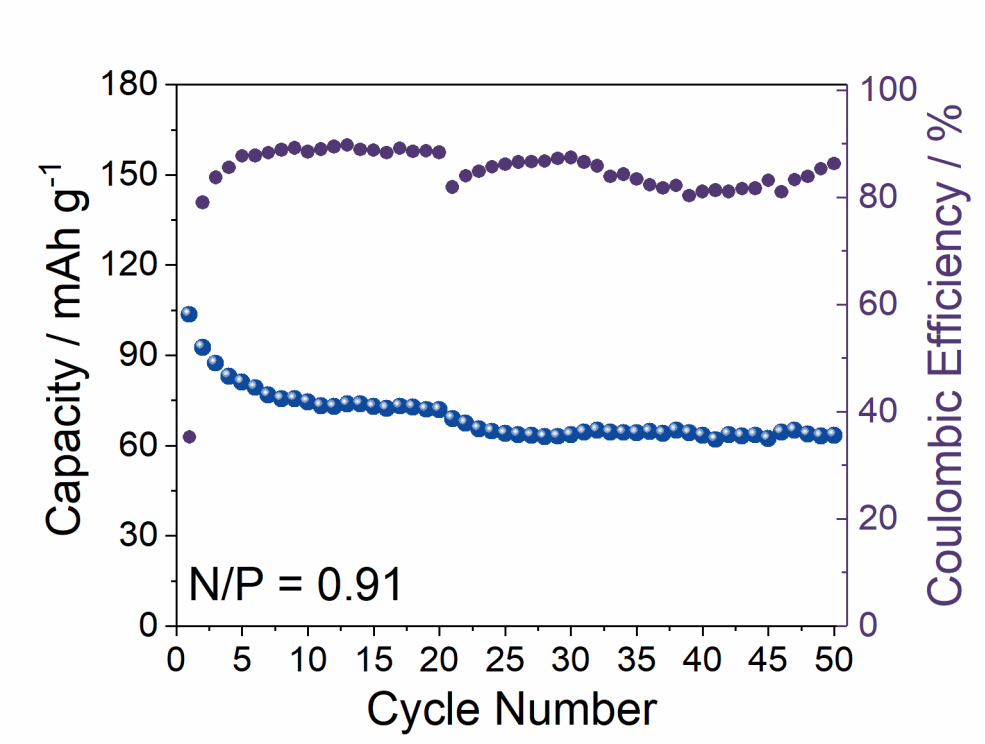

Figure 4.10: *Capacity trend (right y-axes show coulombic efficiency) of the SiO_x|LNCAM full-cell with N/P ratio of 0.91 cycled at the constant current rate of C/10 (1C = 298 mA g^{-1}). Voltage range 1.5 – 4.8 V with an additional constant voltage step at 4.8 V held until a current value of ¼ of the nominal C-rate was reached (CCCV mode). Room temperature (25 °C).*[390]

On the other hand, the study is herein focused on a proof-of-concept Li-ion battery combining electrode materials without any pre-treatment or activation process to overcome one the main critical issues that avoids the large-scale diffusion of these appealing energy storage systems. Indeed, with the aim to further investigating the effects of the selected N/P ratio, a detailed study of the

electrode/electrolyte interphase has been performed on the SiO_x-C|LNCAM cells by carrying out EIS at OCV and at full discharged states after few galvanostatic cycles, as reported in **Figure 4.11**.

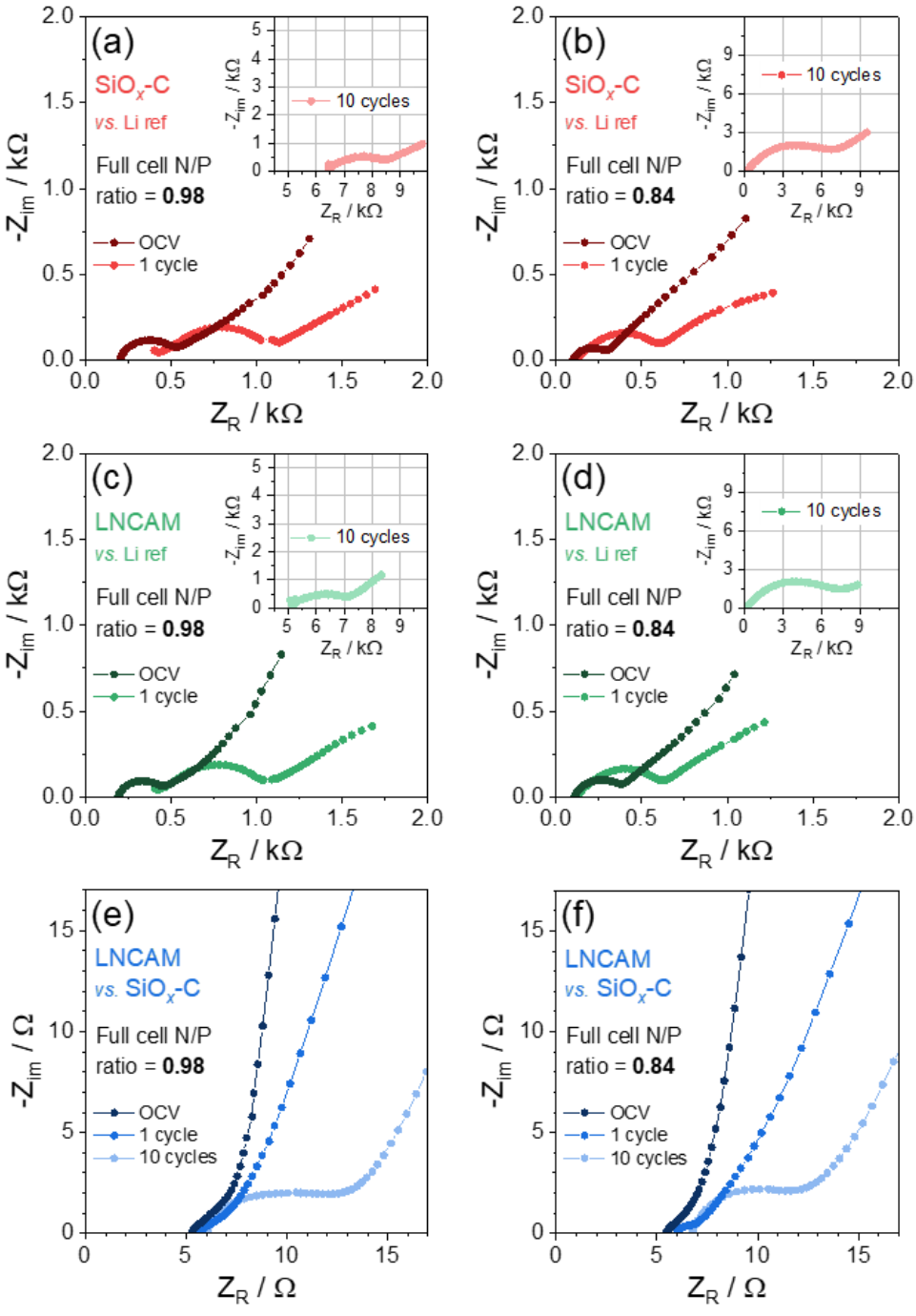

Figure 4.11: *EIS measurements performed on SiO_x-C|LNCAM full-cells. In detail: Nyquist plots related to the* ***(a, b)*** *SiO_x-C anode and* ***(c, d)*** *LNCAM1000_12h cathode collected concomitantly by using a Li reference electrode in* ***(e, f)*** *full-cells with N/P ratio of either* ***(a, c, e)*** *0.98 or* ***(b, d, f)*** *0.84; EIS carried out at the OCV of the cells and after 1 and 10 (insets) galvanostatic cycles depicted in Figure 4.8; frequency range 500 kHz – 100 mHz; alternate voltage signal: 30 mV.*[390]

The use of an additional lithium electrode as reference in the cells allows the study of three different sides of each cell, that is, SiO_x-C vs. Li (**Figure 4.11(a, b)**), LNCAM vs. Li (**Figure 4.11(c, d)**) and SiO_x-C vs. LNCAM (**Figure 4.11(e, f)**) at OCV condition, as well as after 1 and 10 charge/discharge cycles. The NLLS analyses performed on the Nyquist plots, displayed in **Table 4.4**, reveal that all the considered systems can be generally represented by the $R_e(R_iQ_i)Q$ circuit, where R_e is the electrolyte resistance, R_i and Q_i account for the electrode/electrolyte interphase, and Q is a constant phase element that may refer to the cell geometric capacitance or to the Warburg-type Li^+ ions diffusion, depending on the system taken into account.[273,274] It is worth mentioning that **Table 4.4** reports the overall resistance (R_e + R_i) instead of the single values to avoid differences ascribed to the cell geometry in the various configurations, in particular those referring to the reference Li electrode. In fact, the latter cell setup involves a larger amount of electrolyte between electrodes and Li-reference and typically higher resistances compared to a Li-ion cell closely stacking the SiO_x-C anode and the LNCAM cathode. Indeed, the full-cell with N/P ratio of 0.98 exhibits a resistance value referred to the SiO_x-C/Li system (panel **(a)**) around 458 Ω at the OCV condition, that greatly increases to 8259 Ω upon 10 cycles (inset of panel **(a)**). A similar trend is observed for the LNCAM/Li system of the same cell (panel **(c)**) with initial resistance of 399 Ω, that reaches after 10 cycles a value of 7246 Ω (inset of panel **(c)**). On the other hand, the full-cell assembled with N/P = 0.84 presents at the OCV condition a resistance of 268 Ω for the SiO_x-C/Li system (panel **(b)**) and 345 Ω for LNCAM (panel **(d)**), that increases after 10 cycles to 5467 Ω (inset of panel **(b)**) and 8282 Ω (inset of panel **(d)**). Hence, the cell with N/P of 0.84 shows a much lower increase of the anodic side resistance compared to the cell with N/P of 0.98, and a slightly higher increase of the cathodic side value by cycling. This suggests a mitigated degradation of the SiO_x-C anode interphase in the former cell compared to the latter, and a substantial similarity of the LNCAM cathode interphase.

On the other hand, the SiO_x-C/LNCAM cells with N/P = 0.98 (panel **(e)**) and N/P = 0.84 (panel **(f)**) display resistance values two order of magnitude lower compared to the corresponding anode/cathode vs. reference Li electrode systems, due to the abovementioned geometry differences. Despite the similarity, the full-cell with N/P ratio of 0.98 reveals slightly higher resistances compared to the one with N/P of 0.84, with values increasing from 8.3 Ω at the OCV to 13.7 Ω in the former and from 7.5 Ω at the OCV to 12.2 Ω in the latter, which is in line with the combined trend of the corresponding electrodes referred to the additional lithium electrode. Hence, the study of the SiO_x-C or LNCAM electrodes using the Li reference gives additional insights on the electrode/electrolyte interphases of cathode and anode which are not fully revealed by considering the combination of the two materials in a full Li-ion cell.

Table 4.4: *NLLS analyses of the Nyquist plots reported in Figure 4.11 recorded by performing EIS on SiO_x-C|LNCAM full-cells using an additional lithium electrode as reference and N/P ratio of either 0.98 or 0.84. The measurements were performed on the three different sides SiO_x-C vs. Li reference, LNCAM vs. Li reference and SiO_x-C vs. LNCAM.*[390]

N/P ratio	Considered system	Cell condition	Circuit	$R_e + R_i$ (Ω)	χ^2
0.98	SiO_x-C vs. Li reference	OCV	$R_e(R_iQ_i)Q$	458 ± 4	3×10^{-5}
		1 cycle	$R_e(R_iQ_i)Q$	1103 ± 22	3×10^{-4}
		10 cycles	$R_e(R_iQ_i)Q$	8259 ± 101	1×10^{-5}
	LNCAM vs. Li reference	OCV	$R_e(R_iQ_i)Q$	399 ± 8	2×10^{-4}
		1 cycle	$R_e(R_iQ_i)Q$	1044 ± 14	1×10^{-4}
		10 cycles	$R_e(R_iQ_i)Q$	7246 ± 57	1×10^{-5}
	LNCAM vs. SiO_x-C	OCV	$R_e(R_iQ_i)Q$	8.3 ± 0.2	4×10^{-5}
		1 cycle	$R_e(R_iQ_i)Q$	8.5 ± 0.3	3×10^{-5}
		10 cycles	$R_e(R_iQ_i)Q$	13.7 ± 0.3	2×10^{-4}
0.84	SiO_x-C vs. Li reference	OCV	$R_e(R_iQ_i)Q$	268 ± 4	2×10^{-4}
		1 cycle	$R_e(R_iQ_i)Q$	594 ± 15	3×10^{-4}
		10 cycles	$R_e(R_iQ_i)Q$	5467 ± 150	1×10^{-4}
	LNCAM vs. Li reference	OCV	$R_e(R_iQ_i)Q$	345 ± 5	1×10^{-4}
		1 cycle	$R_e(R_iQ_i)Q$	582 ± 14	4×10^{-4}
		10 cycles	$R_e(R_iQ_i)Q$	8282 ± 74	2×10^{-4}
	LNCAM vs. SiO_x-C	OCV	$R_e(R_iQ_i)Q$	7.5 ± 0.2	4×10^{-5}
		1 cycle	$R_e(R_iQ_i)Q$	6.7 ± 0.1	4×10^{-5}
		10 cycles	$R_e(R_iQ_i)Q$	12.2 ± 0.3	2×10^{-4}

In general, the NLLS analyses suggest that the rapid capacity decay observed in **Figure 4.9(a)** for the full-cell using N/P ratio of 0.98 is mainly related with the excessive increase of the SiO_x-C interphase resistance, possibly due to the electrolyte degradation promoted by the voltage change during operation.[221] Instead, the full-cell with N/P ratio of 0.84 allows a limited increase of the SiO_x-C interphase resistance, despite the limited increase of the value ascribed to the LNCAM cathode, which appears to have less effect on the cell decay. Interestingly, the two Li-ion cells have similar resistance values, whilst substantial differences between the anode and cathode detected by the Li reference suggest a kinetic control of the anode, and a better electrode/electrolyte interphase using N/P of 0.84 reflected into a better cycling performance.[45]

4.3 Chemical Approach to Achieve Sodiated Alloying Anode for Direct Application in Na-ion Battery

Na-alloying electrodes such as Sn-C have a relevant irreversible capacity during the first cycle, that limits their direct use in full Na-ion cell without the proper treatment.[151] An original chemical strategy is herein exploited, consisting of capillary contact between the electrode and sodium metal wet by the electrolyte, in order to obtain a chemical partial pre-sodiation. The cycling response and the structural features are reported in **Figure 4.12**. The galvanostatic tests have been performed at a current of 15 mA g^{-1} between 0.01 and 2.0 V on electrodes which had underwent contact with Na for various times and are aimed to assess the actual electrochemical and chemical sodiation degree vs. contact time.

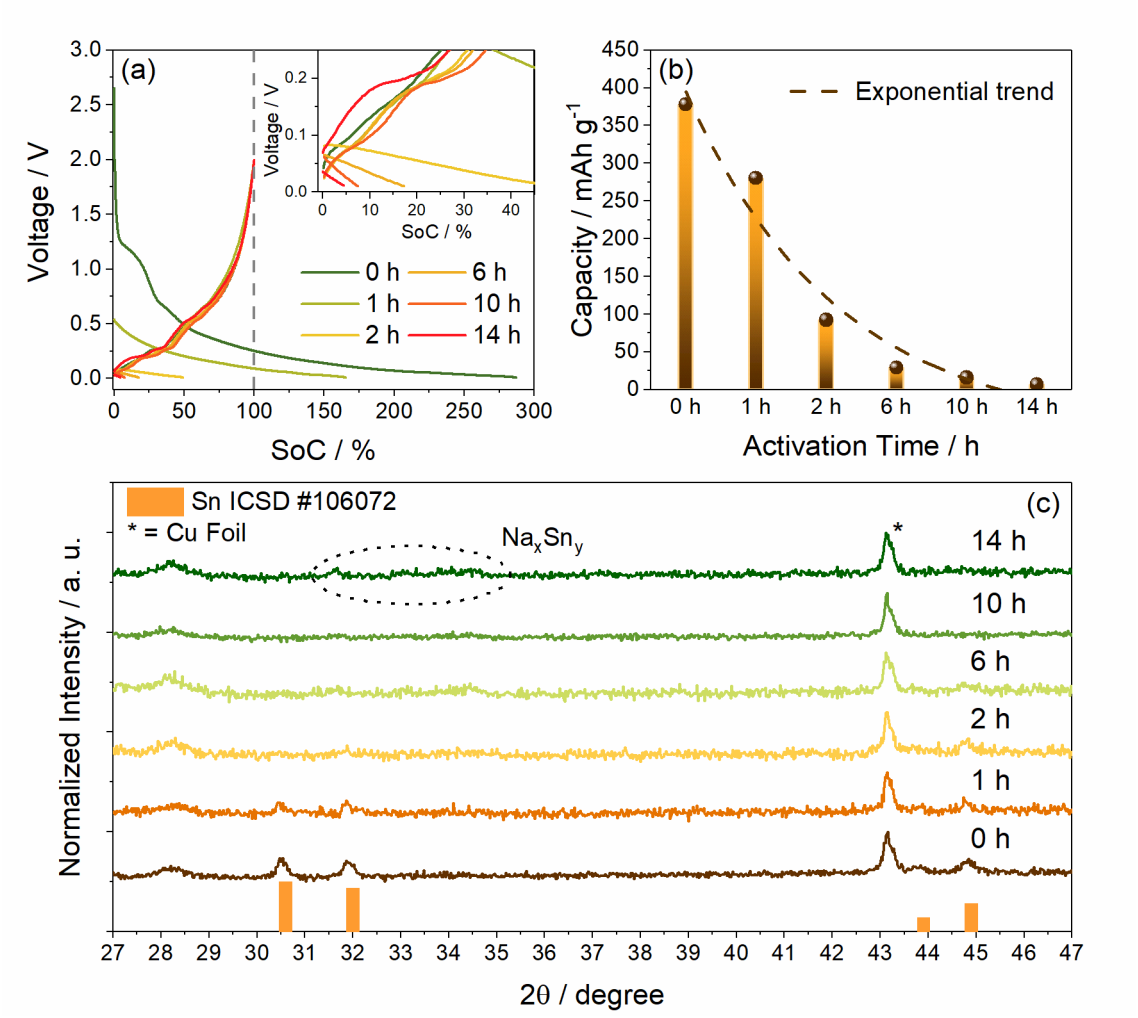

Figure 4.12: *Electrochemical and structural characterization of Sn-C samples with different sodiation times.* ***(a)*** *Voltage profiles as a function of SoC%, corresponding to the degree of sodiation, with magnification of the low SoC% region in the inset. Tests performed by using a constant current of 15 mA g^{-1} in the 0.01 – 2.0 V voltage range.* ***(b)*** *Capacity values at corresponding sodiation time with related exponential trend (dotted line).* ***(c)*** *XRD patterns of sodiated Sn-C samples compared to corresponding reference diffractogram of Sn (ICSD #106072). Room temperature (25 °C).*

Figure 4.12(a) shows the obtained voltage profiles as a function of percent state of charge (SoC%). The SoC% values have been calculated by normalizing, for each cell, the charge/discharge capacity to that obtained upon the first charge half-cycle. Magnification of the low SoC% region is reported in the inset. The discharge capacity of the cell using the pristine Sn-C (0 h of sodiation) shows an irreversibility exceeding by 250 % the reversible value (~150 mAh g^{-1}). This relevant side capacity is mainly due to the concomitant electrolyte decomposition and electrode structural re-organization during first discharge, which is a characteristic of this type of electrodes.[151,431] As the time of Na (chemical) pre-contact increases, the first (electrochemical) discharge capacity shrinks from 170% of SoC% for 1 h of sodiation to less than 50 % of the SoC% for 14 h of sodiation, thus suggesting the gradual suppression of the irreversible capacity, and the concomitant increase of reversible Na storage into the Sn-C structure by progressive alloying. This behavior is also evidenced in **Figure 4.12(b)**, which shows how the values of the first discharge capacity, obtained electrochemically, can be approximated by an exponential function of the chemical activation time (dotted line). On the other hand, the effectiveness of Na-Sn alloying is demonstrated by the XRD patterns of the sodiated Sn-C samples reported in **Figure 4.12(c)**, that reveal the gradual disappearance of the metallic Sn reflections at 2θ of 30.5°, 31.9°,43.8°, and 44.8° (reference ICSD #106072), and the concomitant formation of weak signals attributed to a Na_xSn_y alloy at 2θ between 31.5° and 35°.[151] This response well suggests the tunability of the chemical sodiation process adopted in this work for possible application of the alloying electrode in combination with a vast array of cathodes, that may require different sodiation degree, such as layered oxides,[391] olivines,[113] and Na-conversion materials.[432] The structural and morphological changes of the Sn-C electrodes upon 14 h of sodiation described above, are hereafter investigated by Raman spectroscopy and SEM/EDS. Prior to the analysis on electrodes, a Raman spectrum of micrometric Sn powder was collected as a reference for tin transitions, and the results are shown in **Figure 4.13**.

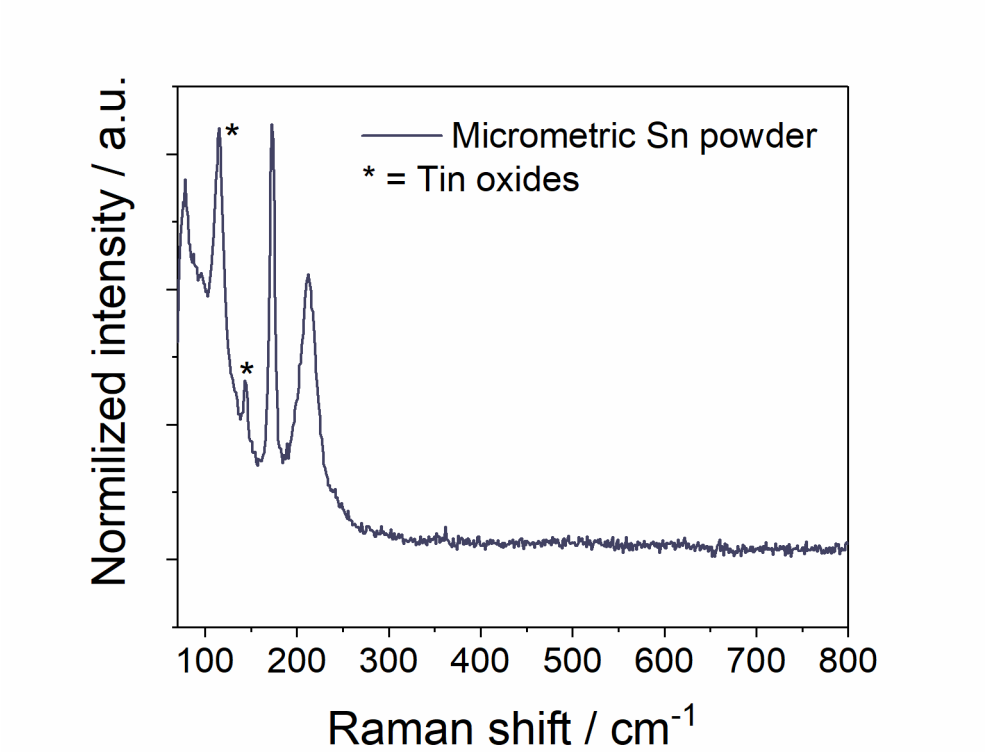

Figure 4.13: *Raman spectrum of micrometric Sn powder recorded in the 70 – 800 cm^{-1} range. Indexed peaks report tin oxides transitions.*

The pattern reveals the presence of the two peaks ascribed to the transition of metal tin centered at 143 and 211 cm^{-1}, while is also reported the presence of two peaks ascribed to the transitions of tin oxides (SnO and SnO_2), indexed with asterisk, probably due to partial oxidation of the powder after moisture exposure.[433] Raman spectra and SEM/EDS images of pristine and sodiated Sn-C samples are reported in **Figure 4.14**. The Raman spectra in panel **(a)** indicate the presence of two strong bands at 1350 and 1600 cm^{-1}, due to D and G vibrations of the carbon matrix. Nevertheless, the pristine electrode (brown line) shows a weak peak around 200 cm^{-1} (indexed with asterisk) ascribed to the vibrational transition of Sn, while in the sodiated sample (green line) this peak almost vanishes. Furthermore, the magnified region between 150 and 800 cm^{-1} reveals for the sodiated sample two additional indexed peaks, possibly ascribed to residual $NaClO_4$ salt and product of the solid electrolyte interphase (SEI) formed at the Sn-C surface after the direct reaction with Na metal.[433,434] On the other hand, the SEM images at different magnifications of the pristine Sn-C electrode (**Figure 4.14(b-d)**) and of the sodiated one (**Figure 4.14(i-k)**) depict changes of the typical submicrometric agglomerated morphology, principally occurring at the material surface. These changes are in part evidenced by the rise of bright spots, highlighted by blue circles and arrows in **Figure 4.14(f)**, likely accounting for the presence of sodium at the activated Sn-C surface.

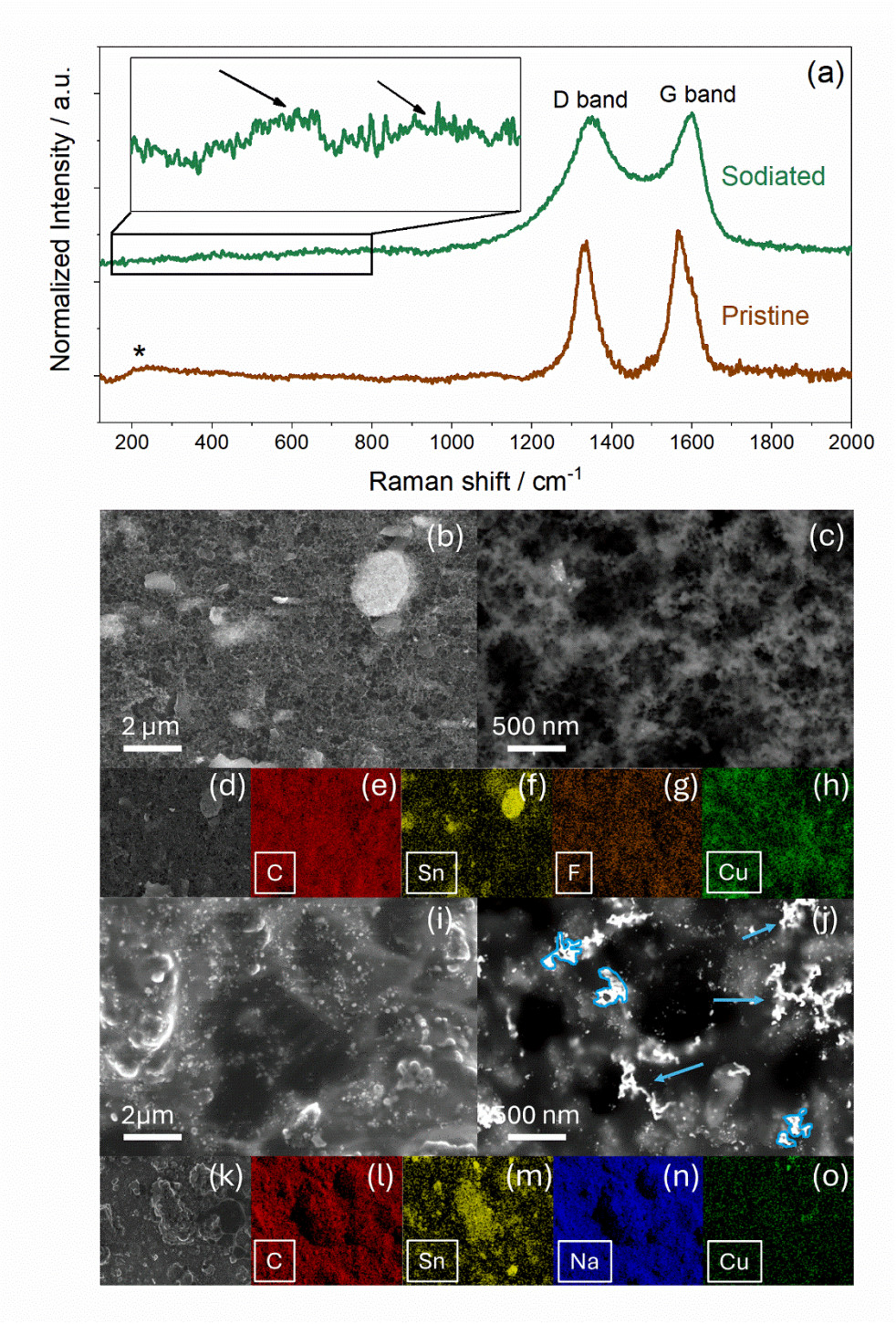

Figure 4.14: *Characterization of the pristine and sodiated (14 h) Sn-C electrodes.* ***(a)*** *Raman spectra recorded in the 150 – 2000 cm^{-1} range. Indexed peaks report transitions identifications. SEM images at different magnifications of* ***(b-d)*** *pristine and* ***(i-k)*** *sodiated electrodes. In details:* ***(c, j)*** *backscattered electrons images. SEM-EDS elemental maps of* ***(e, l)*** *C,* ***(f, m)*** *Sn,* ***(h, o)*** *Cu,* ***(g)*** *F, and* ***(n)*** *Na for* ***(e-h)*** *pristine and* ***(l-o)*** *sodiated electrodes.*

The EDS elemental maps collected on the SEM of the bare Sn-C in **Figure 4.14(d)** show the expected presence of C (**Figure 4.14(e)**) and Sn (**Figure 4.14(f)**) components of the active material, Cu (**Figure 4.14(h)**) of the support, and F (**Figure 4.14(g)**) of the polymeric binder used to form the electrode tape. Instead, F is missing in the maps collected on the SEM of the sodiated electrode of **Figure**

4.14(k) while Cu is weakened (**Figure 4.14(o)**), likely due to the surface covering by SEI. Furthermore, Na is detected (**Figure 4.14(n)**) alongside with C (**Figure 4.14(l)**) and Sn (**Figure 4.14(m)**), thus accounting for the Sn-C sodiation.

Sn-C and NCAM are preliminarily cycled in half-cells at the constant current rate of 15 mA g^{-1}, as reported in **Figure 4.15**, to verify their electrochemical response.

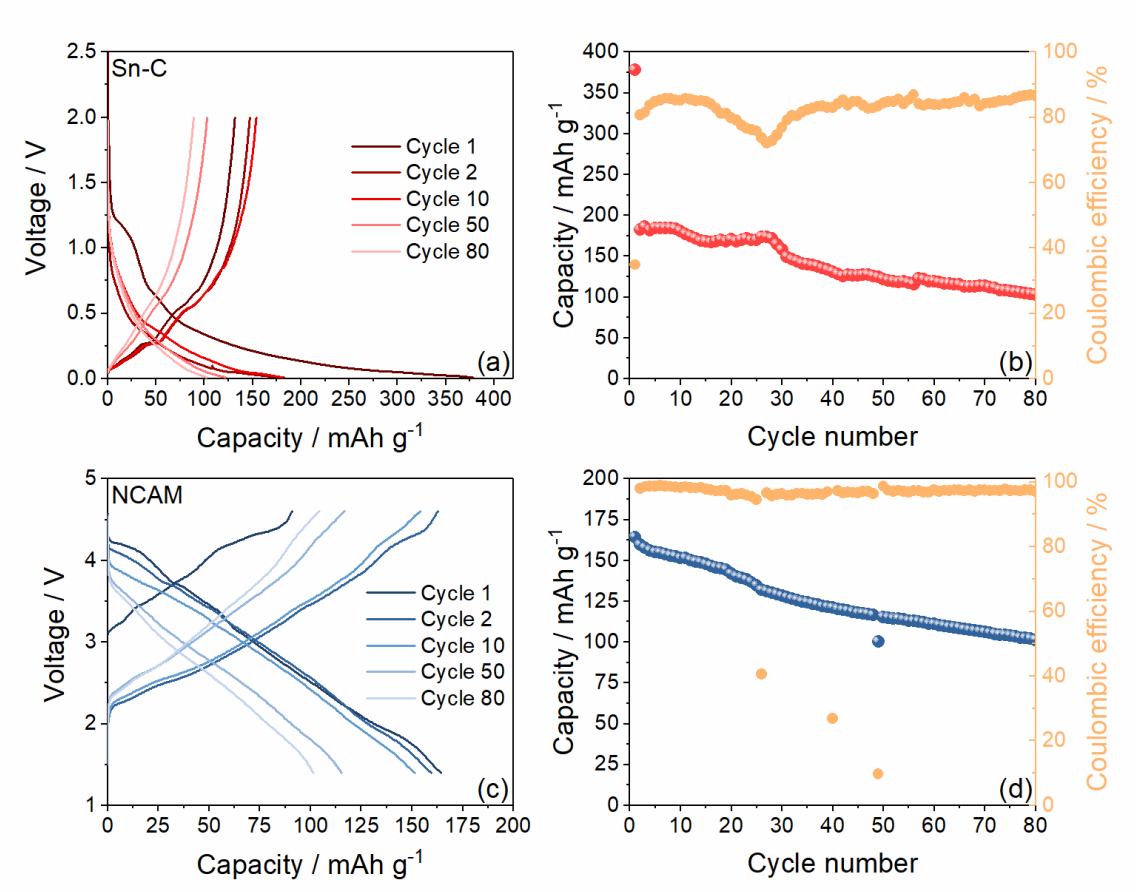

Figure 4.15: *Galvanostatic cycling performance at 25 °C of the* ***(a, b)*** *Na|Sn-C and* ***(c, d)*** *Na|NCAM half-cells at the constant current rate of 15 mA* g^{-1} *in terms of* ***(a, c)*** *selected voltage profiles and* ***(b, d)*** *discharge capacity trend reporting coulombic efficiency on right y-axes. Voltage ranges: 0.01 – 2.0 V and 1.4 – 4.6 V for Sn-C and NCAM, respectively.*

The voltage profiles show for Sn-C (panel **(a)**) the initial irreversibility mentioned above, and the typical sloping behavior and characteristic signatures ascribed with the Na-Sn alloying and Na insertion into the amorphous carbon, with a reversible capacity of about 180 mAh g^{-1}.[151,435,436] Furthermore, the corresponding cycling trend in **Figure 4.15(b)** reveals a coulombic efficiency fluctuating between 72% and 88% after the first cycle, a low value likely due to a concomitant undesired electrolyte decomposition induced by metal Na, which leads to a capacity retention of about 60% over 80 cycles. On the other hand, the NCAM electrode evidences the Na^+ (de-)intercalation in the layered structure, between 2.2 and 4.2 V (panel **(c)**), with an initial charge capacity of about 90 mAh g^{-1}, that is the 55% of the subsequent discharge capacity (164 mAh g^{-1}). The difference between

first charge and first discharge capacity is attributed to the Na-deficient character of the P3/P2-type layered oxide, which has the chemical formula $Na_{0.48}Al_{0.03}Co_{0.18}Ni_{0.18}Mn_{0.47}O_2$.[391] The Na half-cell using NCAM reveals an efficiency exceeding 95%, except for occasional drop-down possibly due to some minor irreversibility, with a retention of about 64 % over 80 cycles (panel **(d)**). It is worth mentioning that the above Na deficiency in the cathode would not allow the use of a typical anode without any Na-reservoir in its structure, necessary for allowing the full discharge of the latter during the subsequent cycles, in a possible full-cell combining the two materials.

Therefore, among the pre-sodiation conditions of the Sn-C shown in **Figure 4.12(b)**, a treatment time of 2 h has been selected as the most suitable for achieving a sufficient Na-reservoir to allow the proper operation of a full-cell combining this anode with the NCAM cathode as reported in **Figure 4.16**.

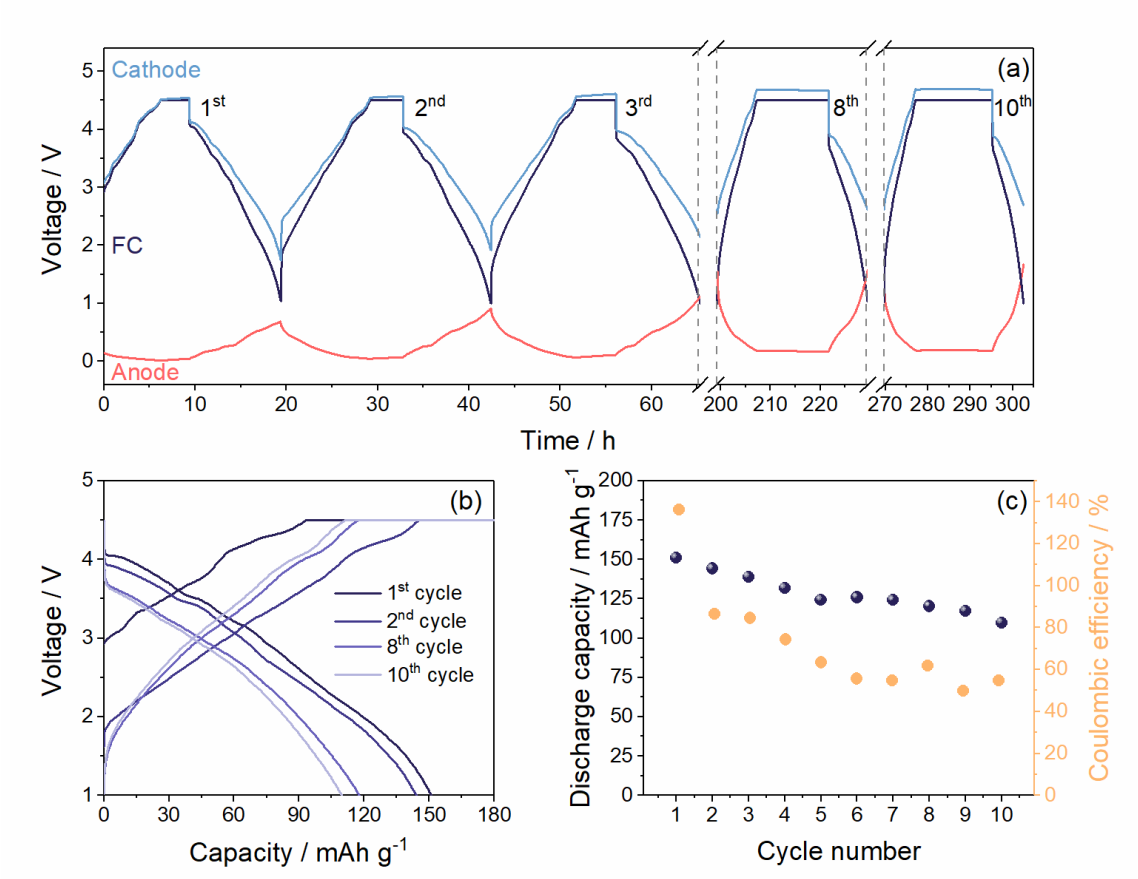

Figure 4.16: (a) *Time evolution of the Sn-C anode and the NCAM cathode voltage concomitantly collected by using an additional Li reference electrode, and of the corresponding Sn-C|NCAM full-cell.* ***(b)*** *Voltage profiles and* ***(c)*** *capacity trend (right y-axes shows coulombic efficiency) of the Sn-C|NCAM full-cell cycled at the constant current rate of 15 mA* g_{cat}^{-1} *in the 1.0 – 4.5 V voltage range with an additional current voltage step at 4.5 V held until a current value of ¼ of the nominal C-rate was reached. Room temperature (25 °C).*

The time evolution of the full-cell voltage during galvanostatic cycling at a current of 15 mA g_{cat}^{-1} in the 1.0 – 4.5 V range is reported in **Figure 4.16(a)** (black line), in addition to the voltage signatures of Sn-C (red line) and NCAM (blue line), collected separately using a Na reference electrode to help a better understanding of the concomitant contributions of anode and cathode. Remarkably, the first

charge profile of the full-cell depicts the combination of the partial de-sodiation of Na-deficient NCAM and of the corresponding sodiation of Sn-C. Subsequently, the cell reversibly operates with a voltage combining the charge/discharge curves of anode and cathode for over 10 cycles, with initial capacity as high as 150 mAh g_{cat}^{-1} and a final value of about 110 mAh g_{cat}^{-1}, as evidenced either by the corresponding cycling profile in **Figure 4.16(b)** and the cycling trend in **Figure 4.16(c)**. However, the full-cell reveals a low coulombic efficiency, fluctuating from 51 to 85% likely due to the reactivity of the electrodes, particularly the anode where the presence of Na metal clusters induces a larger irreversibility with the electrolyte, as already observed in **Figure 4.15**. The obtained results indicate the correct cathode/anode setup in terms of the N/P ratio (*i.e.*, 1.1), and the suitability of the chemical sodiation of the Sn-C electrode for achieving reversible operation of the full-cell. On the other hand, the data also suggest the need for a better tuning of the electrolyte to get a higher efficiency and increase the full-cell stability and cycle life.[192,437]

To shed light on the modification upon cycling of interfacial properties and charge-transfer kinetics of the Sn-C|NCAM full-cell, EIS analysis is performed in **Figure 4.17**. The related Nyquist plots at the OCV and after 1, 8, and 10 galvanostatic cycles at the discharged state of the cell (voltage = 1V) are collected in **Figure 4.17(a)**. All the spectra reveal a low-frequency line typical of diffusion and middle-to-high-frequency semicircle(s) typical of interfacial processes. The low-frequency region, simulated by WQ_W elements, has been subtracted from the overall response to achieve the plots of **Figure 4.17(b)**, with the aim of better evidencing the middle-to-high frequency features related to interfacial kinetics and to meet the boundary conditions ($\omega \rightarrow 0$) required for the subsequent calculation of DRT function with Tikhonov regularization.[262,272–274] The figure reveals two semicircles at middle-to-high frequencies, so that the overall Nyquist plots can be modeled to an equivalent circuit $R_e(R_1Q_1)(R_2Q_2)WQ_W$ in Boukamp's notation.[273,274] Although the individual anode and cathode contributions to the overall cell polarization cannot be properly discerned in the response of the full-cell in **Figure 4(a, b)**, the two evidenced semicircles can be likely related with anode and cathode SEIs ($R_{SEI}Q_{SEI}$) at higher frequencies, and to charge-transfer processes ($R_{ct}Q_{dl}$) at lower frequencies, along with the electrolyte resistance (R_e) detected at the highest-frequency intercept with the real axis.

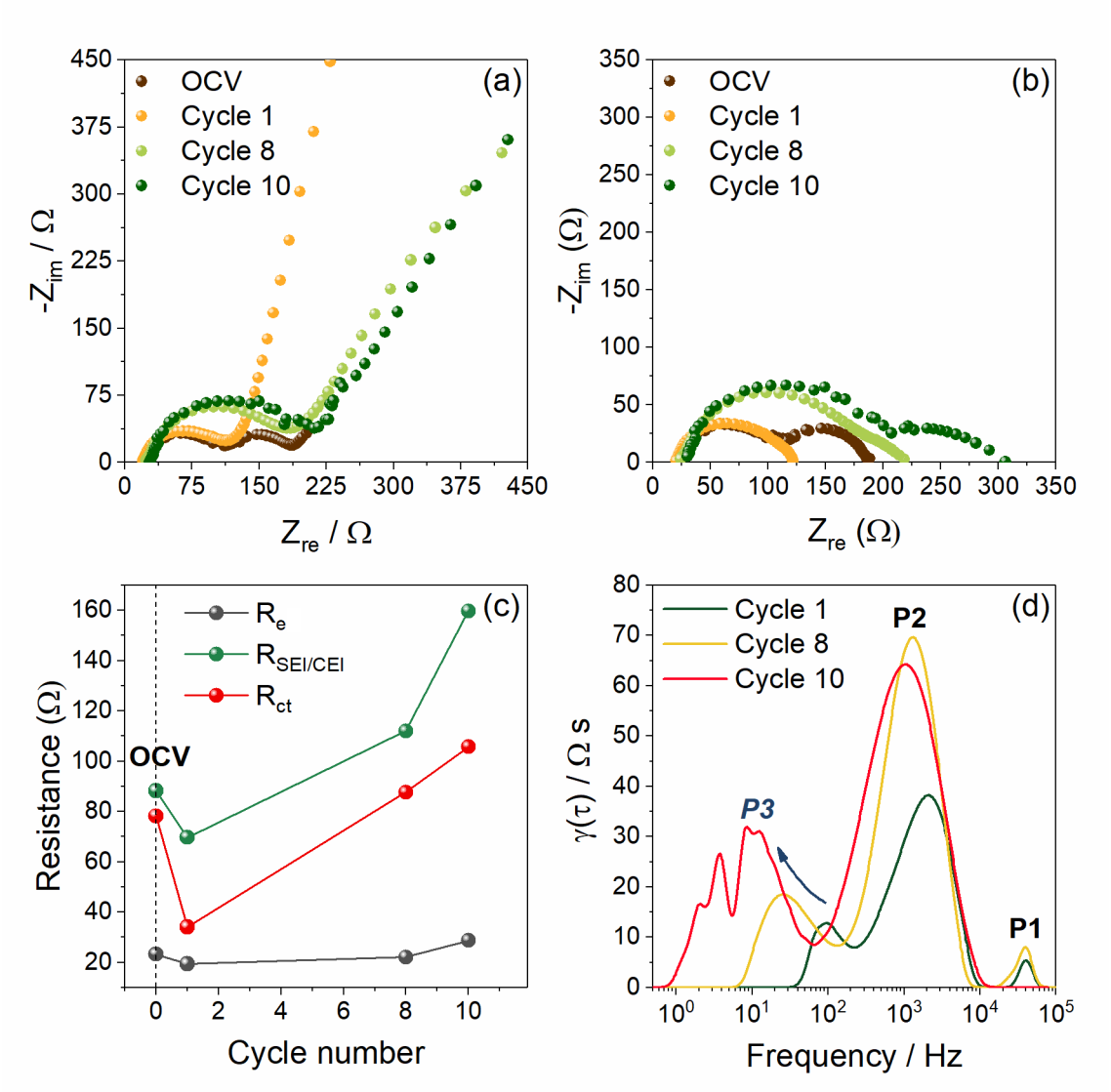

Figure 4.17: *EIS analysis of the Sn-C|NCAM full-cell.* ***(a)*** *Nyquist plots collected at the OCV of the cell and after 1, 8, and 10 galvanostatic cycles and* ***(b)*** *after subtraction of the diffusive contribute.* ***(c)*** *Trend of R_e, R_{SEI}, and R_{ct} as a function of the cycle number obtained from NLLS analysis of the impedance spectra.* ***(d)*** *DRT analyses in terms of γ-factor vs. frequency with associated peak indexing obtained from the Nyquist plot after 1, 8, and 10 galvanostatic cycles. EIS collected in the 500 kHz – 100 mHz frequency range with an alternate voltage signal of 30 mV. Room temperature (25 °C).*

The middle-to-high frequency dispersions in **Figure 4.17(b)** have been fitted according with the equivalent circuit $R_e(R_{SEI}Q_{SEI})(R_{ct}Q_{dl})$, and the results displayed in **Table 4.5** and **Figure 4.17(c)**, which clearly show, after cell formation, a progressive increase of all resistances upon cycling. The increase of R_e value from the 1st to the 8th cycle indicates a progressive consumption of the electrolyte by side reactions, which causes a thickening of the interphases and leads to concomitant increase of R_{SEI} and R_{ct}. At the 10th cycle, both R_e and R_{SEI} abruptly rise up, thus indicating a worsening of the interfaces and, consequently, of the charge-transfer kinetics. Overall, from the 1st to the 10th cycle, R_{SEI} and R_{ct} respectively increase of about 129 % and 210 %, further suggesting the need for a better selection of the electrolyte solution to avoid cell failure.

Table 4.5: *NLLS analysis of the Nyquist plots reported in Figure 4.17(b) recorded by performing EIS on Sn-C|NCAM full-cell using an additional Na electrode as reference, after subtraction of the diffusive contribution.*

Cell condition	Equivalent circuit	R_e (Ω)	R_{SEI} (Ω)	R_{ct} (Ω)	χ^2
OCV	$R_e(R_{SEI}Q_{SEI})(R_{ct}Q_{dl})$	23.2 ± 0.3	88 ± 3	78 ± 2	4 x 10^{-4}
After 1 cycle	$R_e(R_{SEI}Q_{SEI})(R_{ct}Q_{dl})$	19.4 ± 0.1	70 ± 4	34 ± 4	4 x 10^{-5}
After 8 cycles	$R_e(R_{SEI}Q_{SEI})(R_{ct}Q_{dl})$	22.1 ± 0.2	112 ± 4	88 ± 5	9 x 10^{-5}
After 10 cycles	$R_e(R_{SEI}Q_{SEI})(R_{ct}Q_{dl})$	28.6 ± 0.4	160 ± 8	106 ± 15	6 x 10^{-4}

The calculated DRT functions (**Figure 4.17(d)**), with an optimized λ-value of 0.1, deconvolutes the different semicircles into peaks according to their relaxation frequencies.[272] Beside the minor peak labelled as *P*1 in the high-frequency region ($f > 10^4$ Hz) related with particle-particle and particle-current collector contact resistance, two main peaks can be clearly discerned at the 1st cycle: the peak labelled as *P*2 ($f \approx 10^3$ Hz) related with R_{SEI}, and the peak labelled as *P*3 ($f \approx 10^2$ Hz) related with R_{ct}. Both contributions increase progressively in intensity upon cycling, proportionally to the diameters of the associated semicircles, and *P*3 shifts to lower frequencies more markedly. For sake of clarity, the scattered Nyquist dispersion at the 10th cycle makes the gaussian distribution of *P*3 quite noisy; nevertheless, a clear shift from the previous cycles can be identified, thus suggesting worsening kinetics that progressively hinder the electrochemical processes. Although these results cannot fully discern the degradation mechanism in the cell, we may reasonably assume that parasitic reactions ascribed to the electrolyte can actually worsen the electrode/electrolyte interphases.

To further investigate the interfacial properties, the cathode and anode EIS contributions, separately collected from the Sn-C|NCAM full-cell using the additional Na reference, are reported in **Figure 4.18(a, b)**, respectively, and the results of the related NLLS analysis from the obtained Nyquist plots are summarized in **Table 4.6**. The EIS can be represented by the $R_e(R_{int}Q_{int})Q_g$ equivalent circuit, where R_e is the electrolyte resistance, the ($R_{int}Q_{int}$) elements reflect the main semicircle with a total resistance corresponding to the charge transfer and to the SEI at the electrode/electrolyte interphase, while Q_g is a constant phase element related with the cell capacitance.[273,274]

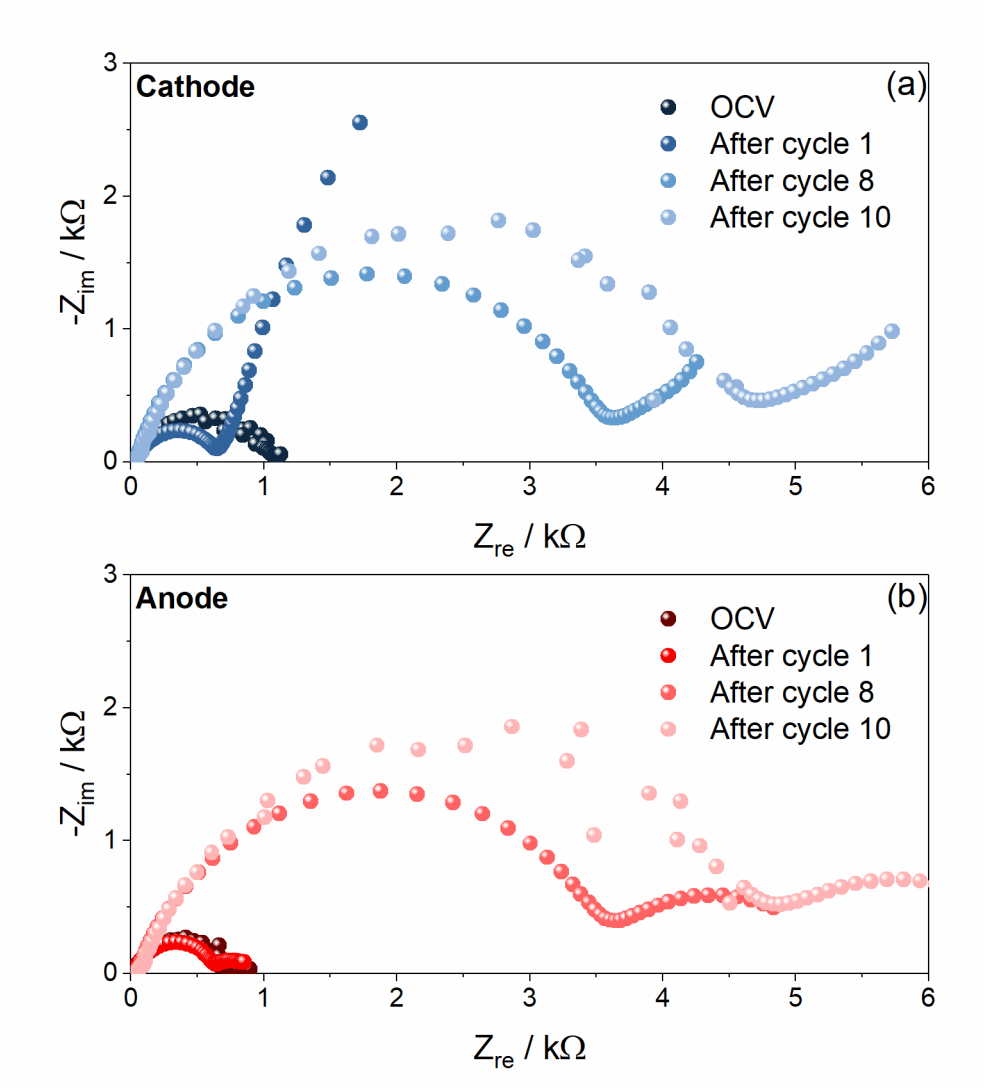

Figure 4.18: *EIS measurements performed on Sn-C|NCAM full-cell. Nyquist plots related to the* ***(a)*** *NCAM cathode and* ***(b)*** *Sn-C anode collected concomitantly by using an additional Li reference electrode. EIS carried out at the OCV of the cell and after 1, 8, and 10 galvanostatic cycles showed in Figure 4.16; frequency range 500 kHz – 100 mHz; alternate voltage signal: 30 mV. Room temperature (25 °C).*

After 1 cycle, the anode response (panel **(b)**) evidences a split of SEI and charge transfer features which allows the fit with two different contributions (see equivalent circuits in **Table 4.6**), hence $R_{int} = R_1 + R_2$ is considered. **Table 4.6** reveals for NCAM the decrease of the total interphase resistance after 1 cycle, and the subsequent increase to about 412 % of the initial value. Analogously, the table shows an increase of the anode total resistance from the OCV to the 10th cycle of about 948 % of the initial value. This behavior is consistent with the results obtained with the analysis of the full-cell polarization in **Figure 4.17**, suggesting parasitic reactions ascribed to the electrolyte that worsen the electrode/electrolyte interphase, especially at the anode side.

Table 4.6: *NLLS analyses of the Nyquist plots reported in Figure 4.18 recorded by performing EIS on Sn-C|NCAM full-cell using an additional sodium electrode as reference, on the two different sides Sn-C vs. Na reference and NCAM vs. Na reference.*

Considered system	Cell condition	Equivalent Circuit	R_{int} (Ω)	χ^2
NCAM vs. Na reference	OCV	$R_e(R_{int}Q_{int})Q_g$	990 ± 27	5×10^{-4}
	After 1 cycle	$R_e(R_{int}Q_{int})Q_g$	652 ± 7	1×10^{-4}
	After 8 cycles	$R_e(R_{int}Q_{int})Q_g$	3433 ± 18	6×10^{-5}
	After 10 cycles	$R_e(R_{int}Q_{int})Q_g$	4086 ± 82	6×10^{-4}
Sn-C vs. Na reference	OCV	$R_e(R_{int}Q_{int})Q_g$	709 ± 9	4×10^{-4}
	After 1 cycle	$R_e(R_1Q_1)(R_2Q_2)Q_g$	1246 ± 21	2×10^{-4}
	After 8 cycles	$R_e(R_1Q_1)(R_2Q_2)Q_g$	5135 ± 77	1×10^{-4}
	After 10 cycles	$R_e(R_1Q_1)(R_2Q_2)Q_g$	6726 ± 128	7×10^{-4}

To partially exclude the electrode structural deterioration or malfunctioning upon full-cell operation, *ex-situ* SEM images of pristine and cycled electrodes retrieved from a Sn-C|NCAM full-cell are reported in **Figure 4.19**. Particularly, the figure shows the pristine NCAM (panels **(a, b)**) and Sn-C (panels **(e, f)**) electrodes, as well as NCAM (panels **(c, d)**) and Sn-C (panels **(g, h)**) electrodes taken from a cell cycled at 15 mA g_{cat}^{-1}. The NCAM before cycling shows a micrometric morphology which reveals the submicron layers of the material when the magnification is increased (panel **(b)**).[391] Furthermore, the cycled NCAM electrode evidences similar morphology at the lower magnification (panel **(c)**), however with a surface covered by electrolyte decomposition products forming the SEI, whilst the higher magnification image (panel **(d)**) still reveals the layers stacking of the material which remains almost unaltered. On the other side, the pristine Sn-C shows the micrometric particles of the glassy carbon formed by resorcinol-formaldehyde annealing (panel **(e)**), and some nanometric Sn particles embedded in its surface at higher magnification (panel **(f)**).[406] Despite the morphological similarity, the SEM of Sn-C after cycling highlights a rougher and more porous surface compared to the pristine state, with some bright spots typically triggered by a lower material conductivity (panel **(g)**), and clear signs of side product precipitation in the SEI (panel **(h)**).

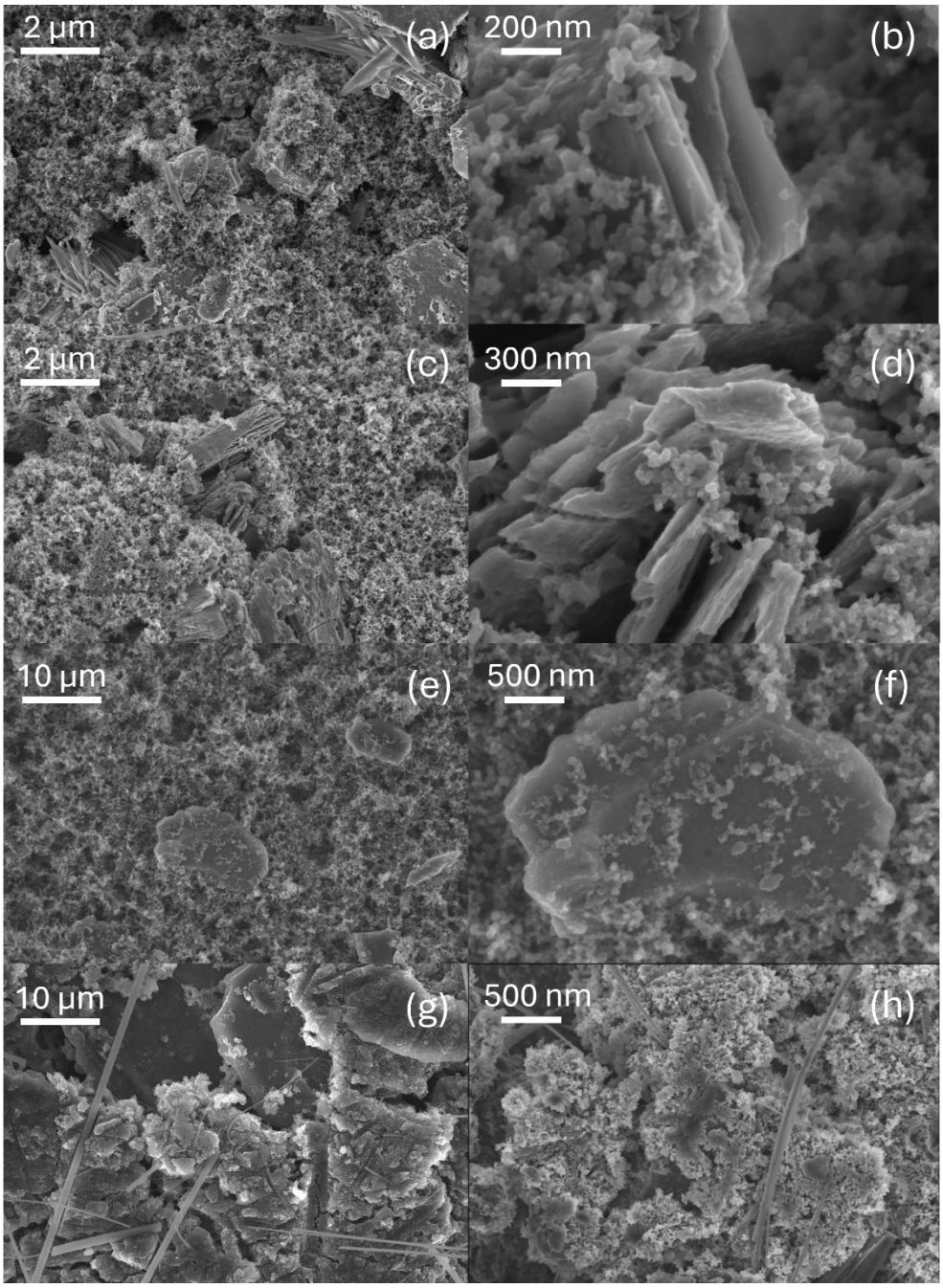

Figure 4.19: *SEM images of pristine* ***(a, b)*** *NCAM and* ***(e, f)*** *Sn-C electrodes and of* ***(c, d)*** *NCAM and* ***(g, h)*** *Sn-C electrodes recovered upon the cycling test at 15 mA* g_{cat}^{-1} *on a Sn-C|NCAM full-cell in the 1.0 – 4.5 V voltage range with an additional constant voltage step at 4.5 V (CCCV mode) until a final current of ¼ referred to the nominal C-rate. Room temperature (25 °C).*

These features well suggest the electrode structural stability and indicate once more the relevant presence of by-products likely precipitated at the electrode surface by electrolyte decomposition. This process appears more evident at the anode side rather than the cathode, as already indicated by the low efficiency of Sn-C in Na half-cell using the same electrolyte (**Figure 4.15(b)**) compared to NCAM (**Figure 4.15(d)**) and confirmed by EIS analysis.

4.4 Conclusions

In this chapter the full-cell balancing by using layered oxide cathodes and alloying anodes has been investigated in both Li-ion and Na-ion systems. In **Section 4.1** the experimental methods adopted in this chapter have been reported.

In **Section 4.2** the synthesis and characterization of a $LiNi_{0.2}Co_{0.2}Al_{0.1}Mn_{0.45}O_2$ (LNCAM) layered oxide cathode, as well as its application in a Li-ion cell employing a SiO_x-C alloying anode without any pre-activation process have been reported. Structural and morphological analysis on the cathode powder evidenced the formation of the P3-type layered structure with trigonal cell unit ($R\bar{3}m$ space group), supported by Raman spectroscopy, and stacked submicrometric flakes forming layered micrometric particles, with homogeneous distribution of the elements, and stoichiometry close to the expected one, confirmed by ICP-MS. The investigation of electrochemical process by coupling CV and EIS revealed an irreversible oxidation process at the first cycle (4.6 V vs. Li^+/Li) due to structural rearrangements with partial oxygen loss and SEI formation, while the subsequent cycles displayed a single-step reversible Li^+ (de-)intercalation process between 3.7 and 3.9 V vs. Li^+/Li with low polarization. The EIS measurements suggested the formation of a suitable passivation layer on the electrodes with a decrease of interphase resistance from 32 Ω at OCV to 16 Ω at the end of the test. Galvanostatic cycling in Li half-cells of LNCAM at constant current of C/20 indicated the 2.5 – 4.8 V voltage range as the most adequate operative condition to achieve fair compromise between delivered capacity (150 mAh g^{-1}), retention (83%), and coulombic efficiency (98% upon initial cycles). *Ex-situ* XRD upon charge/discharge revealed the shift of the (003) and (104) main reflections related to the cathode structure due to occurring of the structural modification suggested by CV. Additional charge/discharge in half-cells at constant currents of C/10 and C/5 in the optimized voltage window displayed a capacity of 137 mAh g^{-1} retained at the 73% at C/10 and respective values of 129 mAh g^{-1} and 66% at C/5.

The LNCAM cathode has been then coupled with the SiO_x-C alloying anode in proof-of-concept Li-ion cells without any pre-activation process. The cells exploited N/P ratios of either 0.98 or 0.84, tuned by considering the characteristic initial irreversibility affecting both materials. Galvanostatic cycling tests on the full-cells at the constant current of C/10 have shown excessive degradation during the first charge for the cell with N/P = 0.98, leading to relevant increase of the voltage of both the electrodes and fast capacity decay. However, the cell with N/P = 0.84 demonstrated a better cycling stability with a maximum delivered capacity of 115 mAh g^{-1}, retention of 63%, and final coulombic efficiency of 87%. The use of additional Li electrode as reference in the full-cells allowed the EIS investigation of cathode and anode interphases, as well as the monitoring of the full-cell behavior. The study indicated a strong influence of the Li-ion cell balancing on the electrode/electrolyte

interphase characteristics and suggested substantial differences between the anode and cathode resistance trends. In particular, the EIS revealed the controlling role of the anode, and a better electrode/electrolyte interphase and cycling performance for the cell using a cathode excess adopting a N/P of 0.84 compared to the one with N/P of 0.98. In summary, the tests demonstrated that the direct combination of the LNCAM layered cathode and the SiO_x-C alloying anode without additional pre-treatments may be a viable strategy to achieve efficient Li-ion systems, despite a further investigation may be required to determine the optimal N/P ratio.

In **Section 4.3** the pre-treatment process of a Sn-C anode for achieving its efficient operation as the alloying electrode in Na-ion battery, in combination with a NCAM layered cathode, has been reported. The treatment consisted of direct Sn-C sodiation by capillary contact of the electrode with Na metal, controlling time and pressure to properly tune the alkali metal content in the electrode. XRD, Raman spectroscopy, SEM/EDS analysis, and electrochemical tests have shown the achievement of different sodiation degrees in the anode, which can allow its combination with various cathodes, including layered oxides, olivines, and conversion materials, in full-cell configuration. Hence, a Sn-C|NCAM cell was assembled with N/P ratio of 1.1 and subjected to charge/discharge tests showing reversible voltage profiles for over 10 cycles. The cell revealed an initial capacity as high as 150 mAh g_{cat}^{-1} and a value of about 110 mAh g_{cat}^{-1} after 10 cycles, with a coulombic efficiency fluctuating from 51 to 85%. The relatively low efficiency has been ascribed to side reactions of the electrodes with the electrolyte, in particular at the anode side, which suggested the need for a better tuning of the solution to achieve higher efficiency and stability. On the other hand, EIS from the 1st to the 10th cycle of the full-cell evidenced an increase of about 129 % of the SEI resistance, and of 210 % of the charge-transfer one, thus further indicating the electrolyte reactivity. The calculated DRT functions indicated that both SEI and charge transfer contributions, revealed as peaks at 10^3 Hz and at 10^2 Hz, respectively, increased progressively in intensity and concomitantly shifted to lower frequencies. This behavior suggested a worsening of the reaction kinetics by cycling, which slows down the electrochemical processes in the cell. On the other hand, *ex-situ* SEM analysis of Sn-C and NCAM have shown the structural integrity of the electrodes upon cycling, which has instead promoted the electrolyte decomposition and precipitation of side product at the surface, principally at the anode. These preliminary outcomes suggest that the direct anode sodiation herein adopted is a suitable approach to achieve electrodes for full-cell application, and indicate the need of further efforts on the tuning of electrode/electrolyte interactions to achieve an efficient and sustainable Na-ion battery.

5. General Conclusions

The herein presented thesis proposed the study of different cathode chemistries for application in innovative Li-ion and Na-ion batteries, coupled with the investigation of the effect of electrode processing on the upscaling of cell manufacturing.

The first chapter is focused on the study of a safe, cheap, and stable olivine cathode for application in both Li-ion and Na-ion systems. The achieved LFMP material presented suitable performance in Li metal cell, suggesting the possible achievement of safe, low cost, high-energy-density and efficient batteries including stable olivine cathodes, solid polymer electrolyte, and the high-energy lithium metal. Furthermore, the electrochemical converted NFMP cathode obtained from the lithium analogue reveals promising performance for application in stationary storage systems. Indeed, the obtained results can shed light on the possibility of achieving low-cost and environmentally friendly cathode with similar structural stability, ion transport, and interfacial properties compared to lithium ones. Moreover, an increased distortion of NFMP olivine structure has been evidenced and confirmed by *ex-situ* and *operando* XAS measurements, with hindered Mn local environment reactivity, despite further analyses are required to better understand the (de-)insertion mechanism and structural dynamics of the cathode.

The second chapter is focused on manufacturing-performance correlation on LMFP73 commercial cathode in upscaled Li-ion batteries. The formulation has been optimized by adding the 0.5% solution of SWCNT to the electrode slurry, while other parameters like mixing strategy, solid content of the slurry, coating speed, calendering, and mechanical properties of the electrodes have been taken into account and adjusted to obtain enhanced performance of the material in coin-type full-cells with graphite anode, and to produce electrodes which met upscaled requirements. Indeed, a 0.1 Ah SLP cell revealed remarkable capacity and retention, confirming the critical role of the manufacturing-performance relationship on cell behavior and cycling stability, particularly when scaling up from lab-scale to industrial cell formats.

The third chapter is focused on proof-of-concept innovative full-cell balancing by using layered oxide cathodes and alloying-based anodes in both Li-ion and Na-ion systems. A layered LNCAM cathode has been synthetized and characterized showing large first cycle irreversible capacity. In this regard, the coupling of the material with a silicon-based anode, also presenting large initial irreversibility, lead to the possibility to achieve full Li-ion batteries with no need of pre-activation of the electrodes, despite further studies are required to determine the optimal negative-to-positive ratio and anode-cathode balancing. Furthermore, a scalable chemical approach to achieve several sodiation degrees

of alloying Sn-C anode has been investigated with the aim of its combination with Na-deficient layered cathode in proof-of-concept Na-ion full-cells. Further ad hoc studies, especially regarding electrode/electrolyte interphase and optimized electrolyte solution are required.

Overall, the results obtained on different cathode chemistries for application in both LIBs and SIBs, especially regarding mixed-olivine cathodes, shed light to their possible employment in a wide range of devices, in particular stationary energy storage. Indeed, the synthesis and cathodes development led to the achievement of sustainable, cheap, safe, and stable materials with good electrochemical features and performance. Particularly, considering the advantages of the Na-ion batteries compared to Li-ion ones in terms of costs and availability of raw materials, the use of cheap, low cost and sustainable olivine cathodes in both devices could increase the benefits of SIBs technology, also related to the possible use renewed of olivine materials deriving from the recycling of LIBs. Furthermore, while further optimization is needed, the in-depth study of electrodes manufacturing-performance correlation and the preliminary results achieved for innovative full-cell balancing are promising to link the lab-scale research to the industrial level requirements. This aspect is mandatory for closing the gap between research and market, as regards the possible improvements of new materials and devices with enhanced properties.

6. References

[1] European Environment Agency (EEA), "Economic losses and fatalities caused by weather - and climate - related extreme events in EU Member States (1980-2023) - per hazard type - www.eea.europa.eu," **2024**.

[2] Intergovernmental Panel on Climate Change (IPCC), *Climate Change 2023 Synthesis Report*, **2023**.

[3] National Centers for Environmental Information (NCEI), "Reporting on the State of the Climate in 2023 -www.ncei.noaa.gov," **2024**.

[4] W. Liu, S.-P. Xie, Z. Liu, J. Zhu, *Sci Adv* **2017**, *3*, e1601666.

[5] Our World in Data, "ourworldindata.org website," **2024**.

[6] International Energy Agency, *World Energy Outlook*, **2024**.

[7] United Nations, *Framework Convention on Climate Change - Adoption of the Paris Agreement*, Paris, **2015**.

[8] K. A. Baumert, T. Herzog, J. Pershing, *Navigating the Numbers: Greenhouse Gas Data and International Climate Policy* , **2005**.

[9] P. T. Moseley, J. Garche, *Electrochemical Energy Storage for Renewable Sources and Grid Balancing*, Elsevier, **2015**.

[10] O. Ellabban, H. Abu-Rub, F. Blaabjerg, *Renewable and Sustainable Energy Reviews* **2014**, *39*, 748.

[11] M. Armand, J.-M. Tarascon, *Nature* **2008**, *451*, 652.

[12] B. Dunn, H. Kamath, J.-M. Tarascon, *Science* **2011**, *334*, 928.

[13] S. Sharma, P. Chand, *Results Chem* **2023**, *5*, 100885.

[14] T. Nagaura, K. Tozawa, *Progress in Batteries and Solar Cells*, **1990**.

[15] Natron, "Natron Energy Achieves First-Ever Commercial-Scale Production of Sodium-Ion Batteries in the U.S. - www.buisnesswire.com/news," **2024**.

[16] CATL, "CATL Unveils Its Latest Breakthrough Technology by Releasing Its First Generation of Sodium-ion Batteries - www.catl.com/en/news," **2021**.

[17] M. He, R. Davis, D. Chartouni, M. Johnson, M. Abplanalp, P. Troendle, R.-P. Suetterlin, *J Power Sources* **2022**, *548*, 232036.

[18] A. Rudola, A. J. R. Rennie, R. Heap, S. S. Meysami, A. Lowbridge, F. Mazzali, R. Sayers, C. J. Wright, J. Barker, *J Mater Chem A Mater* **2021**, *9*, 8279.

[19] B. C. H. Steele, *Fast Ion Transport in Solids: Solid State Batteries and Devices*, North Holland Publ., **1973**.

[20] M. B. Armand, M. S. Whittingham, R. A. Huggins, *Mater Res Bull* **1972**, *7*, 101.

[21] W. F. Meyers, B. Bell, J. W. Simmon, *United States Pat.* **1969**, *28*, 131.

[22] J. B. Goodenough, *Batteries for Sustainability: Selected Entries from the Encyclopedia of Sustainability Science and Technology*, Springer, **2013**.

[23] A. Mauger, C. M. Julien, J. B. Goodenough, K. Zaghib, *J Electrochem Soc* **2020**, *167*, 070507.

[24] M. Lazzari, B. Scrosati, *J Electrochem Soc* **1980**, *127*, 773.

[25] M. S. Whittingham, F. R. Gamble, *Mater Res Bull* **1975**, *10*, 363.

[26] M. S. Whittingham, *Science* **1976**, *192*, 1126.

[27] M. S. Whittingham, N. J. Fanwood, *United States Pat.* **1977**, 1.

[28] L. Bernard, M. Mckelvy, W. Glaunsinger, P. Colombet, *Solid State Ion* **1985**, *15*, 301.

[29] E. Peled, *J Electrochem Soc* **1979**, *126*, 2047.

[30] Z. Xu, *J Phys Conf Ser* **2022**, *2152*, 012026.

[31] J. O. Besenhard, G. Eichinger, *J Electroanal Chem Interfacial Electrochem* **1976**, *68*, 1.

[32] MSE Supplies, "Source of Detrimental Dendrite Growth in Lithium Batteries Discovered," **2019**.

[33] B. M. L. Rao, R. W. Francis, H. A. Christopher, *J Electrochem Soc* **1977**, *124*, 1490.

[34] M. M. Nicholson, *J Electrochem Soc* **1974**, *121*, 734.

[35] J. O. Besenhard, H. P. Fritz, *J Electroanal Chem Interfacial Electrochem* **1974**, *53*, 329.

[36] G. Eichinger, J. O. Besenhard, *J Electroanal Chem Interfacial Electrochem* **1976**, *72*, 1.

[37] J. O. Besenhard, *Carbon N Y* **1976**, *14*, 111.

[38] F. Schipper, D. Aurbach, *Russian Journal of Electrochemistry* **2016**, *52*, 1095.

[39] M. B. Armand, M. Duclot, *United States Pat.* **1981**, *45*.

[40] S. Basu, C. Zeller, P. J. Flanders, C. D. Fuerst, W. D. Johnson, J. E. Fischer, *Materials Science and Engineering* **1979**, *38*, 275.

[41] J. Choi, P. J. Kim, *Curr Opin Electrochem* **2022**, *31*, 100858.

[42] A. Yoshino, *Angewandte Chemie International Edition* **2012**, *51*, 5798.

[43] K. Mizushima, P. Jones, P. Wiseman, J. Goodenough, *Solid State Ion* **1981**, *3–4*, 171.

[44] R. Fong, U. von Sacken, J. R. Dahn, *J Electrochem Soc* **1990**, *137*, 2009.

[45] K. Xu, *Chem Rev* **2014**, *114*, 11503.

[46] S. O'Neill, *Engineering* **2020**, *6*, 487.

[47] M. M. Thackeray, C. Wolverton, E. D. Isaacs, *Energy Environ Sci* **2012**, *5*, 7854.

[48] Y. Sui, X. Ji, *Angewandte Chemie International Edition* **2024**, *63*, e202312585.

[49] Bruno. Scrosati, K. M. Abraham, W. A. van. Schalkwijk, Jusef. Hassoun, *Lithium Batteries : Advanced Technologies and Applications.*, Wiley, **2013**.

[50] M. Li, C. Wang, Z. Chen, K. Xu, J. Lu, *Chem Rev* **2020**, *120*, 6783.

[51] M. Ntombela, K. Musasa, K. Moloi, *World Electric Vehicle Journal* **2023**, *14*, 195.

[52] J. Neubauer, E. Wood, *J Power Sources* **2014**, *259*, 262.

[53] C. Delmas, J. Braconnier, C. Fouassier, P. Hagenmuller, *Solid State Ion* **1981**, *3–4*, 165.

[54] J. J. Braconnier, C. Delmas, P. Hagenmuller, *Mater Res Bull* **1982**, *17*, 993.

[55] R. Yazami, Ph. Touzain, *J Power Sources* **1983**, *9*, 365.

[56] M. H. Han, E. Gonzalo, G. Singh, T. Rojo, *Energy Environ Sci* **2015**, *8*, 81.

[57] P. Ge, M. Fouletier, *Solid State Ion* **1988**, *28*, 1172.

[58] J. L. Sudworth, *J Power Sources* **1994**, *51*, 105.

[59] R. Benato, N. Cosciani, G. Crugnola, S. Dambone Sessa, G. Lodi, C. Parmeggiani, M. Todeschini, *J Power Sources* **2015**, *293*, 127.

[60] D. A. Stevens, J. R. Dahn, *J Electrochem Soc* **2000**, *147*, 1271.

[61] D. A. Stevens, J. R. Dahn, *J Electrochem Soc* **2001**, *148*, A803.

[62] E. A. Olivetti, G. Ceder, G. G. Gaustad, X. Fu, *Joule* **2017**, *1*, 229.

[63] M. Siddi, in *The Implications of Emerging Technologies in the Euro-Atlantic Space*, Springer International Publishing, Cham, **2023**, pp. 73–85.

[64] Z. Yang, J. Zhang, M. C. W. Kintner-Meyer, X. Lu, D. Choi, J. P. Lemmon, J. Liu, *Chem Rev* **2011**, *111*, 3577.

[65] I. Hasa, J. Hassoun, S. Passerini, *Nano Res* **2017**, *10*, 3942.

[66] A. Ponrouch, M. R. Palacín, *Philosophical Transactions of the Royal Society A: Mathematical, Physical and Engineering Sciences* **2019**, *377*, 20180297.

[67] R. Mogensen, D. Brandell, R. Younesi, *ACS Energy Lett* **2016**, *1*, 1173.

[68] J.-Y. Hwang, S.-T. Myung, Y.-K. Sun, *Chem Soc Rev* **2017**, *46*, 3529.

[69] D. Kundu, E. Talaie, V. Duffort, L. F. Nazar, *Angewandte Chemie International Edition* **2015**, *54*, 3431.

[70] CATL, "CATL announces second-generation sodium battery, normal discharge at -40°C - www.carnewschina.com/news," **2024**.

[71] J. Bitenc, K. Pirnat, O. Lužanin, R. Dominko, *Chemistry of Materials* **2024**, *36*, 1025.

[72] J. Wang, Y. Zhou, Y. Zhuo, K. Fang, S. Wang, B. Zhao, J. Zhou, H. Wang, *Chem Sci* **2025**, *16*, 552.

[73] J. Xu, S. Dou, H. Liu, L. Dai, *Nano Energy* **2013**, *2*, 439.

[74] M. Baumann, M. Häringer, M. Schmidt, L. Schneider, J. F. Peters, W. Bauer, J. R. Binder, M. Weil, *Adv Energy Mater* **2022**, *12*, 2202636.

[75] R. P. Santoro, R. E. Newnham, *Acta Crystallogr* **1967**, *22*, 344.

[76] A. K. Padhi, K. S. Nanjundaswamy, J. B. Goodenough, *J Electrochem Soc* **1997**, *144*, 1188.

[77] Y. Wang, P. He, H. Zhou, *Energy Environ Sci* **2011**, *4*, 805.

[78] H. Raj, A. Sil, *Ionics (Kiel)* **2018**, *24*, 2543.

[79] R. Malik, F. Zhou, G. Ceder, *Phys Rev B* **2009**, *79*, 214201.

[80] B. Scrosati, J. Garche, *J Power Sources* **2010**, *195*, 2419.

[81] D. Di Lecce, R. Verrelli, J. Hassoun, *Green Chemistry* **2017**, *19*, 3442.

[82] A. Yamada, S.-C. Chung, *J Electrochem Soc* **2001**, *148*, A960.

[83] N. N. Bramnik, K. Nikolowski, G. Baehtz, K. G. Bramnik, H. Ehrenberg, *Chemistry of Materials* **2007**, *19*, 908.

[84] A. Yamada, M. Hosoya, S. C. Chung, Y. Kudo, K. Hinokuma, K. Y. Liu, Y. Nishi, in *J Power Sources*, **2003**, pp. 232–238.

[85] L.-X. Yuan, Z.-H. Wang, W.-X. Zhang, X.-L. Hu, J.-T. Chen, Y.-H. Huang, J. B. Goodenough, *Energy Environ Sci* **2011**, *4*, 269.

[86] L. Minnetti, F. M. Maddar, A. K. Haridas, M. Capener, F. Nobili, I. Hasa, *Batter Supercaps* **2024**, e202400645.

[87] S. W. Oh, S. T. Myung, S. M. Oh, K. H. Oh, K. Amine, B. Scrosati, Y. K. Sun, *Advanced Materials* **2010**, *22*, 4842.

[88] V. Marangon, E. Barcaro, L. Minnetti, W. Brehm, F. Bonaccorso, V. Pellegrini, J. Hassoun, *Nano Res* **2023**, *16*, 8433.

[89] A. Varzi, C. Täubert, M. Wohlfahrt-Mehrens, M. Kreis, W. Schütz, *J Power Sources* **2011**, *196*, 3303.

[90] V. Aravindan, J. Gnanaraj, Y. S. Lee, S. Madhavi, *J Mater Chem A Mater* **2013**, *1*, 3518.

[91] J. Wolfenstine, J. Allen, *J Power Sources* **2005**, *142*, 389.

[92] K. Amine, H. Yasuda, M. Yamachi, *Electrochemical and Solid-State Letters* **2000**, *3*, 178.

[93] D. Di Lecce, V. Gancitano, J. Hassoun, *ACS Sustain Chem Eng* **2020**, *8*, 278.

[94] J. Jiang, J. R. Dahn, *Electrochem commun* **2004**, *6*, 39.

[95] Z. X. Nie, C. Y. Ouyang, J. Z. Chen, Z. Y. Zhong, Y. L. Du, D. S. Liu, S. Q. Shi, M. S. Lei, *Solid State Commun* **2010**, *150*, 40.

[96] G. Li, H. Azuma, M. Tohda, *Electrochemical and Solid-State Letters* **2002**, *5*, A135.

[97] D. Di Lecce, R. Brescia, A. Scarpellini, M. Prato, J. Hassoun, *ChemSusChem* **2016**, *9*, 223.

[98] L. Minnetti, V. Marangon, J. Hassoun, *Adv Sustain Syst* **2022**, *6*, 2100464.

[99] M. Yonemura, A. Yamada, Y. Takei, N. Sonoyama, R. Kanno, *J Electrochem Soc* **2004**, *151*, A1352.

[100] T. Muraliganth, A. Manthiram, *Journal of Physical Chemistry C* **2010**, *114*, 15530.

[101] A. Yamada, Y. Kudo, K.-Y. Liu, *J Electrochem Soc* **2001**, *148*, A747.

[102] B. Zhang, X. Wang, H. Li, X. Huang, *J Power Sources* **2011**, *196*, 6992.

[103] L. T. N. Huynh, P. P. N. Le, V. D. Trinh, H. H. Tran, V. M. Tran, M. L. P. Le, *J Chem* **2019**, *2019*, 5638590.

[104] Y. Hong, Z. Tang, Z. Hong, Z. Zhang, *J Power Sources* **2014**, *248*, 655.

[105] L. Yang, W. Deng, W. Xu, Y. Tian, A. Wang, B. Wang, G. Zou, H. Hou, W. Deng, X. Ji, *J Mater Chem A Mater* **2021**, *9*, 14214.

[106] P. Moreau, D. Guyomard, J. Gaubicher, F. Boucher, *Chemistry of Materials* **2010**, *22*, 4126.

[107] L. He, H. Li, X. Ge, S. Li, X. Wang, S. Wang, L. Zhang, Z. Zhang, *Adv Mater Interfaces* **2022**, *9*, 2200515.

[108] K. Zaghib, J. Trottier, P. Hovington, F. Brochu, A. Guerfi, A. Mauger, C. M. Julien, *J Power Sources* **2011**, *196*, 9612.

[109] H. Wu, X. Zou, X.-L. Wu, *Nano Futures* **2020**, *4*, 042001.

[110] M. Avdeev, Z. Mohamed, C. D. Ling, J. Lu, M. Tamaru, A. Yamada, P. Barpanda, *Inorg Chem* **2013**, *52*, 8685.

[111] C. Berlanga, I. Monterrubio, M. Armand, T. Rojo, M. Galceran, M. Casas-Cabanas, *ACS Sustain Chem Eng* **2020**, *8*, 725.

[112] S. M. Oh, S. T. Myung, J. Hassoun, B. Scrosati, Y. K. Sun, *Electrochem commun* **2012**, *22*, 149.

[113] L. Minnetti, L. Sbrascini, A. Staffolani, V. Marangon, F. Nobili, J. Hassoun, *Journal of Energy Chemistry* **2024**, *96*, 300.

[114] B. Swain, *Sep Purif Technol* **2017**, *172*, 388.

[115] D. Saurel, M. Giner, M. Galceran, J. Rodríguez-Carvajal, M. Reynaud, M. Casas-Cabanas, *Electrochim Acta* **2022**, *425*, 140650.

[116] C. Henriksen, J. K. Mathiesen, Y. M. Chiang, K. M. Ø. Jensen, D. B. Ravnsbæk, *ACS Appl Energy Mater* **2019**, *2*, 8060.

[117] K. T. Lee, T. N. Ramesh, F. Nan, G. Botton, L. F. Nazar, *Chemistry of Materials* **2011**, *23*, 3593.

[118] S. Jana, G. Lingannan, M. Ishtiyak, G. Panigrahi, A. Sonachalam, J. Prakash, *Mater Res Bull* **2020**, *126*, 110835.

[119] R. Hausbrand, G. Cherkashinin, H. Ehrenberg, M. Gröting, K. Albe, C. Hess, W. Jaegermann, *Materials Science and Engineering: B* **2015**, *192*, 3.

[120] J. B. Goodenough, Y. Kim, *Chemistry of Materials* **2010**, *22*, 587.

[121] J. B. Goodenough, K.-S. Park, *J Am Chem Soc* **2013**, *135*, 1167.

[122] C. Julien, A. Mauger, K. Zaghib, H. Groult, *Inorganics (Basel)* **2014**, *2*, 132.

[123] S. Laubach, S. Laubach, P. C. Schmidt, D. Ensling, S. Schmid, W. Jaegermann, A. Thißen, K. Nikolowski, H. Ehrenberg, *Physical Chemistry Chemical Physics* **2009**, *11*, 3278.

[124] M. E. Arroyo y de Dompablo, C. Marianetti, A. Van der Ven, G. Ceder, *Phys Rev B* **2001**, *63*, 144107.

[125] J. N. Reimers, J. R. Dahn, *J Electrochem Soc* **1992**, *139*, 2091.

[126] A. Van der Ven, M. K. Aydinol, G. Ceder, G. Kresse, J. Hafner, *Phys Rev B* **1998**, *58*, 2975.

[127] J. Li, X. Wang, J. Zhao, J. Chen, T. Jia, C. Cao, *J Power Sources* **2016**, *307*, 731.

[128] P. Rozier, J. M. Tarascon, *J Electrochem Soc* **2015**, *162*, A2490.

[129] Y.-K. Sun, *ACS Energy Lett* **2022**, *7*, 1774.

[130] Z. Chen, D. Chao, J. Lin, Z. Shen, *Mater Res Bull* **2017**, *96*, 491.

[131] Y. Xia, J. Zheng, C. Wang, M. Gu, *Nano Energy* **2018**, *49*, 434.

[132] D. Huang, Y. Shi, A. P. Tornheim, J. Bareño, Z. Chen, Z. Zhang, A. Burrell, H. Luo, *Appl Mater Today* **2019**, *16*, 342.

[133] L. Fang, L. Zhou, M. Park, D. Han, G. Lee, S. Kang, S. Lee, M. Chen, Z. Hu, K. Zhang, K. Nam, Y. Kang, *Advanced Science* **2022**, *9*, 2201896.

[134] X. Zhang, W. J. Jiang, A. Mauger, Qilu, F. Gendron, C. M. Julien, *J Power Sources* **2010**, *195*, 1292.

[135] L. Yang, F. Ren, Q. Feng, G. Xu, X. Li, Y. Li, E. Zhao, J. Ma, S. Fan, *J Electron Mater* **2018**, *47*, 3996.

[136] S. Liu, Z. Dang, D. Liu, C. Zhang, T. Huang, A. Yu, *J Power Sources* **2018**, *396*, 288.

[137] H. Darjazi, E. Gonzalo, B. Acebedo, R. Cid, M. Zarrabeitia, F. Bonilla, M. Á. Muñoz-Márquez, F. Nobili, *Materials Today Sustainability* **2022**, *20*, 100236.

[138] K. Sahni, M. Ashuri, Q. He, R. Sahore, I. D. Bloom, Y. Liu, J. A. Kaduk, L. L. Shaw, *Electrochim Acta* **2019**, *301*, 8.

[139] Z. Li, N. A. Chernova, J. Feng, S. Upreti, F. Omenya, M. S. Whittingham, *J Electrochem Soc* **2011**, *159*, A116.

[140] J. D. Wilcox, E. E. Rodriguez, M. M. Doeff, *J Electrochem Soc* **2009**, *156*, A1011.

[141] Y. Gao, W. Yuan, X. Dou, *Front Phys* **2021**, *9*, 731851.

[142] X. Li, J. Liu, X. Meng, Y. Tang, M. N. Banis, J. Yang, Y. Hu, R. Li, M. Cai, X. Sun, *J Power Sources* **2014**, *247*, 57.

[143] X. Li, J. Liu, M. N. Banis, A. Lushington, R. Li, M. Cai, X. Sun, *Energy Environ. Sci.* **2014**, *7*, 768.

[144] N. Yabuuchi, K. Kubota, M. Dahbi, S. Komaba, *Chem Rev* **2014**, *114*, 11636.

[145] C. Delmas, C. Fouassier, P. Hagenmuller, *Physica B+C* **1980**, *99*, 81.

[146] J. M. Paulsen, J. R. Dahn, *J Electrochem Soc* **2000**, *147*, 2478.

[147] N. Yabuuchi, M. Yano, H. Yoshida, S. Kuze, S. Komaba, *J Electrochem Soc* **2013**, *160*, A3131.

[148] H. Wang, B. Yang, X.-Z. Liao, J. Xu, D. Yang, Y.-S. He, Z.-F. Ma, *Electrochim Acta* **2013**, *113*, 200.

[149] L. Sbrascini, A. Sarapulova, C. Gauckler, L. Gehrlein, F. Jeschull, T. Akçay, R. Mönig, M. Marinaro, F. Nobili, S. Dsoke, *Batter Supercaps* **2024**, *7*, e202400207.

[150] G. Singh, B. Acebedo, M. C. Cabanas, D. Shanmukaraj, M. Armand, T. Rojo, *Electrochem commun* **2013**, *37*, 61.

[151] I. Hasa, J. Hassoun, Y. K. Sun, B. Scrosati, *ChemPhysChem* **2014**, *15*, 2152.

[152] M. M. Thackeray, P. J. Johnson, L. A. de Picciotto, P. G. Bruce, J. B. Goodenough, *Mater Res Bull* **1984**, *19*, 179.

[153] T. Ohzuku, M. Kitagawa, T. Hirai, *J Electrochem Soc* **1990**, *137*, 769.

[154] G. G. Amatucci, C. N. Schmutz, A. Blyr, C. Sigala, A. S. Gozdz, D. Larcher, J. M. Tarascon, *J Power Sources* **1997**, *69*, 11.

[155] M. Y. Abeywardana, N. Laszczynski, M. Kuenzel, D. Bresser, S. Passerini, B. Lucht, *International Journal of Electrochemistry* **2019**, *2019*, 1.

[156] Batteries Europe, *Strategic Research & Innovation Agenda*, **2024**.

[157] L. Balducci, H. Darjazi, E. Gonzalo, R. Cid, F. Bonilla, F. Nobili, *ACS Appl Mater Interfaces* **2023**, *15*, 55620.

[158] S. Levchenko, S. Wei, V. Marangon, J. Hassoun, *Energy Technology* **2022**, *10*, 2200725.

[159] J. Zhang, Y. Liu, X. Zhao, L. He, H. Liu, Y. Song, S. Sun, Q. Li, X. Xing, J. Chen, *Advanced Materials* **2020**, *32*, 1906348.

[160] Z. Jian, L. Zhao, H. Pan, Y. S. Hu, H. Li, W. Chen, L. Chen, *Electrochem commun* **2012**, *14*, 86.

[161] M. Bianchini, N. Brisset, F. Fauth, F. Weill, E. Elkaim, E. Suard, C. Masquelier, L. Croguennec, *Chemistry of Materials* **2014**, *26*, 4238.

[162] J. Peng, W. Zhang, Q. Liu, J. Wang, S. Chou, H. Liu, S. Dou, *Advanced Materials* **2022**, *34*, 2108384.

[163] H. Yi, R. Qin, S. Ding, Y. Wang, S. Li, Q. Zhao, F. Pan, *Adv Funct Mater* **2021**, *31*, 2006970.

[164] L. Li, P. Nie, Y. Chen, J. Wang, *J Mater Chem A Mater* **2019**, *7*, 12134.

[165] A. Patriarchi, J. Caroni, L. Minnetti, L. Sbrascini, H. Darjazi, F. Nobili, M. Á. Muñoz-Márquez, *ChemElectroChem* **2025**, e202400350.

[166] X. Yan, Y. Yang, E. Liu, L. Sun, H. Wang, X. Z. Liao, Y. He, Z. F. Ma, *Electrochim Acta* **2017**, *225*, 235.

[167] F. M. Maddar, D. Walker, T. W. Chamberlain, J. Compton, A. S. Menon, M. Copley, I. Hasa, *J Mater Chem A Mater* **2023**, *11*, 15778.

[168] M. R. Palacín, *Chem Soc Rev* **2009**, *38*, 2565.

[169] L. Bottoni, H. Darjazi, L. Sbrascini, A. Staffolani, S. Gabrielli, G. Pastore, A. Tombesi, F. Nobili, *ChemElectroChem* **2023**, *10*, e202201117.

[170] J. R. Dahn, W. Xing, Y. Gao, *Carbon N Y* **1997**, *35*, 825.

[171] G. Wang, M. Yu, X. Feng, *Chem Soc Rev* **2021**, *50*, 2388.

[172] D. D. L. Chung, *J Mater Sci* **2002**, *37*, 1475.

[173] U. Hofmann, W. Rüdorff, *Trans. Faraday Soc.* **1938**, *34*, 1017.

[174] Y. Zhao, Y. Fu, Y. Meng, Z. Wang, J. Liu, X. Gong, *Chemical Engineering Journal* **2024**, *480*, 148047.

[175] S. Weng, S. Wu, Z. Liu, G. Yang, X. Liu, X. Zhang, C. Zhang, Q. Liu, Y. Huang, Y. Li, M. N. Ateş, D. Su, L. Gu, H. Li, L. Chen, R. Xiao, Z. Wang, X. Wang, *Carbon Energy* **2023**, *5*, e224.

[176] D. Billaud, F. X. Henry, *Solid State Commun* **2002**, *124*, 299.

[177] M. Drüe, M. Seyring, M. Rettenmayr, *J Power Sources* **2017**, *353*, 58.

[178] M. Winter, J. O. Besenhard, M. E. Spahr, P. Novák, *Advanced Materials* **1998**, *10*, 725.

[179] E. Markevich, E. Pollak, G. Salitra, D. Aurbach, *J Power Sources* **2007**, *174*, 1263.

[180] D. G. Papageorgiou, I. A. Kinloch, R. J. Young, *Prog Mater Sci* **2017**, *90*, 75.

[181] B. Marinho, M. Ghislandi, E. Tkalya, C. E. Koning, G. de With, *Powder Technol* **2012**, *221*, 351.

[182] C. Lee, X. Wei, J. W. Kysar, J. Hone, *Science* **2008**, *321*, 385.

[183] R. Raccichini, A. Varzi, S. Passerini, B. Scrosati, *Nat Mater* **2015**, *14*, 271.

[184] S. Iijima, *Nature* **1991**, *354*, 56.

[185] B. J. Landi, M. J. Ganter, C. D. Cress, R. A. DiLeo, R. P. Raffaelle, *Energy Environ Sci* **2009**, *2*, 638.

[186] L. Xie, C. Tang, Z. Bi, M. Song, Y. Fan, C. Yan, X. Li, F. Su, Q. Zhang, C. Chen, *Adv Energy Mater* **2021**, *11*, 2101650.

[187] Y. Chen, X. Guo, A. Liu, H. Zhu, T. Ma, *Sustain Energy Fuels* **2021**, *5*, 3017.

[188] J. Liu, P. Kopold, P. A. van Aken, J. Maier, Y. Yu, *Angewandte Chemie International Edition* **2015**, *54*, 9632.

[189] L. Sbrascini, A. Staffolani, L. Bottoni, H. Darjazi, L. Minnetti, M. Minicucci, F. Nobili, *ACS Appl Mater Interfaces* **2022**, *14*, 33257.

[190] K. Nobuhara, H. Nakayama, M. Nose, S. Nakanishi, H. Iba, *J Power Sources* **2013**, *243*, 585.

[191] I. Hasa, X. Dou, D. Buchholz, Y. Shao-Horn, J. Hassoun, S. Passerini, B. Scrosati, *J Power Sources* **2016**, *310*, 26.

[192] S. Komaba, W. Murata, T. Ishikawa, N. Yabuuchi, T. Ozeki, T. Nakayama, A. Ogata, K. Gotoh, K. Fujiwara, *Adv Funct Mater* **2011**, *21*, 3859.

[193] S. Alvin, H. S. Cahyadi, J. Hwang, W. Chang, S. K. Kwak, J. Kim, *Adv Energy Mater* **2020**, *10*, 2000283.

[194] S. J. R. Prabakar, J. Jeong, M. Pyo, *Electrochim Acta* **2015**, *161*, 23.

[195] F. Xie, Z. Xu, Z. Guo, M.-M. Titirici, *Progress in Energy* **2020**, *2*, 042002.

[196] H. Marsh, F. Rodrìguez-Reinoso, *Activated Carbon*, Elsevier, **2006**.

[197] J. Lu, Z. Chen, F. Pan, Y. Cui, K. Amine, *Electrochemical Energy Reviews* **2018**, *1*, 35.

[198] M. N. Obrovac, V. L. Chevrier, *Chem Rev* **2014**, *114*, 11444.

[199] W.-J. Zhang, *J Power Sources* **2011**, *196*, 13.

[200] P. Sehrawat, A. Shabir, Abid, C. M. Julien, S. S. Islam, *J Power Sources* **2021**, *501*, 229709.

[201] B. N. Loeffler, D. Bresser, S. Passerini, M. Copley, *Johnson Matthey Technology Review* **2015**, *59*, 34.

[202] X. Zhang, J. Weng, C. Ye, M. Liu, C. Wang, S. Wu, Q. Tong, M. Zhu, F. Gao, *Materials* **2022**, *15*, 4264.

[203] M. Winter, J. O. Besenhard, *Electrochim Acta* **1999**, *45*, 31.

[204] J. W. Wang, X. H. Liu, S. X. Mao, J. Y. Huang, *Nano Lett* **2012**, *12*, 5897.

[205] V. L. Chevrier, G. Ceder, *J Electrochem Soc* **2011**, *158*, A1011.

[206] J.-Y. Li, Q. Xu, G. Li, Y.-X. Yin, L.-J. Wan, Y.-G. Guo, *Mater Chem Front* **2017**, *1*, 1691.

[207] X. Su, Q. Wu, J. Li, X. Xiao, A. Lott, W. Lu, B. W. Sheldon, J. Wu, *Adv Energy Mater* **2014**, *4*, 1300882.

[208] A. Franco Gonzalez, N.-H. Yang, R.-S. Liu, *Journal of Physical Chemistry C* **2017**, *121*, 27775.

[209] S. Liang, Y. Cheng, J. Zhu, Y. Xia, P. Müller-Buschbaum, *Small Methods* **2020**, *4*, 2000218.

[210] X. Wu, Y. Guo, L. Wan, *Chem Asian J* **2013**, *8*, 1948.

[211] C. Yuan, H. Bin Wu, Y. Xie, X. W. (David) Lou, *Angewandte Chemie International Edition* **2014**, *53*, 1488.

[212] X. Xu, W. Liu, Y. Kim, J. Cho, *Nano Today* **2014**, *9*, 604.

[213] S. Dong, X. Chen, X. Zhang, G. Cui, *Coord Chem Rev* **2013**, *257*, 1946.

[214] G. Carbonari, F. Maroni, S. Gabrielli, A. Staffolani, R. Tossici, A. Palmieri, F. Nobili, *ChemElectroChem* **2019**, *6*, 1915.

[215] A. S. Aricò, P. Bruce, B. Scrosati, J.-M. Tarascon, W. van Schalkwijk, *Nat Mater* **2005**, *4*, 366.

[216] H. Xu, H. Li, X. Wang, *ChemElectroChem* **2023**, *10*, e202201151.

[217] N. Akhlaghi, G. Najafpour-Darzi, *Journal of Industrial and Engineering Chemistry* **2021**, *103*, 292.

[218] V. Marangon, L. Minnetti, E. Barcaro, J. Hassoun, *Chemistry - A European Journal* **2023**, *29*, e202301345.

[219] V. Marangon, Y. Tominaga, J. Hassoun, *J Power Sources* **2020**, *449*, 227508.

[220] C. Li, Z. Wang, Z. He, Y. Li, J. Mao, K. Dai, C. Yan, J. Zheng, *Sustainable Materials and Technologies* **2021**, *29*, e00297.

[221] D. Aurbach, *J. Power Sources*, **2000**, *89*, 206

[222] L. Carbone, M. Gobet, J. Peng, M. Devany, B. Scrosati, S. Greenbaum, J. Hassoun, *ACS Appl Mater Interfaces* **2015**, *7*, 13859.

[223] G. G. Eshetu, S. Grugeon, H. Kim, S. Jeong, L. Wu, G. Gachot, S. Laruelle, M. Armand, S. Passerini, *ChemSusChem* **2016**, *9*, 462.

[224] C. Bommier, X. Ji, *Small* **2018**, *14*, 1703576.

[225] A. Ponrouch, D. Monti, A. Boschin, B. Steen, P. Johansson, M. R. Palacín, *J Mater Chem A Mater* **2015**, *3*, 22.

[226] M. Á. Muñoz-Márquez, D. Saurel, J. L. Gómez-Cámer, M. Casas-Cabanas, E. Castillo-Martínez, T. Rojo, *Adv Energy Mater* **2017**, *7*, 1700463.

[227] U. Purushotham, N. Takenaka, M. Nagaoka, *RSC Adv* **2016**, *6*, 65232.

[228] V. Sharova, A. Moretti, T. Diemant, A. Varzi, R. J. Behm, S. Passerini, *J Power Sources* **2018**, *375*, 43.

[229] P. G. Balakrishnan, R. Ramesh, T. Prem Kumar, *J Power Sources* **2006**, *155*, 401.

[230] S. Tobishima, H. Morimoto, M. Aoki, Y. Saito, T. Inose, T. Fukumoto, T. Kuryu, *Electrochim Acta* **2004**, *49*, 979.

[231] Y. Choquette, G. Brisard, M. Parent, D. Brouillette, G. Perron, J. E. Desnoyers, M. Armand, D. Gravel, N. Slougui, *J. Electrochem. Soc.*, **1998**, *145*, 3500.

[232] D. Di Lecce, L. Minnetti, D. Polidoro, V. Marangon, J. Hassoun, *Ionics (Kiel)* **2019**, *25*, 3129.

[233] D. Di Lecce, L. Carbone, V. Gancitano, J. Hassoun, *J Power Sources* **2016**, *334*, 146.

[234] L. Carbone, S. Munoz, M. Gobet, M. Devany, S. Greenbaum, J. Hassoun, *Electrochim Acta* **2017**, *231*, 223.

[235] D. Aurbach, E. Granot, *Electrochem. Acta*, **1996**, *42*, 697.

[236] D. Aurbach, E. Pollak, R. Elazari, G. Salitra, C. S. Kelley, J. Affinito, *J Electrochem Soc* **2009**, *156*, A694.

[237] V. Marangon, C. Hernandez-Rentero, S. Levchenko, G. Bianchini, D. Spagnolo, A. Caballero, J. Morales, J. Hassoun, *ACS Appl Energy Mater* **2020**, *3*, 12263.

[238] V. Marangon, L. Minnetti, M. Adami, A. Barlini, J. Hassoun, *Energy and Fuels* **2021**, *35*, 10284.

[239] J. Feng, L. Wang, Y. Chen, P. Wang, H. Zhang, X. He, *Nano Converg* **2021**, *8*, 2.

[240] Z. Xue, D. He, X. Xie, *J Mater Chem A Mater* **2015**, *3*, 19218.

[241] A. Patriarchi, H. Darjazi, L. Minnetti, L. Sbrascini, G. A. Elia, V. Castorani, M. Á. Muñoz-Márquez, F. Nobili, *Batteries* **2024**, *10*, 11.

[242] G. B. Appetecchi, J. Hassoun, B. Scrosati, F. Croce, F. Cassel, M. Salomon, *J Power Sources* **2003**, *124*, 246.

[243] G. B. Appetecchi, F. Croce, J. Hassoun, B. Scrosati, M. Salomon, F. Cassel, *J Power Sources* **2003**, *114*, 105.

[244] L. Carbone, J. Hassoun, *Ionics (Kiel)* **2016**, *22*, 2341.

[245] I. Hasa, S. Passerini, K. Edstrom, P. Stevens, A. Romanello, R. Scipioni, E. Sheridan, *Transportation Research Procedia* **2023**, *72*, 3625.

[246] J. Li, J. Fleetwood, W. B. Hawley, W. Kays, *Chem Rev* **2022**, *122*, 903.

[247] M. E. Spahr, in *Lithium-Ion Batteries*, Springer New York, New York, NY, **2009**, pp. 1–38.

[248] S.-L. Chou, Y. Pan, J.-Z. Wang, H.-K. Liu, S.-X. Dou, *Physical Chemistry Chemical Physics* **2014**, *16*, 20347.

[249] P. Saxena, P. Shukla, *Adv Compos Hybrid Mater* **2021**, *4*, 8.

[250] S. F. Lux, F. Schappacher, A. Balducci, S. Passerini, M. Winter, *J Electrochem Soc* **2010**, *157*, A320.

[251] Z. Du, J. Li, M. Wood, C. Mao, C. Daniel, D. L. Wood, *Electrochim Acta* **2018**, *270*, 54.

[252] P. Sae-Oui, U. Thepsuwan, P. Thaptong, C. Sirisinha, *Advances in Polymer Technology* **2014**, *33*, 21422.

[253] A. Staffolani, L. Sbrascini, L. Bottoni, L. Minnetti, H. Darjazi, A. Trapananti, F. Paparoni, S. J. Rezvani, M. Minicucci, M. Harfouche, F. Nobili, *Energy Advances* **2024**, *3*, 1726.

[254] F. Maroni, R. Raccichini, A. Birrozzi, G. Carbonari, R. Tossici, F. Croce, R. Marassi, F. Nobili, *J Power Sources* **2014**, *269*, 873.

[255] M. F. V Hidalgo, G. Apachitei, D. Dogaru, M. Faraji-Niri, M. Lain, M. Copley, J. Marco, *J Power Sources* **2023**, *573*, 233091.

[256] G. Apachitei, M. Hidalgo, D. Dogaru, M. Lain, R. Heymer, J. Marco, M. Copley, *Batteries* **2023**, *9*, 192.

[257] P. S. Grant, D. Greenwood, K. Pardikar, R. Smith, T. Entwistle, L. A. Middlemiss, G. Murray, S. A. Cussen, M. J. Lain, M. J. Capener, M. Copley, C. D. Reynolds, S. D. Hare, M. J. H. Simmons, E. Kendrick, S. P. Zankowski, S. Wheeler, P. Zhu, P. R. Slater, Y. S. Zhang, A. R. T. Morrison, W. Dawson, J. Li, P. R. Shearing, D. J. L. Brett, G. Matthews, R. Ge, R. Drummond, E. C. Tredenick, C. Cheng, S. R. Duncan, A. M. Boyce, M. Faraji-Niri, J. Marco, L. A. Roman-Ramirez, C. Harper, P. Blackmore, T. Shelley, A. Mohsseni, D. J. Cumming, *Journal of Physics: Energy* **2022**, *4*, 042006.

[258] C. D. Reynolds, P. R. Slater, S. D. Hare, M. J. H. Simmons, E. Kendrick, *Mater Des* **2021**, *209*, 109971.

[259] H. Bockholt, W. Haselrieder, A. Kwade, *ECS Trans* **2013**, *50*, 25.

[260] A. Kraytsberg, Y. Ein-Eli, *Adv Energy Mater* **2016**, *6*, 1600655.

[261] W. B. Hawley, J. Li, *J Energy Storage* **2019**, *25*, 100862.

[262] F. Ciucci, C. Chen, *Electrochim Acta* **2015**, *167*, 439.

[263] S. Dierickx, A. Weber, E. Ivers-Tiffée, *Electrochim Acta* **2020**, *355*, 136764.

[264] E. Goldammer, J. Kowal, *Batteries* **2021**, *7*, 36.

[265] A. Staffolani, A. Baldinelli, G. Bidini, F. Nobili, L. Barelli, *Energies (Basel)* **2022**, *15*, 4978.

[266] E. von Hauff, *The Journal of Physical Chemistry C* **2019**, *123*, 11329.

[267] B. A. Boukamp, *Electrochim Acta* **2015**, *154*, 35.

[268] T. Horlin, *Solid State Ion* **1993**, *67*, 85.

[269] B. A. Boukamp, A. Rolle, *Solid State Ion* **2017**, *302*, 12.

[270] T. H. Wan, M. Saccoccio, C. Chen, F. Ciucci, *Electrochim Acta* **2015**, *184*, 483.

[271] E. Quattrocchi, B. Py, A. Maradesa, Q. Meyer, C. Zhao, F. Ciucci, *Electrochim Acta* **2023**, *439*, 141499.

[272] A. L. Gavrilyuk, D. A. Osinkin, D. I. Bronin, *Russian Journal of Electrochemistry* **2017**, *53*, 575.

[273] B. Boukamp, *Solid State Ion* **1986**, *20*, 31.

[274] B. Boukamp, *Solid State Ion* **1986**, *18–19*, 136.

[275] B. Scrosati, J. Hassoun, Y. K. Sun, *Energy Environ Sci* **2011**, *4*, 3287.

[276] T. P. Narins, *Extr Ind Soc* **2017**, *4*, 321.

[277] P. K. Nayak, L. Yang, W. Brehm, P. Adelhelm, *Angewandte Chemie International Edition* **2018**, *57*, 102.

[278] D. Di Lecce, J. Hassoun, *Journal of Physical Chemistry C* **2015**, *119*, 20855.

[279] W. Xu, J. Wang, F. Ding, X. Chen, E. Nasybulin, Y. Zhang, J. G. Zhang, *Energy Environ Sci* **2014**, *7*, 513.

[280] B. W. Zewde, S. Admassie, J. Zimmermann, C. S. Isfort, B. Scrosati, J. Hassoun, *ChemSusChem* **2013**, *6*, 1400.

[281] M. Wetjen, M. A. Navarra, S. Panero, S. Passerini, B. Scrosati, J. Hassoun, *ChemSusChem* **2013**, *6*, 1037.

[282] G. Derrien, J. Hassoun, S. Sacchetti, S. Panero, *Solid State Ion* **2009**, *180*, 1267.

[283] J. Wang, Y. Wang, X. Zhu, X. Lu, *Journal of Physical Chemistry Letters* **2013**, *4*, 1718.

[284] I. Hasa, S. Mariyappan, D. Saurel, P. Adelhelm, A. Y. Koposov, C. Masquelier, L. Croguennec, M. Casas-Cabanas, *J Power Sources* **2021**, *482*, 228872.

[285] I. U. Mohsin, L. Schneider, Z. Yu, W. Cai, C. Ziebert, *International Journal of Electrochemistry* **2023**, *2023*, 1.

[286] E. Gucciardi, M. Galceran, A. Bustinza, E. Bekaert, M. Casas-Cabanas, E. Gucciardi, *JPhys Materials* **2021**, *4*, 034002.

[287] S. Altundag, S. Altin, S. Yaşar, E. Altin, *Vacuum* **2023**, *210*, 111853.

[288] D. Di Lecce, T. Hu, J. Hassoun, *J Alloys Compd* **2017**, *693*, 730.

[289] L. Lutterotti, *Nucl Instrum Methods Phys Res B* **2010**, *268*, 334.

[290] X. Y. Li, B. Zhang, Z. G. Zhang, L. H. He, H. Li, X. J. Huang, F. W. Wang, *Powder Diffr* **2014**, *29*, 248.

[291] M. Kope¢, A. Yamada, G. Kobayashi, S. Nishimura, R. Kanno, A. Mauger, F. Gendron, C. M. Julien, *J Power Sources* **2009**, *189*, 1154.

[292] P. B. Moore, *American Mineralogist* **1972**, *57*, 1333.

[293] R. Morasch, B. Suthar, H. A. Gasteiger, *J Electrochem Soc* **2020**, *167*, 100540.

[294] D. Wyrzykowski, E. Hebanowska, G. Nowak-Wiczk, M. Makowski, L. Chmurzyński, *J Therm Anal Calorim* **2011**, *104*, 731.

[295] M. M. Barbooti, D. A. Al-Sammerrai, *Thermochim Acta* **1986**, *98*, 119.

[296] A. Ben Mayza, M. Ramanathan, R. Radhakrishnan, S. Ha, V. Ramani, J. Prakash, K. Zaghib, *ECS Trans* **2011**, *35*, 177.

[297] P. Kommu, G. P. Singh, A. S. Bhattacharyya, *J Energy Storage* **2018**, *16*, 156.

[298] D. Di Lecce, J. Hassoun, *ACS Omega* **2018**, *3*, 8583.

[299] C. Delacourt, P. Poizot, M. Morcrette, J.-M. Tarascon, C. Masquelier, *Chemistry of Materials* **2004**, *16*, 93.

[300] J. Chen, J. Graetz, *ACS Appl Mater Interfaces* **2011**, *3*, 1380.

[301] L. B. Mccusker, R. B. Von Dreele, D. E. Cox, D. Loue, P. Scardi, *International Union of Crystallography Journal of Applied Crystallography J. Appl. Cryst* **1999**, *32*, 36.

[302] B. H. Toby, *Powder Diffr* **2006**, *21*, 67.

[303] I. Belharouak, C. Johnson, K. Amine, *Electrochem commun* **2005**, *7*, 983.

[304] S. Brutti, J. Hassoun, B. Scrosati, C.-Y. Lin, H. Wu, H.-W. Hsieh, *J Power Sources* **2012**, *217*, 72.

[305] Y. Wang, Y. Wang, E. Hosono, K. Wang, H. Zhou, *Angewandte Chemie - International Edition* **2008**, *47*, 7461.

[306] D. Di Lecce, C. Fasciani, B. Scrosati, J. Hassoun, *ACS Appl Mater Interfaces* **2015**, *7*, 21198.

[307] G. Kobayashi, A. Yamada, S. ichi Nishimura, R. Kanno, Y. Kobayashi, S. Seki, Y. Ohno, H. Miyashiro, *J Power Sources* **2009**, *189*, 397.

[308] S. Wei, S. Inoue, D. Di Lecce, Z. Li, Y. Tominaga, J. Hassoun, *ChemElectroChem* **2020**, *7*, 2344.

[309] G. Bridgewater, M. J. Capener, J. Brandon, M. J. Lain, M. Copley, E. Kendrick, *Batteries* **2021**, *7*, 38.

[310] P. Xiao, Y. Cai, X. Chen, Z. Sheng, C. Chang, *RSC Adv* **2017**, *7*, 31558.

[311] Y. Wang, H. Yang, C.-Y. Wu, J.-G. Duh, *J Mater Chem A Mater* **2017**, *5*, 18674.

[312] J. Duan, G. Hu, Y. Cao, K. Du, Z. Peng, *Ionics (Kiel)* **2016**, *22*, 609.

[313] Q.-Y. Huang, Z. Wu, J. Su, Y.-F. Long, X.-Y. Lv, Y.-X. Wen, *Ceram Int* **2016**, *42*, 11348.

[314] V. Marangon, C. Hernández-Rentero, M. Olivares-Marín, V. Gómez-Serrano, Á. Caballero, J. Morales, J. Hassoun, *ChemSusChem* **2021**, *14*, 3333.

[315] Q. Wang, P. Ping, X. Zhao, G. Chu, J. Sun, C. Chen, *J Power Sources* **2012**, *208*, 210.

[316] J. Chen, Y. Yan, T. Sun, Y. Qi, X. Li, *J Electrochem Soc* **2014**, *161*, A1241.

[317] D. Saurel, M. Galceran, M. Reynaud, H. Anne, M. Casas-Cabanas, *Int J Energy Res* **2018**, *42*, 3258.

[318] A. S. Cooper, *Acta Crystallogr* **1962**, *15*, 578.

[319] R. Gupta, S. Saha, M. Tomar, V. K. Sachdev, V. Gupta, *Journal of Materials Science: Materials in Electronics* **2017**, *28*, 5192.

[320] W. Wazeer, M. M. Nabil, M. Feteha, M. B. Soliman, A. E.-H. B. Kashyout, *Sci Rep* **2022**, *12*, 16307.

[321] T. Boyadzhieva, V. Koleva, E. Zhecheva, D. Nihtianova, L. Mihaylov, R. Stoyanova, *RSC Adv* **2015**, *5*, 87694.

[322] B. Özdogru, H. Dykes, S. Padwal, S. Harimkar, Ö. Ö. Çapraz, *Electrochim Acta* **2020**, *353*, 136594.

[323] A. Saracibar, J. Carrasco, D. Saurel, M. Galceran, B. Acebedo, H. Anne, M. Lepoitevin, T. Rojo, M. Casas Cabanas, *Physical Chemistry Chemical Physics* **2016**, *18*, 13045.

[324] M. Galceran, V. Roddatis, F. J. Zúñiga, J. M. Pérez-Mato, B. Acebedo, R. Arenal, I. Peral, T. Rojo, M. Casas-Cabanas, *Chemistry of Materials* **2014**, *26*, 3289.

[325] J. Wang, Z. Xu, Q. Zhang, X. Song, X. Lu, Z. Zhang, A. J. Onyianta, M. Wang, M. Titirici, S. J. Eichhorn, *Advanced Materials* **2022**, *34*, 2206367.

[326] M. Giner, V. Roddatis, C. M. López, P. Kubiak, *J Electrochem Soc* **2016**, *163*, A650.

[327] F. Bianchini, H. Fjellvåg, P. Vajeeston, *Mater Chem Phys* **2018**, *219*, 212.

[328] N. Phattharasupakun, P. Bunyanidhi, P. Chiochan, N. Chanlek, M. Sawangphruk, *Electrochem commun* **2022**, *139*, 107309.

[329] J. Hwang, K. Matsumoto, T. Nohira, R. Hagiwara, *Electrochemistry* **2017**, *85*, 675.

[330] D. H. Baek, J. K. Kim, Y. J. Shin, G. S. Chauhan, J. H. Ahn, K. W. Kim, *J Power Sources* **2009**, *189*, 59.

[331] Y. Wang, Z. Cao, Z. Ma, G. Liu, H. Cheng, Y. Zou, L. Cavallo, Q. Li, J. Ming, *ACS Energy Lett* **2023**, *8*, 1477.

[332] Y. Pan, L. Gong, Y. Fu, L. Shi, C. Liu, Y. Pan, J. Yang, H. Zhang, X. Cheng, *Energy Storage Mater* **2022**, *52*, 238.

[333] Y. Wang, Z. Cao, W. Wahyudi, Z. Ma, Y. Liang, L. Cavallo, Q. Li, J. Ming, *Adv Energy Mater* **2023**, *13*, 2301354.

[334] Y. Zhu, Y. Xu, Y. Liu, C. Luo, C. Wang, *Nanoscale* **2013**, *5*, 780.

[335] J. E. B. Randles, *Discuss Faraday Soc* **1947**, *1*, 11.

[336] W. Weppner, R. A. Huggins, *J Electrochem Soc* **1977**, *124*, 1569.

[337] K. Tang, X. Yu, J. Sun, H. Li, X. Huang, *Electrochim Acta* **2011**, *56*, 4869.

[338] C. Heubner, S. Heiden, M. Schneider, A. Michaelis, *Electrochim Acta* **2017**, *233*, 78.

[339] S. D. Kang, W. C. Chueh, *J Electrochem Soc* **2021**, *168*, 120504.

[340] Z. Geng, Y.-C. Chien, M. J. Lacey, T. Thiringer, D. Brandell, *Electrochim Acta* **2022**, *404*, 139727.

[341] A. Baldinelli, A. Staffolani, F. Nobili, L. Barelli, *J Energy Storage* **2023**, *73*, 109117.

[342] A. Ch. Lazanas, M. I. Prodromidis, *ACS Measurement Science Au* **2023**, *3*, 162.

[343] B. Manikandan, V. Ramar, C. Yap, P. Balaya, *J Power Sources* **2017**, *361*, 300.

[344] J. Illig, M. Ender, T. Chrobak, J. P. Schmidt, D. Klotz, E. Ivers-Tiffée, *J Electrochem Soc* **2012**, *159*, A952.

[345] J. P. Schmidt, T. Chrobak, M. Ender, J. Illig, D. Klotz, E. Ivers-Tiffée, *J Power Sources* **2011**, *196*, 5342.

[346] G. Barbero, I. Lelidis, *Physical Chemistry Chemical Physics* **2017**, *19*, 24934.

[347] G. Ali, J. H. Lee, D. Susanto, S. W. Choi, B. W. Cho, K. W. Nam, K. Y. Chung, *ACS Appl Mater Interfaces* **2016**, *8*, 15422.

[348] F. Pouraghajan, H. Knight, M. Wray, B. Mazzeo, R. Subbaraman, J. Christensen, D. Wheeler, *J Electrochem Soc* **2018**, *165*, A2644.

[349] T. Nedoseykina, M. G. Kim, S. A. Park, H. S. Kim, S. B. Kim, J. Cho, Y. Lee, *Electrochim Acta* **2010**, *55*, 8876.

[350] M. Giorgetti, M. Berrettoni, S. Scaccia, S. Passerini, *Inorg Chem* **2006**, *45*, 2750.

[351] H.-W. Chang, Y.-R. Lu, J.-L. Chen, C.-L. Chen, J.-F. Lee, J.-M. Chen, Y.-C. Tsai, C.-M. Chang, P.-H. Yeh, W.-C. Chou, Y.-H. Liou, C.-L. Dong, *Nanoscale* **2015**, *7*, 1725.

[352] A. Perea, L. Castro, L. Aldon, L. Stievano, R. Dedryvère, D. Gonbeau, N. Tran, G. Nuspl, J. Bréger, C. Tessier, *J Solid State Chem* **2012**, *192*, 201.

[353] S. Pongha, B. Seekoaon, W. Limphirat, P. Kidkhunthod, S. Srilomsak, Y. M. Chiang, N. Meethong, *Adv Energy Mater* **2015**, *5*, 1500663.

[354] A. Iadecola, A. Perea, L. Aldon, G. Aquilanti, L. Stievano, *J Phys D Appl Phys* **2017**, *50*, 144004.

[355] O. Haas, A. Deb, E. J. Cairns, A. Wokaun, *J Electrochem Soc* **2005**, *152*, A191.

[356] L. Wang, H. Zhang, Q. Liu, J. Wang, Y. Ren, X. Zhang, G. Yin, J. Wang, P. Zuo, *ACS Appl Energy Mater* **2018**, *1*, 5928.

[357] Y. Huang, J. Fang, F. Omenya, M. O'Shea, N. A. Chernova, R. Zhang, Q. Wang, N. F. Quackenbush, L. F. J. Piper, D. O. Scanlon, M. S. Whittingham, *J Mater Chem A Mater* **2014**, *2*, 12827.

[358] Y.-K. Hou, G.-L. Pan, Y.-Y. Sun, X.-P. Gao, *ACS Appl Mater Interfaces* **2018**, *10*, 16500.

[359] Z. Lei, J. Wang, J. Yang, Y. Nuli, Z. Ma, *ACS Appl Mater Interfaces* **2018**, *10*, 43552.

[360] T. Ruan, B. Wang, F. Wang, R. Song, F. Jin, Y. Zhou, D. Wang, S. Dou, *Nanoscale* **2019**, *11*, 3933.

[361] D. Kong, H. Chen, F. Wu, R. Zhang, J. Li, Y. Mai, Y. Wei, J. Wang, X. Dai, *Electrochim Acta* **2024**, *506*, 145060.

[362] F. Croce, A. D'Epifanio, J. Hassoun, A. Deptula, T. Olczac, B. Scrosati, *Electrochemical and Solid-State Letters* **2002**, *5*, A47.

[363] Y. Liu, J. Manuel, X. Zhao, AnupriyaK. Haridas, GhanshyamS. Chauhan, J.-K. Kim, K.-K. Cho, H.-J. Ahn, J.-H. Ahn, *Sci Adv Mater* **2017**, *9*, 1266.

[364] Y. Gao, L. Zhang, S. Feng, W. Shen, S. Guo, *Journal of Solid State Electrochemistry* **2018**, *22*, 285.

[365] V. A. Nguyen, C. Kuss, *J Electrochem Soc* **2020**, *167*, 065501.

[366] J. Holloway, F. Maddar, M. Lain, M. Loveridge, M. Copley, E. Kendrick, D. Greenwood, *Batteries* **2020**, *6*, 57.

[367] J. T. Frith, M. J. Lacey, U. Ulissi, *Nat Commun* **2023**, *14*, 420.

[368] E. Lyle, R. Vaeli, A. Dutta, M. Metzger, *J Electrochem Soc* **2022**, *169*, 060526.

[369] G. Apachitei, R. Heymer, M. Lain, D. Dogaru, M. Hidalgo, J. Marco, M. Copley, *Batteries* **2023**, *9*, 518.

[370] A. S. Menon, N. Shah, J. A. Gott, E. Fiamegkou, M. J. W. Ogley, G. J. Páez Fajardo, N. Vaenas, I. Ellis, N. Ravichandran, P. Cloetens, D. Karpov, J. M. Warnett, P. Malliband, D. Walker, G. West, M. Loveridge, L. F. J. Piper, *PRX Energy* **2024**, *3*, 013004.

[371] E. Guk, M. F. Niri, T. A. Vincent, G. Apachitei, C. Briggs, B. Gulsoy, S. Chao, Z. Guo, J. E. H. Sansom, J. Marco, *J Power Sources* **2024**, *614*, 235063.

[372] L. S. de Vasconcelos, R. Xu, J. Li, K. Zhao, *Extreme Mech Lett* **2016**, *9*, 495.

[373] C. D. Reynolds, S. D. Hare, P. R. Slater, M. J. H. Simmons, E. Kendrick, *Energy Technology* **2022**, *10*, 2200545.

[374] W. B. Hawley, J. Li, *J Energy Storage* **2019**, *26*, 100994.

[375] C. Reynolds, M. Faraji Niri, M. F. Hidalgo, R. Heymer, L. Román, G. Alsofi, H. Khanom, B. Pye, J. Marco, E. Kendrick, *Batter Supercaps* **2024**, *7*, e202300396.

[376] M. Abdollahifar, H. Cavers, S. Scheffler, A. Diener, M. Lippke, A. Kwade, *Adv Energy Mater* **2023**, *13*, 2300973.

[377] A. van Bommel, R. Divigalpitiya, *J Electrochem Soc* **2012**, *159*, A1791.

[378] C. Seidl, S. Thieme, M. Frey, K. Nikolowski, A. Michaelis, *Batteries* **2024**, *10*, 105.

[379] D. W. Kim, S. M. Hwang, J. B. Yoo, Y. Kim, *ChemElectroChem* **2020**, *7*, 2621.

[380] Y. Liu, H. Zhang, Z. Huang, Q. Wang, M. Guo, M. Zhao, D. Zhang, J. Wang, P. He, X. Liu, M. Terrones, Y. Wang, *J Alloys Compd* **2022**, *905*, 164205.

[381] S. Hamed, F. Obrezkov, S. Huotari, M. Colalongo, S. Mousavihashemi, T. Kallio, *J Power Sources* **2024**, *608*, 234549.

[382] C. Heubner, S. Maletti, O. Lohrberg, T. Lein, T. Liebmann, A. Nickol, M. Schneider, A. Michaelis, *Batter Supercaps* **2021**, *4*, 1310.

[383] V. Augustyn, J. Come, M. A. Lowe, J. W. Kim, P.-L. Taberna, S. H. Tolbert, H. D. Abruña, P. Simon, B. Dunn, *Nat Mater* **2013**, *12*, 518.

[384] M. J. Lain, J. Brandon, E. Kendrick, *Batteries* **2019**, *5*, 64.

[385] Y. Zhang, H. Wang, Z. Li, X. Ge, K. Huang, J. Q. Huang, L. Huang, Z. Li, Y. Huang, *Adv Energy Mater* **2024**, 2403804.

[386] J. Sharma, R. Tao, G. Polizos, N. Kanbargi, B. LaRiviere, J. Li, *J Energy Storage* **2024**, *79*, 110161.

[387] C. X. Zu, H. Li, *Energy Environ Sci* **2011**, *4*, 2614.

[388] D. Larcher, J. M. Tarascon, *Nat Chem* **2015**, *7*, 19.

[389] W. Hua, B. Schwarz, R. Azmi, M. Müller, M. S. Dewi Darma, M. Knapp, A. Senyshyn, M. Heere, A. Missyul, L. Simonelli, J. R. Binder, S. Indris, H. Ehrenberg, *Nano Energy* **2020**, *78*, 105231.

[390] L. Minnetti, V. Marangon, P. Andreotti, A. Staffolani, F. Nobili, J. Hassoun, *Electrochim Acta* **2023**, *452*, 142263.

[391] D. Di Lecce, D. Campanella, J. Hassoun, *Journal of Physical Chemistry C* **2018**, *122*, 23925.

[392] C. Julien, A. Mauger, K. Zaghib, H. Groult, *Materials* **2016**, *9*, 595.

[393] D. Di Lecce, S. Levchenko, F. Iacoviello, D. J. L. Brett, P. R. Shearing, J. Hassoun, *ChemSusChem* **2019**, *12*, 3550.

[394] D. Di Lecce, R. Verrelli, J. Hassoun, *Electrochim Acta* **2016**, *220*, 384.

[395] W. Luo, J.-J. Gaumet, L.-Q. Mai, *Rare Metals* **2017**, *36*, 321.

[396] G. A. Elia, J. Hassoun, *ChemElectroChem* **2017**, *4*, 2164.

[397] D. Di Lecce, P. Andreotti, M. Boni, G. Gasparro, G. Rizzati, J. Y. Hwang, Y. K. Sun, J. Hassoun, *ACS Sustain Chem Eng* **2018**, *6*, 3225.

[398] S. Fang, F. Wu, M. Zarrabeitia, M. Kuenzel, D. Roscher, X. Gao, J. Kim, G. Kim, S. Passerini, *Batter Supercaps* **2022**, *5*, e202200286.

[399] Q. Li, Y. Wu, Z. Wang, H. Ming, W. Wang, D. Yin, L. Wang, H. N. Alshareef, J. Ming, *ACS Appl Mater Interfaces* **2020**, *12*, 16276.

[400] Y. Wu, L. Xie, X. He, L. Zhuo, L. Wang, J. Ming, *Electrochim Acta* **2018**, *265*, 115.

[401] M. Haruta, T. Moriyasu, A. Tomita, T. Takenaka, T. Doi, M. Inaba, *J Electrochem Soc* **2018**, *165*, A1874.

[402] E. Barcaro, V. Marangon, M. Mutarelli, J. Hassoun, *J Power Sources* **2024**, *595*, 234059.

[403] G. Gabrielli, M. Marinaro, M. Mancini, P. Axmann, M. Wohlfahrt-Mehrens, *J Power Sources* **2017**, *351*, 35.

[404] I. Hasa, S. Passerini, J. Hassoun, *J Mater Chem A Mater* **2017**, *5*, 4467.

[405] D. DiLecce, V. Marangon, M. Isaacs, R. Palgrave, P. R. Shearing, J. Hassoun, *Small Methods* **2021**, *5*, 2100596.

[406] J. Hassoun, G. Derrien, S. Panero, B. Scrosati, *Advanced Materials* **2008**, *20*, 3169.

[407] K. S. Park, M. H. Cho, S. J. Jin, K. S. Nahm, Y. S. Hong, *Solid State Ion* **2004**, *171*, 141.

[408] Y. J. Gu, Q. G. Zhang, Y. B. Chen, H. Q. Liu, J. X. Ding, Y. M. Wang, H. F. Wang, L. Chen, M. Wang, S. W. Fan, Q. F. Zang, X. L. Yang, *J Alloys Compd* **2015**, *630*, 316.

[409] M. D. Radin, S. Hy, M. Sina, C. Fang, H. Liu, J. Vinckeviciute, M. Zhang, M. S. Whittingham, Y. S. Meng, A. Van der Ven, *Adv Energy Mater* **2017**, *7*, 1602888.

[410] M. Zukalova, J. Prochazka, B. Pitna Laskova, A. Zukal, L. Kavan, *ECS Trans* **2018**, *87*, 67.

[411] M. Eilers-Rethwisch, M. Winter, F. M. Schappacher, *J Power Sources* **2018**, *387*, 101.

[412] H. Gupta, S. K. Singh, N. Srivastava, D. Meghnani, R. K. Tiwari, R. Mishra, A. Patel, A. Tiwari, A. L. Saroj, R. K. Singh, *ACS Appl Energy Mater* **2021**, *4*, 13878.

[413] Ahmed. M. Hashem, Rasha. S. El-Tawil, M. Abutabl, Ali. E. Eid, *Research on Engineering Structures & Materials* **2015**, *1*, 2.

[414] V. Hebbar, M. Viji, A. K. Budumuru, S. Gautam, K. H. Chae, K. Balaji, N. T. Kalyana Sundaram, A. K. Subramani, C. Sudakar, *ACS Appl Mater Interfaces* **2020**, *12*, 32566.

[415] D. Ren, Y. Yang, L. Shen, R. Zeng, H. D. Abruña, *J Power Sources* **2020**, *447*, 227344.

[416] J. Kasnatscheew, B. Streipert, S. Röser, R. Wagner, I. Cekic Laskovic, M. Winter, *Physical Chemistry Chemical Physics* **2017**, *19*, 16078.

[417] J. Demeaux, M. Caillon-Caravanier, H. Galiano, D. Lemordant, B. Claude-Montigny, *J Electrochem Soc* **2012**, *159*, A1880.

[418] G. A. Elia, J. Wang, D. Bresser, J. Li, B. Scrosati, S. Passerini, J. Hassoun, *ACS Appl Mater Interfaces* **2014**, *6*, 12956.

[419] L. Fang, M. Chen, K.-W. Nam, Y.-M. Kang, *Batteries* **2022**, *8*, 132.

[420] N. Yabuuchi, K. Yoshii, S. T. Myung, I. Nakai, S. Komaba, *J Am Chem Soc* **2011**, *133*, 4404.

[421] M. N. Ates, S. Mukerjee, K. M. Abraham, *J Electrochem Soc* **2014**, *161*, A355.

[422] S. Tan, Z. Zhang, Y. Li, Y. Li, J. Zheng, Z. Zhou, Y. Yang, *J Electrochem Soc* **2013**, *160*, A285.

[423] J. Chen, H. Yang, T. Li, C. Liu, H. Tong, J. Chen, Z. Liu, L. Xia, Z. Chen, J. Duan, L. Li, *Front Chem* **2019**, *7*, 500.

[424] T. Aida, T. Toma, S. Kanada, *Journal of Solid State Electrochemistry* **2020**, *24*, 1415.

[425] L. Zhu, C. Bao, L. Xie, X. Yang, X. Cao, *J Alloys Compd* **2020**, *831*, 154864.

[426] S. Liu, B. Wang, X. Zhang, S. Zhao, Z. Zhang, H. Yu, *Matter* **2021**, *4*, 1511.

[427] H. Sun, K. Zhao, *The Journal of Physical Chemistry C* **2017**, *121*, 6002.

[428] Y.-F. Deng, S.-X. Zhao, Y.-H. Xu, C.-W. Nan, *Appl Surf Sci* **2015**, *351*, 209.

[429] M. Agostini, S. Brutti, J. Hassoun, *ACS Appl Mater Interfaces* **2016**, *8*, 10850.

[430] J. Hassoun, K. S. Lee, Y. K. Sun, B. Scrosati, *J Am Chem Soc* **2011**, *133*, 3139.

[431] D. J. Lee, J. W. Park, I. Hasa, Y. K. Sun, B. Scrosati, J. Hassoun, *J Mater Chem A Mater* **2013**, *1*, 5256.

[432] V. Marangon, E. Barcaro, F. De Boni, M. Prato, D. Bresser, J. Hassoun, *Adv Sustain Syst* **2024**, *8*, 2400268.

[433] L. Y. Kuo, A. Moradabadi, H. F. Huang, B. J. Hwang, P. Kaghazchi, *J Power Sources* **2017**, *341*, 107.

[434] J. S. Weaving, A. Lim, J. Millichamp, T. P. Neville, D. Ledwoch, E. Kendrick, P. F. McMillan, P. R. Shearing, C. A. Howard, D. J. L. Brett, *ACS Appl Energy Mater* **2020**, *3*, 7474.

[435] S. Komaba, Y. Matsuura, T. Ishikawa, N. Yabuuchi, W. Murata, S. Kuze, *Electrochem commun* **2012**, *21*, 65.

[436] B. Zhang, G. Rousse, D. Foix, R. Dugas, D. A. D. Corte, J. Tarascon, *Advanced Materials* **2016**, *28*, 9824.

[437] S. Komaba, T. Ishikawa, N. Yabuuchi, W. Murata, A. Ito, Y. Ohsawa, *ACS Appl Mater Interfaces* **2011**, *3*, 4165.

ACKNOWLEDGEMENTS

After this three-year path, there are many people who deserve a mention and a special thanks.

Firstly, I would like to thank my supervisor Prof. Francesco Nobili for giving me the chance to undertake the PhD journey, and for all the advice and the teachings through these three years; Prof. Miguel Ángel Muñoz-Márquez, for additional help and advices during the time spent in Camerino; Prof. Ivana Hasa for hosting me and for the beautiful time spent in Warwick Manufacturing Group (WMG) Coventry, UK, and for giving me the opportunity to learn new things and improve my knowledge; Dr. Faduma Maddar, Dr. Anupriya K. Haridas, and Dr. Matthew Capener for helping me during my research in WMG and for the contribution to some of the data of this thesis; Dr. Jusef Hassoun for hosting me at University of Ferrara, Italy, for all the advices during all these years and for introducing me in the world of electrochemistry during my Bachelor degree; Dr. Vittorio Marangon for the great help and effort during my research in Ferrara, for all the precious advice during these years, and for being a good colleague and friend; Dr. Javad Rezvani and Francesco Paparoni of the UNICAM Physics Department, and Dr. Andrea Zitolo and Dr. Emiliano Fonda of the SOLEIL Synchrotron (SAMBA beamline), Paris, France, for the help and for contributing to this work.

In second place, I would like to thank my parents and my sister Ilaria, who supported me during this journey and always encouraged me to follow my way. I would also like to thanks my dear friends Luca and Chiara for all their support and for putting up with me.

Finally, I want to thank all the people who I met and collaborated with during these three years. First a special mention goes to Leonardo, Antunes and Asia, for being fantastic colleagues and friends, and for helping and advising me, and, more important, celebrating achievements through this incredible journey, your contribution to this work was fundamental; Luca, Leonardo, Hamideh, Maddalena, Federico, and all the other people who share with me the electrochemistry laboratories in Camerino; Sonila, Benedetta, Noemi, Dario, Sara, Francesca, and all the other people who I met in UNICAM for your support and for all the fun moments that we share together; Paolo, Carla, Noah, Jacob, Teena, Jishnu, Alex and all the other people who I met in WMG for welcoming me and for the good moments we spent together. At the very end, I would also thank all the other people I met and hung out with during these three years, each one of you somehow left me something which made this journey special.